Analysis of B^0 decay to the Charmless Final State $K_S^0\pi^+\pi^-$ at the *BABAR* Experiment

Kelly Elizabeth Ford

A thesis submitted for the degree of
Doctor of Philosophy

Particle Physics Group,
School of Physics and Astronomy,
The University of Birmingham.

February 2005.

Abstract

This thesis investigates neutral B decays to the charmless final state $K^0_S\pi^+\pi^-$ using a sample of $210\,\mathrm{fb}^{-1}$ of data collected by the *BABAR* detector using the PEP-II collider at SLAC. The branching ratios ($\mathcal{B}$) measured are:

$$
\begin{aligned}
\mathcal{B}(B^0 \to K^0\pi^+\pi^- \text{ Inclusive}) &= 43.0 \pm 2.3 \pm 2.3 \times 10^{-6} \\
\mathcal{B}(B^0 \to K^0_S\pi^+\pi^- \text{ nonresonant}) &< 2.1 \times 10^{-6} \\
\mathcal{B}(B^0 \to K^{**\pm}\pi^\mp, K^{**\pm} \to K^0\pi^\pm) &= 24.4 \pm 2.6 \pm 0.9 \times 10^{-6} \\
\mathcal{B}(B^0 \to \rho^0 K^0_S) &= 4.0 \pm 1.0 \pm 0.5 \times 10^{-6} \\
\mathcal{B}(B^0 \to f_0 K^0_S) &= 5.5 \pm 0.7 \pm 0.5 \times 10^{-6} \\
\mathcal{B}(B^0 \to K^{*+}\pi^-) &= 11.0 \pm 1.5 \pm 0.5 \times 10^{-6}
\end{aligned}
$$

In all cases, the first uncertainty is statistical and the second is systematic. An upper limit was set for the nonresonant branching ratio because the significance of the result was only 2.75σ. The result of the $B^0 \to \rho^0 K^0_S$ measurement was significant at the 3.6σ level, which the *BABAR* Collaboration considers to be evidence of the decay, but not observation. The term K^{**} is a collective term for the $K^*_0(1430)$, $K^*_2(1430)$, $K^*(1410)$ and $K^*(1680)$ resonances. The charge asymmetry ($\mathcal{A}_{CP}$) in $B^0 \to K^{*+}\pi^-$ was measured to be:

$$
\mathcal{A}_{CP}(B^0 \to K^{*+}\pi^-) = -0.11 \pm 0.14 \pm 0.05
$$

Acknowledgements

I have a lot of people to thank. I hope that I haven't forgotten anyone. If I have, my most sincere apologies.

Thanks to Manny Olaiya, with whom I worked on the previous iteration of this analysis, for the time, the work, the help and the laughs. Thanks to Alan Watson, a great supervisor, for the help, advice and our endless rantings about American politics. Thanks to Chris Hawkes, Theresa and Paul Harrison, and the Birmingham Babarians for all their help, support, and company. Everyone in the Particle Physics group at the University of Birmingham has been so good to work with, and I thank them for their friendliness and the good working environment. Thanks to PPARC for funding me, and allowing me to experience life at SLAC.

Thanks also to Dr. David Brown, who inspired me to do this degree, and set me on the correct path along with the rest of the Department of Physics at the University of Louisville. I'd also like to thank the members of the *BABAR* Experiment (particularly the Charmless 3-body AWG) and all those who run the PEP-II facility for all their hard work and expertise, and for allowing me to ask questions, however basic.

Thanks to Saher, Bradley, Fiona, all of my patient officemates and the friends

I've made whilst at Birmingham.

Jack, Jamie, Marc and all the rest of the British Babarians: thanks for the help, the laughs, the booze and for being the "bit of home" during our time at SLAC. You helped to make it a fantastic experience, and to make Thanksgiving 2002 one that I'll never forget.

Melissa, Nadia, Lucie and all my mates who have been so supportive, however much you can't understand why I'd ever want to study physics. Thanks for providing an outlet for my frustration and a getaway to the normal world.

Sian, thanks for your support, your assurances that it was everyone else who was mad, and for your friendship. California, Birmingham and The Walkabout would never have been as enjoyable without you.

Tom: I could never have got through this without you. Your patience and your ridiculous fountain of knowledge have helped me immeasurably, both academically and personally. Sharing this experience with you has made it special, and I look forward to our next adventure, whatever it may be.

Mum, Dad, Andrew and the rest of my family - you have all been so supportive, never questioning whether or not I should pursue this, and keeping the "When are you getting a proper job?"'s to a minimum. Thanks for letting me go to America, for being the best reason to come back and for regularly visiting me when I'm long plane rides away. Thanks for all the love and everything ever.

Kelly, 2005

Declaration

No part of the work in this thesis has been previously presented to any university to fulfil the requirements for a higher degree. The data used in the analysis were collected at the *BABAR* Experiment by the *BABAR* Collaboration, of which I have been a contributing member throughout my time as a Ph.D. student.

For this analysis I have used code available to all *BABAR* members in conjunction with code and techniques developed by myself and Emmanuel Olaiya for a previous iteration of the analysis. The data analysis presented here is my own work.

Contents

List of Tables

List of Figures

Chapter 1

CP Violation in the B meson system

1.1 Introduction

One of the most intriguing questions that arises out of the Standard Model is why the universe is mostly composed of matter, as opposed to anti-matter. Our universe is made up almost solely of u and d quarks and the leptons, but the Big Bang theory predicts that, if the initial state was symmetric, as much anti-matter should have been created as matter in the initial explosion. So, where did all that anti-matter go? Anti-matter can annihilate with matter, but since both are destroyed, it cannot all have disappeared in this manner or else all the matter would also not exist.

Therefore, there must exist some asymmetry between matter and anti-matter in the laws of the universe. In the Standard Model, the asymmetry is described by CP violation. The C operator describes the charge conjugation of the quantum numbers of a particle, thereby transforming a particle into its anti-particle. P inverts space, such that $t \to t$ and $\vec{r} \to -\vec{r}$ and is known as the parity operator. In 1956 [1], it was discovered that weak interactions were not invariant under the separate C and P

transformations, and in 1964 Cronin and Fitch [2] found evidence for CP violation in the decay of K^0 mesons by proving that $K^0_L \to \pi^+\pi^-$ occurs. This violation of the simultaneous transformation of C and P proves an asymmetry between matter and anti-matter in weak decays.

The *BABAR* experiment was built to continue the work already done on CP violation with the kaon system, by examining the violation that exists in the B_d meson system. B mesons are a bound state of a b quark and an anti-quark. A bound state of a $b\overline{b}$ pair is known as an $\Upsilon(4S)$ resonance, and 5 states of this resonance have been observed. The Υ(4S) state lies marginally above the energy of a B^+B^- (B^+ is a $\overline{b}u$ state) or $B^0\overline{B^0}$ (B^0 is a $\overline{b}d$ state) pair and always decays to a $B\overline{B}$ pair. A B_s system (where the d quark is replaced by an s quark) also exists, but is too heavy to be produced by the decay of the Υ(4S) resonance. In this thesis references to the B meson system refer to the B_d meson system.

1.2 CP Violation

1.2.1 The CKM Matrix

Within the three generations of fundamental particles in the Standard Model, the weak interaction couples to the left-handed types of these particles. The left-handed quarks can be arranged into doublets:

$$\begin{pmatrix} u \\ d' \end{pmatrix}_L, \quad \begin{pmatrix} c \\ s' \end{pmatrix}_L, \quad \begin{pmatrix} t \\ b' \end{pmatrix}_L \tag{1.1}$$

where the unprimed quarks are the mass eigenstates and the primes denote the weak eigenstates of the quarks which are linear combinations of the mass eigenstates. Since the weak interaction couples to the weak eigenstates, it is possible for the weak charge current to change the flavour of a quark. A quark mixing matrix can be used to transform the mass eigenstates into the weak eigenstates. This matrix is known as the Cabibbo-Kobayashi-Maskawa (CKM) quark mixing matrix [3].

With six quark flavours, quark mixing can be represented as:

$$\begin{pmatrix} d' \\ s' \\ b' \end{pmatrix} = V \begin{pmatrix} d \\ s \\ b \end{pmatrix} \tag{1.2}$$

where V is the CKM matrix. The CKM matrix is unitary and any phases are required to be non-trivial (a redefinition of the fields cannot lead to the phase being zero). These two conditions lead to the CKM matrix consisting of four free parameters (3 mixing angles and a phase angle). In terms of relationships between quarks, V can be written in the following way:

$$V_{CKM} = \begin{pmatrix} V_{ud} & V_{us} & V_{ub} \\ V_{cd} & V_{cs} & V_{cb} \\ V_{td} & V_{ts} & V_{tb} \end{pmatrix} \tag{1.3}$$

Each V_{ij} represents a complex number, and gives the coupling between quarks i and j. The Particle Data Group (PDG) have adopted the parameterisation:

$$\begin{aligned} V_{CKM} &= \begin{pmatrix} 1 & 0 & 0 \\ 0 & c_{23} & s_{23} \\ 0 & -s_{23} & c_{23} \end{pmatrix} \begin{pmatrix} c_{13} & 0 & s_{13}e^{-i\delta_{13}} \\ 0 & 1 & 0 \\ -s_{13}e^{i\delta_{13}} & 0 & c_{13} \end{pmatrix} \begin{pmatrix} c_{12} & s_{12} & 0 \\ -s_{12} & c_{12} & 0 \\ 0 & 0 & 1 \end{pmatrix} \\ &= \begin{pmatrix} c_{12}c_{13} & s_{12}c_{13} & s_{13}e^{-i\delta} \\ -s_{12}c_{23} - c_{12}c_{23}s_{13}e^{-i\delta} & c_{12}c_{23} - s_{12}s_{23}s_{13}e^{-i\delta} & s_{23}c_{13} \\ s_{12}c_{23} - c_{12}c_{23}s_{13}e^{-i\delta} & -c_{12}s_{23} - s_{12}c_{23}s_{13}e^{-i\delta} & c_{23}c_{13} \end{pmatrix} \end{aligned} \tag{1.4}$$

in which $c_{ij} = \cos\theta_{ij}$ and $s_{ij} = \sin\theta_{ij}$ where $i, j = 1, 2, 3$ (the generations), and θ_{12}, θ_{13}, θ_{23} and δ_{13} are all free, real parameters. However, c_{23} and c_{13} are approximately equal to 1. It is because there are few free parameters describing the matrix that the theory is able to be experimentally tested.

Perhaps the most popular parameterisation is the Wolfenstein parameterisation, which is an approximation using the powers of $\lambda = V_{us} \approx 0.22$. V_{cb} is defined as $A\lambda^2$

and V_{ub} as $A\lambda^3(\rho - i\eta)$, where A, ρ and η represent real numbers of the order of 1.

$$V_{CKM} = \begin{pmatrix} 1-\lambda^2/2 & \lambda & A\lambda^3(\rho - i\eta) \\ -\lambda & 1-\lambda^2/2 & A\lambda^2 \\ A\lambda^3(1-\rho-i\eta) & -A\lambda^2 & 1 \end{pmatrix} + \mathcal{O}(\lambda^4) \tag{1.5}$$

λ and A have been determined experimentally (via analyses of the semi-leptonic decays of K mesons and B mesons respectively). However, the parameters ρ and η are not well determined. Since they are related to the *CP* violating phase δ, *BABAR* aims to measure these quantities from their relations to the Unitarity Triangle.

1.2.2 Unitarity Triangles

The CKM matrix satisfies unitarity such that $V^\dagger V = U$, where U is the identity matrix.

$$\begin{pmatrix} V_{ud}^* & V_{cd}^* & V_{td}^* \\ V_{us}^* & V_{cs}^* & V_{ts}^* \\ V_{ub}^* & V_{cb}^* & V_{tb}^* \end{pmatrix} \begin{pmatrix} V_{ud} & V_{us} & V_{ub} \\ V_{cd} & V_{cs} & V_{cb} \\ V_{td} & V_{ts} & V_{tb} \end{pmatrix} = \begin{pmatrix} 1 & 0 & 0 \\ 0 & 1 & 0 \\ 0 & 0 & 1 \end{pmatrix} \tag{1.6}$$

From the above equality come nine equations which represent different systems of particles. There are three of these equations of particular interest for Standard Model predictions.

Equation 1.7 represents the s quark transition to a d quark, which is the case of $K^0 - \overline{K^0}$ mixing.

$$V_{us}^* V_{ud} + V_{cs}^* V_{cd} + V_{ts}^* V_{td} = 0 \tag{1.7}$$

Equation 1.8 describes the transition of b to s and is the mechanism for $B_s^0 - \overline{B_s^0}$ mixing.

$$V_{ub}^* V_{us} + V_{cb}^* V_{cs} + V_{tb}^* V_{ts} = 0 \tag{1.8}$$

For the *BABAR* Experiment, Equation 1.9 is the most important as it describes the b to d decay of $B^0 - \overline{B^0}$ mixing.

$$V_{ub}^* V_{ud} + V_{cb}^* V_{cd} + V_{tb}^* V_{td} = 0 \tag{1.9}$$

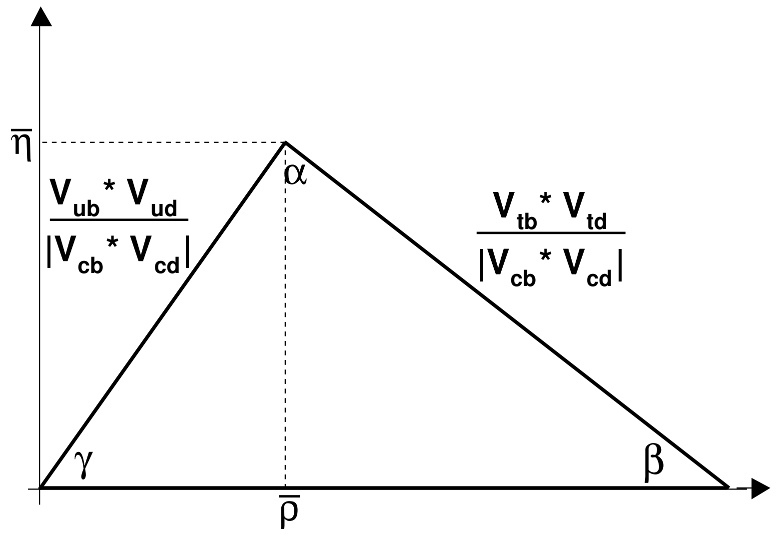

Figure 1.1: The $B^0-\overline{B^0}$ Unitarity Triangle, rotated such that $V_{cb}^*V_{cd}$ is real and scaled so that the real axis side is of length 1. $\rho' = \rho(1-\lambda^2/2)$, and $\eta' = \eta(1-\lambda^2/2)$, where$\rho$, η and λ are Wolfenstein parameters from the CKM matrix, and α, β and γ are the three angles of the Unitarity Triangle. Measuring all three angles and all three sides of the triangle to test Equation 1.9 are goals of the BABAR Experiment.

Since the summation of three components in each of the above equations is zero, it is possible to visually interpret them in the complex plane as triangles, which are known as the Unitarity Triangles. Figure 1.1 shows the Unitarity Triangle for the B meson system. The $K^0 - \overline{K^0}$ and $B_s^0 - \overline{B_s^0}$ triangles are very thin, almost a flat line, with one side much shorter than the other two. The larger angles and similar length sides in the triangle describing the B system mean that it is experimentally easier to measure.

1.3 Mixing in the Neutral B Sector

Mixing takes place within the neutral B meson system, where B^0 and $\overline{B}^0$ are the flavour eigenstates but not the mass eigenstates. The mixing box diagrams are shown in Figure 1.2, and show the second order weak interactions which enable any neutral self-conjugate pairs (such as K^0 and B^0) to mix. The particle which propagates the loop must be one of the quarks with charge 2/3, and therefore u, c or t. In the B meson system, the greater mass of the t means that the t quark loop gives the dominant contribution [4] and therefore $V_{td}V_{tb}^*$ is the dominant CKM factor in the matrix element. Thus, the CP violating phase δ enters the mixing amplitude via V_{td}.

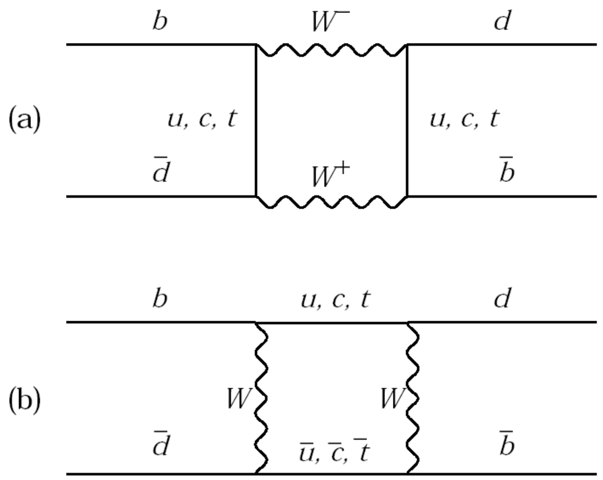

Figure 1.2: The box diagrams which show mixing between a B^0 and $\overline{B}^0$ [5].

The mass eigenstates, i.e. the eigenstates of the Hamiltonian which propagate through space, are linear combinations of the flavour eigenstates. They are called B_L (L for Light) and B_H (H for Heavy) and are written as:

$$\begin{aligned} |B_L\rangle &= p|B^0\rangle + q|\overline{B^0}\rangle \\ |B_H\rangle &= p|B^0\rangle - q|\overline{B^0}\rangle \end{aligned} \tag{1.10}$$

where the complex coefficients p and q are subject to:

$$| q |^2 + | p |^2 = 1 \tag{1.11}$$

This linear combination can be generalised to:

$$a|B^0\rangle + b|\overline{B^0}\rangle \tag{1.12}$$

which is governed by the time dependent Schrödinger equation:

$$i\frac{d}{dt}\begin{pmatrix} a \\ b \end{pmatrix} = H\begin{pmatrix} a \\ b \end{pmatrix} \equiv (M - \frac{i}{2}\Gamma)\begin{pmatrix} a \\ b \end{pmatrix} \tag{1.13}$$

where M is a 2×2 Hermitian matrix which stems from mixing[1] and Γ is also a 2×2 Hermitian matrix which is from the decays. $H_{11} = H_{22}$ due to CPT invariance, and H_{12} and H_{21} are $B^0 \rightleftharpoons \overline{B^0}$ transition amplitudes. If these matrix elements are zero, then mixing does not occur. The mass eigenstates become equal to the *CP* eigenstates if *CP* symmetry is imposed ($H_{12}^* = H_{21}$). Therefore, if B_L and B_H are *CP* eigenstates then $| p |=| q |$. Therefore, *CP* violation in mixing occurs if $| \frac{p}{q} |\neq 1$. Equation 1.13 has the following eigenstates:

$$\begin{aligned} (\Delta m_B)^2 - \frac{1}{2}(\Delta\Gamma_B)^2 &= 4\left(| M_{12} |^2 - \frac{1}{4}| \Gamma_{12} |^2\right) \\ \Delta m_B \Delta\Gamma_B &= 4\Re(M_{12}\Gamma_{12}^*) \end{aligned} \tag{1.14}$$

in which $\Delta m_B = M_H - M_L$ and $\Delta\Gamma_B = \Gamma_H - \Gamma_L$, the differences between the mass and lifetimes of the mass eigenstates. Experimental measurements show that $\Delta\Gamma_B \ll \Delta m_B$, which therefore also leads to $\Gamma_{12} \ll M_{12}$, which reduce Equations 1.14 to:

$$\Delta m_B \approx 2 | M_{12} |, \qquad \Delta\Gamma_B \approx 2\Re(M_{12}\Gamma_{12}^*)/ | M_{12} |, \tag{1.15}$$

The ratio p/q is described by:

$$\frac{p}{q} = -\frac{2(M_{12} - \frac{i}{2}\Gamma_{12})}{\Delta m_B - \frac{i}{2}\Delta\Gamma_B} \tag{1.16}$$

[1] The size of the off-diagonal element of the mixing matrix, M_{12}, is proportional to the mass of the quark in the loop [4]. Thus, the top quark provides the greatest contribution to the total matrix element for the mixing process.

which simplifies to

$$\frac{p}{q} \approx -\frac{M_{12}}{\mid M_{12} \mid}. \tag{1.17}$$

when using the above approximations. Therefore, calculations to first order give $\mid p/q \mid = 1$, and no *CP* violation in mixing, but the second order term can estimate the amount of violation.

An admixture of B_H and B_L can describe any B state. The amplitudes of the admixture, which are subject to evolution over time, obey:

$$\begin{aligned} a_H(t) &= a_H(0)e^{-iM_H t}e^{-\frac{1}{2}\Gamma_H t} \\ a_L(t) &= a_L(0)e^{-iM_L t}e^{-\frac{1}{2}\Gamma_L t}. \end{aligned} \tag{1.18}$$

These amplitudes enable the formulation of purely B^0 and $\overline{B}^0$ states. For the pure B^0 state, $|B^0_{phys}\rangle$, $a_L(0) = a_H(0) = 1/(2p)$ and for the pure $\overline{B}^0$ state, $|\overline{B}^0_{phys}\rangle$, $a_L(0) = -a_H(0) = 1/(2q)$. They can therefore be written:

$$\begin{aligned} |B^0_{phys}(t)\rangle &= g_+(t)|B^0\rangle + (q/p)g_-(t)|\overline{B}^0\rangle \\ |\overline{B}^0_{phys}(t)\rangle &= (q/p)g_-(t)|B^0\rangle + g_+(t)|\overline{B}^0\rangle \end{aligned} \tag{1.19}$$

where $M = (M_H + M_L)/2$ and $\Gamma = (\Gamma_H + \Gamma_L)/2$, and g_+ and g_- are defined as:

$$\begin{aligned} g_+(t) &= e^{-iMt}e^{-\Gamma t/2}\cos(\Delta m_B t/2) \\ g_-(t) &= e^{-iMt}e^{-\Gamma t/2} i\sin(\Delta m_B t/2). \end{aligned} \tag{1.20}$$

Oscillation will occur in an initially pure B^0 meson, such that it changes between a B^0 and a $\overline{B}^0$.

CP violation in mixing is one of three types of *CP* violation. The second kind is *CP* violation due to interference between the mixing and decay processes. This occurs in decays where both the B^0 and the $\overline{B}^0$ decay to the same final state, which is constrained to be a *CP* eigenstate. If A is the amplitude of the decay $B^0 \to f$ and $\overline{A}$ the amplitude for $\overline{B}^0 \to f$, the following quantity must be equal to unity if no *CP* violation is present:

$$\lambda_f = \frac{q}{p}\frac{\overline{A}}{A}. \tag{1.21}$$

The time-dependent asymmetry is defined to be

$$A_{CP}(t) = \frac{\Gamma(B \to f)(t) - \Gamma(\overline{B} \to f)(t)}{\Gamma(B \to f)(t) + \Gamma(\overline{B} \to f)(t)} \tag{1.22}$$

$$= \left(\frac{1- \mid \lambda_f \mid^2}{1+ \mid \lambda_f \mid^2}\right) \cos \Delta m_B t - \left(\frac{2\Im(\lambda_f)}{1+ \mid \lambda_f \mid^2}\right) \sin \Delta m_B t. \tag{1.23}$$

The *CP* violation in decay is described by the cosine term, which is zero if $\lambda_f = 1$, since $\mid p/q \mid \approx 1$. The sine term represents the interference between the decays and the mixing of the neutral Bs and is zero if $\Im(\lambda_f) = 0$. To measure the *CP* violation in such decays, it is crucial that the initial state of the decay (whether B^0 or $\overline{B}^0$) is known. Section 1.3.1 discusses the method implemented by the *BABAR* Collaboration.

The third type of *CP* violation is *CP* violation in decay (or direct *CP* violation) which describes any asymmetry in the decay process. This occurs when the amplitude for a decay process does not equal the amplitude for its *CP* conjugate process. A full discussion of this asymmetry for the case of $B^0 \to K^{*+}\pi^-$ is included in Section 1.6.1.

1.3.1 Time Evolution at *BABAR*

As described in the discussion of Chapter 2, the *BABAR* Experiment collides electrons with positrons at an energy which maximises the production of the $\Upsilon(4S)$ resonance. This resonance decays to a $B\overline{B}$ pair. When a pair of neutral B mesons are produced, they exist in a coherent L=1 state (where L is the relative orbital angular momentum), such that each of the two particles evolves in time according to the outline above. The pair will evolve in phase, so that there is precisely one B^0 and one $\overline{B}^0$ present at any time before they decay. However, once one meson decays, it is possible for the other to continue oscillating, allowing events with two B^0 or two $\overline{B}^0$ decays.

Many analyses require that the type of B meson decaying is known. This is done via a technique known as tagging, and the coherent state of the pair of B mesons allows investigation of the mixing between the mesons. For example, if the B^0 decays at time $t = t_{tag}$, the other meson must be a $\overline{B}^0$ at that time. The $\overline{B}^0$ is free to continue oscillating until it decays at a later time, $t = t_{decay}$. The decay products of the first decay are used to give information as to the type of B meson. This is achieved by looking at decays to leptons or kaons. Knowing the flavour of one of the B mesons which decayed means that the flavour of the other B meson is also known at time t_{tag}. If the decays of the second B are fully reconstructed in a flavour specific decay mode then the flavour of the B at time t_{decay} is also known. Measurements of the distance between the two decay vertices allow the time difference to be calculated ($\Delta t = t_{decay} - t_{tag}$). Therefore the time that the B had to mix is known and the time dependence of the mixing parameters can be seen.

This technique can be used within analyses which require knowledge of what flavour of B is decaying in order to calculate the CP violation. It is possible to make a reasonable guess at the flavour using the flavour of the other B and the time difference between the decays. The full reconstruction of the second decay is not required although, for analyses with sufficiently large decay cross-sections, this gives excellent data sample purity.

1.4 Kinematics of Three-body B decay

The kinematic constraints for three-body B decays, such as $B^0 \to K^0_S \pi^+ \pi^-$, help to distinguish intermediate resonant decays with the same final state. For the decay of a B meson, at rest with mass m_B, to three daughter particles with masses m_i, momenta p_i and energies E_i (with i = 1,2,3), the momenta p_{ij} can be defined as $p_{ij} = p_i + p_j$ and $m^2_{ij} = p^2_{ij}$ [6]. Therefore,

$$m^2_{12} + m^2_{13} + m^2_{23} = m^2_B + m^2_1 + m^2_2 + m^2_3 \tag{1.24}$$

and

$$m_{ij}^2 = (p_B - p_k)^2 = m_B^2 + m_k^2 - 2m_B E_k \tag{1.25}$$

The relative orientation of the daughter particles' momenta is fixed for known energies, and lie in a plane in the B rest frame.

The Lorentz invariant phase space for a three-body decay can be written

$$dN \propto \delta^4 \left(p_B - \sum_{i=1}^{3} p_i \right) \prod_{i=1}^{3} \frac{d^3 p_i}{E_i} = \delta \left(m_B - \sum_{i=1}^{3} E_i \right) \frac{p_1^2 dp_1 p_2^2 dp_2 d\Omega_1 d\Omega_2}{E_1 E_2 E_3}. \tag{1.26}$$

The scalar nature of the B meson leads to the orientation of the decay system being uniformly distributed, and therefore the direction of $\overrightarrow{p_1}$ can be fixed, which gives $\int d\Omega_1 = 4\pi$. Thus, $\int d\Omega_1 = 2\pi \int d\cos\theta_{12}$, where θ_{12} is the angle between $\overrightarrow{p_1}$ and $\overrightarrow{p_2}$. Using,

$$E_3 = \sqrt{p_1^2 + p_2^2 + 2p_1 p_2 \cos\theta_{12} + m_3^2}, \tag{1.27}$$

Equation 1.26 becomes

$$dN \propto \delta \left(m_B - E_1 - E_2 - \sqrt{p_1^2 + p_2^2 + 2p_1 p_2 \cos\theta_{12} + m_3^2} \right) d\cos\theta_{12} \frac{p_1^2 dp_1 p_2^2 dp_2}{E_1 E_2 E_3} \tag{1.28}$$

Once integrated, this becomes

$$\begin{aligned} dN &\propto \frac{E_3}{p_1 p_2} \frac{p_1^2 dp_1 p_2^2 dp_2}{E_1 E_2 E_3} \\ &\propto \frac{p_1 dp_1}{E_1} \frac{p_2 dp_2}{E_2}. \end{aligned} \tag{1.29}$$

Finally, since $E_i dE_i = p_i dp_i$,

$$\begin{aligned} dN &\propto dE_1 dE_2 \\ &\propto dm_{12}^2 dm_{23}^2. \end{aligned} \tag{1.30}$$

Thus, the decay rate of for a three-body decay is proportional to

$$\mid \mathcal{M} \mid^2 dm_{12}^2 dm_{23}^2 \tag{1.31}$$

where $\mid \mathcal{M} \mid$ is the matrix element for the decay.

1.4.1 Dalitz Plots

A Dalitz plot [7] is defined as plot of m_{ij}^2 versus m_{ik}^2. Only two of the invariant mass combinations are independent, since the third can be constructed using Equation 1.24. The boundaries of the plot at a point along one axis occur when the angle between the momenta of the particles of the other axis obey $\cos\theta_{ij} = \pm 1$. For the $B^0 \to K_S^0\pi^+\pi^-$ Dalitz plot, this can be written

$$
\begin{aligned}
(m_{K_S^0\pi}^2)_{max} &= (E_{K_S^0} + E_\pi)^2 - (p_{K_S^0} - p_\pi)^2 && (1.32)\\
(m_{K_S^0\pi}^2)_{min} &= (E_{K_S^0} + E_\pi)^2 - (p_{K_S^0} + p_\pi)^2 && (1.33)
\end{aligned}
$$

If $\mid \mathcal{M} \mid$ is a constant, the Dalitz plot will have a uniform distribution as the decay proceeds according to phase space only. A distribution which is not uniform indicates a matrix element which has a kinematic dependence, such as an intermediate resonant decay. A resonance will appear as a narrow band in the Dalitz plane at the invariant mass of the resonance. An illustration of a $B^0 \to K_S^0\pi^+\pi^-$ Dalitz plot, using simulated data, equal branching ratios for all contributions and no interference, is shown in Figure 1.3. $m_{K_S^0\pi^-}^2$ is plotted on the x-axis, and $m_{K_S^0\pi^+}^2$ on the y-axis.

A Dalitz plot may also be described using the helicity angle, defined as the angle between particles i and j in the rest frame of ik, due to the relationship between helicity angle and invariant mass described by:

$$\cos\theta_{ik} = 1 - 2\left(\frac{m_{ij}^2 - (m_{ij}^2)_{min}}{(m_{ij}^2)_{max} - (m_{ij}^2)_{min}}\right) \tag{1.34}$$

The helicity angle is a useful variable since it allows the spin of the resonance to be determined, and be seen in the Dalitz plot. For example, the resonance bands of the vector $K^{*\pm}$ in Figure 1.3 clearly exhibit a depopulation in the centre of their resonance structure. This reflects the $\cos^2\theta$ helicity distribution of a vector resonance. The scalar resonances, such as the $K^{*\pm}(1430)$, do not show any such structure, reflecting the flat nature of the helicity of a scalar.

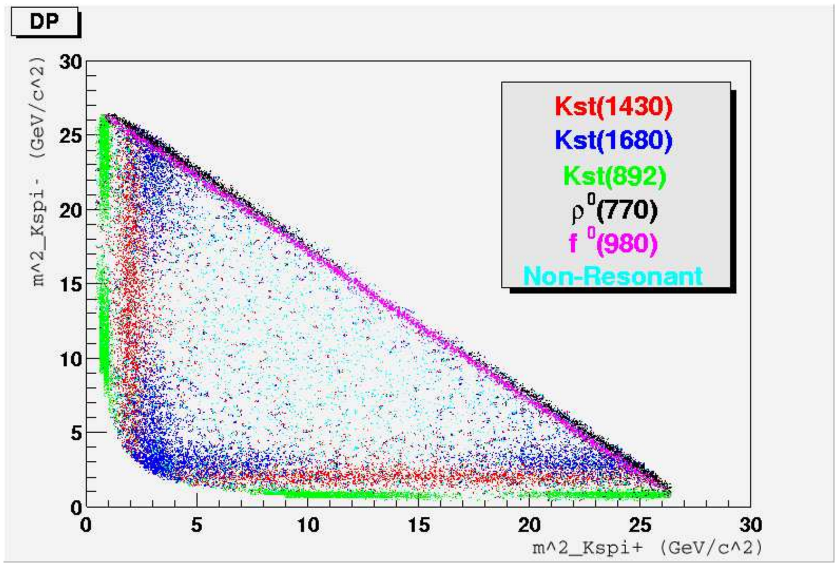

Figure 1.3: An example Dalitz plot, made with simulated data and with equal branching fractions assumed for all the included contributions. The structure of the resonance due to the spin can be seen in the parallel dimension to the mass of the resonance, e.g. the vector structure of the $K^{*\pm}$ resonance is apparent due to the single depopulated area in the centre of the structure of the resonance band.

A Dalitz plot analysis models the signal and the backgrounds within the Dalitz plane, fitting for the amplitudes and phases of the various contributions to the signal. This technique correctly models the quantum mechanical interference between the various signal contributions and as higher statistics become available, this technique becomes the optimal method for three-body analyses. By measuring the magnitudes and phases of the resonant and nonresonant amplitudes, the analysis becomes sensitive to several CP violating parameters, see for example [8].

1.5 $B^0 \to K^0_S \pi^+ \pi^-$

In 1991, Lipkin, Nir, Quinn and Snyder, suggested that $K\pi\pi$ channels can be used to extract the weak phase γ [9], but this method assumes a negligible electroweak

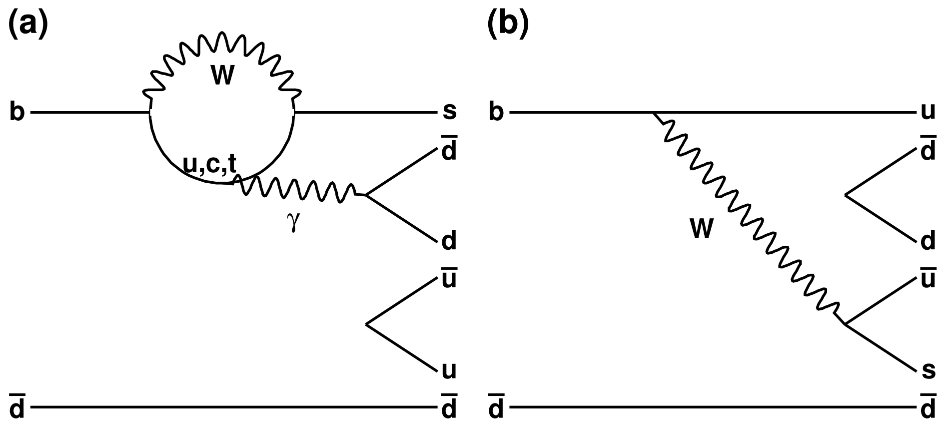

Figure 1.4: The penguin (a) and tree (b) nonresonant contributions for $B^0 \to K_S^0\pi^+\pi^-$.

penguin (a process in which an electroweak gauge boson is exchanged, as shown in Figure 1.4(a)) contribution, which is no longer considered to be a valid assumption. In 2002, Deshpande, Sinha and Sinha [10] extended this work by proposing a method in which the electroweak penguin contribution is included. Their method is also free from approximations, and sensitive to the relative weak phase between the tree and penguin contributions. The method requires an isospin analysis of the $K\pi\pi$ modes, as well as time dependent asymmetry and differential decay widths in the $B^0 \to K_S^0\pi^+\pi^-$ modes with even isospin $\pi\pi$ states.

There are six independent isospin amplitudes in the $K\pi\pi$ sector, which can be described as $A(I_t, I_{\pi\pi}, I_f)$. I_t is the transition isospin which describes the transformation under isospin of the weak Hamiltonian. In the Standard Model, it can only be 0 or 1. $I_{\pi\pi}$ is the value of isospin for the pair of pions. It can take the values 0, 1 or 2. Finally, I_f is the final isospin, which can be either 1/2 or 3/2. For the two pions to be in a symmetric state (even under the exchange of two pions), $I_{\pi\pi}$ must be even, and the pair will also have even angular momentum. Analogously, states with odd $I_{\pi\pi}$ must be anti-symmetric. Through studying the Dalitz plot, separation between odd and even isospins should be attainable.

However, current *BABAR* statistics are not sufficient for a full Dalitz plot analysis in $B^0 \to K^0_S\pi^+\pi^-$. Therefore, studies of the inclusive branching fractions, as well as those of quasi two body modes within this Dalitz plot, along with time dependent studies of the modes with a $\pi^-\pi^+$ resonance, provide the first step in moving towards a measurement of γ from $B^0 \to K^0_S\pi^+\pi^-$.

1.6 $B^0 \to K^{*+}\pi^-$

1.6.1 Charge Asymmetry

Consider the decay amplitude A of a B meson to a final state f and its *CP* conjugated decay amplitude $\overline{A}$, which describes the decay $\overline{B} \to \overline{f}$. These amplitudes can be written as:

$$A = \langle f|H|B\rangle = \sum_j A_j e^{i\delta_j} e^{i\phi_j}, \quad \overline{A} = \langle \overline{f}|H|\overline{B}\rangle = \sum_j A_j e^{i\delta_j} e^{-i\phi_j} \tag{1.35}$$

where A_j are partial amplitudes and δ_j and ϕ_j are the strong and weak (*CP* violating) phases respectively. In order for direct *CP* violation to be present, the condition

$$\frac{\overline{A}}{A} \neq 1 \tag{1.36}$$

must be met. It is best to observe such *CP* violation in "self-tagged" decays so that the effects of mixing do not complicate the calculation. $B^0 \to K^{*+}\pi^-$is such a decay since B^0 only decays to $K^{*+}\pi^-$ and $\overline{B}^0$ only decays to $K^{*-}\pi^+$. The charge asymmetry which is observed is

$$A_{CP} = \frac{\Gamma(\overline{B} \to \overline{f}) - \Gamma(B \to f)}{\Gamma(\overline{B} \to \overline{f}) + \Gamma(B \to f)} \tag{1.37}$$

in general, and

$$A_{CP} = \frac{\Gamma(\overline{B}^0 \to K^{*-}\pi^+) - \Gamma(B^0 \to K^{*+}\pi^-)}{\Gamma(\overline{B}^0 \to K^{*-}\pi^+) + \Gamma(B^0 \to K^{*+}\pi^-)} \tag{1.38}$$

for the case of $B^0 \to K^{*+}\pi^-$. Γ is the branching fraction of the decay.

In order for direct CP violation to occur, at least two partial amplitudes are necessary, with different strong and weak phases. This suggests looking at decays in which both tree and penguin contributions occur. The magnitudes of the contributions are also required to be of similar size, and therefore modes with a suppressed or forbidden tree amplitude are good candidates.

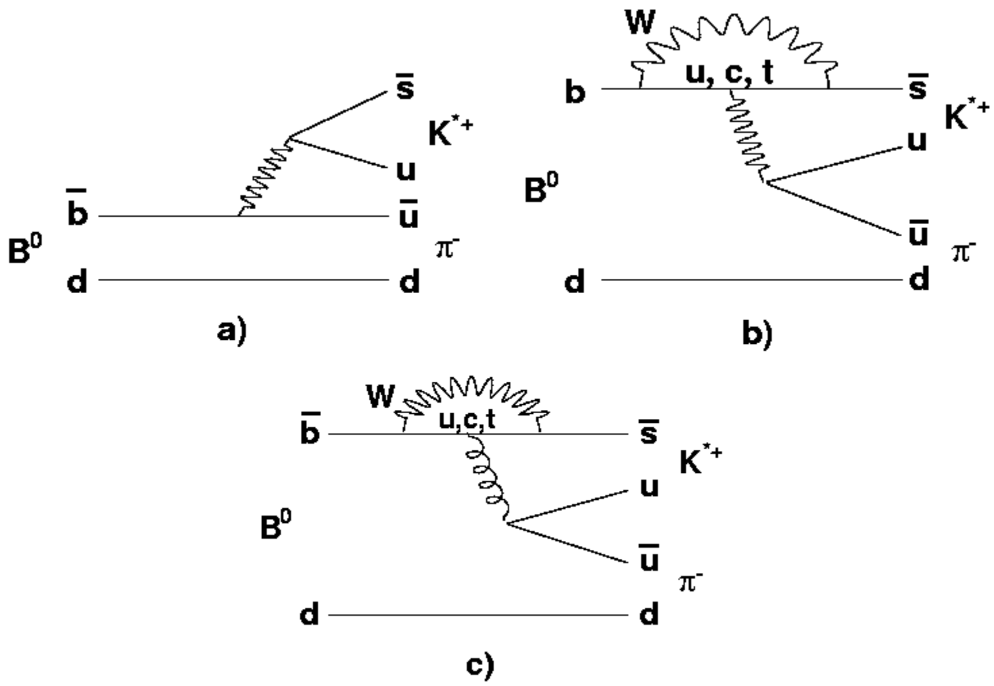

Figure 1.5: The tree and penguin contributions for $B^0 \to K^{*+}\pi^-$. a) is the external tree diagram, b) is the internal, colour-suppressed, electroweak penguin diagram and c) is the internal gluonic penguin diagram.

1.6.2 QCD Factorisation

There is currently a great deal of phenomenological work being undertaken in the prediction of branching fractions and CP asymmetries for $B \to PP$ and $B \to PV$ decays, where P is a pseudoscalar meson and V a vector meson.

QCD Factorisation (QCDF) [11] can be used to estimate the amplitudes and asymmetries of decays. Each possible decay diagram, such as the tree and penguin Feynman diagrams in Figures 1.5, has a term in the amplitude calculation to describe it. The summation of all the possible diagrams should yield a prediction of the branching fraction or asymmetry (if relevant) for each mode considered.

Factorisation breaks up a matrix element into a product of two elements:

$$\langle K^{*+}\pi^-|Q_n|B^0\rangle \rightarrow \langle K^{*+}|J_n^1|0\rangle\langle\pi^-|J_n^2|B^0\rangle \tag{1.39}$$

$$\text{or} \quad \langle\pi^-|J_n^1|0\rangle\langle K^{*+}|J_n^2|B^0\rangle \tag{1.40}$$

where Q_n is a suitable current-current operator, and $J_n^{1,2}$ is a suitable current operator. The operator depends on the kind of decay diagram being described. QCDF assumes that soft gluons are not exchanged between quarks in different elements, which is rational in the case of charmless B decays as the quarks should be produced with enough energy to make interactions with gluons unlikely. The current operators, $J_n^{1,2}$ can be described as products of quantities which can be experimentally determined, e.g. decay rates and form factors. The currents are constrained to have the correct colour content and flavour for the hadrons being studied.

The basic model, introduced by Beneke and Neubert [12] for $B \rightarrow PP$, used factorisation to make predictions of branching ratios and charge asymmetries, whilst neglecting some types of decay diagrams. This method has since been built on with, for example, the addition of the $B \rightarrow PV$ and annihilation diagrams [13] or with the consideration of charming penguins [14].

Table 1.1 shows the phenomenological predictions made using this method for the branching fractions of $B^0 \rightarrow K^{*+}\pi^-$ and for $B^0 \rightarrow \rho^0 K^0$ in comparison to experimental measurements. Table 1.2 shows the predictions and experimental measurements for the charge asymmetries. Included for comparison are the predictions made by Chiang *et al.* [15] using SU(3) flavour symmetry and isospin relations to predict branching fractions from other experimentally measured results. This method is sensitive to the CKM phase γ and predicts the branching fractions and asymmetries using $\gamma = 26°, 63°$ and $162°$. The range of these predictions is shown in the tables.

Mode	Cottingham 2002 [14]	Du 2002 [16]	BBNS 2003 [12]	Chiang 2003 (SU(3)) [15]
$K^{*-}\pi^{+}$	5.0	1.838 - 4.36	$3.3^{+1.4+1.3+0.8+6.2}_{-1.2-1.2-0.8-1.6}$	12.4 ± 0.9 - $15.3 \pm 15.5\ ^{+1.2}_{-1.1}$
$\rho^0 K^0$	N/A	0.918 - 1.297	$4.6^{+0.5+4.0+0.7+6.1}_{-0.5-2.1-0.7-2.1}$	$5.3^{+1.8}_{-1.5}$ - $7.2^{+2.1}_{-1.9}$

Mode	CLEO [17]	Belle [18]	*BABAR* 2004,1 [19,20]	*BABAR* 2004, 2 [21]
$K^{*-}\pi^{+}$	26.0 ± 9.0	$16^{+6}_{-5} \pm 2$	$10.9 \pm 2.3 \pm 1.5$	$12.9 \pm 2.4 \pm 1.4$
$\rho^0 K^0$	<12.4	N/A	$5.1 \pm 1.0 \pm 1.2$	N/A

Table 1.1: Predictions of the branching fractions of $B^0 \to K^{*+}\pi^-$ and $B^0 \to \rho^0 K^0$ (top) compared with experimental results (bottom). All measurements are in units of 10^{-6}.

Du 2002 [16]	BBNS 2003 [12]	Chiang 2003 (SU(3)) [15]
14.36 - 47.0	$2.1^{+0.6+8.2+5.1+62.5}_{-0.7-7.9-5.8-64.2}$	-3^{+5}_{-4} - 6 ± 4

CLEO 2003 [22]	*BABAR* 2004,1 [19]	*BABAR* 2004,2 [21]
26^{+33+10}_{-34-8}	$23 \pm 18 \pm^{9}_{6}$	$-25 \pm 17 \pm 2 \pm 2$

Table 1.2: Predictions of charge asymmetry in $B^0 \to K^{*+}\pi^-$(top) compared to experimental results (bottom). All measurements are percentages.

1.7 The *BABAR* Experiment and Collaboration

The *BABAR* Collaboration is a group of approximately 600 physicists from around 75 institutions in 10 countries based around the globe. The experiment began to take data in 1999, and is expected to run until at least 2008.

The experiment is run from the PEP-II storage facility at SLAC, which is an asymmetric B factory with a high energy (9 GeV) electron beam and a low energy (3.1 GeV) positron beam. To create the B mesons, the energy of the collision must be great enough to create the $\Upsilon(4S)$ resonance, which decays to either a $B^0\overline{B^0}$ pair or a B^+B^- pair. Each one of these decays has a branching ratio of approximately

50%. This choice of energy gives the biggest cross section of B meson production. It is in the decays of these B mesons that CP violation parameters can be measured. The system's asymmetry causes the B mesons to move in the direction of the high energy beam rather than being produced at rest, as would occur with symmetric beams. This allows the mesons, which are moving at approximately half the speed of light, to travel a small, yet easily measurable, distance (approximately 250 μm) before they decay. Thus, the decay vertices can be reconstructed and the distance between decay positions can be measured, yielding a precision lifetime difference. The ultimate goal of the experiment is to measure CP asymmetries and test the Standard Model.

There are several decays of $B/\overline{B}$ which are expected to provide a measurement of direct CP violation. Some such decay modes may exhibit CP violation so strongly that only around several hundred observations of that decay would be necessary to measure its asymmetry. However, these decays are all exceedingly rare, often with branching ratios of only $\approx 10^{-6}$. Therefore, it is expected that the *BABAR* experiment must produce more than 10^8 $B^0\bar{B}^0$ pairs in order to get a measurement of these asymmetries with an error of better than 10%. Direct *CP* violation has recently been observed by the *BABAR* collaboration in $B^0 \rightarrow K^+\pi^-$ decays [23].

There are three measurements that are required in order to observe the time-dependent violation. The exclusive final state must be completely reconstructed, whether the decaying particle is of flavour beauty or anti-beauty must be tagged, and the proper time that the B^0 decays relative to to the tagged decay needs to be determined. The latter is required because usually the violation goes to zero when doing time-integrated measurements at electron-positron colliders.

The data, along with those from the rival experiment, Belle [24] at the KEK facility in Japan, are producing the most accurate CP measurements so far. These measurements are of the CP violating parameters, the three unitarity angles (α, β, γ), and of the three sides of the triangle, which together entirely describe the SM weak coupling of the six quarks in the Cabibbo-Kobayashi-Maskawa (CKM) quark mixing matrix. The particles and their decay modes are detected using the specially built *BABAR* detector, which is described in detail in Section 2.

The first *CP* results from *BABAR* were submitted for publication in July 2001 and since then *BABAR* has published many results which have succeeded in restricting the possible ranges of the CKM angles considerably. For sin2β, several modes have been analysed, including $B^0 \to J/\psi K^0_S$, where sin2β is measured to be 0.75 ± 0.04 (where the error is statistical only) using 227 million $B\overline{B}$ pairs [25], and $B^0 \to f_0(980)K^0_S$, where sin2β is measured to be $0.95 \pm^{+0.23}_{-0.32} \pm 0.10$ in 209 million $B\overline{B}$ pairs [26]. The world average is sin$2\beta = 0.665 \pm 0.033$ [27]. For sin2α, *BABAR* conducts time-dependent analyses on the decays $B^0 \to \pi^+\pi^-$ [28], $B^0 \to \rho^\pm\pi^\mp$ [29] and $B^0 \to \rho^+\rho^-$ [30] to produce the combined constraint $\alpha = (100 \pm ^{+9}_{-10}[1\sigma] \pm ^{+29}_{-20}[2\sigma])^\circ$ [27].For the angle γ, *BABAR* has measured $\gamma = (73 \pm 45 \pm 10 \pm 10)^\circ$ (where the first uncertainty is statistical, the second is systematic and the third is theoretical) using a Dalitz plot analysis of $B^- \to D^{(*)0}K^-, D^{(*)0} \to D^0\pi^0, D^0 \to K^0_S\pi^+\pi^-$ [31].

Chapter 2

The *BABAR* Detector

2.1 The Linear Accelerator and The PEP-II B Factory

The Stanford Linear Accelerator Center's (SLAC) main apparatus is a 2 mile long linear accelerator. For the *BABAR* experiment, electrons and positrons are accelerated along it until they reach their target energy, and then fed into the storage rings via bypass lines. The PEP-II storage rings store beams for interaction inside the detector.

The PEP-II B Factory is an asymmetric e^+e^- collider, whose two beams are tuned to collide at the mass of the $\Upsilon(4S)$ resonance ($\sqrt{s} = 10.58\,\mathrm{GeV}$), which is just above the production threshold for $B\overline{B}$ pairs. This is optimal because the $\Upsilon(4\mathrm{S}) \rightarrow B\overline{B}$ branching fraction is almost 100%. However, an $\Upsilon(4S)$ is only produced in approximately 20% of hadronic events, with a cross section of 1.09nb. The remaining 80% of events are made up of light quark continuum events, where the colliding electrons produce a $q\overline{q}$ pair (with q being a u, d, s or c quark), which has a cross section of 3.2nb, or of τ events whose cross section is 0.9nb.

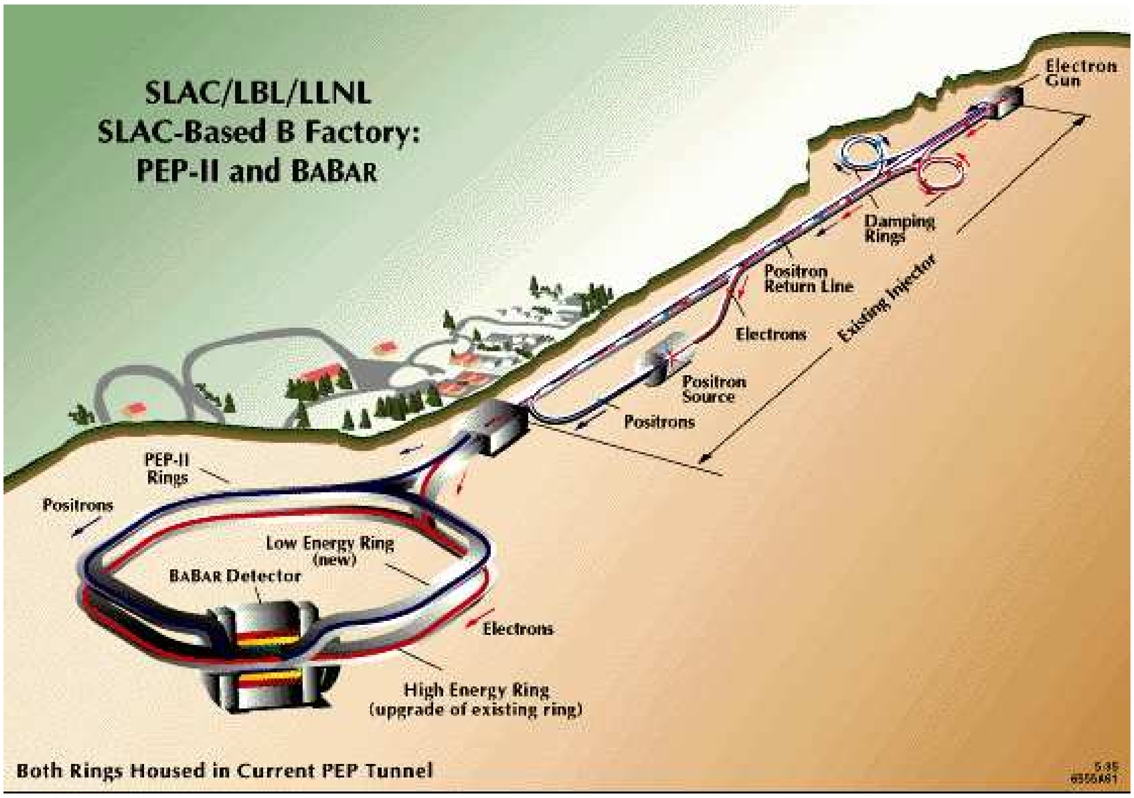

Figure 2.1: A view of the PEP-II storage ring and the BABAR detector.

The unequal beams boost the B mesons in the laboratory frame with $\beta\gamma = 0.56$, allowing the lifetimes of the particles to be calculated from their decay lengths and to measure any time dependence in their decay rates. The high-energy ring (HER) stores the electron beam, which has an energy of 9.0 GeV, whilst the low-energy ring stores positrons at 3.1 GeV, which was chosen when studies showed this 3:1 ratio to be optimal [32] . It was also necessary for the B Factory to produce an extremely high luminosity of above $10^{33}\mathrm{cm}^2\mathrm{s}^{-1}$ so that a significant number of B mesons can be produced, allowing extremely rare decays with branching fractions smaller than 10^{-6} to be accurately measured. PEP-II has performed excellently since May 1999 and, as of July 2004, *BABAR* has reached a peak luminosity of $9.213 \times 10^{33}\mathrm{cm}^2\mathrm{s}^{-1}$. $250\,\mathrm{fb}^{-1}$ of data have been recorded in this time period, and this entire data set is used for the analysis which follows.

e^+e^- collisions were chosen because of several key advantages over hadronic systems, including that they provide a high signal-to-background ratio, clean B meson events with low multiplicity which allows for reconstruction of final states with photons and π^0 s, and low interaction rates (so that the detector is not flooded with data during its dead-time).

The layout for the linac and the PEP-II rings can be seen in Figure 2.1. An electron gun creates the electron bunches which are then accelerated to 9.0 GeV by the linac before being injected into the HER. By accelerating electron bunches in the linac and colliding them with a fixed target, positron bunches are produced. The linac then accelerates these positron bunches to 3.1 GeV and they are injected into the LER.

Figure 2.2 shows the beam interaction region (IR). The bunches must be brought into focus for collisions just before the interaction point (IP) and separated directly afterwards, to avoid secondary collisions. At *BABAR* the collisions are made with no crossing angle. Focusing the beams requires the use of the quadrupoles labelled QD and QF. QD4 and QF5 are used for focusing the HER, whilst QF2 is responsible for focusing the LER. These are iron magnets which are placed outside the field of the *BABAR* solenoid. The QD1 quadrupole is the final focus for both the HER and the LER and is a permanent magnet located within the solenoid. A strong dipole (B1) in close proximity to the IP ($\pm$ 21cm away) is necessary to bring together and separate the beams by causing horizontal displacement. The IR is within a beam pipe which has an outer radius of 27.9mm and is water cooled. This beam pipe, with the permanent magnets and the silicon vertex tracker, is enclosed within a 4.5m long support tube.

High machine backgrounds cause significant problems due to high occupancies within the subsystems of the *BABAR* detector. This can cause dead-time inside the detector, resulting in a loss of data, and also radiation damage to the subdetectors. It is imperative that these backgrounds are kept to an absolute minimum. There are three sources of this background: luminosity background, synchrotron radiation

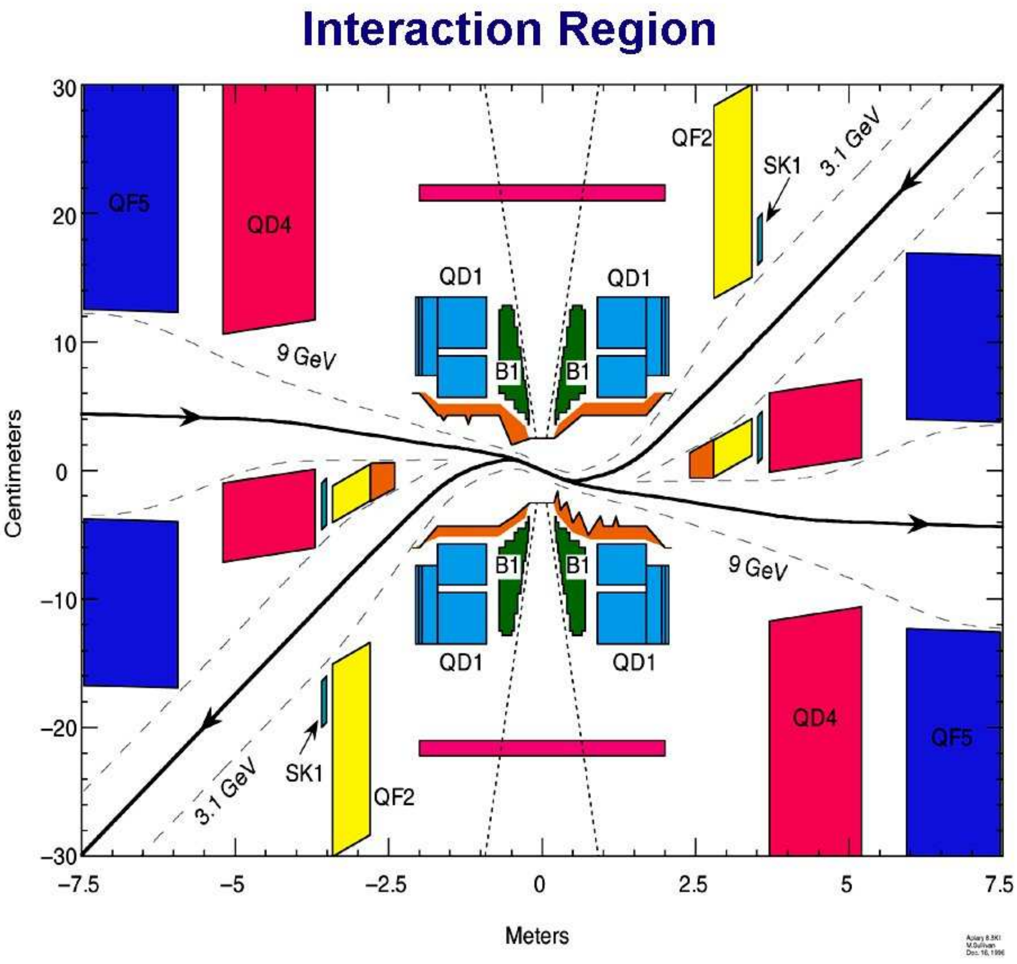

Figure 2.2: A view of the Interaction Region and the surrounding PEP-II components. The components labelled QD and QF are focusing quadrupoles, and those labelled B1 are dipoles used to separate the beams after collision.

and particles lost due to interactions with the beam-pipe or residual gas molecules within the beam-pipe.

Luminosity backgrounds are caused by radiative Bhabha scattering which can result in electromagnetic showers within the detector. This is an unavoidable source of background, and will increase along with luminosity. Backgrounds due to collisions with gas molecules in the beam-pipe are reduced by having a strong vacuum within the beam-pipe near the IP. Focusing and separating the asymmetric beams within the IR generates a great deal of synchrotron radiation, which is the greatest source of machine background. Various components within the IR are designed to channel and absorb synchrotron photons so that they never enter the detector, and copper masks are used to prevent interaction with the beam-pipe.

2.2 The *BABAR* Detector

To describe the *BABAR* experiment, it is necessary to employ a consistent co-ordinate system. The *BABAR* system is a right handed system, with the z-axis lying in the direction of the high energy beam. Therefore, the y-axis lies vertically upwards and the x-axis points horizontally away from the centre of the PEP-II rings. The polar (θ) and azimuthal (ϕ) angles are defined in the traditional way, relative to the z-axis.

There are five major components that comprise the *BABAR* detector, shown in Figure 2.3. It was designed and built in order to reach *BABAR*'s objectives in the most productive manner possible. In order to do this, there were several specific requirements of the detector [4, 33].

These features were [4]:

1. To have the greatest attainable detection rate in the centre-of-mass (CM) system. Since *BABAR* has asymmetric beams, acceptance is increased by designing an asymmetric detector as well.

2. Due to the the unusual beam optics needed to attain the high luminosities that the *BABAR* machine requires in order to measure rare decay, it was necessary to organise the detector components very close to the IP.

3. To obtain superior vertex resolution in the z direction so that the distance between the decay vertices of the B mesons can be measured, and in ϕ so that the secondary vertices can be separated.

4. To detect tracks and have excellent reconstruction efficiency over a traverse momentum (p_t) from approximately 60 MeV to 4 GeV.

5. To be able to differentiate between e, μ, π, K and p over a broad kinematic range. Since tagging of the flavour of the B-meson decays is often required, it is necessary to be able to accurately identify electrons, muons and kaons in order to do such tagging efficiently. At around 2-4 GeV, the detector had to be designed to be able to discriminate between pions and kaons so that the decay modes of the B^0s are distinguishable.

6. To have excellent momentum, energy and angle resolution for photons and π^0s over the approximate energy range of 20 MeV to 5 GeV so that small signals can be differentiated from the background.

7. To be capable of identifying neutral hadrons.

BABAR consists of several main subsystems, all of which are described later in this chapter. They are the Silicon Vertex Tracker, the Drift Chamber, the Detector of Internally Reflected Cherenkov Radiation, the Electromagnetic Calorimeter, a solenoid magnet and the Instrumented Flux Return. The detector is purposefully compact as a compromise between performance and expense. As well as CP measurements, the detector is suited for precision measurements of charm, B and τ physics.

2.3 The Silicon Vertex Tracker

The Silicon Vertex Tracker, or SVT, is the first subdetector around the collision point. The SVT reconstructs the decay vertices from the charged particle tracks in order to give information about which particles originate from the collision point. The data are used to determine the different decay times of the B^0 mesons which is

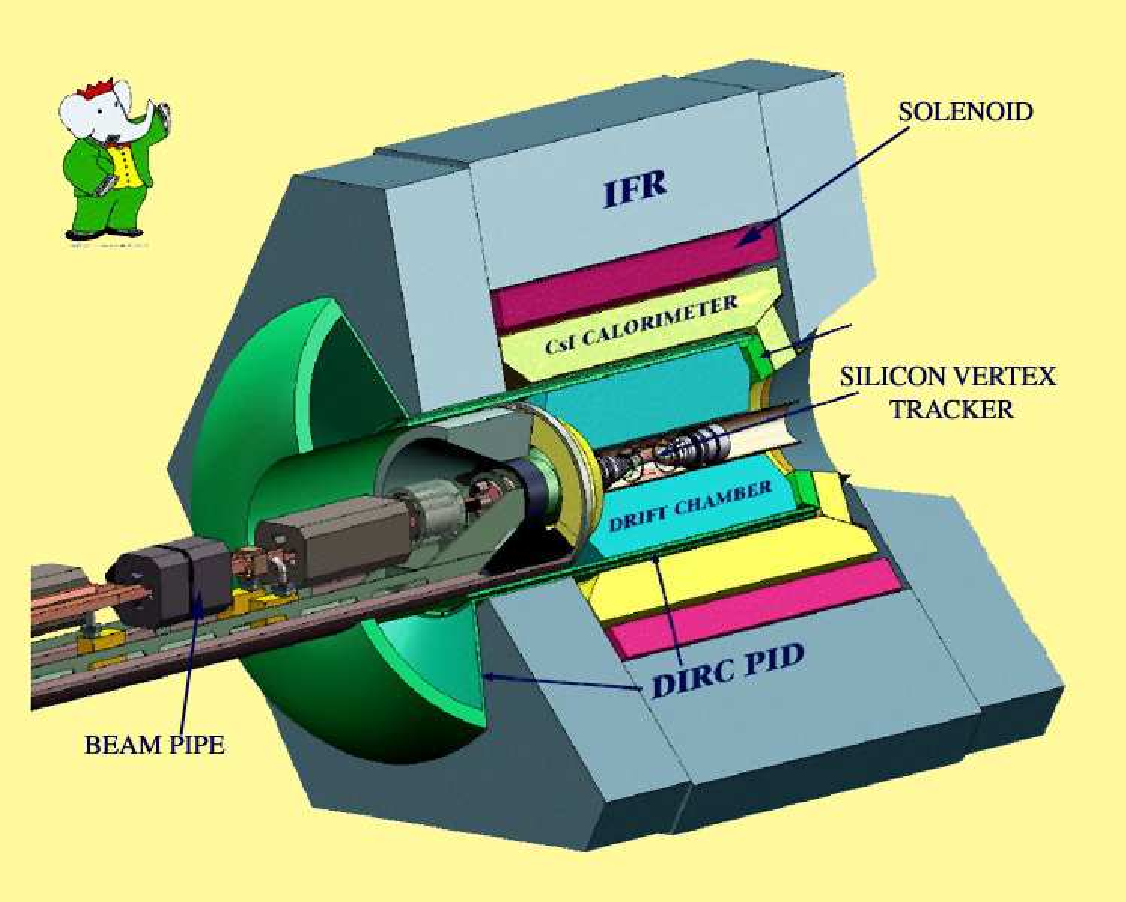

Figure 2.3: A simple view of the BABAR Detector with the major areas labelled.

vital for measurements of time-dependent asymmetries. For these measurements, the SVT must be capable of fully reconstructing B decays with a mean vertex resolution in the direction of the z axis of better than 80μm. To enable the reconstruction of secondary vertices, a vertex resolution of better than 100μm is required in the transverse direction. The SVT is also the only available method of detecting and tracking low energy particles (which have a transverse momentum (p_t) of less than 120 MeV/c) as they are incapable of reaching further into the detector. The SVT also contributes to Particle Identification (PID), particularly for particles with momenta below 700 MeV/c, using measurements of ionisation loss, $\mathrm{d}E/\mathrm{d}x$.

The SVT consists of five layers of double-sided silicon strip detectors, as shown in Figures 2.4 and 2.5. The first three layers are positioned very close to the beam pipe

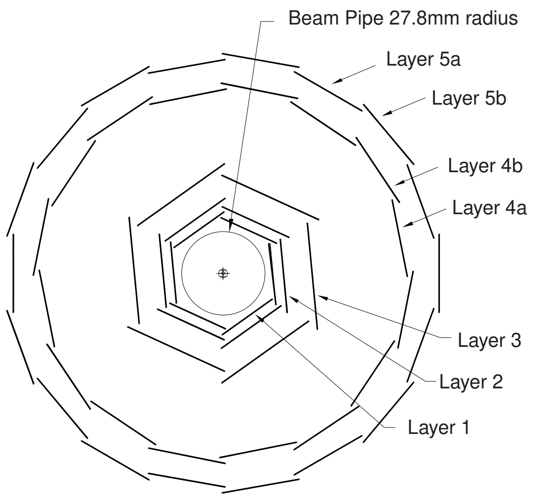

Figure 2.4: An end-on view of the 5 SVT layers

(3-5cm from the IP) to help to minimise the effect that multiple scattering within the beam pipe could have on the vertex position calculation. They mainly provide location and angle information for this calculation. The remaining two layers are further away from the beam pipe, and measure coordinates and angles which help to link tracks between the SVT and the next tracking system, the Drift Chamber. The total amount of material within the SVT is minimised in order to reduce the effect of Bremsstrahlung and multiple scattering.

The silicon strip sensors are arranged as modules, with the layout shown in Figure 2.4. Figure 2.5 shows the arched design of the two outer layers, intended to reduce the amount of material a track will pass through and to increase angular coverage. Each of the three inner layers consists of six modules, whilst the fourth layer has 16 modules, and the fifth has 18 modules due to their greater radii. The silicon strips on each side of a sensor are positioned orthogonally to each other, enabling measurements of both the z and ϕ positions. Each layer is constructed with flat, square silicon wafers arranged so there is no uncovered region in ϕ and so that there is maximum tracking acceptance in θ. The design has a 90% geometric acceptance of the solid angle in the centre-of-mass frame, and has kept the amount

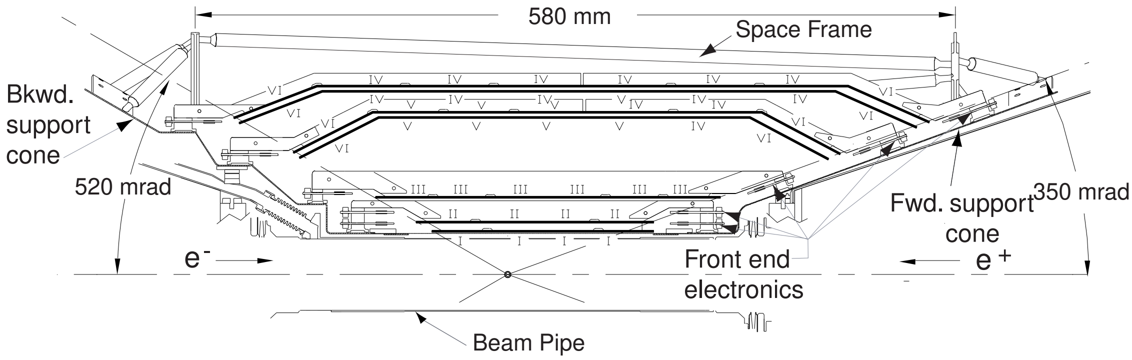

Figure 2.5: An view of the 5 SVT layers taken from the side.

of material that a particle must traverse to $\approx 4\%$ of a radiation length.

An electrical pulse is created within a strip when a charged particle traverses the silicon. These are carried to the Front End Electronics (FEE), where the quantity measured is the time for which a pulse is over a threshold (TOT). This is related logarithmically to the charge, and gives a better signal to noise ratio than measuring the charge or pulse height. Clusters are formed by grouping adjacent strips which have consistent timing information. It is possible for clusters that are separated by one strip to be merged together. Clusters are then passed to an algorithm with pattern recognition abilities which interprets the data. The positions of hits are expressed in terms of the position of the silicon sensors within the SVT.

It is essential that the SVT's alignment, both internally (locally) and with the rest of the detector (globally), is correct so that the best position and momentum resolutions are obtained. The alignment calibration uses two-prong events to test the detector's alignment.

PIN diodes instrument the SVT to measure the amount of background which the subsystem is exposed to. The limit for instantaneous radiation is 1 rad/ms and if conditions approach this, the beam is tripped automatically. Over the detector's lifetime, the integrated radiation limit is 2 MRad, and since the background levels are expected to scale with luminosity, this problem is getting worse. The modules in the horizontal plane receive most of the dosage due to synchrotron radiation.

2.4 The Drift Chamber

The second subsystem from the beam pipe is the Drift Chamber, or DCH. This system gives tracking information on the higher momentum charged particles (particles with momentum >120 MeV/c and with $0.1 < p_t < 5.0\,\mathrm{GeV}/c$) which travel further than the SVT, taking up to 40 measurements of spatial coordinates per track. It also measures momentum for charged particles, passes information to the trigger and takes dE/dx measurements which are used for particle identification (see Figure 2.9). This is particularly important for tracks with $p_t < 700\,\mathrm{MeV}/c$ which do not reach the principal PID detector, the DIRC (Section 2.5). These features allow B and D mesons to be accurately reconstructed, as well as providing all the necessary information for K^0_S reconstruction. The DCH also provides timing measurements which are used by the trigger to select events.

The DCH features an 2.8m long cylinder which is placed asymmetrically around the IP in order to provide the forward region with more detector acceptance. The design is shown in Figure 2.6. The chamber has an inner radius of 23.6 cm and an outer radius of 80.9 cm. Multiple scattering is reduced by using low mass wires (some of which are positioned at small angles to the beam axis, to obtain longitudinal information) and by filling the cylinder with a helium-based gas mixture (containing helium and isobutane in a 4:1 ratio). Together, the amount of gas and wires form 0.28% of a radiation length for a particle traversing the detector.

The endplates of the chamber are constructed using aluminium. The backward plate is 24mm thick, and the forward plate is 12mm thick, which serves to reduce the amount of material in front of the endcap of the calorimeter. The design of the drift cells for the four innermost superlayers is shown in Figure 2.7. The sense wires have diameters of 20μm and are made of gold plated tungsten-rhenium. The field wires have diameters of 120μm and are gold plated aluminium. The typical size of a drift cell is $1.2 \times 1.8\text{cm}^2$. Each drift cell consists of one sense wire surrounded by six field wires. The field wires are at ground potential, but a high voltage is applied to the sense wires creating a field with almost circular symmetry over a large portion of the cell (Figure 2.8). Passing charged particles ionise the gas and the resultant electrons are accelerated towards the sense wire. An avalanche of charge is created, acting as an amplification of the ionisation near to the sense wire for the detector.

There are 40 layers within the chamber, which are grouped into 10 superlayers of 4 layers each. The superlayers each have one of three stereo angles. There are axial (A), positive and negative (U,V) stereo layers in the order AUVAUVAUVA. The stereo angles range between ± 45 mrad in the innermost layers, and to ± 76 mrad in the outer layers. This structure helps the fast local segment finder which is required by the trigger.

Electronics read out measurements of the drift time and the integrated charge

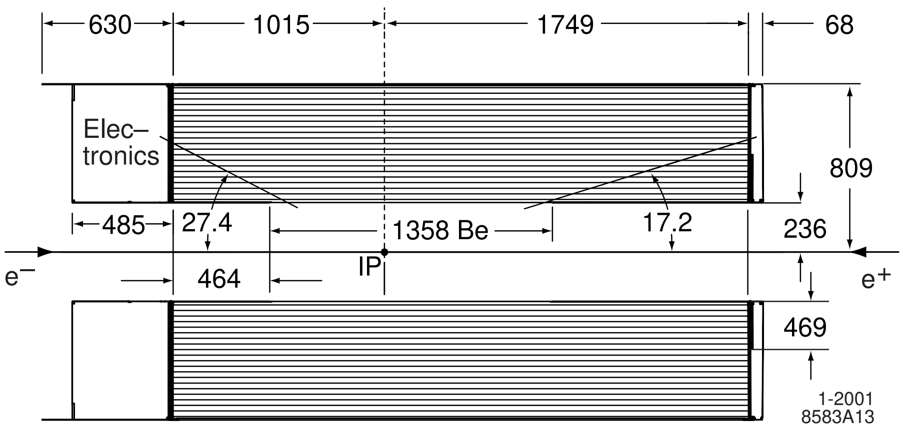

Figure 2.6: The Drift Chamber's design from the side. All measurements are in mm.

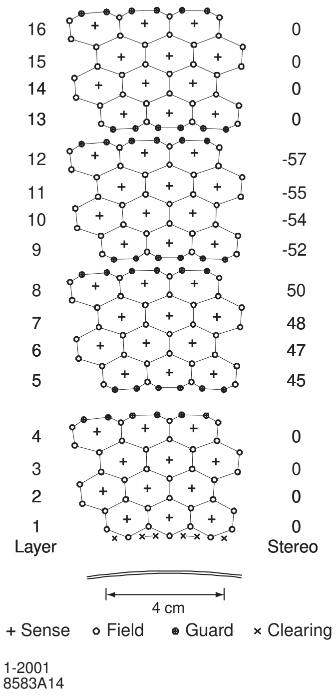

Figure 2.7: DCH cell layout for the first four superlayers. The right hand column shows the stereo angle of the layers in mrad. The guard wires match the gain in the boundary cells to the gains in the inner layers, and the clearing wires remove charges from the photon conversion in the material of the wall.

of passing particles. In order to reduce the amount of material in the detector, the electronics used for the trigger interface, digitisation and amplification are housed outside the detector within boxes on the rear end plate of the detector.

Charged particle tracks are reconstructed from data collected in both the DCH and the SVT. Reconstruction begins with the information collected for the trigger tracking algorithm, which first finds track segments (a superlayer with hits in all four layers within a small range of ϕ) from the Level 1 trigger (see Section 2.9) and then the Level 3 trigger combines these segments into five parameter helical tracks.

The offline reconstruction refits the DCH hits in the Level 3 tracks and searches for additional DCH hits which belong to the same track. Other techniques are used

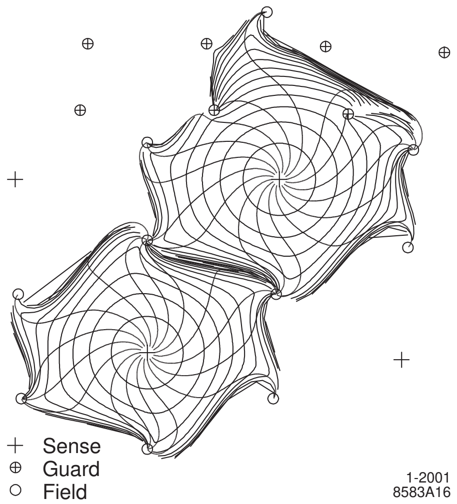

Figure 2.8: Contours of equal drift time in a DCH cell. The contours are 100ns apart, shown for ions in the cells of layers 3 and 4 of an axial superlayer.

to find tracks which do not traverse the entire DCH or do not come from the IP. Tracks are then extrapolated back into the SVT and those hits are added to the track. Other SVT hits are passed to an SVT only track finding system in order to find tracks which only traverse one of the detector subsystems. Finally, the tracks are all fitted again taking into account a detailed description of the material in the detector and the full map of the magnetic field.

The DCH dominates the track efficiency, which is measured by the ratio of the number of reconstructed tracks to the number of tracks detected in the SVT which fall within the DCH acceptance (correcting for fake SVT tracks). The tracking efficiency is around 98% for a charged track. p_t resolution is also dominated by the DCH, and is measured using muons from cosmic rays. The resolution is calculated by fitting the upper and lower halves of the track separately and the difference between the measured parameters is used to estimate the resolution.

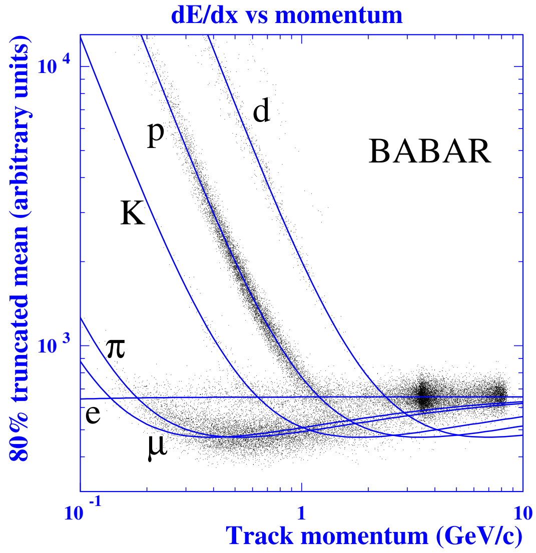

Figure 2.9: Particle Identification in the DCH. The graph shows $\mathrm{d}E/\mathrm{d}x$ *measurements from the DCH as a function of track momenta, which separates the particles into bands and enables identification. This shows that the separation between pions and kaons in the DCH is particularly good below 1* GeV/c*, but that the DCH alone has difficulty separating pions from electrons and muons.*

2.5 The Detector of Internally Reflected Cherenkov Radiation

The next subsystem is the Detector of Internally Reflected Cherenkov radiation (DIRC), which is used for particle identification (PID). The DIRC was specifically created to identify kaons extremely well, for purposes of both tagging (with momenta up to 2 GeV/c) and for rare B meson decay at higher momenta (as large as 4.2 GeV), since the DCH and SVT can only provide PID up to 700 MeV/c. Since it is important to differentiate between kaons and pions, the DIRC is required to have a significant separation of pions and kaons over the range 0.7-4.5 GeV/c at large dip angles (the angle between the track momentum vector and the x-y plane) within the lab frame [4]. The DIRC should also have minimal thickness to reduce the degradation of the calorimeter measurements.

The DIRC detects Cherenkov photons that are trapped in its radiator due to total internal reflection. The radiator is constructed from long quartz bars, which have a reflective index, n, of 1.472. If a traversing charged particle has a velocity, β, which is greater than $1/n$, it will emit Cherenkov light at an angle $\cos\theta_c = 1/n\beta$. The DIRC extends through the solenoid flux in the backwards direction, transporting the Cherenkov radiation outside of the tracking and magnetic sections using successive total internal reflections, to an array of photomultiplier tubes (PMT) inside a large tank of water. This is called the Standoff Box (SOB). The propagation of the light along the bar maintains the Cherenkov angle at which the photon is produced. The forward end has a mirror to reflect any light going in the other direction. At the instrumented end of the bar, inside the water, is a fused silica wedge which reflects photons at large angles, which serves to reduce the necessary size of the detection surface. At the outside edge, the light is allowed to expand in purified water, which has a similar refractive index to the bars so there is minimal total internal reflection at the silica-water boundary. The photomultiplier tubes are

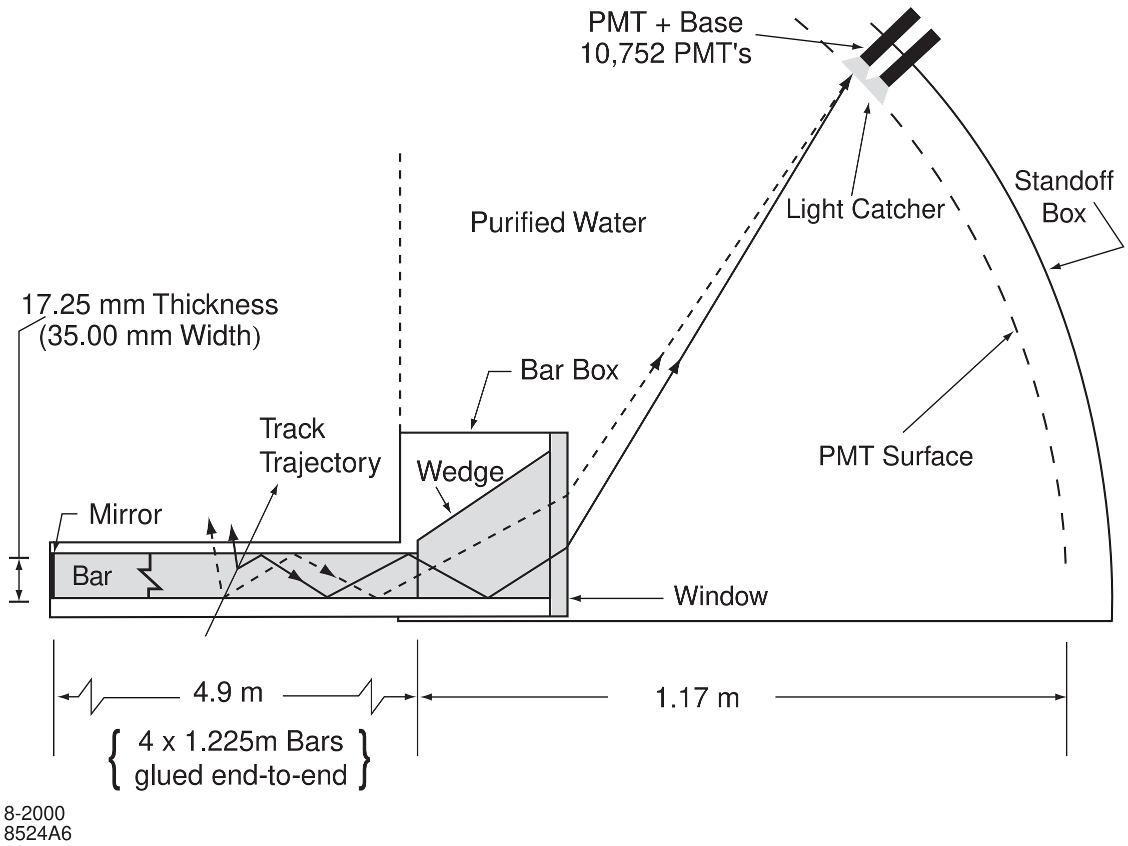

Figure 2.10: A schematic diagram of a DIRC radiator bar and the Standoff Box imaging region.

capable of detecting Cherenkov photons in the visible and near-UV range. The original rings of Cherenkov light are then reproduced using the information about the time and position of the light signals within the bank of photomultipliers [4,33]. The final photon detection efficiency is about 5%, with the main loss in the efficiency being in the PMTs which have an efficiency of about 25%. A schematic diagram of the DIRC imaging region is shown in Figure 2.10, and a longitudinal section is in Figure 2.11.

The DIRC bars are arranged in 12 "bar boxes", with 12 bars in each box, which form a 12-sided polygon. Each bar is 17 mm thick, 35 mm wide and 4.9 m long. They are built of four 1.225 m pieces which are glued together. Inside the SOB are 6,000 litres of purified water, which was chosen as it is inexpensive and its refractive

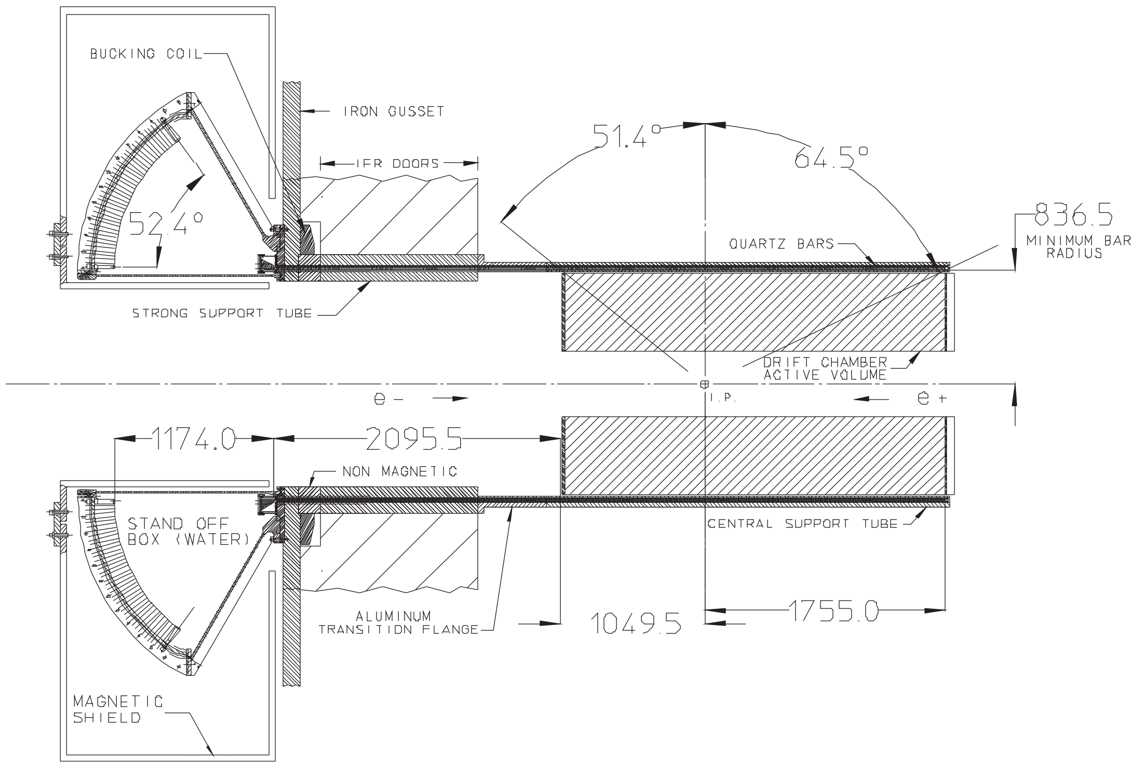

Figure 2.11: Elevation view of the DIRC geometry. All dimensions are in mm.

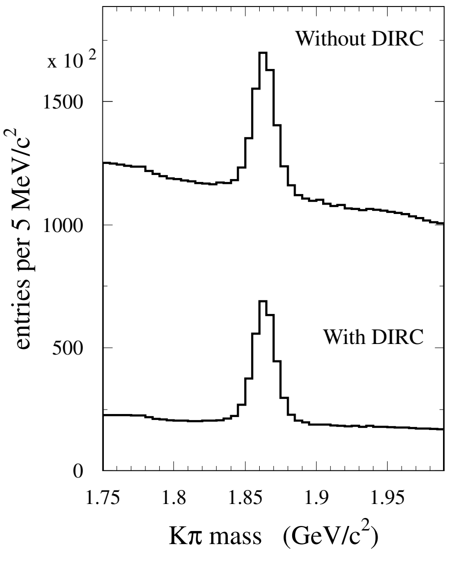

Figure 2.12: The $\pi^{\pm}K^{\mp}$ inclusive mass spectrum with and without the DIRC information for kaon identification. The peak corresponds to the mass of the D^0 particle.

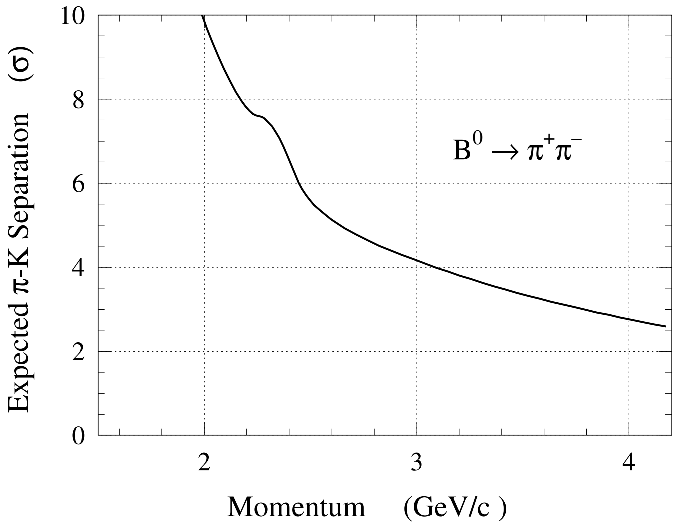

Figure 2.13: The separation in the DIRC between kaons and pions across the momentum range which is used for separating two body decays $B^0 \rightarrow \pi^+K^-$ and $B^0 \rightarrow \pi^+\pi^-$.

index is ≈ 1.346, and therefore near that of the bars. A steel shield and "bucking coil" (consisting of 10 layers of water-cooled copper coil) surround the SOB, reducing the magnetic field in the PMTs. Each of these regions contains 896 PMTs with a 29mm diameter, and they are closely packed. A hexagonal light catcher cone in front of each PMT gives a total active surface area of about 90%. The DIRC only occupies 8cm of radial space inside the detector, which is approximately 17% of a radiation length. The quartz bars cover a solid angle of 94% in the azimuth and 83% of the cosine of the CM polar angle.

Figure 2.12 shows the inclusive mass spectra for $\pi^{\pm}K^{\mp}$ with and without using DIRC information for kaon identification. The peak corresponds to the D^0 decay, and the combinatoric background is visibly reduced when DIRC information is used, whilst the signal is not significantly affected. Figure 2.13 shows the achievable $K\pi$ separation, which is about 4.2σ at $3\,\mathrm{GeV}/c$.

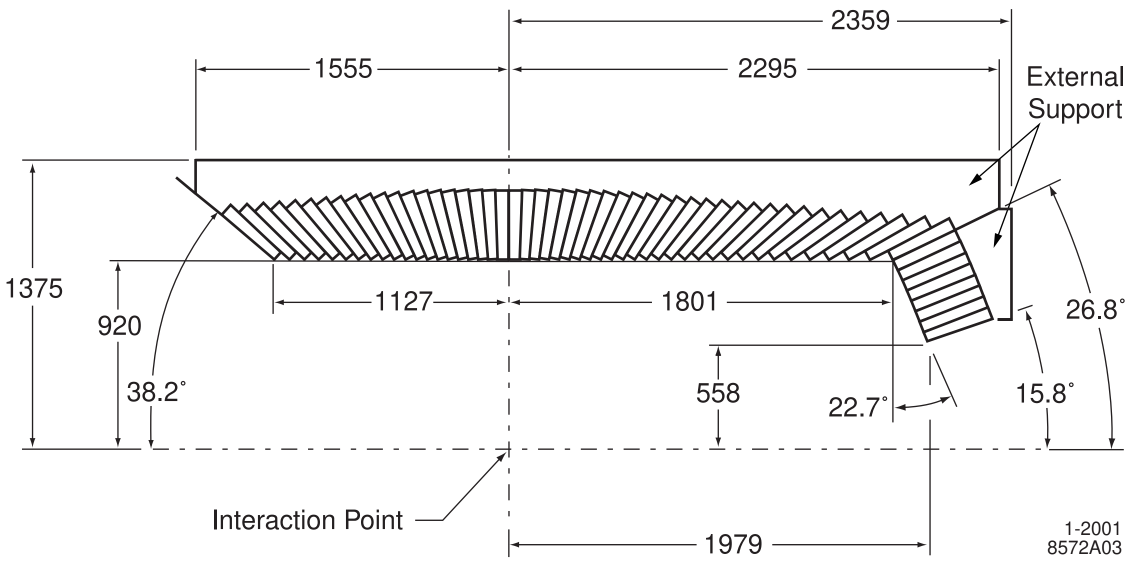

Figure 2.14: The electromagnetic calorimeter seen as a longitudinal section. All distances are in mm.

2.6 The Electromagnetic Calorimeter

The Electromagnetic Calorimeter (EMC), next in the detector, measures the energy of traversing particles. It is built from 6580 Cesium Iodide crystals doped with Thallium (CsI(Tl)) which scintillate light as charged particles from electromagnetic showers pass through.

The EMC was designed to be able to detect photons in the range of 20 MeV to 9 GeV. 50% of photons from π^0s have energies below 200 MeV and photons from processes which are important for calibration and luminosity ($e^+e^- \to e^+e^-\gamma$ and $e^+e^- \to \gamma\gamma$) can reach energies of 9 GeV.

The calorimeter consists of a conical forward end-cap and a cylindrical barrel, and is complete in azimuthal angle with coverage of 90% of the solid angle in the CM system. The crystals in the barrel are arranged within 48 rings of 120 crystals. The end-cap has 8 rings of differing size with a total of 820 crystals. A longitudinal cross-section is shown in Figure 2.14. The crystals each have a tapered trapezoidal

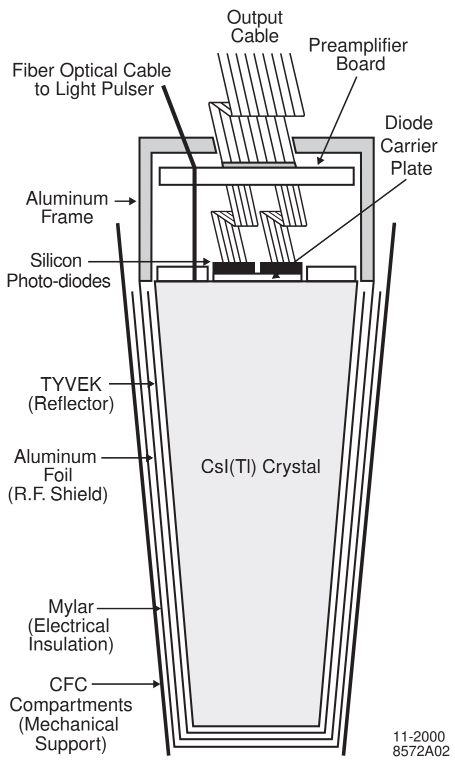

Figure 2.15: A schematic representation of the layout of a CsI(Tl) crystal and the front-end read-out package [33].

cross-section and they are each placed so that their axis is orientated towards the interaction point (IP). A schematic of a crystal is shown in Figure 2.15. Material in between the crystal modules is kept to a minimum in order to obtain the necessary resolution by having the crystals as close together as possible, and there is less than 60% of a radiation length of material in front of the crystals. This material, as well as beam related background, is what makes the minimum measurable energy in colliding beam data 20 MeV, even though in CsI(Tl) the intrinsic efficiency for photon detection is 100% down to a few MeV.

CsI(Tl) was chosen because it has a high light yield and a small Molière radius (radius of spread of electromagnetic showers). These give very good energy and position resolutions from which high reconstruction rates and good separation of nearby showers can be achieved, which are helpful when trying to identify π^0s. A short radiation length allows complete containment of the electromagnetic showers in the $\approx$30 cm crystals. The transverse length of the crystals was chosen to be comparable with the Molière radius so that a particle traversing the detector will leave energy in several crystals. The sides of the crystals are polished and covered in a reflective material to retain light. The scintillated light is detected by 2×1 cm PIN diodes glued to the rear end of the crystal, which show in which crystal the scintillation occurred and how much light was produced.

The EMC is able to separate hadrons from electrons using the electromagnetic shower shapes, energies and track momenta. The value of E/p (the ratio of the calorimeter energy to the track momentum) for electrons and hadrons is shown in Figure 2.16, which shows the electron efficiency and pion misidentification probabilities derived from radiative Bhabha and $e^+e^- \to e^+e^-e^+e^-$ events.

2.7 Superconducting Coil

The superconducting coil, between the EMC and most of the Instrumented Flux Return, creates a magnetic field of 1.5T. This is necessary to achieve good momentum resolution, whilst not increasing tracking volume and EMC cost. The magnet has an inner radius of 1.4m for the coil dewar and a cryostat length of 3.85m. The coil and the cryostat together have a total thickness of between 0.25 and 0.4 interaction lengths. This is thin enough to allow neutral hadrons to pass through reasonably well [4].

2.8 Instrumented Flux Return

The Instrumented Flux Return (IFR) is the outermost part of the detector. The IFR detects neutral hadrons and identifies muons, which are both essential for accurate

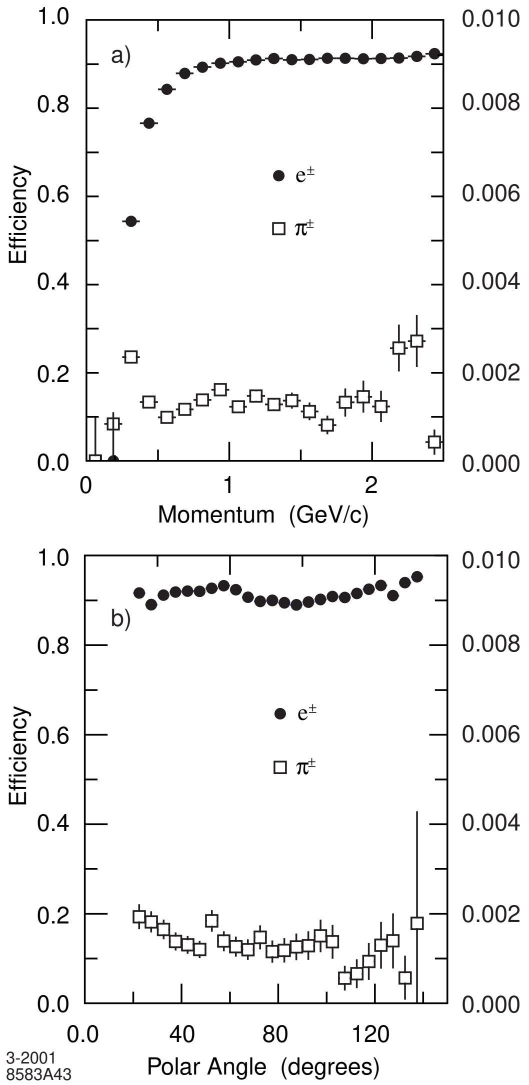

Figure 2.16: The probability of electron efficiency and pion misidentification as a function of a) the particle momentum and b) the polar angle. The units of efficiency are shown on the left-hand side for electrons and on the right-hand side for pions. Both are measured in the laboratory system.

CP measurements. Muons are important for tagging the flavour of neutral B mesons and for reconstructing J/ψ mesons in CP eigenstate decays, which can decay to both e^+e^- and $\mu^+\mu^-$. Coverage is necessary across a large solid angle as well as a good efficiency and high background rejection for muons down to momenta below 1 GeV/c. In order to study more neutral B meson decays to CP eigenstates, a good K_L^0 detection efficiency and angular resolution was also necessary in the design.

The IFR uses single detectors between layers of iron absorbers. The detectors are Resistive Plate Chambers (RPCs), and the barrel has 21 active layers. After the EMC and before the coil there is a double layer of RPCs plus a layer of planar RPCs immediately after the coil but before the iron. There are then 17 layers in gaps between the iron layers and a further layer outside the iron [4]. The total area of the detector is 2000m^2.

The magnet provides a steel flux return which the IFR uses as a muon filter and hadron absorber. The RPCs are built using two bakelite sheets, each 2 mm deep, separated by a 2 mm gap, which is filled with a gas mixture composed mostly of argon (see Figure 2.17). The external surfaces of the sheets are coated with graphite and one is connected to a 8kV voltage supply whilst the other is grounded. On top of this graphite layer is an insulation layer and then aluminium readout strips (labelled 'X strips' and 'Y strips' on Figure 2.17), one side having ϕ-measuring strips, and the other z-measuring strips, as they are placed orthogonally. The modules have a total of 32 z-measuring strips and 96 ϕ-measuring strips in the barrel (the geometry of which is shown in Figure 2.18).

The muon detection efficiency and the pion mis-identification probability are shown in Figure 2.19, which were obtained from studies of clean control samples of pions and muons in data. In the momentum region 1.5-3.0 GeV/c, a muon efficiency of more than 90% can be reached with a pion mis-identification rate of less than 8%.

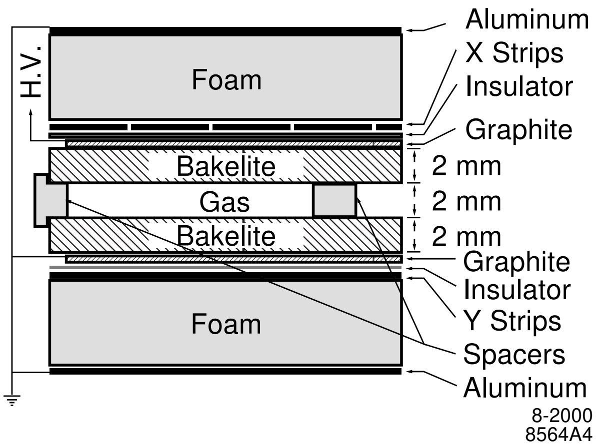

Figure 2.17: Diagram showing the cross-sectional structure of a RPC.

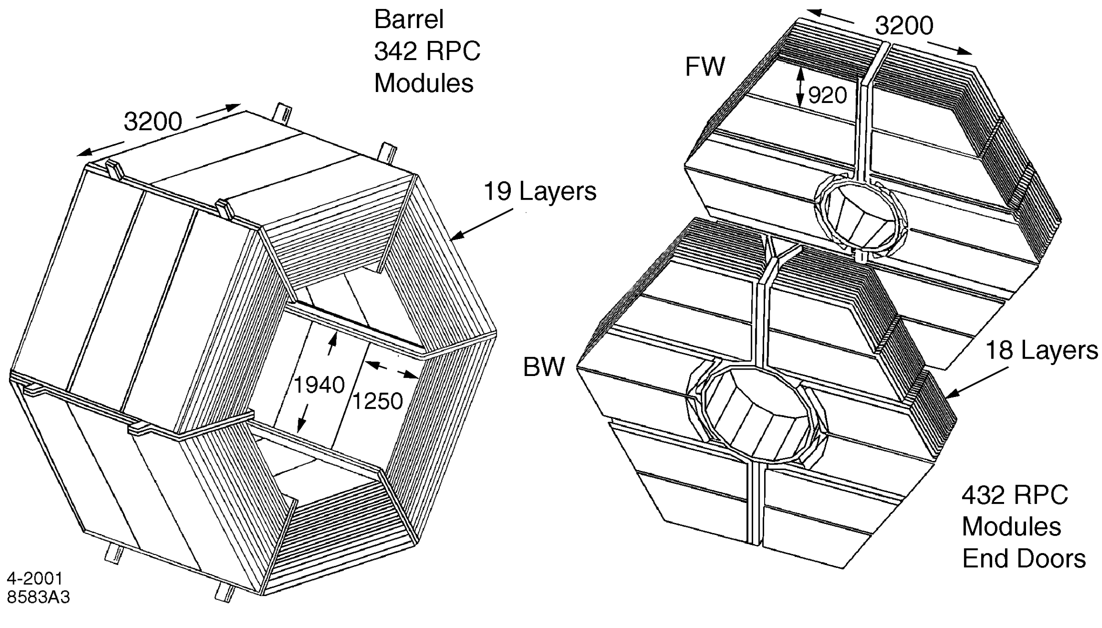

Figure 2.18: Diagram showing the geometry of the barrel and the end-cap doors in the Instrumented Flux Return. Dimensions are in mm.

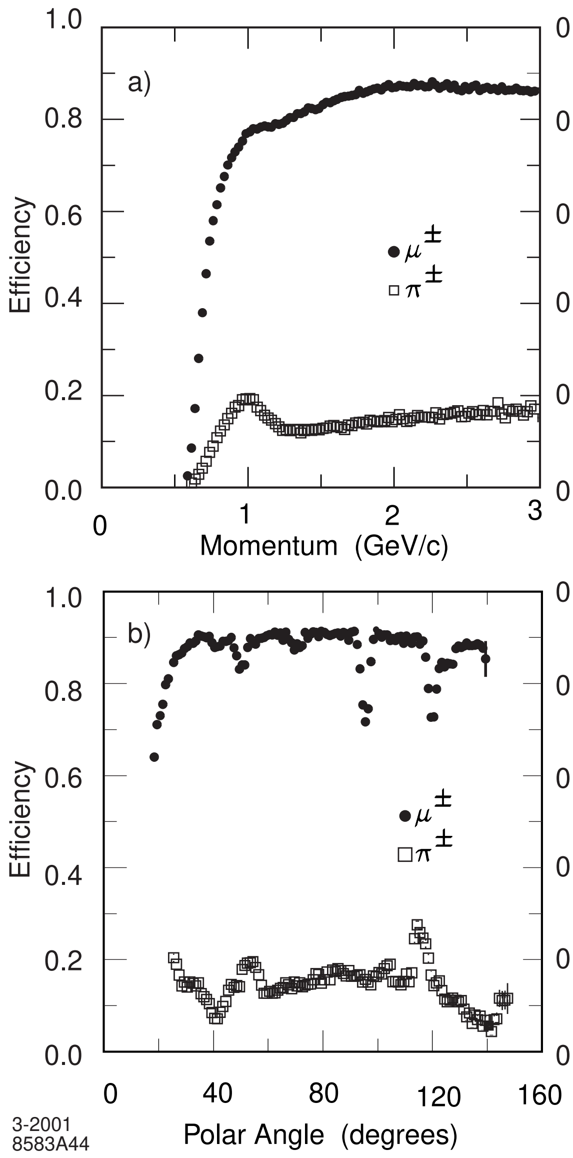

Figure 2.19: The probability of muon identification and pion mis-identification as function as momentum and polar angle in the IFR. The efficiency scale for muons is shown on the left-hand side, whilst the efficiency scale for pions is shown on the right-hand side.

2.9 Trigger

A trigger is necessary to reduce the level of background data which are recorded, especially events coming from beam pipe interactions, or cosmic rays which are of no physical value. There are two tiers of trigger within the *BABAR* system: the Level 1 (L1) hardware based trigger and the Level 3 (L3) software based trigger. The L1 trigger primarily removes a great deal of background events whilst aiming to retain all physics events, and the L3 system then selects those physics events of interest from the subset which passes the L1 selection. The efficiency of the trigger is required to be greater than 99% for $b\bar{b}$ events and greater than 95% for light quark continuum and $\tau^+\tau^-$ events. However, the trigger must not contribute more than 1% dead-time.

The Level 1 trigger comprises 3 subsystems: a drift chamber trigger (DCT), an electromagnetic trigger (EMT) and an instrumented flux return trigger (IFT), which are all in turn connected to a global level trigger (GLT). The EMT and the DCT are the main components which select events, whilst the IFT is mostly used for diagnostic purposes. Each subsystem produces signals (*primitives*) for the GLT which bases its decision on the tracks in the DCH, showers in the EMT and clusters in the IFR. The primitives are combined to form trigger lines and if these satisfy selection criteria, then the event is accepted (*Level 1 Accept*).

The primitive objects for the DCT are long and short tracks which reach different layers of the DCH, along with high p_t tracks. In the EMT, towers are the primitive objects, which sum the energy of rows of calorimeter crystals with the same ϕ angle over the length of the calorimeter. The towers each have various energy thresholds that correspond to different primitive objects.

The L1 trigger was designed to select events up to a rate of 2 kHz, since this is the maximum rate at which the data acquistion system can work. Since the DCT and EMT are two separate systems, their efficiency can be calculated separately, and each is known to be greater than 99% for $b\bar{b}$ events. Therefore, when combined they have an efficiency of around 99.9%, assuming the inefficiencies are uncorrelated.

The Level 3 trigger reduces the amount of data received from the L1 system to a rate at which Online Prompt Reconstruction (OPR) can accept data ($\approx$ 100 Hz) and the rate at which data can be stored. Using timing information, simple track finding and calorimeter clustering, the L3 system carries out a complete analysis of an event in order to decide whether to accept or reject an event. This analysis is based on simple track cluster topologies, not recognition of physics processes. The trigger lines can be prescaled to keep the rate under control, which is especially necessary for processes with high cross-sections, such as Bhabhas which are necessary for calibration purposes and luminosity measurements.

The software runs on the Online Event Processing (OEP) farm, and classifies events into categories of various physics events, cosmic rays, Bhabha events or other types used for monitoring and calibration. The output lines from the L3 are formed using logical combinations of script flags that determine whether events pass or fail. If any of the output lines fire, the event is stored for full reconstruction and offline processing.

2.10 Data Acquisition and Online Prompt Reconstruction

A schematic diagram of the data acquisition system is shown in Figure 2.20. The Front End Electronics (FEE) on each detector subsystem perform initial processing before passing the collected data to the Readout Modules (ROM) via optical fibres. The ROMs perform high level feature extraction (FEX) using system-dependent algorithms which are designed to minimise backgrounds and noise whilst preserving signal. The data then go to the L3 trigger (if an L1 accept is received) and if the

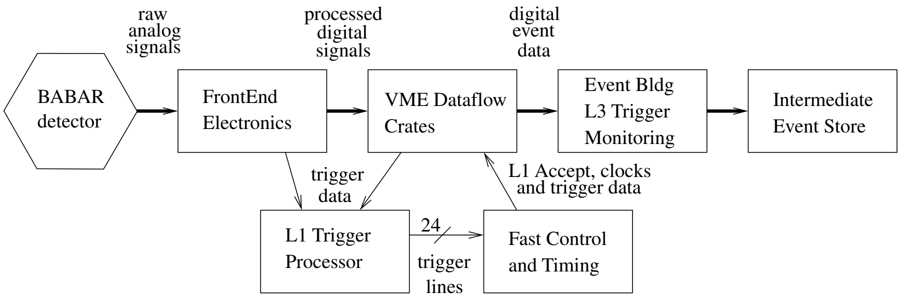

Figure 2.20: Schematic of the BABAR dataflow system.

event passes, the data are written to a temporary file before being sent to the Online Prompt Reconstruction (OPR) for the events to be processed and reconstructed.

OPR fully reconstructs the data, calculating physics quantities using information from the detector subsystems. Rolling calibrations are applied to the data and there exists a fully automated iterative system of keeping these correct. The constants are applied to data taken at that time, but then calibration code is run which aims to improve on the conditions already applied. If the new constants are an improvement, they are written to the conditions database with their validity time and the next new run will use these constants, and the process is repeated.

The OPR procedure is implemented in two steps. First a subset of the data are run so that a quick look can be taken at each run to check that the run looks correct and to run the calibration procedure. This is known as the Prompt Calibration (PC) run. Secondly the Event Reconstruction (ER) phase fully reconstructs every event using the up to date constants. This stage may have to be repeated if the calibration or reconstruction code is improved.

Many such quantities are continuously monitored for data quality purposes using software which is run at the end of each phase of reconstruction. A set of histograms is produced for each subsystem which are strictly monitored to check for problems. From this, sets of good and bad runs are identified.

Chapter 3

Analysis Method: Data, Event Selection and Background Identification

The analysis aims of this thesis are branching fraction measurements of the charmless inclusive B^0 decay to any $K^0_S\pi^+\pi^-$ final state, and of the intermediate resonant decay modes $B^0 \to K^{*+}\pi^-$, $B^0 \to \rho^0 K^0_S$ and $B^0 \to f_0 K^0_S$. In addition, the rate of charge asymmetry in $B^0 \to K^{*+}\pi^-$will be measured. The analyses are all based on Maximum Likelihood fitting, and the data, variables, methods and tools used are described in the following two chapters. The analysis is performed "blind", which means that the signal area is not viewed or fit to until the analysis has been thoroughly checked and tested using Monte Carlo data, and actual data which are far from the signal region. For each decay mode, the charge conjugate is also implied.

3.1 Data Sample

This analysis uses the Runs 1-4 data sample of 210.6 fb^{-1}, which was recorded between 1999 and 2004 by the *BABAR* detector. This sample contains approximately 232 million $B\overline{B}$ pairs collected at the $\Upsilon(4S)$ resonance [34]. 21.6 fb^{-1} of data taken at 40 MeV below the $\Upsilon(4S)$ resonance was also used to characterise the background due to the light quark continuum. Additionally, a great deal of Monte Carlo (MC) simulation of both the signal and backgrounds of the analyses was used for choosing selection requirements, estimating their contribution to the dataset and modelling their distributions for the fits.

3.1.1 Simulation Production

MC enables a blind, unbiased fit to the on-resonant data in the signal region to be performed and the expected efficiencies to be calculated. These simulated data must accurately mimic the event characteristics and the effect of the *BABAR* detector on the event. The *BABAR* experiment uses `EvtGen` [35] for the event generation, with an interface to `JETSET` [36] for production of continuum events. The output four-vectors and vertices are then input into a full `GEANT4` [37] based simulation which imitates the detector geometry and the effects of traversing each subsystem on the particle 4-vectors. The data are generated using configurations and running conditions taken from the *BABAR* detector, such that the simulated data samples accurately reflect the changes which occur to the running conditions. The output of this includes detector signals and information for each event, such that all output variables of genuine data are included. The quality of the MC is checked by comparing decay modes and key physics quantities between samples of MC and of real data.

3.2 Event Preselection

In order to obtain a reduced sample of data which is suitable for analysis, the raw data from the *BABAR* detector are filtered in two stages. The skim production reduces the data sample to events which are consistent with the skim hypothesis, which in this case is a three-body decay with a final state compatible with two charged particles and a K_S^0. Ntuple generation calculates analysis variables that give information about each event and track, which can be used to separate signal from background in an analysis.

3.2.1 Inclusive Skims

A skim reduces the amount of data which each type of analysis must run over in order to collate its final data sample. A filter was used which selects candidate B decays to four charged particles, two of which are associated with a K_S^0 candidate taken from the `KsDefault` list. This is a list of pairs of oppositely charged tracks with a fitted mass within 0.025 GeV/c^2 of the PDG [38] mass for the K_S^0 [39]. The two tracks not associated with a K_S^0 are tested with both the $\pi^\pm$ and $K^\pm$ mass hypotheses, and together with the K_S^0 candidate, were required to pass the `GoodTracksLoose` criteria in order to be considered a B candidate:

- Each track has a transverse momentum greater than 0.1 GeV/c,
- Each track has a total momentum less than 10 GeV/c,
- Each track must have at least 12 hits in the drift chamber,
- The distance of closest approach to the interaction point for a track is less than 10 cm along the z-axis,
- The distance of closest approach to the interaction point for a track is less than 1.5 cm in the x-y plane,

Events are also subjected to a filter to remove background events. However, some background events in sideband regions (as discussed in Section 4.4) are kept to help characterise the backgrounds which are present in the signal region. The filter applies the following restrictions:

- For each candidate the sum of the charges of the tracks must be 0.
- The event must have at least 5 tracks,
- The total energy of the event must be < 20 GeV,
- The variable $m_{\rm ES}$ is less than 0.1 GeV/c^2 from the kinematic end point (the centre-of-mass beam energy). $m_{\rm ES}$ is the beam energy substituted mass and is defined as

  $$m_{\rm ES} = \sqrt{(\frac{s}{2} + \vec{p}_{\Upsilon} \cdot \vec{p}_B)^2 / E_{\Upsilon}^2 - \vec{p}_B^{\,2}} \tag{3.1}$$

  where $\vec{p}_{\Upsilon}$ and $\vec{p}_B$ are the three-momenta of the $\Upsilon(4S)$ and the B respectively in the laboratory frame and E_{Υ} is the energy of the $\Upsilon(4S)$ in the laboratory frame [40],
- The magnitude of ΔE is less than 0.45 GeV, where

  $$\Delta E \ = E_x - E_B. \tag{3.2}$$

  E_x is defined as the reconstructed energy of the candidate in the laboratory frame, and E_B is the energy expected for a B decay. This condition is tested with all permutations of masses assigned to the tracks and if any of these pass, the event is selected [40].

The events selected by the skim were output to reduced collections which were subjected to further selection criteria to reject as much background as possible while keeping the majority of signal events.

3.2.2 Ntuple production

The second stage of reducing the dataset not only filters but takes the opportunity to refine the existing variables and add extra discriminating analysis variables. The result is a `Root` [41] analysis file containing an ntuple, which is a collection of variables arranged in a structured format.

Firstly, the vertex for the B candidate was recalculated, and the vertex χ^2 was determined by a vertexing algorithm. The algorithm found a vertex using both a kinematic and a geometric fit to tracks in an iterative χ^2 minimisation procedure for all track mass hypotheses (pion or kaon). The kinematic fit forced momentum to be conserved at the decay vertex. The geometric fit required that all the tracks have the same origin, based on the distance of closest approach of a set of tracks to a point. To improve the energy and momentum resolution of the daughters of the B meson candidate, the momenta of their tracks were adjusted within their errors during the fit. A loose cut on the χ^2 value of the fit was applied, which had little effect on the signal efficiency, but helped to reduce combinatorial background.

This initial vertexing procedure calculates the ΔE and m_{ES} variables and then the vertexing is repeated with the additional constraint that the invariant masses of the B candidate daughters must sum to the B mass. All other variables are recorded from this second vertexing.

Furthermore, the vertices and invariant masses of intermediate states were then calculated. The K^0_S vertex was reconstructed in the same way as the B vertex, and the invariant mass was calculated. In this analysis only $K^0_S \to \pi^+ \pi^-$ decays were reconstructed. The invariant masses of $K^0_S\pi^\pm$ and $\pi^-\pi^+$ combinations were also calculated so that resonances could be reconstructed. In the case of $K^0_S\pi^\pm$ combinations, a vertex was calculated for all combinations of charged tracks with a K^0_S from the `KsDefault` list. For a $\pi^+\pi^-$ resonance, such as f_0, a vertex was calculated for all combinations of two oppositely charged tracks. In both cases the invariant mass was evaluated for each combination considered and tested against the Particle Data Group (PDG) values, so the candidate could be vetoed for charmed or charmonium mesons or selected in the case of charmless mesons. In turn, the vertex information enabled better measurements of ΔE and m_{ES} to be recorded.

In addition, various calculated event shape variables, described in Section 3.3, were stored, along with information from Particle Identification (PID) selectors, described in Sections 3.5.1 and 3.5.2, and invariant mass quantities. Selection criteria were then applied to this ntuple in order to achieve the final data sample for analysis. This is discussed in Section 3.6.1.

3.3 Discriminating Variables

There are several discriminating variables used in this analysis to differentiate between signal and background. The variables which are parameterised in the maximum likelihood fit are m_{ES}, ΔE, and Fisher.

- m_{ES} is the energy substituted mass of an event, as defined in Section 3.2. It peaks around the B mass for signal B decays as opposed to background which generally does not. Typically, the light quark background m_{ES} distribution can be described by an Argus function (discussed in Section 4.4.1) [42].

- ΔE which is also defined in Section 3.2, is essentially the difference between the reconstructed energy of the B candidate and the energy that would be expected from a B decay. B decays peak around zero and light quark background events have an approximately linear distribution.

- The Fisher discriminant ($\mathcal{F}$) [43, 44] uses several variables x_i to discriminate between different types of event. The variables are arranged in a linear combination to form the discriminant:

$$\mathcal{F} = \sum \lambda_i x_i \qquad [3.3]$$

The λ_i, which are the coefficients of x_i, are chosen to maximise the significance of the difference between the $\mathcal{F}$ distributions for the background and signal events. The variables chosen for use in the Fisher are discussed in 3.4. The Fisher differentiates between the jet-like $q\overline{q}$ events and spherically distributed B events, and the coefficients maximise the separation between the two forms of event.

- $\cos\theta_{thr}$ is the cosine of the angle between the thrust axis of the "Rest of the Event" (ROE) and the momentum of the B candidate in the centre-of-mass frame. The thrust axis is the direction which maximises the sum of the longitudinal momenta of the particles in the event. It is used to discriminate against light quark background. In the centre-of-mass frame, light quark events have a back-to-back "jet" structure and therefore the two thrust axes tend to be aligned. However for a B-meson event, the $B\overline{B}$ pair is at rest in the centre of mass frame so the thrust axes are distributed isotropically.

- The K^0_S mass ($m_{K^0_s}$) cut is used to discriminate the K^0_S from random track combinations or other short-lived mesons which can be reconstructed from a pair of oppositely charged pions.

- K^0_s lifetime significance. The K^0_s meson has a distinctly long flight length before it decays, which can be used to discriminate it from combinatoric background. The lifetime significance is defined as:

$$\text{lifetime significance} = \frac{c\tau}{\sigma_{c\tau}} \qquad (3.4)$$

  where c is the speed of light, τ is the measured lifetime of the K^0_S candidate and $\sigma_{c\tau}$ is the error on the product of these two values.

- $\cos\theta_{K_s}$. The angle between the line of flight of the K^0_S and its momentum vector is a good discriminating variable for the K^0_S.

$$\cos\theta_{K_s} = \frac{\vec{p}\cdot\vec{r}}{|\,\vec{p}\,||\,\vec{r}\,|} \qquad [3.5] \qquad (3.5)$$

where $\vec{p}$ is the momentum of the K_S^0 and $\vec{r}$ is the vector between the K_S^0 and B vertices. This variable also helps to distinguish between real K_S^0 candidates and combinatoric background as in the latter case there is no correlation between the line of flight to the B vertex and the momentum vector.

The signal and background distributions for the above variables used in this analysis can be seen in Figures 3.1 and 3.2. The signal distribution is obtained from Monte Carlo and the light quark background is taken from either off-resonance data or on-resonance sideband data. The cuts used to obtain the data samples are described in Section 3.6.1

3.4 Studies of various Fisher discriminants

A study has been conducted of 8 different Fisher discriminants to see which type of Fisher gives the greatest discrimination power between signal and background. The variables used were:

- the zeroth and second order Legendre Polynomials ($\mathcal{L}_0$ and $\mathcal{L}_2$)

$$\mathcal{L}_0 = \sum^{ROE} p_i, \qquad \mathcal{L}_2 = \sum^{ROE} p_i \times \frac{1}{2}(3\cos^2(\theta_i) - 1) \tag{3.6}$$

  where ROE means the "Rest Of the Event" (the other B meson in the event), p_i and θ_i are the momentum and the polar angle of tracks summed over the candidates in the ROE.

- `TFlv` - the output of the Moriond tagger [45]. The tagger uses information for the ROE to find whether the second B in the event was a B^0 or a $\overline{B}^0$ meson. This variable contributes information about the topology of the ROE when used in a Fisher.

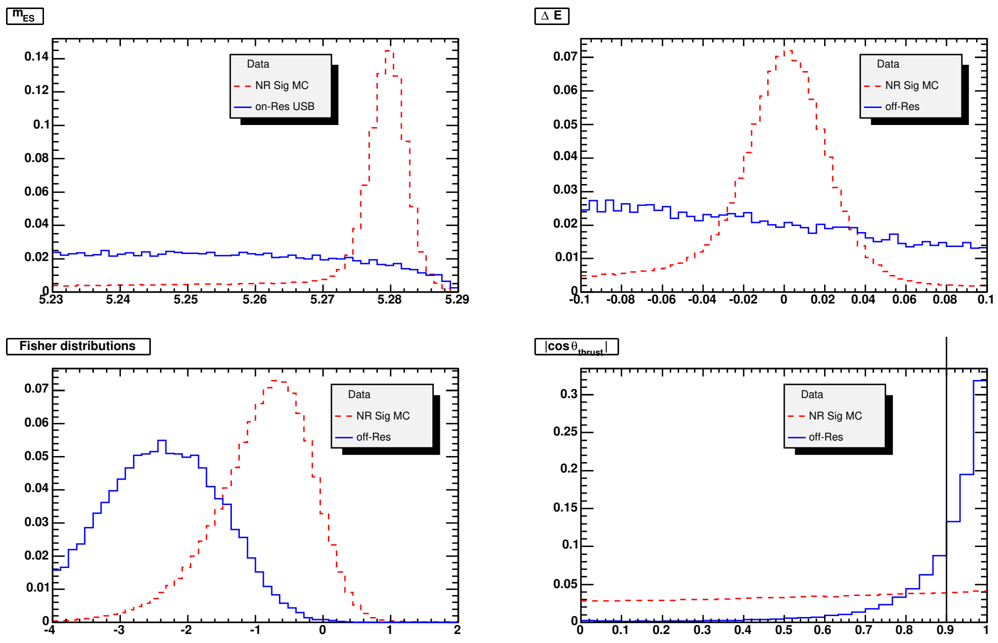

Figure 3.1: Plots of discriminating variables for both signal and background used in this analysis, where the integrated value of each distribution is 1. The distributions plotted are $m_{\rm ES}$ (top left), ΔE (top right), $\mathcal{F}$ (bottom left) and $\cos\theta_{thr}$ (bottom right). In all of the plots the dashed red line is nonresonant Monte Carlo and the solid blue line is off-resonance data except in the case of the $m_{\rm ES}$ plot where the solid blue line is upper sideband data. This analysis used $m_{\rm ES}$, ΔE and Fisher in the ML fit (Section 4.1), whilst the selection criterion for thrust was $\mid \cos\theta_{thr} \mid < 0.9$, as indicated with a black solid line on the corresponding plot.

- $\cos(\theta_{B_{mom}})$ - the cosine of the angle between the B momentum vector and the positive z-axis,
- $\cos(\theta_{B_{thr}})$ - the cosine of the angle between the B thrust axis as the positive z-axis,
- the 9 CLEO cones [46] - 9 concentric, contiguous cones (in both the forward and backwards directions) about the thrust axis of the B meson. Each cone has a radius $10°$ wider than the one inside it, and each cone's volume does not

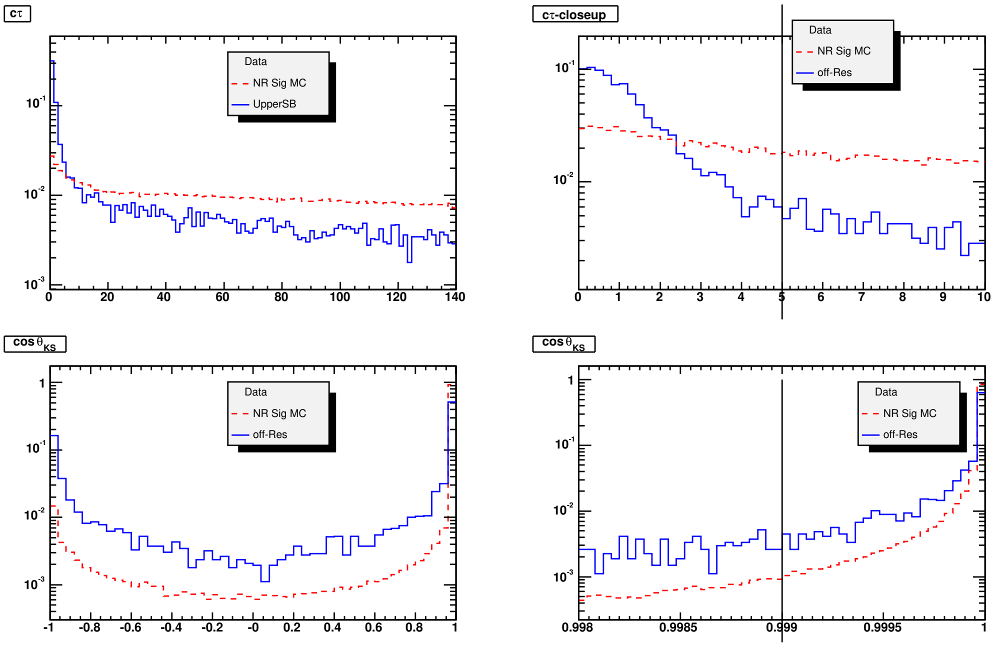

Figure 3.2: Plots of discriminating variables for both signal and background, where the integrated value of each distribution is 1. The distributions plotted are lifetime significance (top left) and the same distribution plotted over a smaller range (top right). The $\cos\theta_{K_s}$ *distributions are plotted (bottom left) and repeated for a smaller range (bottom right). The selection criterion for lifetime significance was chosen to be greater than 5, and for* $\cos\theta_{K^0_S}$ *to be greater than 0.999, as indicated with a black line on the right hand distributions. In each case, the dashed red line is the nonresonant MC, and the solid blue line is off-resonance data.*

include that of cones within it. The sum of the ROE energy (for both charged and neutral candidates) within the volume of each cone gives topological information for each event.

The 8 combinations of these variables which were tested were:

- Legendre Polynomials ($\mathcal{L}_0$, $\mathcal{L}_2$), 2 variables
- Legendre Polynomials ($\mathcal{L}_0$, $\mathcal{L}_2$) + abs(`TFlv`), 3 variables

- Legendre Polynomials ($\mathcal{L}_0$, $\mathcal{L}_2$) + abs($\cos(\theta_{B_{mom}})$) + abs($\cos(\theta_{B_{thr}}$), 4 variables)

- Legendre Polynomials ($\mathcal{L}_0$, $\mathcal{L}_2$) + abs($\cos(\theta_{B_{mom}})$) + abs($\cos(\theta_{B_{thr}})$) + abs(`TFlv`), 5 variables

- 9 CLEO cones, 9 variables

- 9 CLEO Cones + abs(`TFlv`), 10 variables

- 9 CLEO Cones + abs($\cos(\theta_{B_{mom}})$) + abs($\cos(\theta_{B_{thr}})$), 11 variables

- 9 CLEO Cones + abs($\cos(\theta_{B_{mom}})$) + abs($\cos(\theta_{B_{thr}})$) + abs(`TFlv`), 12 variables

As described in Section 3.3, a Fisher represents a linear combination of the included variables. To maximise the separation between the distributions of signal and background events, the coefficients of the variables were optimised on $B^0 \to K^0_S\pi^+\pi^-$ nonresonant MC and off-resonant data. Cross-checks on the results of this test were performed on the MC for each of the 4 quasi-two body modes, which reproduced the results from the nonresonant sample. The results are shown in Figure 3.3.

This test shows that the 5 variable Fisher ($\mathcal{L}_0$, $\mathcal{L}_2$, abs($\cos(\theta_{B_{mom}})$), abs($\cos(\theta_{B_{thr}})$), abs(`TFlv`)) has the greatest discriminating power of the eight tested. Therefore, the 5 variable Fisher is used in the ML fit, and henceforth is simply referred to as the Fisher.

3.5 Particle Identification

The standard *BABAR* particle identification (PID) procedures enable analysts to discriminate effectively between pions, kaons, protons and electrons.

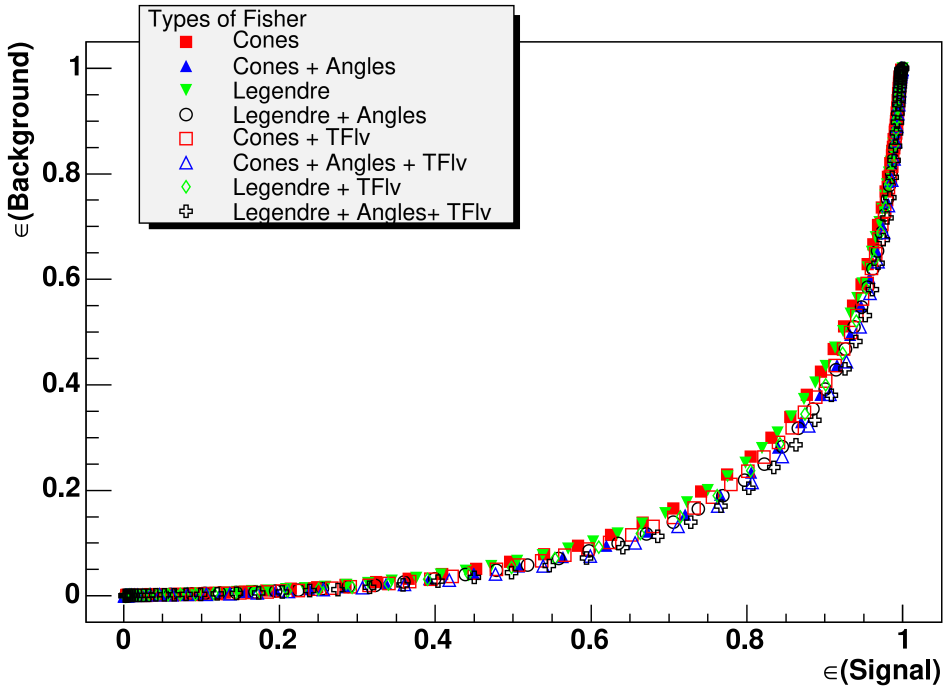

Figure 3.3: Signal efficiency vs. background efficiency for 8 different types of Fisher. The legend describes which Fisher is represented by which marker.

3.5.1 Pion Selection

In order to select the pions for the final state, it is necessary for the two charged B daughters to fail the kaon selector, `SMSKaonSelector` [47], which has several selection modes: `veryloose`, `loose`, `notAPion`, `tight` and `verytight`.

The `SMSKaonSelector` uses information from the SVT, DCH and DIRC sub-detectors to separate particle signatures. The SVT and DCH provide truncated mean $\mathrm{d}E/\mathrm{d}x$ information below momenta of $0.6\,\mathrm{GeV}/c$ and $0.7\,\mathrm{GeV}/c$ respectively, producing around a 2σ separation between kaons and pions. The DCH can also provide a 2σ separation above $1.5\,\mathrm{GeV}/c$. DIRC information is used for particles with momenta above $0.6\,\mathrm{GeV}/c$.

Figure 3.4 shows the distributions of $\mathrm{d}E/\mathrm{d}x$ for the SVT and the DCH, whilst

Figure 3.5 shows the dE/dx against momentum in both subsytems.

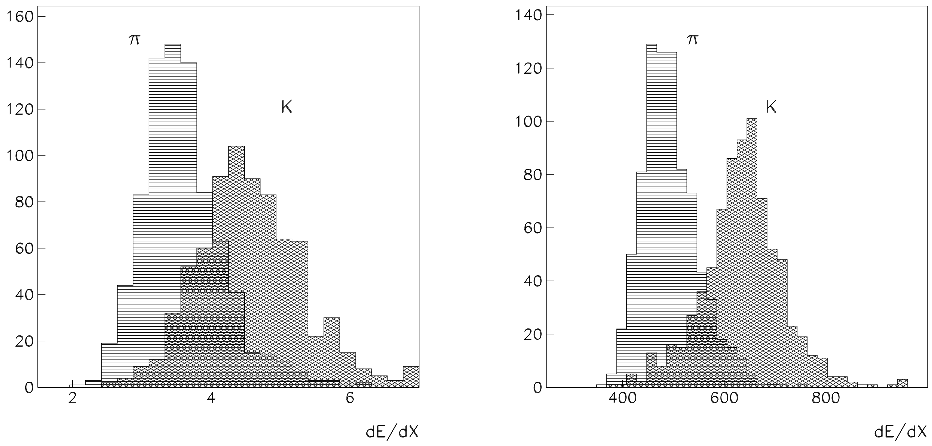

Figure 3.4: The truncated-mean dE/dx *distributions for pions and kaons in the SVT (left) and the DCH (right). These figures were made using a very pure D^* decay sample in the momentum range of 0.5-0.6* GeV/c *for the SVT plot and 0.6-0.7* GeV/c *in the DCH, which correspond to the energies of particles for which these subdetectors are the primary source of PID information.*

Kaons traversing the DIRC emit Cherenkov light in the quartz bars if the momentum of the kaon is above the threshold which is defined as:

$$p > \frac{m}{\sqrt{n^2 - 1}}, \tag{3.7}$$

where m and p are the particle's mass and momentum, respectively, and n is the refractive index of the bars ($n = 1.473$). The value of the Cherenkov emission angle (the angle between the emission vector and the track), θ_C can be described by:

$$\cos\theta_C = \frac{1}{n\beta}, \quad \text{where} \quad \beta = pc/E \tag{3.8}$$

This is used to parameterise the mean of the Cherenkov angle for each particle type (e, μ, π, K and p).

The number of photons produced by a particle with a fixed path follows Poissonian statistics and the central value of the distribution depends on the particle type,

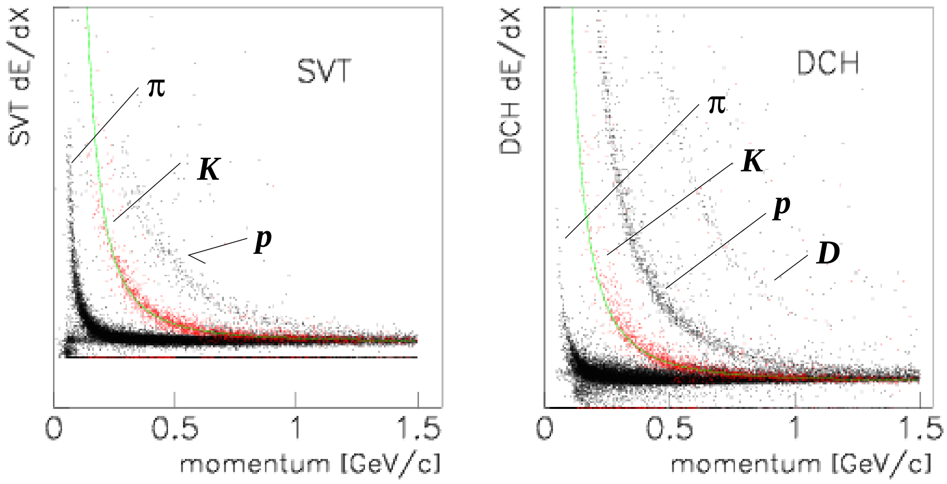

Figure 3.5: dE/dx *vs particle momentum distributions for the SVT and the DCH using MC data for the SVT (left) and the DCH (right).*

its momentum, charge, polar angle and the position in the DIRC. This information about the expected number of photons as functions of these parameters is stored in a lookup table. The left hand plot of Figure 3.6 shows the distribution of the Cherenkov angle as a function of momentum.

The selection of kaons is based on a likelihood method, using the expected Cherenkov angle distributions of kaons (θ_K) and pions (θ_π). The distribution is assumed to be Gaussian and the error (σ_{θ_C}) is assumed to be well-known. The pull of each angle from zero is defined as:

$$\Delta_i = \frac{\theta_C - \theta_i}{\sigma_{\theta_C}}, \quad \text{where} \quad i = K, \pi \tag{3.9}$$

The left hand plot of Figure 3.7 shows that Δ_K is centred at zero. For kaons, Δ_π is shifted towards higher values by an amount corresponding to the separation between the two mean values, $\theta_\pi - \theta_K$. The probability density function (PDF) is a Gaussian function g_i, written as:

$$g_i = \frac{1}{\sqrt{2\pi}\sigma_{\theta_C}} e^{-0.5\cdot\Delta_i^2}. \tag{3.10}$$

A cut on the ratio can be used to separate pions from kaons:

$$g_K/g_\pi > r \tag{3.11}$$

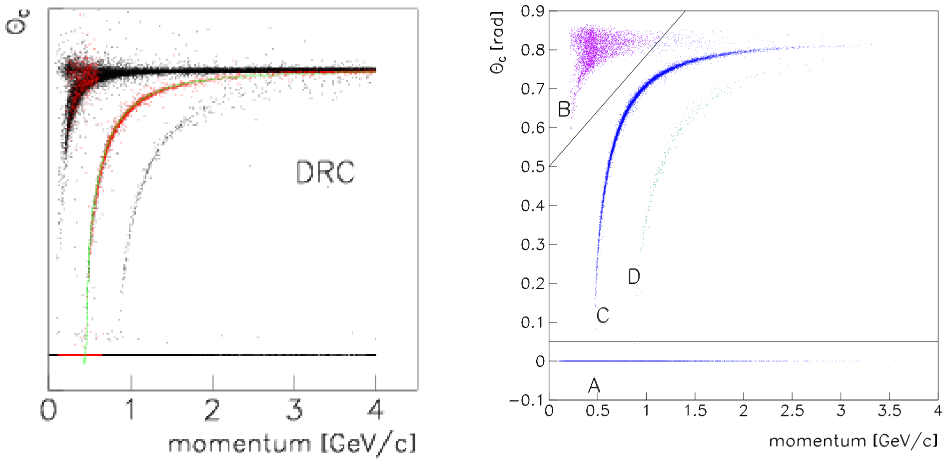

Figure 3.6: Both plots show momentum vs the Cherenkov angle within the DIRC. The left plot gives the distribution using generic B-decay MC. The right plot shows the same plot using simulated kaon tracks. The band which represents kaons is band C, but kaons appear in the bands for all particle types. Band A shows particles for which no Cherenkov angle fit is performed, either because they produced a small number of photons compared with the background photons near the particle threshold, because the particle did not reach the DIRC, or because the fit failed to converge. Band B is populated by electrons, muons and pions, which are the decay or interaction products of the original kaon which did not deviate a lot from the original path of the mother kaon. Band D contains protons which result from hadronic interactions.

but because of the overlap shown in Figure 3.7, there will always be some pions selected when kaons are required.

The calculation of the likelihood uses a Gaussian distribution (g_i, where i is the types of particle) for the PDF for each dE/dx detector (the SVT and the DCH). The dE/dx calibration provides the mean for the Gaussian and the calibration for each subsystem provides the momentum dependent relative error. For the DIRC parameters, the `SMSKaonSeletor` uses a Gaussian plus a Poissonian PDF (p_i) which results from a maximum likelihood fit to the DIRC θ_C output. The likelihood is

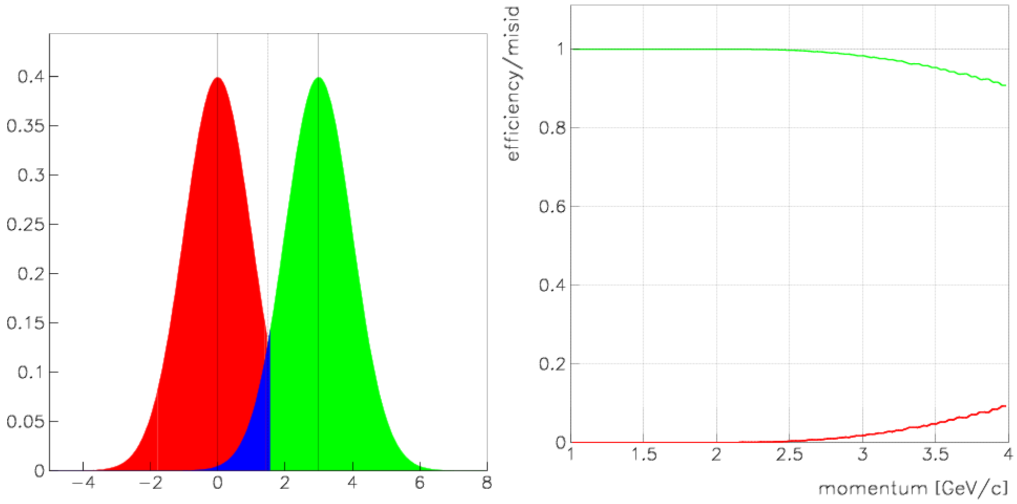

Figure 3.7: The Gaussian distribution (left plot) of the Cherenkov angle (θ_C) around its mean for kaons (left peak) and pions (right peak). The number of selected kaons and pions can be calculated using a certain cut between the two particle distributions. The right plot gives the results of such a calculation using $r = 1$, beginning with an equal number of kaons and pions, and showing the efficiency of kaon identification (top distribution) against the rate of pion-misidentification (bottom distribution).

defined as:

$$l_i = g_i \dot{p}_i / \sum_i g_i \dot{p}_i \tag{3.12}$$

Information about the Cherenkov angle and the number of photons in the quartz crystals due to the particle's interaction is used to form the likelihood distribution, and the selector is based on the ratio of likelihoods mainly for pions (l_π), kaons (l_K) and protons (l_p).

For this analysis, pion candidates are required to fail the `SMSKaonSelector` in its `notAPion` form. The tracks must:

- have the following momentum range (in GeV/c) in order to use PID information from each of these sub-detectors:
  - SVT : < 0.5

  - DCH : < 0.6
  - DIRC : > 0.6

- pass a likelihood cut of $r_\pi l_\pi \leq l_K$ & $r_\pi l_\pi \leq l_p$ where r and l are defined in Equations 3.11 and 3.12 respectively. r_π is set to be:
  - $r_\pi = 0.1$ when $p \leq 0.5\,\mathrm{GeV}/c$
  - $r_\pi = 1.0$ when $p > 0.5\,\mathrm{GeV}/c$

These criteria are optimised for maximum kaon efficiency, and so are rather tight cuts when seeking pions. This selection mode was chosen as it exhibited the best signal-to-background ratio, and also such tight criteria reduce the feed down from the $B^0 \to K_S^0 K^\pm \pi^\mp$ mode, which can happen when the kaon is misidentified as a pion.

A correction to the MC efficiency is required to account for differences between the simulation and data. A description of this correction and its associated uncertainty is in Section 6.1.2.

3.5.2 Electron Vetoing

Electrons are also vetoed from being misidentified as pions using a similar method which utilises information from the EMC and the DIRC. A likelihood based selector, LHESelector, is used, where probability density functions (PDFs) are utilised for the energy deposited and the lateral shower shapes in the EMC and the Cherenkov angle measured by the DIRC. Reconstruction computes the likelihood measurements for $\mathrm{d}E/\mathrm{d}x$ and this is combined with the PDFs to give a likelihood value which can be used to differentiate electrons from hadrons [48].

3.6 Event selection

3.6.1 Candidate Selection

In order to identify candidates consistent with $B^0 \rightarrow K^0_S\pi^+\pi^-$, selection criteria are applied to the ntuples. The criteria are summarised in Table 3.1, which details the effect of these selection criteria on the three data types: on-resonance data, off-resonance data and Monte Carlo for $B^0 \rightarrow K^0_S\pi^+\pi^-$.

The K^0_S mass window is chosen to be $15\,\mathrm{MeV}/c^2$ either side of the K^0_S PDG mass value of $0.498\,\mathrm{GeV}/c^2$. The K^0_S mass distribution (after all other selection has been implemented) is shown in Figure 3.8.

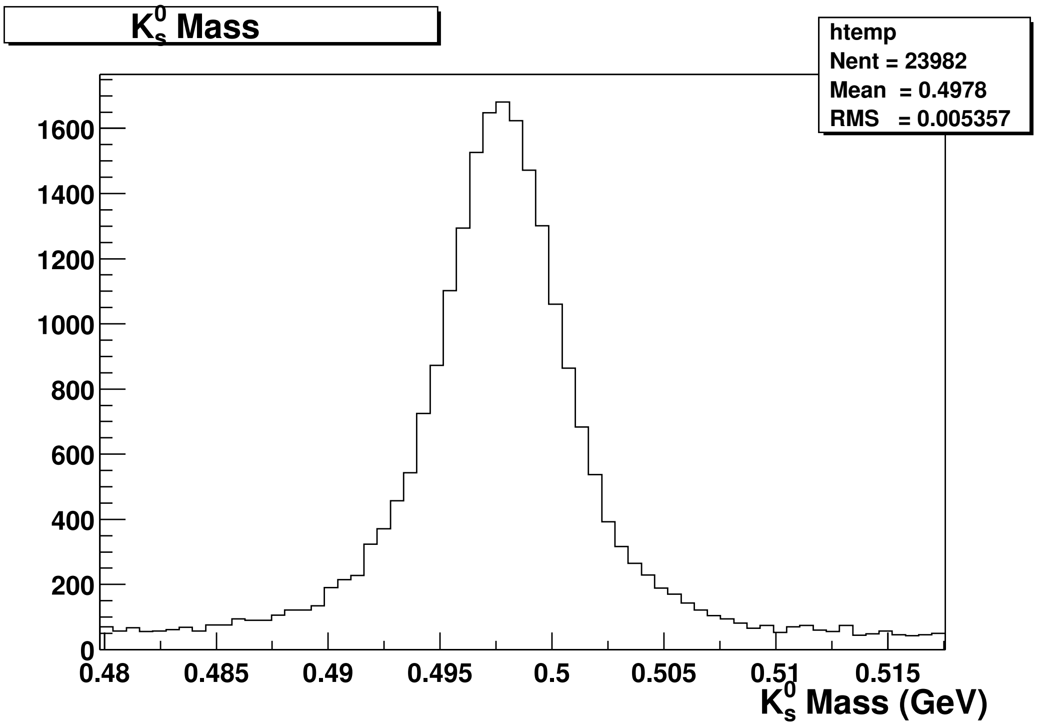

Figure 3.8: K^0_S mass distribution in nonresonant MC after all cuts for $B^0 \rightarrow K^0_S\pi^+\pi^-$ candidates.

Plots of other discriminating variables which are used to characterise background

Cut	On-res	Off-res	MC (True-B)	MC (CF)
Reconstruction and Preselection			0.65	
Tracks 1 and 2 fail `notApion SMSKaonSelector`	0.40	0.40	0.67	0.66
Tracks 1 and 2 fail electron selector (LHESelector)	0.95	0.95	1.00	1.00
π's have opposite charge	1.00	1.00	1.00	1.00
$5.22 < m_{ES} < 5.29$ GeV/c^2	0.71	0.71	1.00	0.81
$-0.3 < \Delta E < 0.3$	0.87	0.87	1.00	0.91
$0.483 < m_{K^0_S} < 0.513$ GeV/c^2	0.70	0.70	0.97	0.83
$\lvert\cos\theta_{thr}\rvert < 0.9$	0.38	0.36	0.88	0.87
K^0_S Lifetime significance > 5.0	0.44	0.44	0.96	0.75
$\cos\theta_{K^0_S} > 0.999$	0.78	0.78	0.98	0.83
Charm veto	0.88	0.90	0.78	0.64
$\lvert\Delta E\rvert < 0.1$ GeV	0.32	0.33	0.97	0.41

Table 3.1: $B^0 \to K^0_S\pi^+\pi^-$ efficiencies. The MC used was the nonresonant $B^0 \to K^0_S\pi^+\pi^-$ signal MC. True-B refers to a set of particles that make up a candidate and have the same B meson parent particle. Cross-feed (CF) accounts for 6.2% of the final data sample. Multiple candidates are found in 12.4% of events, and a candidate is selected based on $\cos\theta_{thr}$.

are shown in Figures 3.1 and 3.2. These compare the distributions of each variable for both signal MC and sideband on-resonant data.

It is helpful to further reduce the background by selecting a narrower band in the variable ΔE, and fitting for signal within that region only. The signal region is defined to be $|\Delta E| < 0.1$ GeV. The regions above and below this band, up to 0.3 GeV, are used to characterise backgrounds to the signal sample, which is described in detail in Section 3.7. Charm vetoes (discussed in Section 3.7.2) were implemented to remove the majority of charm and charmonium background, which otherwise would have dominated the signal region.

After these selection criteria have been met, it was possible for more than one candidate to exist in an event. Signal MC for nonresonant $B^0 \to K_S^0\pi^+\pi^-$ indicates that multiple candidates occurred in 12.4% of events, with an average of 1.16 candidates per event. One candidate was chosen by selecting the candidate with its $\cos\theta_{thr}$ value closest to zero. This method selected the correct candidate 43.1% of the time, which is the same as what would have been expected if selecting a candidate at random. This did slightly bias the $\cos\theta_{thr}$ distribution, however this variable is not used for any fits. Monte Carlo tests concluded that 99.6% of $B^0 \to K_S^0\pi^+\pi^-$ events contained only one K_S^0 candidate, and therefore K_S^0 reconstruction had little effect on the number events with multiple candidates. With the final sample of candidates, Monte Carlo shows that all cases of multiple candidates are a consequence of cross feed (CF). CF events are events in which the final state particles are not all daughters of the same B meson. For example, the final state $K_S^0\pi^+\pi^-$ may be reconstructed with the correct $K_S^0\pi^+$ but the π^- may actually belong to the decay of the other B meson in the event.

3.7 Types of the Backgrounds

However stringent the selection process is, there will always be background events contaminating the signal events. There are two types of background that must be accounted for within the scope of this analysis method, continuum background and B-related background.

3.7.1 Continuum Background

Continuum background is composed of $q\overline{q}$ events (where $q\overline{q}$ represents $u\overline{u}$, $d\overline{d}$, $s\overline{s}$ and $c\overline{c}$) that pass the selection cuts. Since the final state does not originate from the decay of a B meson, the reconstructed masses of such events are not focused around the B mass in m_{ES} and varies smoothly across the m_{ES}-ΔE plane. Its m_{ES} dependence can be characterised using sidebands of the m_{ES}-ΔE plane between $0.1 < \Delta E < 0.3$ GeV and $-0.3 < \Delta E < -0.1$ GeV. However, the sideband with $\Delta E < -0.1$ was found to be significantly contaminated with B related background, so the upper sideband is used to characterise the shape of the m_{ES} and Fisher variables. Off-resonance data can be used to describe the shape of the continuum ΔE distribution, so that a substantial ΔE range can be utilised. The parameterisation of this background is discussed in Section 4.4.1.

3.7.2 B-Related Background

B-related background consists of B-meson decays with a different final state than the signal mode but which mimic the signal modes such that they pass the preliminary cuts and populate the signal region. This type of background often peaks around the B-meson mass in m_{ES}.

B decays to charm and charmonium states are a factor 100 more frequent than charmless decays, and therefore such modes with a $K^0_S\pi^+\pi^-$ final state are a major source of B background, and efficient vetoes are a necessity. Using generic $B\overline{B}$ Monte Carlo data, many charmed and charmonium decay modes were identified as having signal-like distributions in m_{ES} and $\mathcal{F}$. The most dominant modes were vetoed to remove the vast majority of their contamination. These modes (and their corresponding vetoes) were:

- $B^0 \to D^-\pi^+$, $D^- \to K^0_s\pi^-$ ($1.81 < m_{K^0_S\pi^\pm} < 1.91$ GeV/c^2)

- $B^0 \to J/\psi K^0_s$ ($3.04 < m_{\pi^+\pi^-} < 3.16$ GeV/c^2),

- $B^0 \to \psi(2S) K^0_s$ ($3.63 < m_{\pi^+\pi^-} < 3.74$ GeV/c^2) and

- $B^0 \to \chi_{0c} K^0_s$ ($3.32 < m_{\pi^+\pi^-} < 3.51$ GeV/c^2)

and their charge conjugates. The charmonium mesons decay to either $\mu^+\mu^-$ or $\pi^+\pi^-$ producing either a genuine $K^0_s\pi^+\pi^-$ final state or a mis-identified $K^0_S\mu^+\mu^-$ final state. Another strong contribution to the background comes from the decay $B^0 \to \eta' K^0_S, \eta' \to \rho^0\gamma$. Unfortunately, creating a veto for $\eta' K^0_S$ is not optimal since the η' meson mass overlaps the masses of the ρ^0 and f_0 resonances. Therefore, a component is included in the fit to account for its contribution instead. The widths of the veto bands were calculated using Monte Carlo for each of the problematic modes, after selection cuts have been made. A Gaussian was fitted to the mass peak and the veto was chosen to be the $\pm 5\sigma$ band about the mean.

Contaminating modes (calculated after the implementation of vetoes) can be seen in Tables 3.2, 3.3, 3.4, 3.5, 3.6. Particle misidentification provides B background from the $B^0 \to K^0_S\pi^\pm K^\mp$ and $B^0 \to K^0_S K^\pm K^\mp$ modes, and such modes are also considered within these B-background tables. Figure 3.9 shows m_{ES}-ΔE scatter plots for neutral and charged generic B-background.

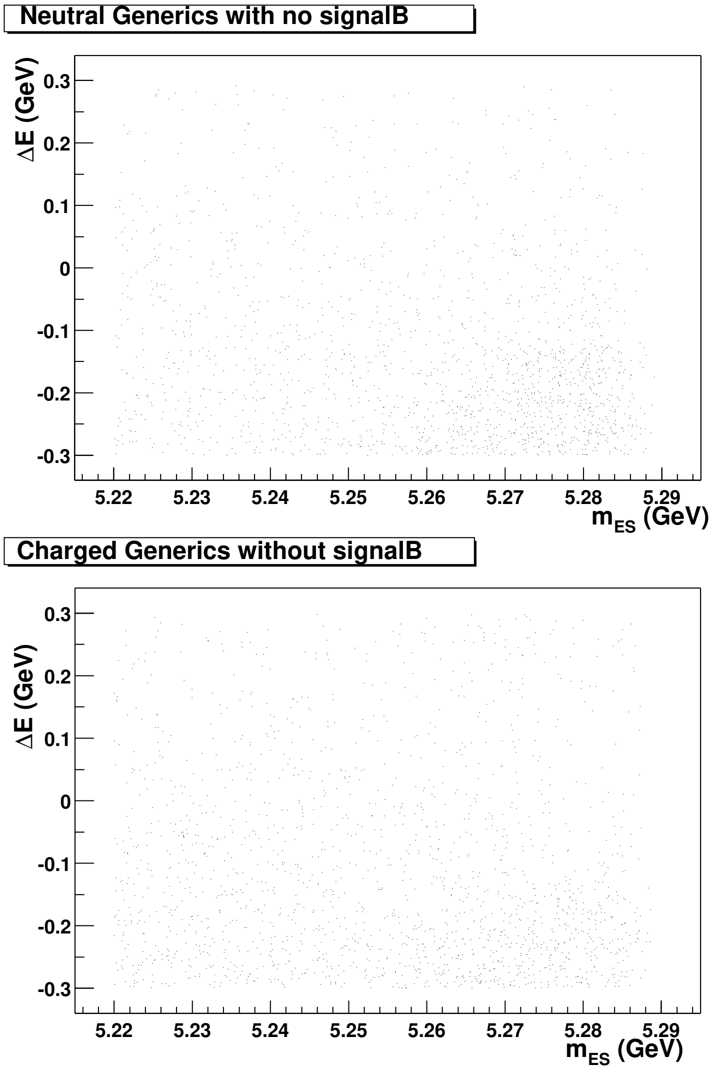

Figure 3.9: Top: Neutral generic B events shown in the $m_{\rm ES}$-ΔE plane after all $B^0 \to K^0_S\pi^+\pi^-$ cuts have been applied. All true signal events (referred to as signalB in the title) have been removed from this plot using Monte Carlo truth information. Bottom: Charged generic B events shown in the $m_{\rm ES}$-ΔE plane after all the selection criteria have been applied.

Mode (+ C.C)	Eff. after Veto (%)	B.F.	# Expected
$B^0 \to D^0 K^0_S, D^0 \to K^+K^-$	8.60×10^{-4}	$(6.71\pm 1.90)\times10^{-8}$	0.0 ± 0.0
$B^0 \to D^0 K^0_S, D^0 \to K^\pm\pi^\mp$	1.6×10^{-2}	$(6.55 \pm 1.84)\times10^{-7}$	2.5 ± 0.7
$B^0 \to D^0 K^0_S, D^0 \to \pi^+\pi^-$	0.30	$(2.38 \pm 0.67) \times10^{-8}$	1.7 ± 0.5
$B^\pm \to D^0\pi^\pm, D^0 \to K^0_S\pi^0$	0.01	$(5.73 \pm 0.64) \times10^{-5}$	151.9 ± 17.4
$B^\pm \to D^0\pi^\pm, D^0 \to K^0_S\pi^+\pi^-$	2.63×10^{-3}	$(1.44 \pm 0.12)\times10^{-4}$	87.8 ± 8.5
$B^\pm \to D^0\rho^\pm, D^0 \to K^0_S\pi^+\pi^-$	1.25×10^{-3}	$(1.16 \pm 0.44)\times10^{-5}$	3.4 ± 1.3
$B^0 \to D^\mp K^\pm, D \to K^0_S\pi$	5.14×10^{-4}	$(3.89 \pm 1.20)\times10^{-6}$	0.5 ± 0.2
$B^0 \to D^\mp e^\pm\nu, D^\mp \to K^0_S\pi^\mp$	2.83×10^{-4}	$(4.16\pm 0.48)\times10^{-4}$	27.3 ± 5.0
$B^0 \to D^\mp \mu^\pm\nu, D^\mp \to K^0_S\pi^\mp$	3.80×10^{-4}	$(4.16\pm 0.48)\times10^{-4}$	36.7 ± 6.1
$B^0 \to D^\mp\pi^\pm, D^\mp \to K^0_S K^\mp$	8.45×10^{-3}	$(1.63\pm 0.22)\times10^{-5}$	31.9 ± 4.4
$B^0 \to D^\mp\pi^\pm, D^\mp \to K^0_S\pi^+\pi^0$	2.33×10^{-3}	$(9.23\pm 2.97)\times10^{-5}$	49.9 ± 16.3
$B^0 \to D^\mp\rho^\pm, D^\mp \to K^0_S\pi^\mp$	1.24×10^{-3}	$(2.17\pm 0.39)\times10^{-4}$	62.7 ± 12.2
$B^\pm \to D^{*0}\pi^\pm, D^{*0} \to D^0\gamma, D^0 \to K^0_S\pi^0$	5.82×10^{-3}	$(4.03\pm 0.60)\times10^{-5}$	54.4 ± 8.4
$B^\pm \to D^{*0}\pi^\pm, D^{*0} \to D^0\gamma, D^0 \to K^0_S\pi^+\pi^-$	1.20×10^{-3}	$(1.01\pm 0.13)\times10^{-4}$	28.1 ± 4.2
$B^\pm \to D^{*0}\pi^\pm, D^{*0} \to D^0\pi^0, D^0 \to K^0_S\pi^0$	5.41×10^{-3}	$(6.55\pm 0.90)\times10^{-5}$	82.2 ± 11.6
$B^\pm \to D^{*0}\pi^\pm, D^{*0} \to D^0\pi^0, D^0 \to K^0_S\pi^+\pi^-$	1.22×10^{-3}	$(1.65 \pm 0.19)\times10^{-4}$	46.6 ± 6.3
$B^0 \to D^{*\mp}e^\pm\nu, D^{*\mp} \to D^0\pi^\mp, D^0 \to K^0_S\pi^0$	1.14×10^{-4}	$(5.80\pm 0.61)\times10^{-4}$	15.3 ± 4.6
$B^0 \to D^{*\mp}e^\pm\nu, D^{*\mp} \to D{*\mp}\pi^0, D{*\mp} \to K^0_S\pi{*\mp}$	1.84×10^{-4}	$(6.62\pm 0.50)\times10^{-4}$	28.3 ± 6.5
$B^0 \to D^{*\mp}\mu^\pm\nu, D^{*\mp} \to D^0\pi^\mp, D^0 \to K^0_S\pi^0$	1.84×10^{-4}	$(5.80\pm 0.61)\times10^{-4}$	24.8 ± 6.0
$B^0 \to D^{*\mp}\mu^\pm\nu, D^{*\mp} \to D{*\mp}\pi^0, D{*\mp} \to K^0_S\pi^\mp$	2.63×10^{-4}	$(6.62 \pm 0.50)\times10^{-4}$	40.4 ± 8.0
$B^0 \to D^{*\mp}\pi^\pm, D^{*\mp} \to D^0\pi^\mp, D^0 \to K^0_S\pi^0$	5.07×10^{-3}	$(4.30\pm 0.53)\times10^{-5}$	50.5 ± 6.5
$B^0 \to D^{*\mp}\pi^\pm, D^{*\mp} \to D{*\mp}\pi^0, D{*\mp} \to K^0_S\pi{*\mp}$	3.29×10^{-3}	$(4.91\pm 0.48) \times10^{-5}$	37.4 ± 4.0
$B^0 \to D^{*\mp}\rho^\pm, D^{*\mp} \to D^0\pi^\mp, D^0 \to K^0_S\pi^0$	3.24×10^{-4}	$(1.06\pm 0.17)\times10^{-4}$	8.0 ± 1.7
$B^0 \to D^{*\mp}\rho^\pm, D^{*\mp} \to D{*\mp}\pi^0, D{*\mp} \to K^0_S\pi{*\mp}$	3.58×10^{-4}	$(1.21\pm 0.18)\times10^{-4}$	10.0 ± 1.9
$B^0 \to \chi_{0c}K^0_S$	2.73×10^{-5}	$(3.45 \pm 0.01)\times10^{-4}$	2.2 ± 1.3
$B^0 \to \psi(2S)K^0_S$	6.31×10^{-5}	$(4.27\pm 0.48)\times10^{-4}$	6.3 ± 2.5
$B^0 \to J\psi K^0_S$	1.86×10^{-3}	$(2.93 \pm 0.17)\times10^{-4}$	126.4 ± 8.0
$B^0 \to K^0_S K^\pm\pi^\mp$ nonres	9.75×10^{-3}	7.2×10^{-6}	$< 16.3\pm0.3$
$B^0 \to \eta' K^0_S$	3.54×10^{-2}	$(6.63 \pm 2.33)\times10^{-6}$	54.4 ± 19.1
$B^0 \to D^\mp\pi\pm, D^\mp \to K^0_S\pi^\mp$	1.14×10^{-2}	$(2.68 \pm 0.30)\times10^{-5}$	70.9 ± 8.4

Table 3.2: The B modes which mimic the signal for the inclusive measurement. These reflect the efficiencies after vetoes are implemented around the J/ψ, $D^\mp$, χ_{0c} and $\psi(2\mathrm{S})$ resonances. The expected numbers of events are normalised to $210 fb^{-1}$.

Mode (+ C.C)	Eff. after Veto (%)	B.F.	# Expected
$B^0 \to D^0 K_S^0, D^0 \to K^+K^-$	5.26×10^{-5}	$(6.71\pm1.90)\times10^{-8}$	0.0
$B^0 \to D^0 K_S^0, D^0 \to K^{pm}\pi^\mp$	6.67×10^{-4}	$(6.55\pm1.84)\times10^{-7}$	0.1 ± 0.0
$B^0 \to D^0 K_S^0, D^0 \to \pi^+\pi^-$	7.10×10^{-3}	$(2.38\ \pm0.67)\times10^{-8}$	0.0
$B^\pm \to D^0\pi^{pm}, D^0 \to K_S^0\pi 0$	4.31×10^{-4}	$(5.73\ \pm0.64)\times10^{-5}$	$5.7\pm\ 0.9$
$B^\pm \to D^0\pi^{pm}, D^0 \to K_S^0\pi^+\pi^-$	9.50×10^{-5}	$(1.44\ \pm0.12)\ \times10^{-4}$	$3.2\pm\ 0.8$
$B^0 \to D^0\rho^0, D^0 \to K_S^0\pi^+\pi^-$	7.02×10^{-5}	$(1.16\ \pm\ 0.44)\times10^{-5}$	$0.2\pm\ 0.1$
$B^0 \to D^\mp K, D^\mp \to K_S^0\pi$	9.43×10^{-3}	$(3.89\pm1.20)\times10^{-6}$	$8.5\pm\ 2.6$
$B^0 \to D^\mp e\nu, D^\mp \to K_S^0\pi$	4.62×10^{-5}	$(4.16\ \pm\ 0.48)\ \times10^{-4}$	$4.5\ \pm\ 1.7$
$B^0 \to D^\mp \mu\nu, D^\mp \to K_S^0\pi$	8.94×10^{-5}	$(4.16\ \pm0.48)\times10^{-4}$	$8.6\pm\ 2.4$
$B^0 \to D^\mp\pi, D^\mp \to K_S^0 K$	3.18×10^{-4}	$(1.63\pm0.22)\times10^{-5}$	$1.2\pm\ 0.2$
$B^0 \to D^\mp\pi, D^\mp \to K_S^0\pi^+\pi^- 0$	1.06×10^{-4}	$(9.23\ \pm2.97)\times10^{-5}$	$2.3\pm\ 0.9$
$B^0 \to D^\mp\rho, D^\mp \to K_S^0\pi$	1.46×10^{-4}	$(2.17\pm0.39)\times10^{-4}$	$7.4\pm\ 2.0$
$B^\pm \to D^{*0}\pi, D^{*0} \to D^0\gamma, D^0 \to K_S^0\pi 0$	3.35×10^{-4}	$(4.03\ \pm0.60)\times10^{-5}$	$3.1\pm\ 0.6$
$B^\pm \to D^{*0}\pi, D^{*0} \to D^0\gamma, D^0 \to K_S^0\pi^+\pi^-$	5.03×10^{-5}	$(1.01\ \pm0.13)\times10^{-4}$	$1.2\pm\ 0.4$
$B^\pm \to D^{*0}\pi, D^{*0} \to D^0\pi, D^0 \to K_S^0\pi 0$	2.29×10^{-4}	$(6.55\ \pm0.90)\times10^{-5}$	$3.5\pm\ 0.7$
$B^\pm \to D^{*0}\pi, D^{*0} \to D^0\pi, D^0 \to K_S^0\pi^+\pi^-$	5.20×10^{-5}	$(1.65\pm0.19)\times10^{-4}$	$2.0\ \pm\ 0.7$
$B^0 \to D^{*\mp}e\nu, D^{*\mp} \to D^0\pi, D^0 \to K_S^0\pi 0$	0	$(5.80\ \pm\ 0.60)\times10^{-4}$	0
$B^0 \to D^{*\mp}e\nu, D^{*\mp} \to D\pi 0, D \to K_S^0\pi^\mp$	0	$(6.62\ \pm0.50)\times10^{-4}$	0
$B^0 \to D^{*\mp}\mu\nu, D^{*\mp} \to D^0\pi, D^0 \to K_S^0\pi 0$	0	$(5.80\ \pm0.61)\times10^{-4}$	0
$B^0 \to D^{*\mp}\mu\nu, D^{*\mp} \to D\pi 0, D^\mp \to K_S^0\pi^\mp$	1.75×10^{-5}	$(6.62\ \pm0.50)\times10^{-4}$	$2.7\ \pm\ 1.9$
$B^0 \to D^{*\mp}\pi, D^{*\mp} \to D^0\pi^\mp, D^0 \to K_S^0\pi 0$	1.91×10^{-4}	$(4.30\ \pm\ 0.53)\times10^{-5}$	$1.9\pm\ 0.4$
$B^0 \to D^{*\mp}\pi, D^{*\mp} \to D^\mp\pi 0, D^\mp \to K_S^0\pi^\mp$	5.61×10^{-4}	$(4.91\pm0.48)\times10^{-5}$	$6.4\pm\ 0.9$
$B^0 \to D^{*\mp}\rho^{pm}, D^{*\mp} \to D^0\pi^\mp, D^0 \to K_S^0\pi 0$	$1.68\ \times10^{-5}$	$(1.06\ \pm0.17)\times10^{-4}$	$0.4\pm\ 0.3$
$B^0 \to D^{*\mp}\rho^\pm, D^{*\mp} \to D^\mp\pi 0, D \to K_S^0\pi^\mp$	2.79×10^{-5}	$(1.21\pm0.18)\times10^{-4}$	$0.8\pm\ 0.4$
$B^0 \to \chi_{0c}K_S^0$	9.09×10^{-6}	$(3.45\ \pm0.01)\times10^{-4}$	$0.7\pm\ 0.7$
$B^0 \to \psi(2S)K_S^0$	0	$(4.27\pm\ 0.48)\times10^{-4}$	0
$B^0 \to J\psi K_S^0$	9.27×10^{-5}	$(2.93\pm0.17)\times10^{-4}$	$6.3\pm\ 0.7$
$B^0 \to K_S^0 K\pi$ nonres	3.45×10^{-4}	$<7.24\times10^{-6}$	<0.58
$B^0 \to \eta' K_S^0$	2.48×10^{-4}	$(6.63\ \pm2.33)\times10^{-6}$	$0.4\pm\ 0.1$
$B^0 \to K_S^0\pi^+\pi^-$ nonres	4.78×10^{-4}	$<\ 2.1\ \times10^{-6}$	$<\ 0.23$
$B^0 \to K_0^{*+}(1430)\pi$	4.37×10^{-3}	$(2.46\ \pm0.85)\times10^{-6}$	$2.5\ \pm\ 0.9$
$B^0 \to K^{*+}(1410)\pi$	1.74×10^{-2}	0	0
$B^0 \to K^{*+}(1680)\pi$	3.70×10^{-3}	$(1.78\ \pm0.11)\times10^{-6}$	$1.5\ \pm\ 0.1$
$B^0 \to K_2^{*+}(1430)\pi$	$3.04\ \times10^{-4}$	$(\ 4.12\ \pm0.12)\times10^{-6}$	$0.3\ \pm0.1$
$B^0 \to K^{*+}\pi$	3.95×10^{-3}	$(3.00\ \pm0.42)\times10^{-6}$	$2.7\pm\ 0.4$
$B^0 \to f_0(1370)K_S^0$	4.79×10^{-4}	0	0
$B^0 \to f_0 K_S^0$	2.89×10^{-3}	$(2.07\pm0.55)\times10^{-6}$	$1.4\ \pm\ 0.4$
$B^0 \to f_2 K_S^0$	1.01×10^{-3}	$(1.70\ \pm\ 1.70)\times10^{-6}$	0.4 ± 0.4
$B^0 \to \rho^0 K_S^0$	8.94×10^{-4}	$(1.79\pm0.55)\times10^{-6}$	$0.4\pm\ 0.1$

Table 3.3: B-related background contributions for the $B^0 \to D^\mp\pi^\pm$ measurement. These efficiencies are calculated after the implementation of vetoes around the charm and charmonium states. The expected number of events are normalised to $210\,fb^{-1}$.

Mode (+ C.C)	Eff. after Veto (%)	B.F.	# Expected
$B^0 \to D^0 K^0_S, D^0 \to K^+ K^-$	1.05×10^{-4}	$(6.71 \pm 1.90)\times10^{-8}$	0
$B^0 \to D^0 K^0_S, D^0 \to K^\pm \pi^\mp$	1.04×10^{-3}	$(6.55 \pm 1.84)\times10^{-7}$	0.2 ± 0.1
$B^0 \to D^0 K^0_S, D^0 \to \pi^+ \pi^-$	3.90×10^{-3}	$(2.38 \pm 0.67)\times10^{-8}$	$(2.2 \pm 1.0)\times10^{-2}$
$B^\pm \to D^0 \pi^\pm, D^0 \to K^0_S \pi^0$	1.94×10^{-3}	$(5.73 \pm 0.64)\times10^{-5}$	25.7 ± 3.2
$B^\pm \to D^0 \pi^\pm, D^0 \to K^0_S \pi^+ \pi^-$	2.35×10^{-4}	$(1.44 \pm 0.12)\times10^{-4}$	7.9 ± 1.4
$B^\pm \to D^0 rho^\pm, D^0 \to K^0_S \pi^+ \pi^-$	9.65×10^{-5}	$(1.16 \pm 0.45)\times10^{-5}$	0.3 ± 0.1
$B^0 \to D^\mp K^\pm, D \to K^0_S \pi$	1.91×10^{-4}	$(3.89 \pm 1.20) \times10^{-6}$	0.2 ± 0.1
$B^0 \to D^\mp e^\pm \nu, D^\mp \to K^0_S \pi^\mp$	2.31×10^{-5}	$(4.16 \pm 0.48)\times10^{-4}$	2.2 ± 1.2
$B^0 \to D^\mp \mu^\pm \nu, D^\mp \to K^0_S \pi^\mp$	3.35×10^{-5}	$(4.16 \pm 0.48)\times10^{-4}$	3.2 ± 1.4
$B^0 \to D^\mp \pi^\mp_D \to K^0_S K$	5.59×10^{-4}	$(1.63 \pm 0.22)\times10^{-5}$	2.1 ± 0.4
$B^0 \to D^\mp \pi^\mp_D \to K^0_S \pi^+ \pi^- 0$	1.79×10^{-4}	$(9.23 \pm 2.97)\times10^{-5}$	3.8 ± 1.4
$B^0 \to D^\mp \rho^\mp_D \to K^0_S \pi$	1.65×10^{-4}	$(2.17 \pm 0.40)\times10^{-4}$	8.3 ± 2.2
$B^0 \to D^{*0}\pi, D^{*0} \to D^0\gamma, D^0 \to K^0_S \pi^0$	5.98×10^{-4}	$(4.03 \pm 0.61)\times10^{-4}$	5.6 ± 1.0
$B^0 \to D^{*0}\pi, D^{*0} \to D^0\gamma, D^0 \to K^0_S \pi^+ \pi^-$	2.23×10^{-5}	$(1.01 \pm 0.13)\times10^{-4}$	0.5 ± 0.3
$B^0 \to D^{*0}\pi, D^{*0} \to D^0\pi, D^0 \to K^0_S \pi^0$	6.59×10^{-4}	$(6.55 \pm 0.90)\times10^{-5}$	10.0 ± 1.7
$B^0 \to D^{*0}\pi, D^{*0} \to D^0\pi, D^0 \to K^0_S \pi^+ \pi^-$	5.20×10^{-5}	$(165 \pm 0.19)\times10^{-4}$	2.0 ± 0.7
$B^0 \to D^{*\mp} e\nu, D^{*\mp} \to D^0\pi, D^0 \to K^0_S \pi^0$	8.77×10^{-6}	$(5.80 \pm 6.09)\times10^{-4}$	1.2 ± 1.2
$B^0 \to D^{*\mp} e\nu, D^{*\mp} \to D^\mp\pi^0, D^\mp \to K^0_S \pi^\mp$	8.77×10^{-6}	$(6.62 \pm 0.50)\times10^{-4}$	1.4 ± 1.4
$B^0 \to D^{*\mp} \mu\nu, D^{*\mp} \to D^0\pi, D^0 \to K^0_S \pi^0$	0	$(5.80 \pm 0.61)\times10^{-4}$	0
$B^0 \to D^{*\mp} \mu\nu, D^{*\mp} \to D^\mp\pi^0, D^\mp \to K^0_S \pi^\mp$	0	$(6.61 \pm 0.50)\times10^{-4}$	0
$B^0 \to D^{*\mp} \pi, D^{*\mp} \to D^0\pi, D^0 \to K^0_S \pi^0$	4.57×10^{-4}	$(4.30 \pm 0.53)\times10^{-5}$	4.6 ± 0.8
$B^0 \to D^{*\mp} \pi, D^{*\mp} \to D^\mp\pi^0, D^\mp \to K^0_S \pi^\mp$	4.51×10^{-4}	$(4.91 \pm 0.48)\times10^{-5}$	5.1 ± 0.8
$B^0 \to D^{*\mp} \rho, D^{*\mp} \to D^0\pi, D^0 \to K^0_S \pi^0$	2.23×10^{-5}	$(1.06 \pm 0.17)\times10^{-4}$	0.6 ± 0.3
$B^0 \to D^{*\mp} \rho, D^{*\mp} \to D^\mp\pi^0, D^\mp \to K^0_S \pi^\mp$	1.12×10^{-5}	$(1.21 \pm 0.18)\times10^{-5}$	0.3 ± 0.2
$B^0 \to \chi_{0c} K^0_S$	9.09×10^{-6}	$(3.45 \pm 0.00)\times10^{-4}$	0.7 ± 0.7
$B^0 \to \psi(2S) K^0_S$	0	$(4.27 \pm 0.48)\times10^{-4}$	0
$B^0 \to J\psi K^0_S$	0	$(2.93 \pm 0.17)\times10^{-4}$	0
$B^0 \to K^0_S K^\pm \pi^\mp NR$	5.57×10^{-4}	$<7.24\times10^{-6}$	<0.94
$B^0 \to \eta' K^0_S$	1.05×10^{-2}	$(6.63 \pm 2.33)\times10^{-6}$	16.2 ± 5.7
$B^0 \to D^\mp \pi\pm, D^\mp \to K^0_S \pi^\mp$	3.37×10^{-3}	$(2.68 \pm 0.30)\times10^{-5}$	21.0 ± 2.7
$B^0 \to K^0_S \pi^+ \pi^- NR$	1.25×10^{-2}	$<2.07\times10^{-6}$	<6.0
$B^0 \to K^{**\pm} \pi^\mp$	1.98×10^{-2}	$(7.65 \pm 0.90)\times10^{-6}$	35.2 ± 4.1
$B^0 \to K^{*\pm} \pi^\mp$	1.31×10^{-2}	$(2.90 \pm 0.41\times10^{-6}$	5.4 ± 0.8
$B^0 \to f_0(1370) K^0_S$	1.27×10^{-2}	0	0
$B^0 \to f_0 K^0_S$	2.12×10^{-2}	$(2.07 \pm 0.55)\times10^{-6}$	10.2 ± 2.7
$B^0 \to f_2 K^0_S$	1.32×10^{-2}	$(1.70 \pm 1.70)\times10^{-6}$	5.2 ± 5.2

Table 3.4: B-related background for the $B^0 \to \rho^0 K^0_S$ measurement. These efficiencies include the application of charm and charmonium vetoes to the MC. The expected number of events are normalised to 210 fb^{-1}.

Mode (+ C.C)	Eff. after Veto (%)	B.F.	# Expected
$B^0 \to D^0 K^0_S, D^0 \to K^+K^-$	1.23×10^{-4}	$(6.71 \pm 1.90)\times10^{-8}$	$(1.9 \pm 0.9) \times10^{-3}$
$B^0 \to D^0 K^0_S, D^0 \to K^{\pm}\pi^{\mp}$	9.30×10^{-4}	$(6.55 \pm 1.84) \times10^{-7}$	0.1 ± 0.0
$B^0 \to D^0 K^0_S, D^0 \to \pi^+\pi^-$	3.08×10^{-3}	$(2.38 \pm 0.67) \times10^{-8}$	$(1.7 \pm 0.5) \times10^{-2}$
$B^{\pm} \to D^0\pi^{\pm}, D^0 \to K^0_S\pi^0$	1.34×10^{-3}	$(5.73 \pm0.64) \times10^{-5}$	17.8 ± 2.3
$B^{\pm} \to D^0\pi^{\pm}, D^0 \to K^0_S\pi^+\pi^-$	1.84×10^{-4}	$(1.44 \pm 0.12) \times10^{-4}$	6.2 ± 1.2
$B^0 \to D^0\rho^0, D^0 \to K^0_S\pi^+\pi^-$	4.39×10^{-5}	$(1.16 \pm 0.44) \times10^{-5}$	0.1 ± 0.1
$B^0 \to D^{\mp}K^{\pm}, D^{\mp} \to K^0_S\pi^{\mp}$	6.94×10^{-5}	$(3.89\pm 1.20)\times10^{-6}$	$(6.3 \pm 2.6) \times10^{-2}$
$B^0 \to De\nu, D \to K^0_S\pi$	2.31×10^{-5}	$(4.16 \pm 0.48) \times10^{-4}$	2.2 ± 1.2
$B^0 \to D\mu\nu, D \to K^0_S\pi$	3.91×10^{-5}	$(4.16 \pm 0.48) \times10^{-4}$	3.8 ± 1.5
$B^0 \to D^{\mp}\pi^{\pm}, D^{\mp} \to K^0_S K$	4.36×10^{-4}	$(1.63 \pm 0.22) \times10^{-5}$	1.7 ± 0.3
$B^0 \to D^{\mp}\pi^{\pm}, D^{\mp} \to K^0_S\pi^+\pi^-$	1.34×10^{-4}	$(9.23 \pm 2.97) \times10^{-5}$	2.9 ± 1.1
$B^0 \to D^{\mp}\rho^{\pm}, D^{\mp} \to K^0_S\pi$	1.40×10^{-4}	$(2.17 \pm0.39)\times10^{-4}$	7.1 ± 2.0
$B^{\pm} \to D^{*0}\pi^{\pm}, D^{*0} \to D^0\gamma, D^0 \to K^0_S\pi^0$	4.86×10^{-4}	$(4.03 \pm0.60)\times10^{-5}$	4.6 ± 0.8
$B^{\pm} \to D^{*0}\pi^{\pm}, D^{*0} \to D^0\gamma, D^0 \to K^0_S\pi^+\pi^-$	5.03×10^{-5}	$(1.01 \pm0.13) \times10^{-4}$	1.2 ± 0.4
$B^{\pm} \to D^{*0}\pi^{\pm}, D^{*0} \to D^0\pi, D^0 \to K^0_S\pi^0$	4.25×10^{-4}	$(6.55 \pm 0.90)\times10^{-5}$	6.5 ± 1.2
$B^{\pm} \to D^{*0}\pi^{\pm}, D^{*0} \to D^0\pi, D^0 \to K^0_S\pi^+\pi^-$	3.47×10^{-5}	$(1.65 \pm0.19)\times10^{-4}$	1.3 ± 0.6
$B^0 \to D^{*\mp}e\nu, D^{*\mp} \to D^0\pi, D^0 \to K^0_S\pi^0$	0	$(5.80\pm0.61)\times10^{-4}$	0
$B^0 \to D^{*\mp}e\nu, D^{*\mp} \to D^{\mp}\pi^0, D^{\mp} \to K^0_S\pi^{\mp}$	0	$(6.62 \pm0.50)\times10^{-4}$	0
$B^0 \to D^{*\mp}\mu\nu, D^{*\mp} \to D^0\pi, D^0 \to K^0_S\pi^0$	8.77×10^{-6}	$(5.80\pm0.61)\times10^{-4}$	1.2 ± 1.2
$B^0 \to D^{*\mp}\mu\nu, D^{*\mp} \to D^{\mp}\pi^0, D^{\mp} \to K^0_S\pi^{\mp}$	0	$(6.62\pm0.50)\times10^{-4}$	0
$B^0 \to D^{*\mp}\pi, D^{*\mp} \to D^0\pi, D^0 \to K^0_S\pi^0$	2.47×10^{-4}	$(4.30 \pm0.53) \times10^{-5}$	2.5 ± 0.5
$B^0 \to D^{*\mp}\pi, D^{*\mp} \to D^{\mp}\pi^0, D^{\mp} \to K^0_S\pi^{\mp}$	3.29×10^{-4}	$(4.91 \pm0.48)\times10^{-5}$	3.8 ± 0.6
$B^0 \to D^{*\mp}\rho, D^{*\mp} \to D^0\pi, D^0 \to K^0_S\pi^0$	1.12×10^{-5}	$(1.06\pm0.17)\times10^{-4}$	0.3 ± 0.2
$B^0 \to D^{*\mp}\rho, D^{*\mp} \to D^{\mp}\pi^0, D^{\mp} \to K^0_S\pi^{\mp}$	2.79×10^{-5}	$(1.21 \pm0.17)\times10^{-4}$	0.8 ± 0.4
$B^0 \to \chi_{0c}K^0_S$	0	$(3.45 \pm0.01)\times10^{-4}$	0
$B^0 \to \psi(2S)K^0_S$	0	$(4.27 \pm0.48)\times10^{-4}$	0
$B^0 \to J\psi K^0_S$	4.21×10^{-6}	$(2.93\pm0.17)\times10^{-4}$	0.3 ± 0.1
$B^0 \to K^0_S K^{\pm}\pi^{\mp}$ nonres	4.32×10^{-4}	$<7.24\times10^{-6}$	<0.73
$B^0 \to \eta' K^0_S$	1.20×10^{-2}	$(6.63\pm2.33)\times10^{-6}$	18.5 ± 6.5
$B^0 \to D^{\mp}\pi, D^{\mp} \to K^0_S\pi^{\mp}$	2.16×10^{-3}	$(2.68\pm0.30) \times10^{-5}$	13.4 ± 1.8
$B^0 \to K^0_S\pi^+\pi^-$ nonres	1.09×10^{-2}	$< 2.1\times10^{-6}$	<5.2
$B^0 \to K^{**\pm}\pi^{\mp}$	1.77×10^{-2}	$(7.65 \pm 0.90)\times10^{-6}$	31.4 ± 3.7
$B^0 \to K^{*\pm}\pi^{\mp}$	6.95×10^{-3}	$(2.90 \pm 0.41)\times10^{-6}$	4.7 ± 0.7
$B^0 \to f_0(1370)K^0_S$	1.19×10^{-2}	0	0
$B^0 \to f_2K^0_S$	1.67×10^{-2}	$(1.70\pm 1.70)\times10^{-6}$	6.6 ± 6.6
$B^0 \to \rho^0K^0_S$	3.31×10^{-2}	$(1.79 \pm0.55)\times10^{-6}$	13.8 ± 4.2

Table 3.5: B related background and mode vetoes for the $B^0 \to f_0K^0_S$ measurement. These efficiencies include the application of charm and charmonium vetoes to the MC. The expected number of events are normalised to 210 fb^{-1}.

Mode (+ C.C)	Eff. after Veto (%)	B.F.	# Expected
$B^0 \to D^0 K^0_S, D^0 \to K^+K^-$	5.26×10^{-5}	$(6.71\pm1.90)\times10^{-8}$	$(8.2\pm5.3)\times10^{-4}$
$B^0 \to D^0 K^0_S, D^0 \to K^\pm\pi^\mp$	1.33×10^{-3}	$(6.55\pm1.84)\times10^{-7}$	0.2 ± 0.1
$B^0 \to D^0 K^0_S, D^0 \to \pi^+\pi-$	1.74×10^{-2}	$(2.38\pm0.67)\times10^{-8}$	0.1 ± 0.0
$B^\pm \to D^0\pi^\pm, D^0 \to K^0_S\pi^0$	1.50×10^{-3}	$(5.73\pm0.64)\times10^{-5}$	19.9 ± 2.5
$B^\pm \to D^0\pi^\pm, D^0 \to K^0_S\pi^+\pi-$	3.18×10^{-4}	$(1.44\pm0.12)\times10^{-4}$	10.7 ± 1.7
$B^\pm \to D^0\rho^0, D^0 \to K^0_S\pi^+\pi-$	1.23×10^{-4}	$(1.16\pm0.44)\times10^{-5}$	0.3 ± 0.2
$B^0 \to D^-K, D \to K^0_S\pi$	1.10×10^{-4}	$(3.89\pm1.20)\times10^{-6}$	$(9.9\pm3.8)\times10^{-2}$
$B^0 \to D^-e^+\nu, D \to K^0_S\pi$	5.78×10^{-6}	$(4.16\pm0.48)\times10^{-4}$	0.6 ± 0.6
$B^0 \to D^-\mu^+\nu, D \to K^0_S\pi$	0	$4.160\pm0.48\times10^{-4}$	0
$B^0 \to D^-\pi^+, D^- \to K^0_S K$	6.65×10^{-4}	$(1.63\pm0.22)\times10^{-5}$	2.5 ± 0.41
$B^0 \to D^-\pi^+, D^- \to K^0_S\pi^+\pi-^0$	2.35×10^{-4}	$(9.23\pm2.97)\times10^{-5}$	5.0 ± 1.8
$B^0 \to D^-\rho^+, D^- \to K^0_S\pi$	3.66×10^{-5}	$(2.17\pm0.39)\times10^{-4}$	1.8 ± 0.8
$B^\pm \to D^{*0}\pi^\pm, D^{*0} \to D^0\gamma, D^0 \to K^0_S\pi^0$	4.36×10^{-4}	$(4.0\pm0.6)\times10^{-5}$	4.08 ± 0.77
$B^\pm \to D^{*0}\pi^\pm, D^{*0} \to D^0\gamma, D^0 \to K^0_S\pi^+\pi-$	8.94×10^{-5}	$(1.0\pm0.1)\times10^{-4}$	2.10 ± 0.59
$B^\pm \to D^{*0}\pi^\pm, D^{*0} \to D^0\pi, D^0 \to K^0_S\pi^0$	4.41×10^{-4}	$(6.6\pm0.9)\times10^{-5}$	6.71 ± 1.19
$B^\pm \to D^{*0}\pi^\pm, D^{*0} \to D^0\pi, D^0 \to K^0_S\pi^+\pi-$	9.83×10^{-5}	$(1.7\pm0.2)\times10^{-4}$	3.76 ± 1.01
$B^0 \to D^{*\pm}e\nu, D^{*\pm} \to D^0\pi, D^0 \to K^0_S\pi^0$	0	$(5.80\pm0.61)\times10^{-4}$	0
$B^0 \to D^{*\pm}e\nu, D^{*\pm} \to D^\mp\pi^0, D^\mp \to K^0_S\pi^\mp$	0	$(6.6\pm0.5)\times10^{-4}$	0
$B^0 \to D^{*\pm}\mu\nu, D^{*\pm} \to D^0\pi, D^0 \to K^0_S\pi^0$	0	$(5.80\pm0.61)\times10^{-4}$	0
$B^0 \to D^{*\pm}\mu\nu, D^{*\pm} \to D^\mp\pi^0, D^\mp \to K^0_S\pi^\mp$	1.75×10^{-5}	$(6.62\pm0.50)\times10^{-4}$	2.7 ± 1.9
$B^0 \to D^{*\pm}\pi^\mp, D^{*\pm} \to D^0\pi, D^0 \to K^0_S\pi^0$	4.75×10^{-4}	$(4.30\pm0.53)\times10^{-5}$	4.7 ± 0.8
$B^0 \to D^{*\pm}\pi^\mp, D^{*\pm} \to D^\mp\pi^0, D^\mp \to K^0_S\pi^\mp$	3.99×10^{-4}	$(4.91\pm0.48)\times10^{-5}$	4.5 ± 0.7
$B^0 \to D^{*\pm}\rho^\mp, D^{*\pm} \to D^0\pi, D^0 \to K^0_S\pi^0$	5.59×10^{-6}	$(1.06\pm0.17)\times10^{-4}$	0.1 ± 0.1
$B^0 \to D^{*\pm}\rho^\mp, D^{*\pm} \to D^\mp\pi^0, D^\mp \to K^0_S\pi^\mp$	0	$(1.21\pm0.18)\times10^{-4}$	0
$B^0 \to \chi_{0c}K^0_S$	0	$(3.44\pm0.01)\times10^{-4}$	0
$B^0 \to \psi(2S)K^0_S$	0	$(4.27\pm0.48)\times10^{-4}$	0
$B^0 \to J/\psi K^0_S$	9.27×10^{-5}	$(2.93\pm0.17)\times10^{-4}$	6.3 ± 0.7
$B^0 \to K^0_S K^\pm\pi^\mp$ nonres	1.48×10^{-3}	$<7.24\times10^{-6}$	<2.5
$B^0 \to \eta' K^0_S$	9.39×10^{-4}	$(6.63\pm2.33)\times10^{-6}$	1.4 ± 0.5
$B^0 \to D^\mp\pi^\pm D^\mp \to K^0_S\pi^\mp$	2.58×10^{-3}	$(2.68\pm0.30)\times10^{-5}$	16.1 ± 2.1
$B^0 \to K^0_S\pi^+\pi-$ nonres	1.35×10^{-2}	$<2.1\times10^{-6}$	<6.5
$B^0 \to K^{**\pm}\pi^\mp$	1.27×10^{-2}	$(7.65\pm0.90)\times10^{-6}$	22.9 ± 2.7
$B^0 \to f_0(1370)K^0_S$	1.62×10^{-2}	0	0
$B^0 \to f_0 K^0_S$	8.90×10^{-3}	$(2.07\pm0.55)\times10^{-6}$	4.3 ± 1.2
$B^0 \to f_2 K^0_S$	4.89×10^{-2}	0	0
$B^0 \to \rho^0 K^0_S$	1.24×10^{-2}	$(1.79\pm0.55)\times10^{-6}$	5.2 ± 1.6

Table 3.6: B related background and mode vetoes for the $B^0 \to K^{*+}\pi^-$ measurement. These efficiencies include the application of charm and charmonium vetoes to the MC. The expected number of events are normalised to 210 fb^{-1}.

Chapter 4

Analysis Method: Fit Procedure

4.1 Maximum Likelihood Method

An unbinned multivariate maximum likelihood (ML) fit was used to discriminate between signal and background for all the decay modes under study. The cuts described in Section 3.6.1 are intentionally loose in order to achieve a high signal efficiency. A high signal efficiency leads to a high background efficiency, but the event types can be separated due to the discriminating power within the probability density functions (PDFs). For each candidate, the likelihood ($\mathcal{L}_i$) is defined as:

$$\mathcal{L}_i = \sum_{j=1}^{k} f_j \mathcal{P}_j(x_i) \tag{4.1}$$

where f_j is the fraction of events associated with the jth hypothesis and can be a free parameter. The hypothesis is either signal, $B\overline{B}$ background or continuum background such that k is 3. $\mathcal{P}_j(x_i)$ is the probability of the fit hypothesis evaluated with x_i which is a vector of observables, $m_{\rm ES}$, ΔE and $\mathcal{F}$, for the ith event. This probability is the product of PDFs and can be written as:

$$\mathcal{P}_j(x_i) = \mathcal{S}_j(m_{\mathrm{ES}i}) \cdot \mathcal{T}_j(\mathcal{F}_i) \cdot \mathcal{U}_j(\Delta E_i) \tag{4.2}$$

when considering signal and continuum hypotheses and

$$\mathcal{P}_j(x_i) = \mathcal{W}_j(m_{\mathrm{ES}i}, \Delta E_i) \cdot \mathcal{T}_j(\mathcal{F}_i) \tag{4.3}$$

for a $B\overline{B}$ background hypothesis. The PDFs $\mathcal{S}_j(m_{\mathrm{ES}}\ )$, $\mathcal{T}_j(\mathcal{F}\ )$ and $\mathcal{U}_j(\Delta E\ )$ are for m_{ES}, Fisher and ΔE respectively. In the case of $B\overline{B}$ background $\mathcal{W}_j(m_{\mathrm{ES}i}, \Delta E_i)$ represents a 2D PDF with dimensions of m_{ES} and ΔE. These 2D PDFs are used in the case of $B\overline{B}$ background to take into account correlations between the dimensions. The PDFs themselves are described in the Section 4.4.

For the case of N events, an extended likelihood function is used, since it normalises each PDF component to its event yield. This is described by:

$$\mathcal{L} = \frac{\exp\left(-\sum_j N_j\right)}{N!} \prod_i^N \mathcal{L}_i \tag{4.4}$$

where $\mathcal{L}_i$ is now described by $\mathcal{L}_i = \sum_{j=1}^{k} N_j P_j(x_i)$, N_j is the number of events for the jth hypothesis and the first term takes into account Poissonian fluctuations for the observed number of events.

For a set of free parameters that are used in the extended likelihood function, the expression $-\ln\mathcal{L}$ is minimised. At this point the signal yield, which is the free parameter of interest, is extracted.

The statistical significance of the result can be calculated using the following formula:

$$\sigma = \sqrt{\chi^2(f(0))} \tag{4.5}$$

where $f(0)$ is the the result of the fit when the number of signal events is set to zero. $\chi^2(f(0))$ is described by:

$$\chi^2(f(0)) = -2\ \ln\left[\frac{\mathcal{L}_0}{\mathcal{L}_{max}}\right] \tag{4.6}$$

where $\mathcal{L}_{max}$ is the maximum likelihood and $\mathcal{L}_0$ is the likelihood when the fit is constrained to having zero signal events.

4.1.1 Charge Asymmetry Measurement

The $B^0 \to K^{*+}\pi^-$ charge asymmetry is calculated using Equation 1.38. This can be rearranged to give equations for the number of events in the K^{*-} resonance band and the number in the K^{*+} resonance band:

$$\Gamma(\overline{B}^0 \to K^{*-}\pi^+) = \text{Yield}\frac{(1+\mathcal{A}_{CP})}{2}, \quad \text{and} \quad \Gamma(B^0 \to K^{*+}\pi^-) = \text{Yield}\frac{(1-\mathcal{A}_{CP})}{2} \tag{4.7}$$

where

$$\text{Yield} = \Gamma(\overline{B}^0 \to K^{*-}\pi^+) + \Gamma(B^0 \to K^{*+}\pi^-) \tag{4.8}$$

In the ML fit, each hypothesis (signal, continuum background and B background) is split into two, such that each now has a positive K^* and a negative K^* hypothesis However, since the number of positive and negative events are a function of the total yield and asymmetry, it is these quantities that are the result of the ML fit.

4.2 Signal Efficiency

Many selection criteria affect kinematically different regions of the Dalitz plot to varying degrees. For example, a cut on the lifetime significance of the K_S^0 candidate will reduce the number of low energy K_S^0's that pass selection, leaving a lower efficiency in that region of the Dalitz plot. Therefore, the varying efficiency across the Dalitz plane must be studied and accounted for.

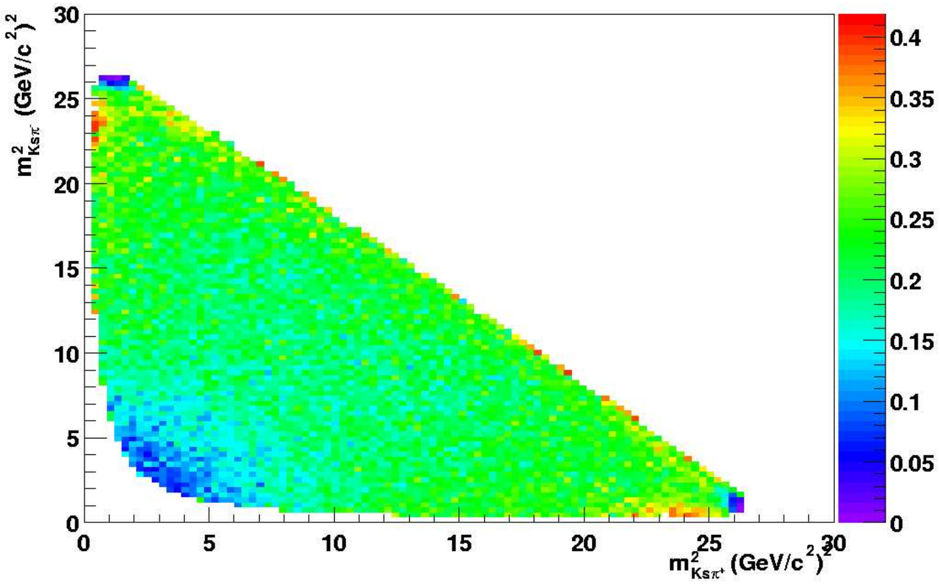

Figure 4.1: The efficiency variation across the Dalitz Plot projection, using non-resonant $B^0 \rightarrow K^0_S\pi^+\pi^-$ MC. The MC histogram after selection has been divided by the histogram of generated events to give the correct efficiency in each bin. The nonresonant MC was generated flat across the Dalitz plane and the truth information is used to locate the origin of the event. To the right of the plot is the colour code corresponding to efficiency values at which the top of the range is 40%. This representation shows how the efficiency slowly changes with respect to position in the Dalitz plot.

In order to estimate the efficiency, nonresonant Monte Carlo was used and the Dalitz plot distribution is shown in Figure 4.1. There was only a slight variation in the efficiency across the Dalitz plane, mainly in the corners. More significant variation was created when adding charm vetoes. To account for this variation, the Dalitz plot was divided into 20 by 20 bins which are shown in Figure 4.2. Relatively large bins were chosen to minimise the number of events which migrate from their true position during reconstruction into a different bin.

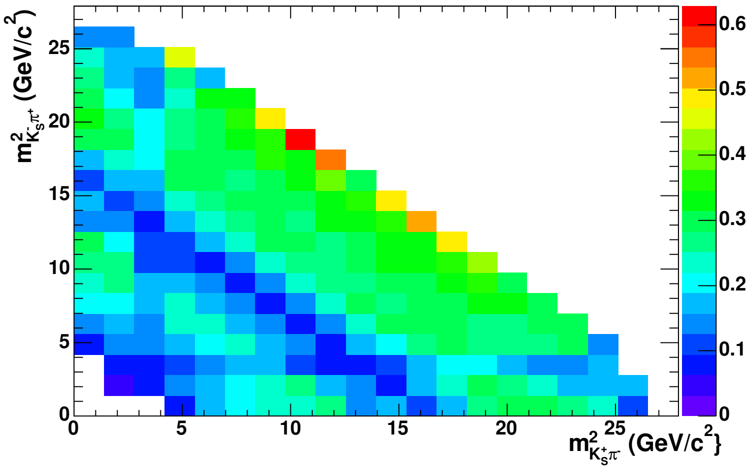

Figure 4.2: The efficiency across the Dalitz plot for $B^0 \rightarrow K^0_S\pi^+\pi^-$ events after all cuts. This efficiency variation is input into the Maximum Likelihood fit in order to calculate the $B^0 \rightarrow K^0_S\pi^+\pi^-$ branching fraction. A few intense bins at the edge of the Dalitz plot with an efficiency greater than 50% are observed. This is due to statistical fluctuations as these bins capture only a few events right at the end of the plot (no more than 20 in each) compared to more than a million used in total. For these cases, the bin contents are replaced with an average calculated from those bins surrounding them.

Whilst conducting the analysis, there was no knowledge of the data distribution in the Dalitz plot, and hence via what resonances the B mesons might decay. For example, it is possible all events could be resonant in origin. Therefore, a check is made to see that the efficiency of resonances in the Dalitz plot agrees with that of the nonresonant Monte Carlo in the corresponding region, as one would expect. Comparisons are made using the simulations of three resonant modes which can contribute to the Dalitz plot. These modes are $B^0 \rightarrow K^{*+}\pi^-$, $B^0 \rightarrow \rho^0 K^0_S$ and $B^0 \rightarrow f^0 K^0_S$. Figure 4.3 shows the ratio of efficiencies of each of the resonant modes compared with that of the nonresonant Monte Carlo in the corresponding area. As expected, there is no evidence of disagreement between the different Monte Carlos.

It was also seen that the effects due to migration (the movement of an event from one bin to another due to reconstruction inaccuracies) were negligible as the event resolution is orders of magnitude smaller than the bin size. The distribution of mis-reconstructed events (cross-feed) tends to be focused in the corners of the Dalitz plot, causing a slightly higher efficiency in those bins.

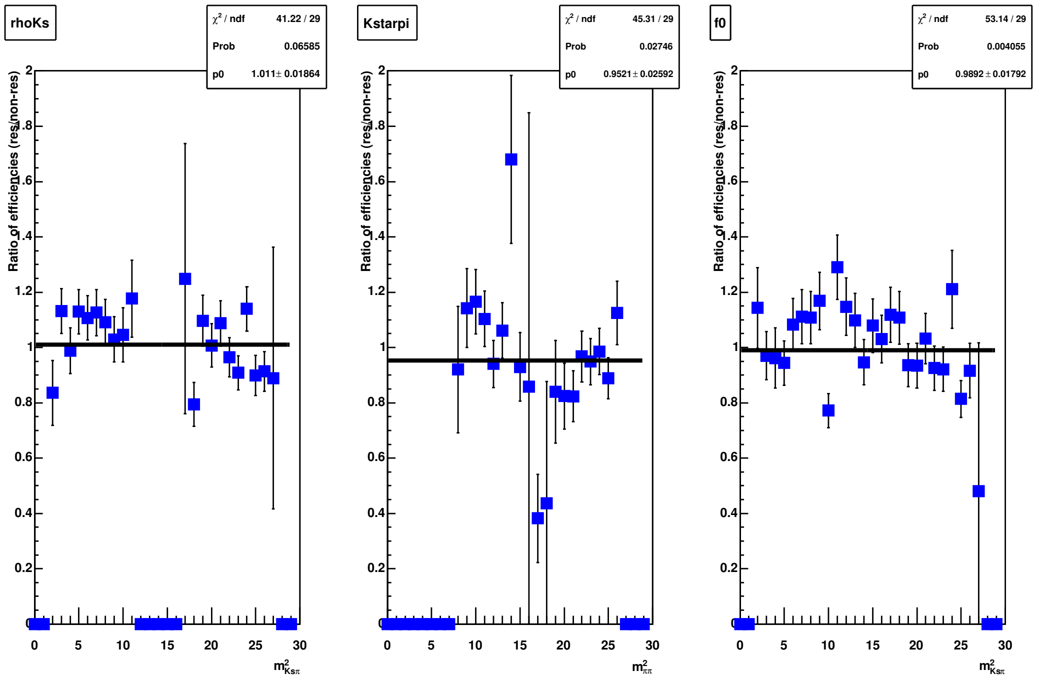

Figure 4.3: From left to right, the ratio of efficiencies of $B^0 \to \rho^0 K^0_S$, $B^0 \to K^{*+}\pi^-$ and $B^0 \to f^0 K^0_S$ resonant Monte Carlo compared to the same region in the Dalitz plot for nonresonant MC. The Dalitz plot was split into 30 parallel slices along the $m^2_{K^0_S\pi}$ axis for $B^0 \to K^{*+}\pi^-$ and along the $m^2_{\pi^+\pi^-}$ axis for $B^0 \to \rho^0 K^0_S$ and $B^0 \to f_0 K^0_S$ and the events in each bin were analysed. The three plots show agreement between the regions of resonant and nonresonant Monte Carlo. The vector nature of the K^*, combined with the reduced efficiency which occurs in the same area due to charm vetoes, results in only a few events in the region $13 < {m_{K^0_S\pi^+}}^2 < 18$, leading to the statistical fluctuations from unity seen in the centre plot, which drive the average down from unity.

When Particle Identification (PID), tracking and K_S^0 reconstruction are applied to MC data, the selection efficiencies differ from when the same procedures are applied to data. Therefore, the overall efficiency must be corrected for these differences. The corrections and uncertainties for each of these are discussed in Chapter 6.

4.3 Branching Fraction Calculation with Variable Efficiency

When measuring the branching fraction of a decay to a resonance, the efficiency can usually be taken as a constant value because of the narrow band of phase space that the resonance falls in. When the efficiency is constant, the equation for calculating the branching fraction is:

$$\mathcal{B} = \frac{N_{sig}}{\epsilon N_{B\overline{B}}} \tag{4.9}$$

where N_{sig} is the number of signal events in the fit, $N_{B\overline{B}}$ is the number of $\Upsilon(4S) \rightarrow B\overline{B}$ decays in the data sample and ϵ is the constant efficiency.

However, for an inclusive analysis, the efficiency cannot be considered a constant and in order to calculate correctly the branching fraction, it is necessary that the efficiency is included as a variable in the fit. The ${}_sPlot$ technique described in Appendix A and in [49] is used to incorporate the efficiency calculation into the fit to directly yield a branching fraction. A short description is given here. All calculations must be made after an initial fit to data finds the yields for each of the species which are floated in the fit (i.e. signal or background).

For each event e included in the fit, an "${}_sWeight$" can be defined for the signal hypothesis. An ${}_sWeight$ is calculated using the covariance matrix from the likelihood fit to data:

$${}_s\mathcal{P}_{sig}(y_e) = \frac{\sum_{j=1}^{N_s} \mathbf{V}_{sig,j} f_j(y_e)}{\sum_{k=1}^{N_s} N_k f_k(y_e) + \sum_{i=1}^{N_t} N_i f_i(y_e)}. \tag{4.10}$$

Here,

- ${}_s\mathcal{P}_{sig}$ is the ${}_s\mathit{Weight}$ for the signal hypothesis,
- y is the set of fit variables (e.g. m_{ES}, ΔE and Fisher),
- $\mathbf{V}_{sig,j}$ is the element of the covariance matrix for the fit which corresponds to the signal hypothesis and hypothesis j,
- $f(y_e)$ is the value of the combined PDF of set y for an event e,
- N_s is the number of species floated in the fit,
- N_t is the number of species not floated in the fit and
- N_k and N_i are the number of events for each hypothesis

${}_s\mathit{Weights}$ are then used to calculate the efficiency corrected number of events, N_{cor}, which can then be used to calculate the branching ratio:

$$N_{cor} = \sum_{i=1}^{N} \frac{{}_s\mathcal{P}_i + \sum_{t=1}^{N_t} c_{sig} M_t}{\epsilon_i} \tag{4.11}$$

where

- ϵ_i is the efficiency of the ith event as a function of position in the Dalitz plot,
- $c_{sig} = N_{sig} - \sum_j \mathbf{V}_{sig,j}$ (where N_{sig} is the number of signal events fitted) and
- M_t is the known distribution of the fixed species included in the fit, described by the variables which are used in the fit.

The term $\sum_{t=1}^{N_t} c_{sig} M_t$ is only needed when fixed species are present in the ML fit.

The branching fraction can then be simply calculated by:

$$\mathcal{B} = \frac{N_{cor}}{N_{B\overline{B}}} \tag{4.12}$$

where $N_{B\overline{B}}$ is the total number of $B\overline{B}$ events.

This method stems from a method of creating signal-only plots, ${}_s\mathit{Plots}$. By plotting the distribution of a variable (which is not included in the fit) weighted by the signal ${}_s\mathit{Weight}$, signal only plots can be created. More information is included in Appendix A and examples of ${}_s\mathit{Plots}$ are shown in Chapter 5.

4.4 Method and PDFs

For this analysis, fits were made to the m_{ES}, ΔE and Fisher distributions, using the functions that best describe the data. For the inclusive measurement, the distributions of signal and continuum are shown in Figures 4.4 and 4.6 respectively. Non-resonant $K^0_S\pi^+\pi^-$ Monte Carlo was used to find the signal shapes and offpeak or upper sideband data were used for continuum background. Table 4.2 shows the functions chosen for each of the modes.

4.4.1 PDF parameterisation

As mentioned in Section 4.1, there were three categories (hypotheses) for events that combine to form the total number of candidates. These three categories are

- Signal
- Continuum background
- Peaking B background

For each category a PDF was formed for each of the three kinematic variables m_{ES}, ΔE and $\mathcal{F}$. The type of PDF which gave the best χ^2 value when all the shape parameters were floated was chosen in each case.

There were several different types of PDF used to model the MC. The most commonly used PDF was the Gaussian distribution in different forms. In addition to one Gaussian distribution, various types of double Gaussians were also used. The term "double Gaussian" will be used to describe a sum of two Gaussians with distinct σ's but constrained to have the same mean. The term "double-meaned double Gaussian" will be used to describe the addition of two Gaussians with distinct σ's and distinct means. Finally, a "bifurcated Gaussian" refers to an asymmetric distribution, where the left side of the distribution is described by a Gaussian with σ_1 and the right side is described by a Gaussian of σ_2, where σ_1 and σ_2 are distinct.

Signal PDFs

Using signal Monte Carlo (i.e. nonresonant $B^0 \to K^0_S\pi^+\pi^-$ MC for the inclusive PDFs, $B^0 \to K^{*+}\pi^-$ MC for the $B^0 \to K^{*+}\pi^-$PDFs etc), a fit to the m_{ES} distribution was performed using a Crystal Ball [50] function, which is a single Gaussian with an exponential tail (in this case to the left side of the distribution). A double Gaussian is used for ΔE and a double-meaned double Gaussian for $\mathcal{F}$. The signal PDFs for each distribution are shown in Figure 4.4.

Continuum PDFs

An Argus function [42] is used to parameterise the distribution of the m_{ES} variable for continuum background. The function is:

$$\frac{dN}{dx} = Ax\sqrt{1-x^2}e^{[-c(1-x^2)]} \tag{4.13}$$

in which $x = m_{\mathrm{ES}}/E_{beam}$, A is a normalisation factor, and c is the Argus shape parameter.

Two different data samples can be used to find PDFs for continuum events. Off-resonance data is free of contamination from B decays, but it is a low statistics

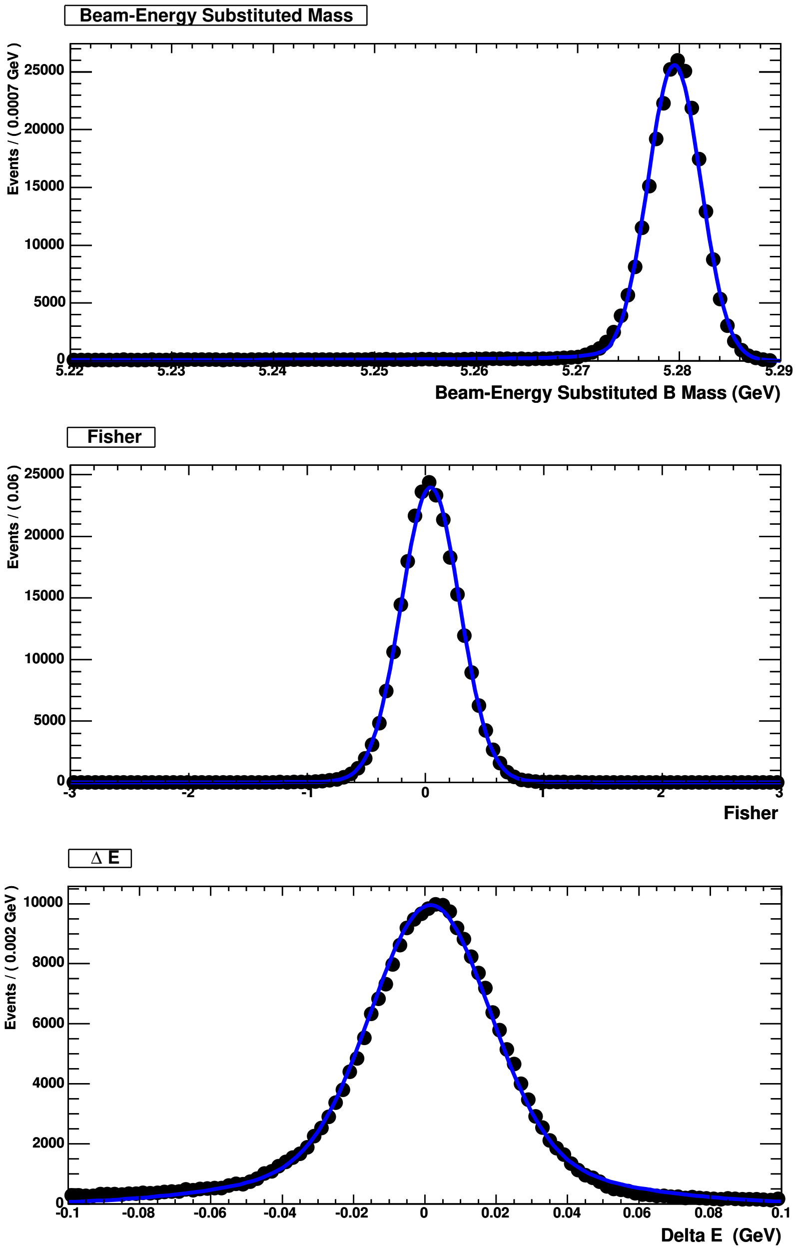

Figure 4.4: The $K^0_S\pi^+\pi^-$ nonresonant MC shapes of $m_{\rm ES}$, Fisher and ΔE. A Crystal Ball function is fitted to $m_{\rm ES}$, a double-meaned double Gaussian to the Fisher and a double Gaussian to ΔE.

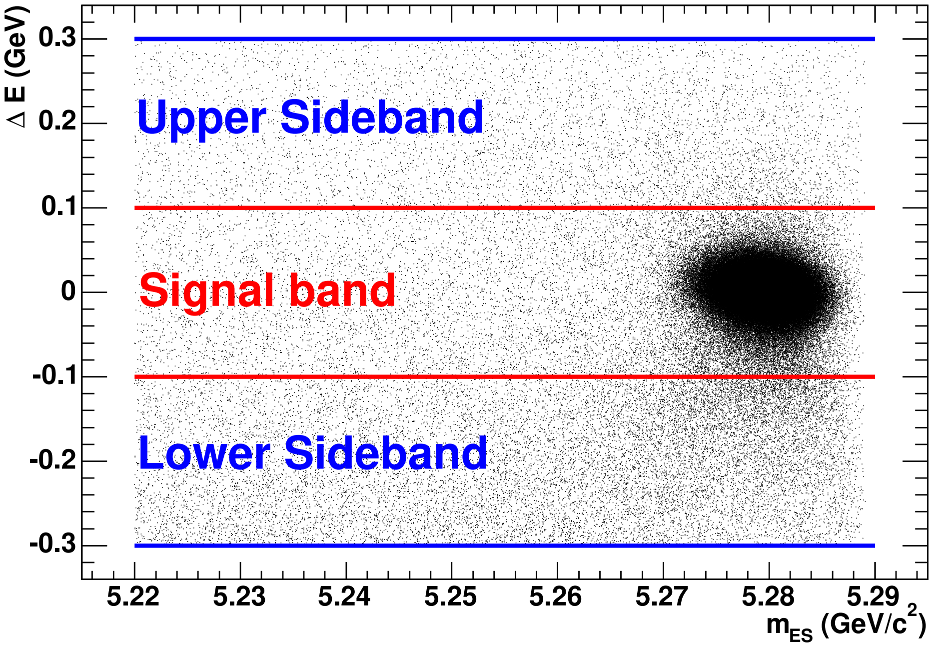

Figure 4.5: The regions of the ΔE-m_{ES} plane. The upper sideband was used for continuum background studies, but was polluted with a small amount of two-body B background. The lower sideband was too polluted with four-body B background to be used to parameterise the continuum. The signal band was the area of the plane to which the final PDFs are fitted. Nonresonant MC is used to produce the data points.

sample. It is also possible to use the on-resonance m_{ES} sidebands (as shown in Figure 4.5) as they have significantly more statistics than the off-resonance sample. However, the lower sideband tends to be contaminated with peaking B background and is therefore unsuitable for the study of continuum events. The upper sideband is used for modelling m_{ES} and Fisher, but ΔE must be modelled using the off-resonance data in order to be able to use a wide range on ΔE. In order to account for the low statistics of this sample the shape is floated in the fit if possible.

Fits were performed to the upper and lower sidebands and off-resonance m_{ES} distributions using an Argus function. Table 4.1 shows that the fitted values for the

Sideband	Argus shape parameter, c
Off-resonance	-19.35 $\pm$ 0.92
Upper sideband	-19.42 $\pm$ 0.66
Lower sideband	-26.84 $\pm$ 0.43

Table 4.1: The Argus shape parameter c for the off-resonance and the upper m_{ES} sideband data.

Argus parameter (c), and therefore the Argus shape, in the upper sideband and off-resonance data are consistent. Therefore it can be assumed that the upper sideband is not heavily polluted by peaking B events, and that it can provide a good source of data for modelling the continuum distribution. The fit to the lower sideband data is very inconsistent with the other two results, revealing that a large amount of B-related background pollutes that region of the m_{ES}-ΔE plane. This data sample should therefore not be used for the parameterisation of backgrounds.

For the Fisher discriminant, a double Gaussian model was found to provide the best model in a fit to upper sideband data. A first-order polynomial was fitted to the ΔE distribution of the off-resonance data sample. The continuum PDFs for each distribution are shown in Figure 4.6.

Peaking B-background

In order to parameterise the PDFs for peaking B background, the Monte Carlo simulation of the contributing decays are used. A 2D Keys PDF [51] is a 2-dimensional histogram which takes into account correlations between the variables, which is useful for modeling m_{ES} and ΔE in this case. This is because the distributions of both two-body backgrounds (where a random particle is erroneously associated with the decay when trying to reconstruct a three-body decay) and four-body backgrounds

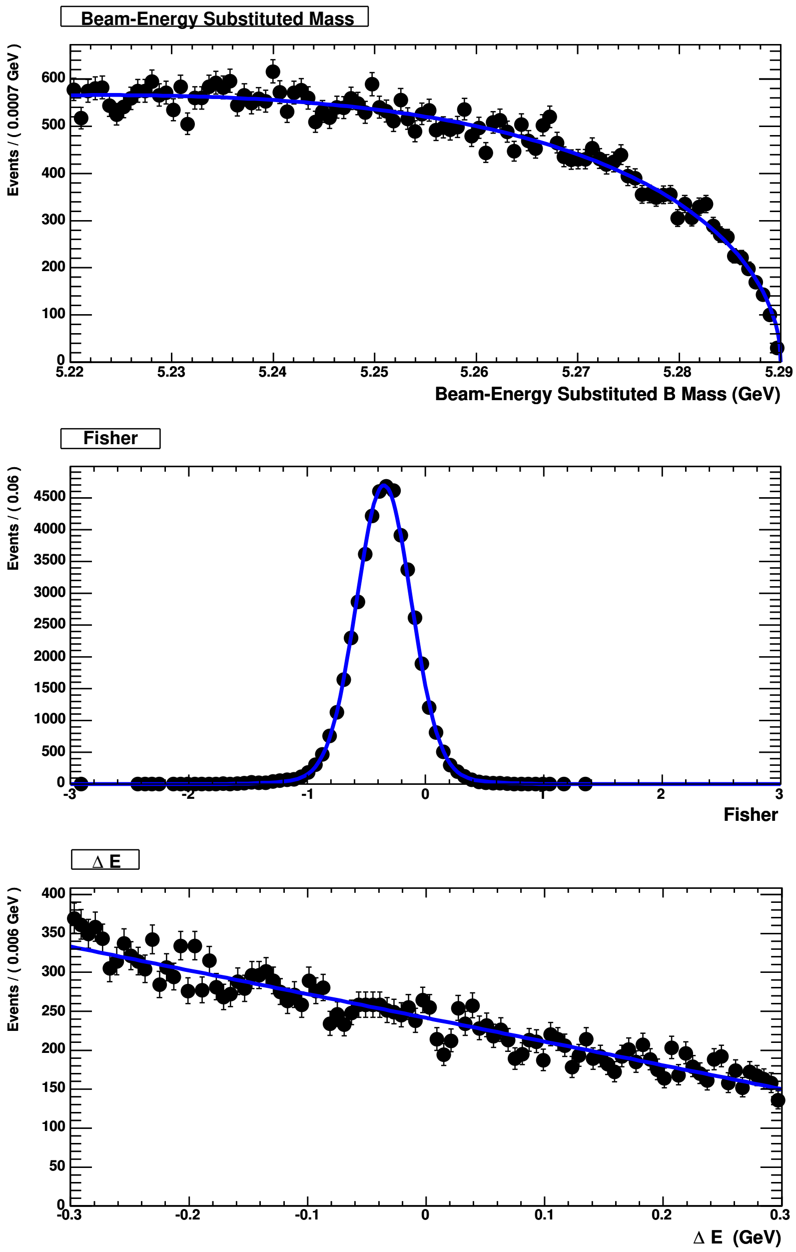

Figure 4.6: The parameterisation of m_{ES} and Fisher using upper sideband data, and the off-resonance data parameterisation of ΔE. An Argus function is fitted to m_{ES}, a straight line to ΔE and a double Gaussian to Fisher. The upper sideband is defined as $5.22 < m_{\mathrm{ES}} < 5.3$ and $0.1 < \Delta E < 0.3$.

(where a daughter particle, often a π^0 or a photon, fails to be included in the reconstruction) show correlations between their m_{ES} and ΔE distributions. Figure 4.7 shows the m_{ES} and ΔE projections of the 2D Keys PDF for the four-body background $B^0 \to \eta' K_S^0, \eta' \to \rho\gamma$ and the high correlation between the variables can be seen in Figure 4.8.

No significant correlations are observed between $\mathcal{F}$ and m_{ES} or $\mathcal{F}$ and ΔE for the B-background modes used in this analysis (See Section 6.1.5). Therefore, a bifurcated Gaussian is used to describe the remaining $\mathcal{F}$ distribution.

Table 4.2 provides a summary of the m_{ES}, ΔE and $\mathcal{F}$ PDFs used for each category.

<table>
<tr><th>Mode</th><th>Data Type</th><th>Variable</th><th>Function</th></tr>
<tr><td rowspan="9">All</td><td rowspan="3">Signal</td><td>m_{ES}</td><td>Crystal Ball</td></tr>
<tr><td>ΔE</td><td>Double Gaussian</td></tr>
<tr><td>Fisher</td><td>Double-meaned Double Gaussian</td></tr>
<tr><td rowspan="3">Continuum</td><td>m_{ES}</td><td>Argus</td></tr>
<tr><td>ΔE</td><td>Linear</td></tr>
<tr><td>Fisher</td><td>Double Gaussian</td></tr>
<tr><td rowspan="3">B-related Background, $\eta' K_S^0$</td><td>m_{ES}</td><td rowspan="2">2D Keys</td></tr>
<tr><td>ΔE</td></tr>
<tr><td>Fisher</td><td>Bifurcated Gaussian</td></tr>
</table>

Table 4.2: The signal, continuum and B related background shapes chosen to model the data.

PDF Correlations

There must be no strong correlations between the variables used in the fit so that the ML fit is not biased. Those correlations observed for peaking B background

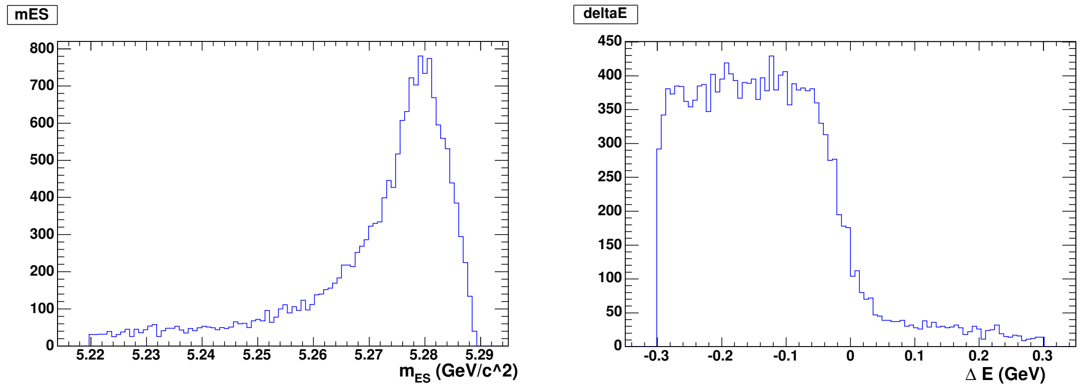

Figure 4.7: Projections of the 2D Keys PDF for the B background $B^0 \to \eta' K^0_S, \eta' \to \rho\gamma$. This mode displays the typical correlation for a 4-body background to a three body mode in m_{ES} and ΔE, as illustrated in Figure 4.8.

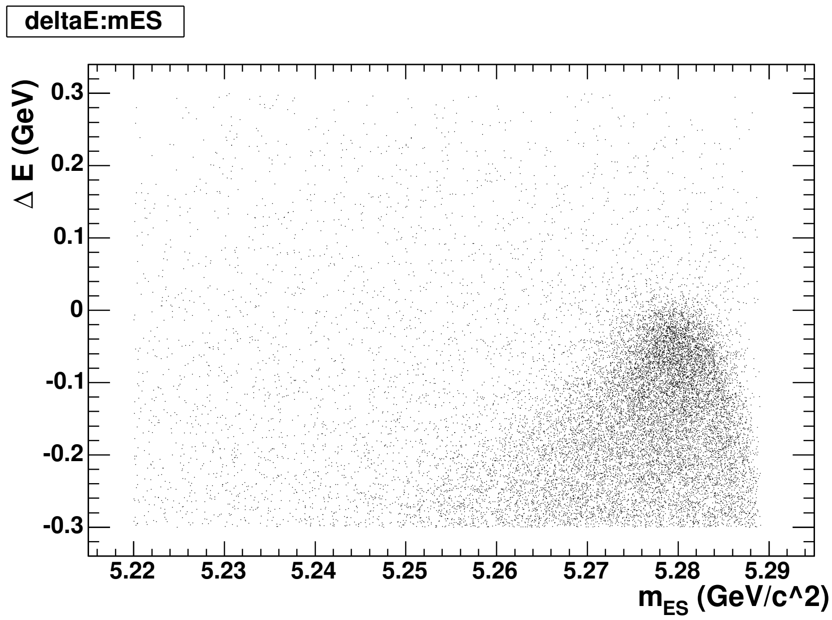

Figure 4.8: The m_{ES}-ΔE plane of $B^0 \to \eta' K^0_S, \eta' \to \rho\gamma$. The two variables can be seen to be highly correlated and show a typical distribution for a 4-body background to a 3-body decay. The γ from the η' decay has probably been lost in reconstruction, while the ρ^0 decays to $\pi^+\pi^-$ incorrectly giving a final state of $K^0_S\pi^+\pi^-$.

have been taken into account using 2D Keys PDFs. The correlations between the PDFs which describe the signal and the background are studied in this section.

	m_{ES}	ΔE	$\mathcal{F}$
m_{ES}	1	0.006508	0.034776
ΔE	0.006508	1	0.006425
$\mathcal{F}$	0.034776	0.006425	1

Table 4.3: Elements of the correlation matrix for m_{ES}, ΔE and $\mathcal{F}$ distributions using signal Monte Carlo.

Table 4.3 shows the elements of the correlation matrix ρ between the three Monte Carlo signal distributions. The correlation matrix is defined to be:

$$\rho_{x,y} = \frac{cov(x,y)}{\sigma_x \sigma_y} \tag{4.14}$$

where x and y are distribution variables, $cov(x,y)$ is their covariance and σ_x and σ_y are their respective variances. No significant correlations were seen between the variables in the fit with the greatest being between m_{ES} and $\mathcal{F}$ which was measured to be 0.03.

	m_{ES}	ΔE	$\mathcal{F}$
m_{ES}	1	0.005880	-0.016157
ΔE	0.005880	1	0.011330
$\mathcal{F}$	-0.016157	0.011330	1

Table 4.4: Elements of the correlation matrix for m_{ES}, ΔE and $\mathcal{F}$ distributions using the upper sideband data.

Table 4.4 shows the elements of the correlations matrix between the three distributions in the ML fit for upper sideband data. There are again no significant correlations between the variables with the greatest being between m_{ES} and $\mathcal{F}$ which was measured to be -0.016.

	m_{ES}	ΔE	$\mathcal{F}$
m_{ES}	1	-0.000867	-0.009813
ΔE	-0.000867	1	0.022341
$\mathcal{F}$	-0.009813	0.022341	1

Table 4.5: Elements of the correlation matrix for m_{ES}, ΔE and $\mathcal{F}$ distributions using offpeak data.

Table 4.5 shows the elements of the correlations matrix between the three fit variables for offpeak data. Again, it is seen that there are no significant correlations with the greatest being between ΔE and $\mathcal{F}$ which was measured to be 0.022.

It may not sufficient to calculate the linear correlation coefficient in order to determine whether two variables are correlated as non-linear correlation could cancel out. This effect can be studied by plotting each set of variables against each other in the form of x versus the sum of y for the bin. Figure 4.9 shows these plots for all the possible pairing between m_{ES}, ΔE and $\mathcal{F}$. This is done using signal Monte Carlo to observe any effects for signal and offpeak and upper sideband data to observe any effects for background. These studies show a small correlation between signal m_{ES} and ΔE, but no significant correlations are present between any other variables for signal or background. The correlation between m_{ES} and ΔE for signal has been studied within the *BABAR* Collaboration and found to be sufficiently low enough to be considered negligible [52].

The only significant correlations are between parameters used to describe a PDF. These correlations are shown and described in Appendix B.

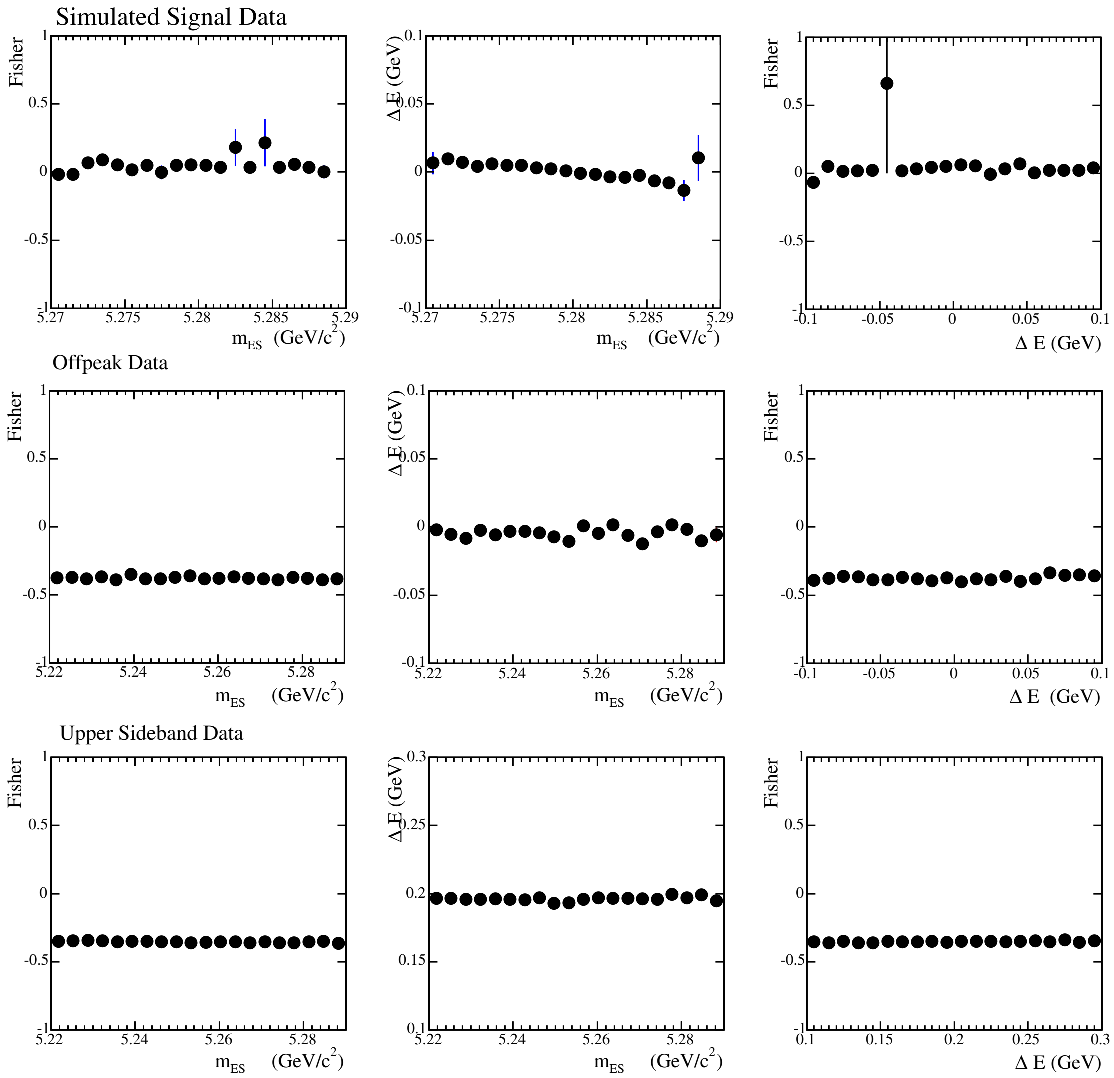

Figure 4.9: m_{ES}, $\mathcal{F}$ and ΔE correlation profiles. The top row is signal Monte Carlo (blue data points), the middle row is offpeak data (red data points) and the bottom row is upper sideband data (green data points). In each column from left to right is plotted m_{ES} versus $\mathcal{F}$, m_{ES} versus ΔE and ΔE versus $\mathcal{F}$.

4.5 $B^0 \to D^-\pi^+$ Calibration Channel

4.5.1 PDF Validation

This analysis is absolutely reliant on Monte Carlo for the description of the signal and B-background PDFs. Therefore it was necessary to be confident that the MC accurately described the data. $B^0 \to D^{\mp}\pi^{\pm}$ is a charmed mode with a final state of $K^0_S\pi^+\pi^-$ which can be used as a calibration channel to check for any discrepancies between data and MC, as a comparison mode for assigning systematic errors and as a cross-check to test the fitting package.

The world average branching fraction for $B^0 \to D^-\pi^+, D^- \to K^0_S\pi^-$ is $(38.9 \pm 4.39) \times 10^{-6}$ [6]. This is comparable to the PDG values for the inclusive $B^0 \to K^0\pi^+\pi^-$ channel under study, but has the benefit of a much improved signal-to-background ratio and little B-related background.

The selection criteria used to select the calibration channel and the corresponding efficiencies for data and Monte Carlo are shown in Table 4.6. These cuts were applied sequentially, and a reconstructed state of $K^0_S\pi^+\pi^-$ was classed as being a B candidate regardless of whether the truth information showed it to be a consequence of cross-feed. Therefore, it should be noted that the signal PDFs are a combination of "true" B event PDFs and cross-feed PDFs. However, Table 4.6 shows the contribution to the signal from cross-feed events to be small (3.5%). After applying tracking, PID and K^0_S reconstruction corrections (discussed in Chapter 6), the signal efficiency was estimated to be $20.9 \pm 0.14\%$.

The signal and sideband regions are as described in Figure 4.5 and the PDFs are as described in Table 4.2. Only one B-background is found to significantly contaminate the signal region, $B^0 \to K^{*+}\pi^-$, with an estimated 2.7 ± 0.4 events.

After obtaining the PDFs for signal and background, and conducting the fit

TITLE* Cut	On-res	Off-res	MC (True B)	MC (CF)
Tracks 1 & 2 fail the `notAPion SMSKaonSelector`	0.40	0.40	0.66	0.65
Tracks 1 & 2 fail electron selector (LHESelector)	0.95	0.95	1.00	1.00
$q_1 \times q_2 = 1$	1.00	1.00	1.00	1.00
$5.22 < m_{\mathrm{ES}} < 5.29$ GeV/c^2	0.71	0.71	1.00	0.82
-0.3 < ΔE < 0.3 GeV/	0.87	0.87	1.00	0.92
$1.834 < m_{D^-} < 1.895$ GeV/c^2	0.03	0.03	0.93	0.16
$0.483 < m_{K_S^0} < 513$ GeV/c^2	0.68	0.67	0.98	0.71
$\lvert\cos\theta_{thr}\rvert < 0.9$	0.43	0.38	0.88	0.88
K_S^0 Lifetime significance > 5.0	0.45	0.42	0.94	0.62
$\cos\theta_{K_S^0} > 0.999$	0.72	0.65	0.94	0.68
Veto	0.59	0.54	0.79	0.60
$\lvert\Delta E\rvert < 0.1$ GeV	0.50	0.41	0.99	0.76

Table 4.6: $B^0 \to D^-\pi^+$ cuts and the efficiency of each cut on the number of events. Each efficiency is relative to the one above it. Cross-feed represents 1.7% of the signal in the final data sample.

tests explained in Section 5.1 (the results of which are shown in Appendix C), a maximum likelihood fit was performed to on-resonance data in the signal region. All the parameters in the signal PDFs, with the exception of the parameters α and n in the tail of the Crystal Ball function which described m_{ES}, were allowed to float in the fit which enabled the fitted values to be compared with those obtained from the original fits using Monte Carlo. These two parameters were not allowed to float in the fit because the shape of the tail which they describe is very close to the shape of the Argus function, and therefore floating them would cause bias within the fit. Table 4.7 shows the values obtained in both cases, while Figure 4.10 shows the data plotted along with the fitted PDFs for the three projections previously mentioned. In the charmless branching fraction measurements that follow, the signal parameters taken from MC are adjusted using the differences between the signal and MC parameters for this calibration mode. The differences between the PDFs can be seen in Figure 4.11, where the PDFs using the data and Monte Carlo parameters are drawn.

Signal PDFs	Parameter	Fitted value (MC/sideband)	Fitted value (data)
Crystal Ball (m_{ES})	mean	$5.28 \pm (2.04\times10^{-5})$	$5.28 \pm (7.72\times10^{-5})$
	sigma	$(2.5983 \pm 0.0016) \times10^{-3}$	$(2.5280 \pm 0.0061) \times10^{-3}$
	α	2.41 ± 0.24	FIXED
	n	2.408 ± 0.074	FIXED
Double Gaussian (ΔE)	mean	$(2.27 \pm 1.65) \times10^{-4}$	$(-2.74 \pm 0.68) \times10^{-3}$
	sigma 1	$(3.8 \pm 1.1) \times10^{-2}$	$(4.9 \pm 1.1) \times10^{-2}$
	sigma 2	$(1.824 \pm 0.0025) \times10^{-2}$	$(1.88 \pm 0.11) \times10^{-2}$
	ratio of Gaussians	0.212 ± 0.018	0.192 ± 0.073
Double meaned Double Gaussian (Fisher)	mean 1	$(4.38 \pm 0.19) \times10^{-2}$	$(3.16 \pm 0.75) \times10^{-2}$
	mean 2	$(7.7 \pm 7.8) \times10^{-2}$	0.4887 ± 0.0026
	sigma 1	1.0623 ± 0.0076	0.1623 ± 0.0058
	sigma 2	0.2476 ± 0.0020	0.2333 ± 0.0057
	ratio of Gaussians	$(1.63 \pm 0.11) \times10^{-2}$	$(1.36 \pm 0.18) \times10^{-2}$

Table 4.7: The signal PDF parameters from a fit to $B^0 \to D^{\mp}\pi^{\pm}$ signal Monte Carlo and a fit to data.

The following numbers were obtained for signal and continuum background $B^0 \to D^-\pi^+$ events

$$N_{sig} = 1282.3 \pm 36.3 \tag{4.15}$$

$$N_{cont} = 1155.1 \pm 36.7 \tag{4.16}$$

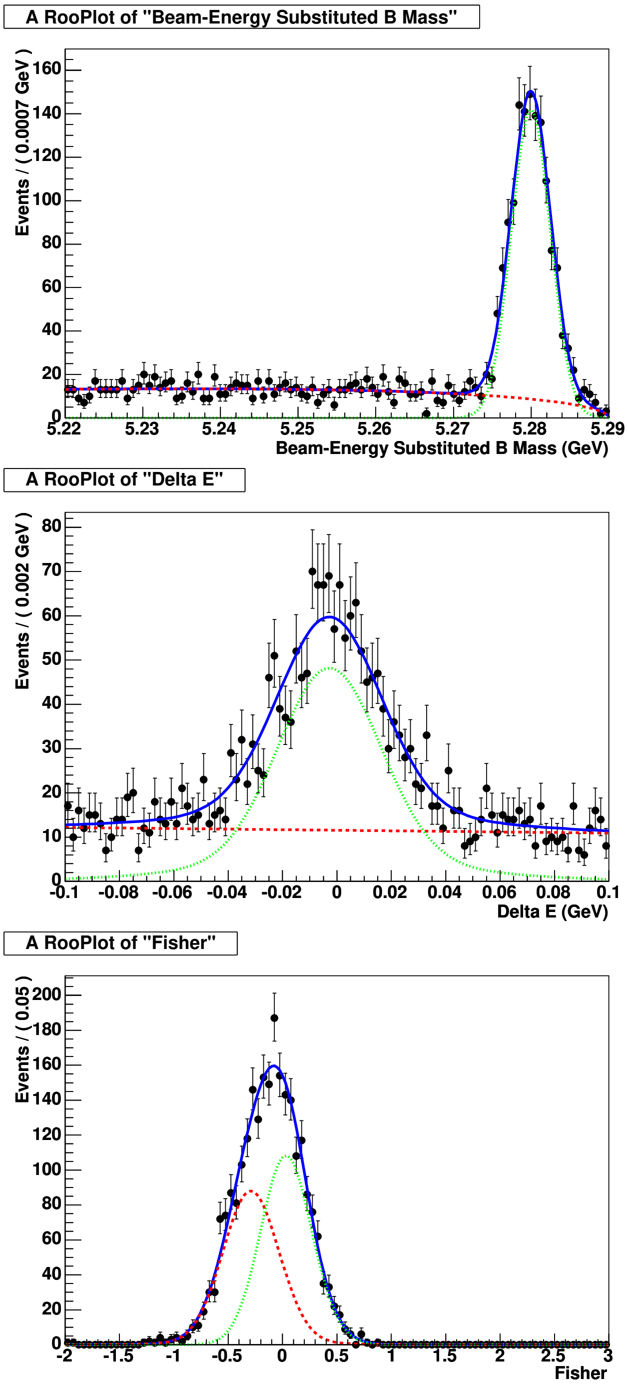

Figure 4.10: Plots of the maximum likelihood fit to on-resonance data for $B^0 \to D^-\pi^+$. For this fit all signal parameters were floated. The points represent on-resonance data, the green dotted line is the fitted signal PDF, the red dashed line is the fitted background PDF and the blue line is the sum of the fitted signal and background PDF.

With an overall efficiency of 20.9 $\pm$ 0.14%, and 2.32 $\times 10^6$ $B^0\overline{B}^0$ pairs in the data sample, the following branching fraction was obtained:

$$\mathcal{B} = 38.4 \pm 1.1 \times 10^{-6}$$

where the error is statistical only. This branching ratio is fully consistent with the PDG value and therefore this calibration measurement confirmed that the method and the fitting technique used for this analysis were viable. The fit plots for the ML variables are shown in Figure 4.10.

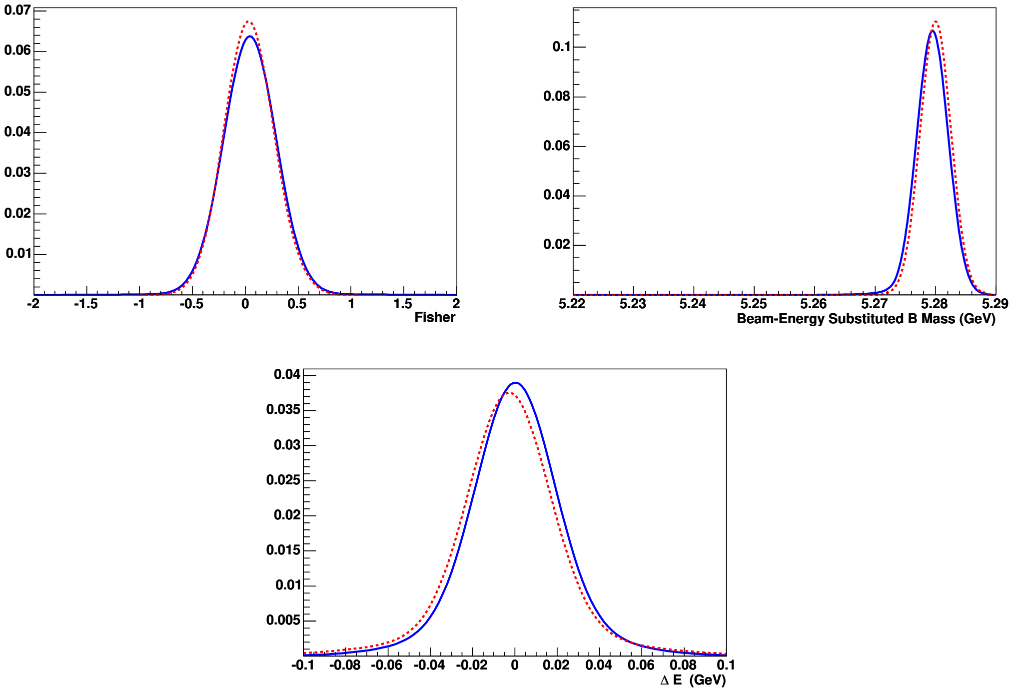

Figure 4.11: Illustrations of the shift in $B^0 \rightarrow D^-\pi^+$ signal PDF parameters, Fisher (top left), m_{ES} (top right) and ΔE (bottom). The red dashed line represents the PDF obtained from a fit to on-resonance data and the blue solid line represents the PDF obtained from a fit to Monte Carlo. The shifts in the PDFs are implemented in the fits to data for the other signal modes.

Chapter 5

Results

5.1 Inclusive $B^0 \to K_S^0 \pi^+ \pi^-$

Before unblinding results, the fitting package must be tested to ensure the fits are reliable, stable and unbiased. These tests are described in full in this section for the inclusive analysis, but are the same in method for all the modes which follow.

5.1.1 The Fit Model

The tests were conducted using estimates for the amount of each type of data expected in the fit. The estimates for the expected amount of signal and B-related background came from the efficiency of the signal MC for each mode, the current world average branching fraction measurement (from either the *BABAR* analysis on $81\,\mathrm{fb}^{-1}$ [19] or the PDG [6]) and the size of the on-resonance data sample. For the continuum background estimation, an average was taken of the number of events in the upper and lower sidebands (see Figure 4.5). The final model was:

- Signal - 850 events
- Background - 80,000 events

The numbers of signal and background events were floated in the fit, and the number generated was Poissonianly fluctuated about the input values for each experiment. 500 individual experiments were conducted for each test.

5.1.2 Toy Tests

It was first important to check that the fitting package found the same number of events as were put into the fit. The primary test used Monte Carlo data which were generated using each of the PDFs for each type of event (signal, background, B background). This type of MC is known as toy MC. The PDFs were then fit to these data to see if the fit could reproduce the number of events of each type which were generated.

Using this method, it is possible to test which parameters can be floated in the fit, and which B backgrounds produce a significant change in the number of signal events fitted. Tests were done for each of the modes by adding in all of the B backgrounds listed in Tables 3.2-3.6 in the quantities expected. The errors on these quantities are used later to assess a systematic due to the uncertainty in the number expected of each type of B-background. For the inclusive measurement, it was found that the following modes needed to be added to the final fit model:

- $B^0 \to \eta' K^0_S, \eta' \to \rho^0 \gamma$ - 54.4 events
- $B^0 \to D^{\mp} \pi^{\pm}, D^{\mp} \to K^0_S \pi^{\mp}$ - 70.9 events
- $B^0 \to D^{\mp} \pi^{\pm}, D^{\mp} \to K^0_S K^{\mp}$ - 31.9 events
- $B^0 \to D^{\mp} \rho^{\pm}, D^{\mp} \to K^0_S \pi^{\mp}$ - 62.7 events

- $B^0 \to J/\psi K_S^0, J/\psi \to \mu^+\mu^-$ - 126.4 events
- $B^0 \to \psi(2S) K_S^0, \psi(2S) \to \mu^+\mu^-$ - 6.3 events
- $B^\pm \to D^0\pi^\pm, D^0 \to K_S^0\pi^0$ - 151.9 events
- $B^0 \to D^\mp\pi^\pm, D^\mp \to K_S^0\pi^\mp\pi^0$ - 49.9 events
- $B^0 \to D^{*\mp}\pi^\pm, D^{*\mp} \to D^0\pi^\mp, D^0 \to K_S^0\pi^0$ - 50.5 events

The number of each type of B background was fixed in the fit because `Minuit` [53] finds it difficult or impossible to converge with them floated. It was also found that no biases were introduced by floating the Argus parameter c in the continuum background m_{ES} PDF and the slope of the line which describes the continuum ΔE shape. This eliminates any uncertainty from the values taken from off-resonance or upper sideband data.

The amount of "pull" that each experiment experienced was calculated using:

$$\frac{N_{gen} - N_{fit}}{\sigma} \tag{5.1}$$

where N_{gen} is the number of events generated and N_{fit} is the number of events fitted for a particular category (signal or continuum) for each toy experiment. A Gaussian is fitted to the distribution of the pulls of many experiments, which is expected to have a mean of zero and a width of unity.

The toy test of the final inclusive model is shown in Figure 5.1. Both the signal and continuum distributions are consistent with a mean of zero and sigma of 1, and so no biases are evident in this toy test.

5.1.3 Negative Log Likelihood Test

A test considering Negative Log Likelihoods (NLL) was conducted in order to check that the PDFs which modelled the data were accurate. A blind fit to the final data

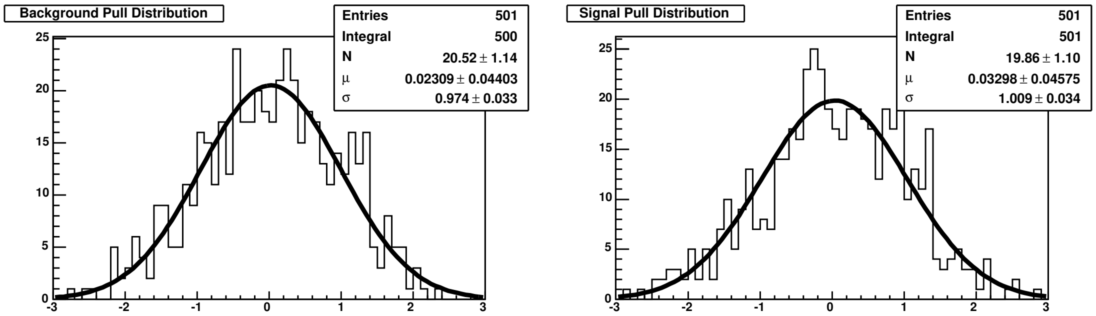

Figure 5.1: Signal and continuum events pulls distributions based on 500 toy MC experiments, generated with 850 signal events and 80000 continuum background events in each experiment. The numbers of signal and continuum events, the Argus parameter c, and the slope parameter of the continuum ΔE PDF are all allowed to float in the ML fit.

sample was performed and the numbers of signal and background events that were the result of that fit were used as inputs to 500 toy experiments. For both the fit to data and the toy fits, the total likelihood was stored. The test for the inclusive measurement is shown in Figure 5.2. The arrow representing the data NLL value is in good agreement with the distribution of toy NLL values, which provides additional confidence in the fit procedure.

5.1.4 Embedded Fits

Further experiments were performed using signal MC samples instead of toy MC samples. Instead of generating the Monte Carlo from the PDFs, events were selected at random from a sample of MC data for the signal and all the B-background modes. The use of MC for the continuum was not possible due to the sheer amount of MC that would be required, and so toy MC was still used in this case. Once again the pull was calculated and used as a measurement of bias in the fit. In this case, a significant pull was seen in the mean of the distributions (Figure 5.3), and is included

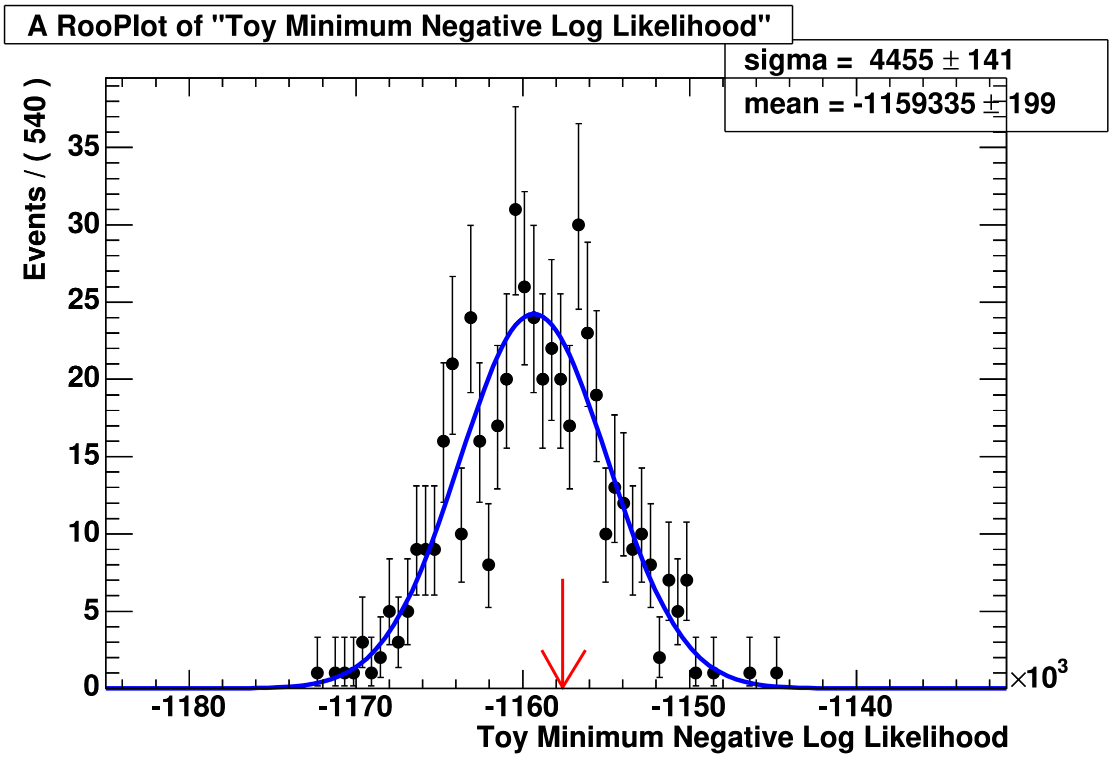

Figure 5.2: The NLL value of the fit to the data sample is shown as the red arrow. The distribution of the NLL values of the 500 toy experiments is plotted in black and the Gaussian fit to the distribution is shown as solid blue line.

as a systematic in the final result (see Chapter 6),.

5.1.5 Upper Sideband Test

A fit was made to the upper sideband data to see if any signal was found. This serves to test whether or not the fitting procedure is biased to finding a signal even when there is none. The B-background PDFs were removed from the fit model since they would be an inaccurate model of what would be expected in the upper sideband region.

The test produced the following results for the number of signal and continuum

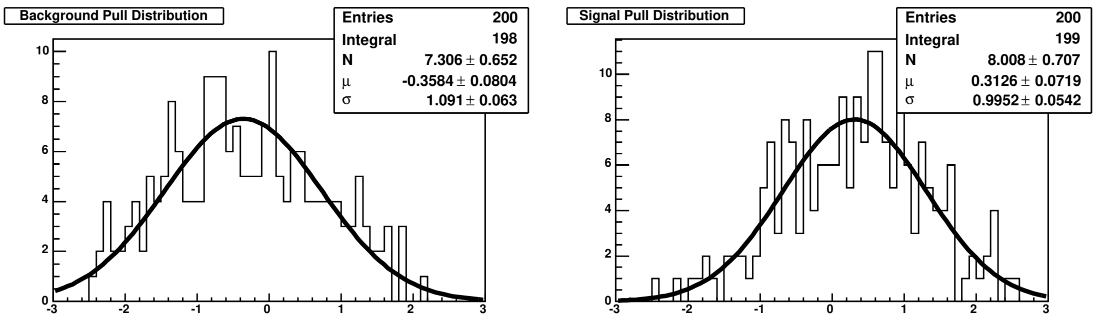

Figure 5.3: The pull distributions of the Embedded Fit test for the Inclusive $B^0 \rightarrow K^0_S\pi^+\pi^-$ mode. A pull of 0.31σ can be seen for the signal distribution and this fit bias is included as a systematic in the result.

background events:

$$\text{Signal Events} \quad -0.446 \pm 5.94 \tag{5.2}$$

$$\text{Continuum Background Events} \quad 1338.6 \pm 37.00 \tag{5.3}$$

$$\tag{5.4}$$

These results show there is no bias towards finding a signal in the ML fit.

5.1.6 Unblind results

Number of Signal events fitted	Number of Background events fitted
860.2 ± 46.6	79347 ± 284.0

Table 5.1: The fitted signal and background yields from the fit to on-resonant data.

For the final fit to data for the inclusive $B^0 \rightarrow K^0_S\pi^+\pi^-$ branching fraction, the numbers of signal and background events were floated along with the Argus parameter c and the slope of the background ΔE polynomial. The number of B-background events was held constant along with all other PDF parameters. The resultant yields are shown in Table 5.1, the fit projections are shown in Figure 5.4 and the signal only ${}_sPlot$ histograms are shown in Figure 5.5.

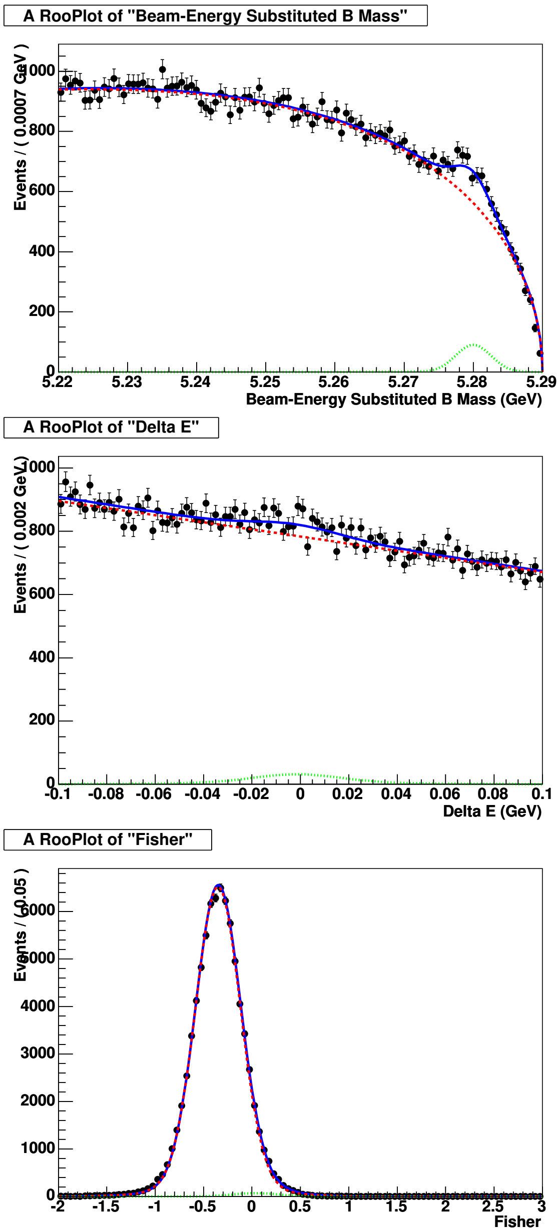

Figure 5.4: The fits to data for the inclusive branching fraction result. In all cases, the total PDF is shown solid blue, the continuum PDF in dashed red and the signal PDF in dotted green. The top figure shows the fit to the m_{ES} distribution, the middle shows the fit to ΔE and the bottom shows the fit to the Fisher.

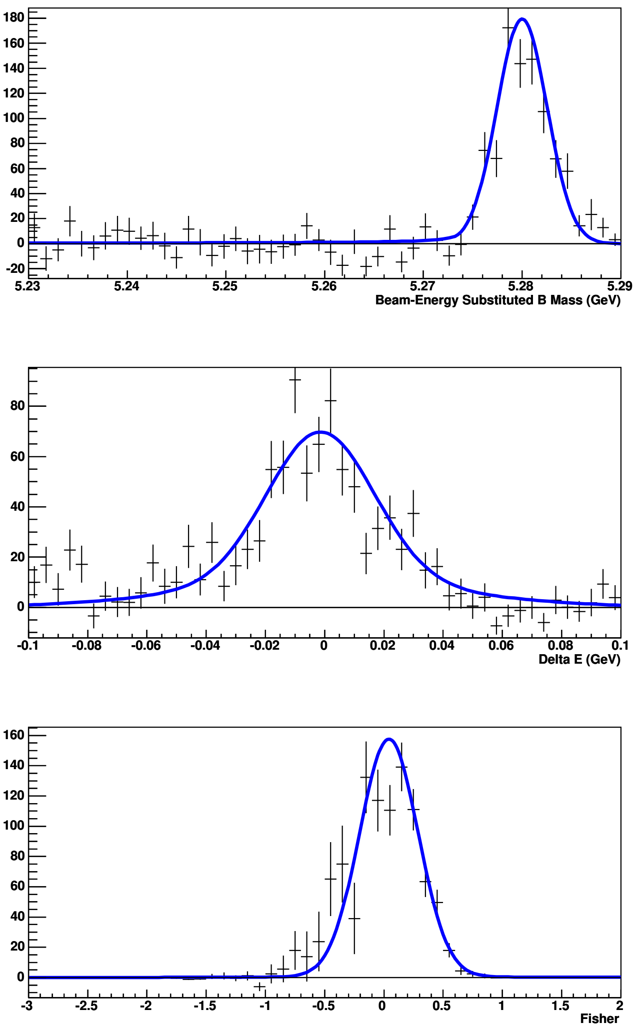

Figure 5.5: The $_s$Plots for the inclusive branching fraction measurement. These plots (top: m_{ES}, middle: ΔE, bottom: Fisher) show the signal distribution in the three variables in the ML fit. The blue line shows the signal PDF that was fitted to the on-resonance data. The $_s$Plot method is described fully in Appendix A.

Using the ${}_sWeight$ method, the branching fraction was calculated to be

$$\mathcal{B}(B^0 \to K^0\pi^+\pi^-\text{Inclusive}) = 43.0 \pm 2.3 \times 10^{-6} \tag{5.5}$$

where the error is statistical only.

Figure 5.6 shows the candidate-by-candidate ratio of signal likelihood to total likelihood for data (solid red line). The results from the fit to data are then used as inputs to a toy experiment which Poissonally varies those input numbers and then fits to that toy MC. The signal likelihood to total likelihood ratio for that toy experiment is shown as the dashed black line.

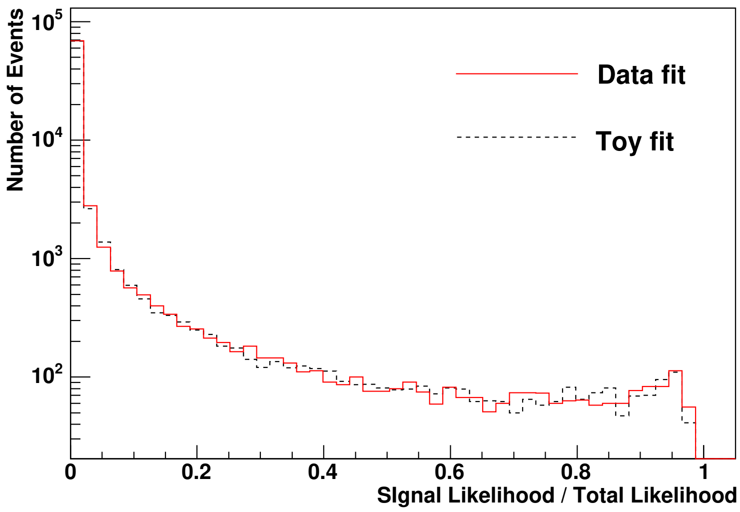

Figure 5.6: The solid red line shows the signal likelihood to total likelihood ratio for the fit to data. The dashed black line shows the ratio of the signal likelihood to total likelihood for a toy experiment based on the event yields from the data fit. The two histograms compare favourably.

It is illustrative to consider several plots which can be viewed after the unblinding of the inclusive branching fraction measurement. An ${}_sPlot$ of the Dalitz plot distribution of $m^2_{K^0_S\pi^+}$ vs. $m^2_{K^0_S\pi^-}$ is shown in Figure 5.7. The majority of events lie around the edges of the Dalitz plot, which indicates that most of the events lie in resonant bands assuming that the nonresonant contribution lies flat across phase space. Figure 5.8 shows the signal-only distributions for the two $m_{K^0_S\pi^\pm}$ projections for two ranges: the left-hand plots show the full mass range and the right-hand plots show the distribution in the $K^{*\pm}(892)$ and the higher $K^{*\pm}$ regions ($0.6 < m_{K^0_S\pi}$ $1.8\,\mathrm{GeV}/c^2$) where the main resonance distribution is expected. Evidence can be seen of peaks around $0.9\,\mathrm{GeV}/c^2$ and also higher in the spectrum. Figure 5.9 shows the $m_{\pi^+\pi^-}$ projection, for the full distribution on the left-hand side and for the ρ^0-$f_0(980)$ region on the right-hand side. The resonance structure is difficult to discern in these plots, although a peak seems evident around $1\,\mathrm{GeV}/c^2$.

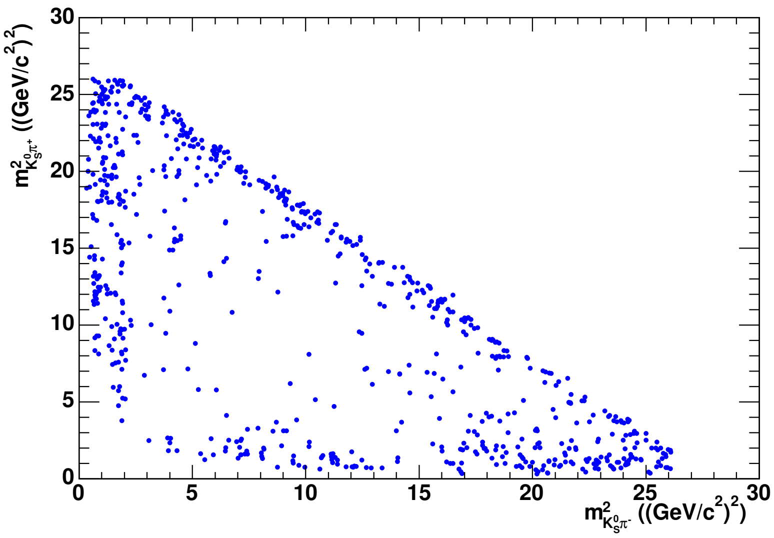

Figure 5.7: The $_s$Plot of the Dalitz plot for the inclusive $B^0 \to K^0_S\pi^+\pi^-$ analysis. The resonance structure is not easily discernible in this plot, but one can see that the signal tends to lie towards the edges of the Dalitz plot. Assuming that the non-resonant contribution is flat in phase space, this indicates that the majority of the signal events lie in resonant bands.

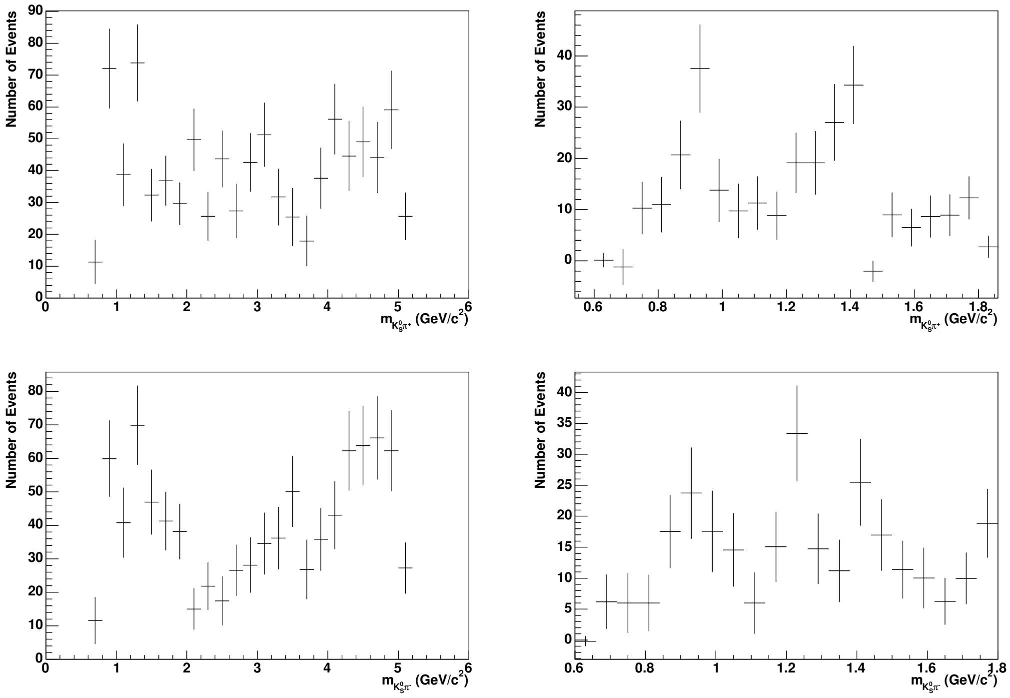

Figure 5.8: The $m_{K_S^0\pi^\pm}$ $_s$Plot projections of the data for the inclusive BF measurement. The top left plot shows the distribution of $m_{K_S^0\pi^+}$ from the inclusive fit to data and the top right plot shows a close-up of the $m_{K_S^0\pi^+}$ distribution in the range $0.6 - 1.8\,\mathrm{GeV}/c^2$. A clear peak can be seen around the $K^{*+}(892)$ region and some structure can be seen in the region consistent with K^{**+} resonances. The bottom left plot shows the $m_{K_S^0\pi^-}$ distribution and the bottom right plot shows a close-up in the region $0.6 - 1.8\,\mathrm{GeV}/c^2$. A peak can again be seen in the region consistent with $K^{*-}(892)$, whilst the K^{**-} region again shows some structure, but it is quite different from the distribution seen in the K^{**+} close-up projection. However, the projections look consistent within statistical errors.

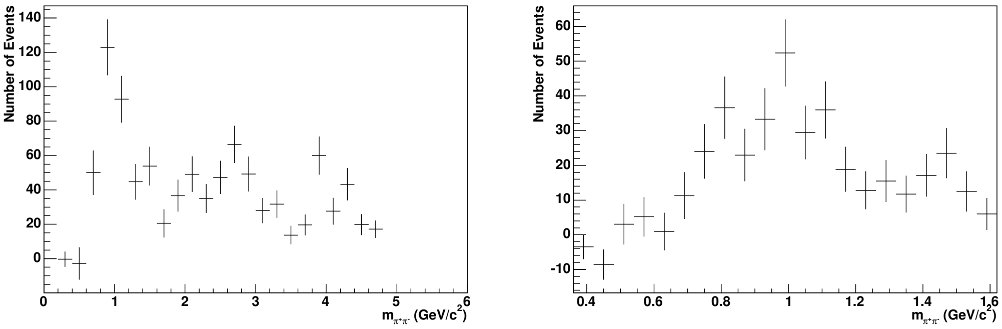

Figure 5.9: The $m_{\pi^+\pi^-}$ $_s$Plot projections of the data for the inclusive BF measurement. The left plot show the projection of the full range of $m_{\pi^+\pi^-}$. A clear peak can be seen around the mass of the $f_0(980)$ but other structure is difficult to identify. The right hand plot shows a close-up of the range $0.4 - 1.6\,\mathrm{GeV}/c^2$. The $f_0(980)$ no longer appears so defined, and there is some structure below this which could be $B^0 \to \rho^0 K^0_S$. There is some potential for resonance structure around 1.5 GeV/c^2, given greater statistics.

5.2 Estimating the nonresonant $B^0 \to K^0_S\pi^+\pi^-$ Branching Fraction

The nonresonant contribution to this final state is small and not yet measured. This decay mode is considered to be a B-related background to the quasi-two body modes $B^0 \to K^{*+}\pi^-$, $B^0 \to \rho^0 K^0_S$ and $B^0 \to f_0 K^0_S$, and therefore an accurate branching fraction, or at least an improved upper limit, would help the accuracy of the other measurements by not overestimating the nonresonant contribution to the signal. When this analysis was performed on $81\,\mathrm{fb}^{-1}$ of data at *BABAR* [19], the upper limit for this contribution was found to be 5.58×10^{-6}.

In order to measure this mode, the $_s$*Plot* mass projections of the Dalitz plot (Figures 5.8 and 5.9) for the inclusive measurement were studied, and an area chosen in $m_{\pi^+\pi^-}$ which was believed to be resonance free. All known $K^0_S\pi^\pm$ resonances were vetoed from the data sample as well as the charmonium states J/ψ and $\psi(2S)$. It was assumed in this measurement that the nonresonant contribution lies flat across the phase space of the Dalitz plane. It is not possible with the current statistics to study the shape of the nonresonant $K^0_S\pi^+\pi^-$, but this could be studied in a Dalitz plot analysis [7] in the future, using various models for the nonresonant contribution [54].

Cut	On-res	Off-res	MC (True-B)	MC (CF)
Reconstruction and Preselection			0.65	
Tracks 1 and 2 fail `notApion SMSKaonSelector`	0.40	0.40	0.67	0.66
Tracks 1 and 2 fail electron selector (LHESelector)	0.95	0.95	1.00	1.00
π's have opposite charge	1.00	1.00	1.00	1.00
$5.22 < m_{ES} < 5.29$ GeV/c^2	0.71	0.71	1.00	0.82
$-0.3 < \Delta E < 0.3$	0.87	0.87	1.00	0.91
$3 < m_{\pi^+\pi^-}$ GeV/$c^2 < 4$	0.19	0.19	0.28	0.16
$0.483 < m_{K^0_S} < 0.513$ GeV/c^2	0.69	0.68	0.97	0.68
$\lvert\cos\theta_{thr}\rvert < 0.9$	0.36	0.34	0.88	0.83
K^0_S Lifetime significance > 5.0	0.42	0.41	0.96	0.51
$\cos\theta_{K^0_S} > 0.999$	0.73	0.71	0.98	0.58
Charm veto	0.10	0.08	0.38	0.31
$\lvert\Delta E\rvert < 0.1$ GeV	0.27	0.37	0.97	0.61

Table 5.2: $B^0 \to K^0_S\pi^+\pi^-$ nonresonant efficiencies. True-B refers to a set of particles that make up a candidate and have the same B meson parent particle. Cross-feed (CF) accounts for 2.0% of the final data sample.

The region chosen was $3.0 < m_{\pi^+\pi^-} < 4.0\,\mathrm{GeV}/c^2$. The efficiencies for the cuts can be seen in Table 5.2. The toy test, NLL test and fit bias (embedded) test results are shown in Figure 5.10 and show no significant pulls or biases. The model used in these tests and in the final fit to data was:

- Signal - 25 events
- Background - 1000 events
- B background:
  - $J/\psi K^0_s$ - 95 events
  - $\psi(2S)K^0_s$ - 6 events.

5.2.1 Result

The fit yields:

$$\text{Signal Events} \quad 24.4 \pm 7.9 \tag{5.6}$$

$$\text{Background Events} \quad 1154.4 \pm 35.2 \tag{5.7}$$

The fits to data are shown in Figure 5.11, and the corresponding ${}_s\mathcal{P}lots$ in Figure 5.12.

The ${}_s\mathcal{W}eight$ method [49] was used to calculate the branching fraction due to the large area of the Dalitz plot which was used for this analysis. The branching fraction was:

$$\mathcal{B}(B^0 \to K^0_S\pi^+\pi^-\text{nonresonant}) = (1.42 \pm 0.5) \times 10^{-6}. \tag{5.8}$$

where the error is statistical only. The statistical significance (discussed in Section 4.1) was calculated to be 4σ, and since a 5σ statistical and systematic significance is required for discovery by the *BABAR* Experiment, a new upper limit must

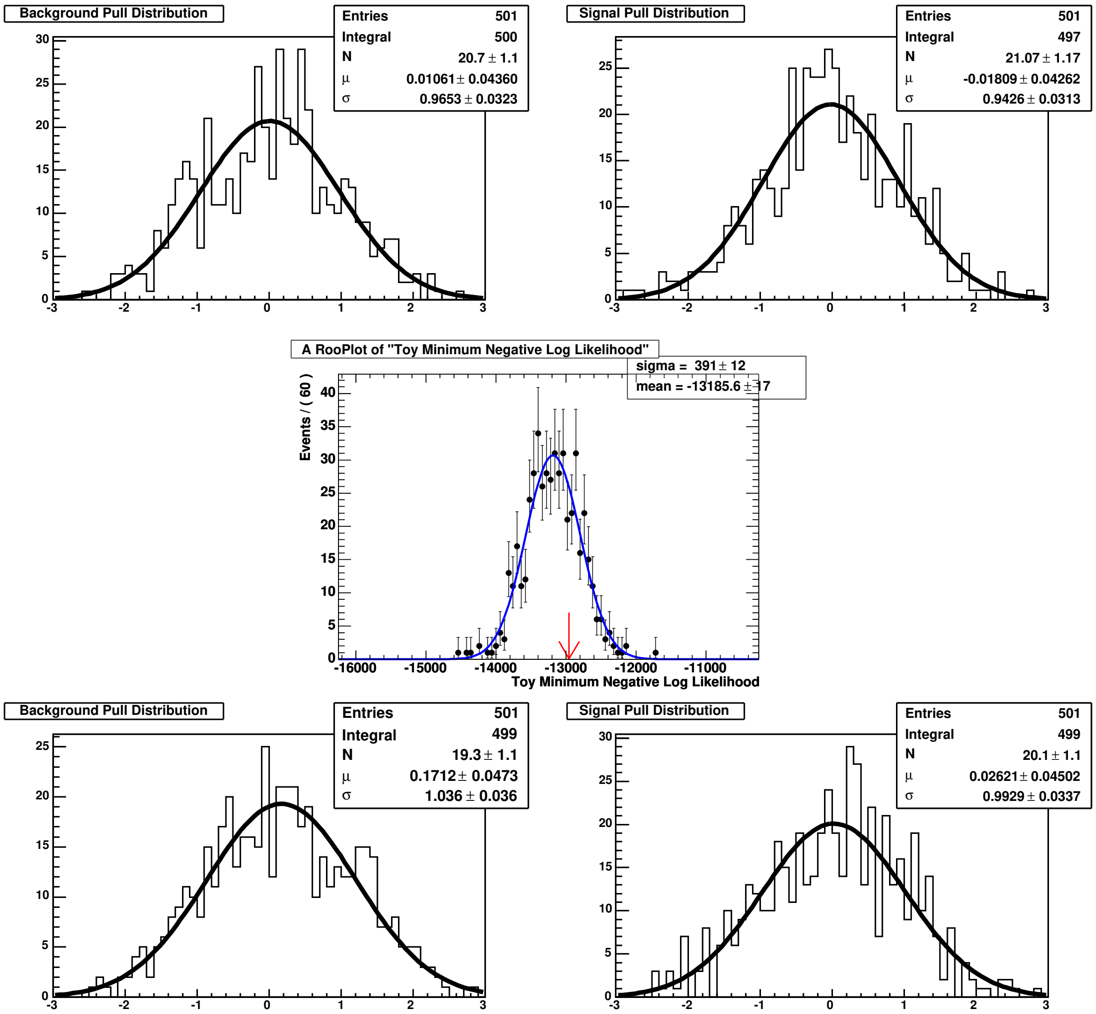

Figure 5.10: The fit tests for the analysis of the nonresonant $B^0 \to K^0_S\pi^+\pi^-$ branching fraction. The top figure shows the results of the toy test which shows no significant pulls for 500 experiments. Middle is the result of the negative log likelihood test where the data result is consistent with the toy distribution. The bottom figure shows the results of the embedded fit test where no significant pull is seen for 500 experiments.

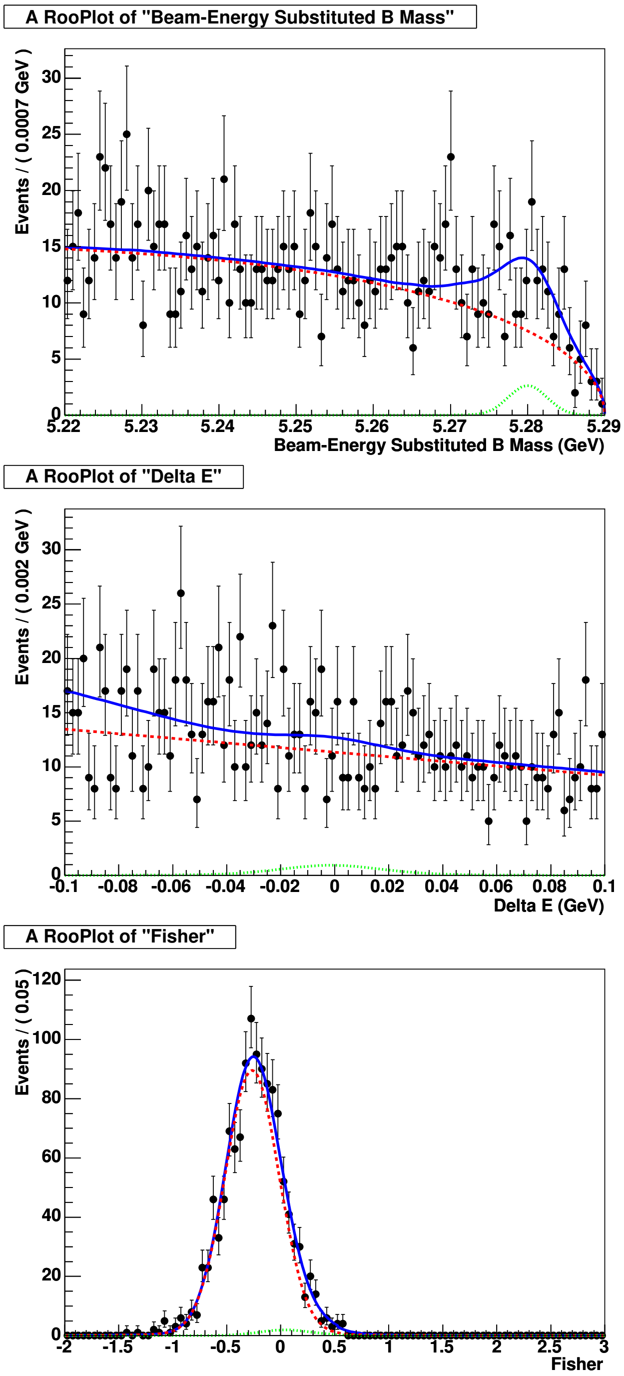

Figure 5.11: The fits to data for the nonresonant result. In all cases, the total PDF is shown solid blue, the continuum PDF in dashed red and the signal PDF in dotted green. The top figure shows the fit to the m_{ES} distribution, the middle shows the fit to ΔE and the bottom shows the fit to the Fisher.

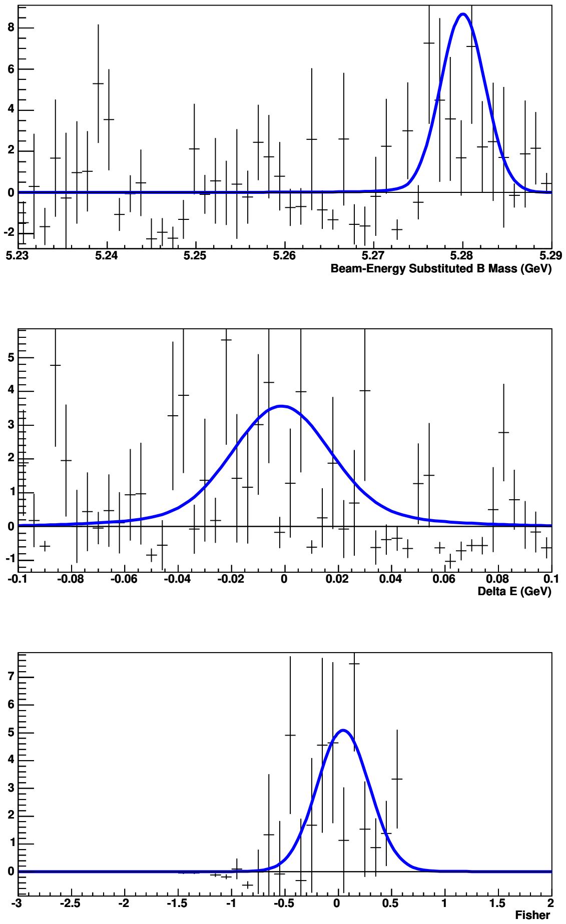

Figure 5.12: The ${}_s$Plots for the nonresonant branching fraction measurement. These plots (top: m_{ES}, middle: ΔE, bottom: Fisher) show the signal distribution in the three variables in the ML fit. The blue line shows the signal PDF that was fitted to the on-resonance data. The ${}_s$Plot method is described fully in Appendix A.

be set. The systematic error for this mode (discussed in Chapter 6) was found to be 0.1×10^{-6}, which gave a total significance of 2.8σ. Therefore the branching fraction

$$\mathcal{B}(B^0 \to K^0_S \pi^+ \pi^-) = (1.42 \pm 0.5 \pm 0.1) \times 10^{-6}. \tag{5.9}$$

led to the upper limit

$$\mathcal{UL}(B^0 \to K^0_S \pi^+ \pi^-) = 2.1 \times 10^{-6}. \tag{5.10}$$

at the 90% confidence level.

5.3 Measuring the total Branching Fraction of the heavier $B^0 \to K^{*+}\pi^-$ states

In order to correctly model the amount of higher $K^{*\pm}\pi^{\mp}$ that act as a B background for the other resonance modes, it is necessary to find their branching fractions. The four resonance states which populate the region are $K^*(1410)$, $K^*_0(1430)$, $K^*_2(1430)$ and $K^*(1680)$. These will collectively be known as K^{**} for the purposes of this thesis. Since they all have similar masses they are very difficult to separate in the kind of analysis conducted here, and a Dalitz analysis is necessary to separate the different spin states. Therefore, for this analysis, a simple measurement of the total rate for all four modes is performed, without considering any interference.

The region $1.09 < m_{K^0_S\pi} < 1.6$ was selected, and all other known resonance modes (D, $J\psi$, $\psi(2S)$, χ_{0c}, f_0, ρ^0, and $K^*(892)$) were vetoed from the region. Any other B backgrounds were modelled as part of the fit. The efficiency changes due to cuts are shown in Table 5.3. The final model for the $B^0 \to K^{**\pm}\pi^{\mp}$ fit tests was:

- Signal Events - 300
- Background Events - 15000

Cut	On-res	Off-res	MC (True-B)	MC (CF + True-B)
Reconstruction and Preselection			0.72	
Tracks 1 and 2 fail `notApion SMSKaonSelector`	0.40	0.40	0.69	0.69
Tracks 1 and 2 fail (LHESelector)	0.95	0.95	1.00	1.00
π's have opposite charge	1.00	1.00	1.00	1.00
$5.22 < m_{ES} < 5.29$ GeV/c^2	0.71	0.71	0.99	0.86
$-0.3 < \Delta E < 0.3$	0.87	0.87	1.00	0.93
$1.01 < m_{K^0_S\pi^\pm} < 1.60$ GeV/c^2	0.34	0.34	0.79	0.65
$0.483 < m_{K^0_S} < 0.513$ GeV/c^2	0.69	0.69	0.97	0.82
$\lvert\cos\theta_{thr}\rvert < 0.9$	0.37	0.35	0.87	0.87
K^0_S Lifetime significance > 5.0	0.41	0.41	0.94	0.73
$\cos\theta_{K^0_S} > 0.999$	0.70	0.70	0.97	0.80
Charm veto	0.62	0.62	0.72	0.44
$\lvert\Delta E\rvert < 0.1$ GeV	0.32	0.33	0.97	0.44

Table 5.3: The efficiencies were assessed using $K_0^{*\pm}(1430)\pi^\mp$ MC. This MC was chosen as it is expected to be the dominant decay mode in this region. Cross-feed (CF) is found to be at the 6.3% level in the final data sample.

- $\eta' K^0_S, \eta' \to \rho^0\gamma$ - 3 events
- $D^\mp\pi^\pm, D^\mp \to K^0_S\pi^\mp$ - 49 events
- $K^0_S\pi^+\pi^-$ nonresonant - 15 events
- $K^{*\pm}\pi^\mp$ - 10 events
- $f_0 K^0_S$ - 5 events
- $\rho^0 K^0_S$ - 6 events.

The number of signal events used was the sum of the expected signal of each type of $B^0 \to K^{**\pm}\pi^{\mp}$. The results of the fit tests can be seen in Figure 5.13.

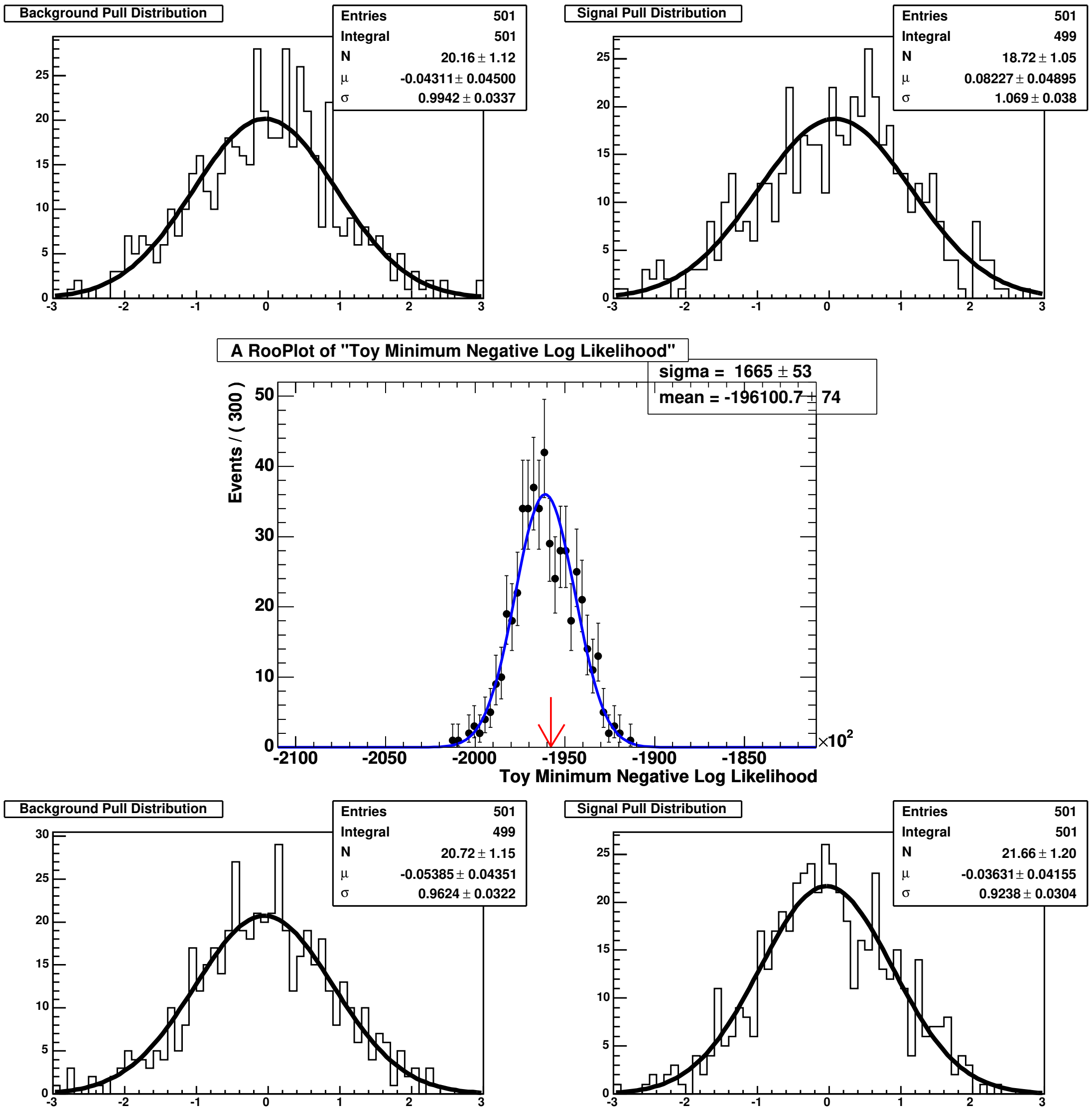

Figure 5.13: The fit tests for the $K^{**\pm}\pi^{\mp}$. Each test consisted of 500 experiments. The plot at the top is the toy test which shows no pulls. The middle plot is the NLL test where the data NLL value (red arrow) agrees well with the toy distribution (black points and the blue Gaussian distribution). At the bottom is the embedded MC fit test which also shows no bias in the fit.

The final model that was fitted to data floated the number of signal and background events, the Argus parameter c and the slope of the polynomial which describes the ΔE continuum background. The fit also included the following numbers of B background events:

- $\eta' K_S^0, \eta' \to \rho^0 \gamma$ - 2.9 events,
- $D^{\mp}\pi^{\pm}, D^{\mp} \to K_S^0 \pi^{\mp}$ - 48.9 events,
- $K_S^0 \pi^+ \pi^-$ nonresonant - 14.7 events,
- $K^{*\pm}\pi^{\mp}$ - 10.5 events,
- $f_0 K_S^0$ - 5.1 events,
- $\rho^0 K_S^0$ - 6.0 events.

The shift between the signal PDFs taken from MC and on-resonance data in the $B^0 \to D^{\mp}\pi^{\pm}$ calibration channel was also implemented in the fit.

5.3.1 Results

The yield fit for $B^0 \to K^{**\pm}\pi^{\mp}, K^{**\pm} \to K_S^0\pi^{\pm}$ uses the same model as the fit tests but with the number of signal and continuum (background) events floated. The result was:

$$\text{Signal Events} \quad 226.2 \pm 23.3 \tag{5.11}$$

$$\text{Background Events} \quad 15135 \pm 123.6 \tag{5.12}$$

and the fit plots and ${}_sPlots$ are shown in Figures 5.14 and 5.15 respectively. Since the area selected within the Dalitz plot is quite large, the ${}_sPlot$ technique is again used to calculate the branching fraction:

$$\mathcal{B}(B^0 \to K^{**\pm}\pi^{\mp}, K^{**\pm} \to K_S^0\pi^{\pm}, K_S^0 \to \pi^+\pi^-) = 8.4 \pm 0.9 \times 10^{-6} \tag{5.13}$$

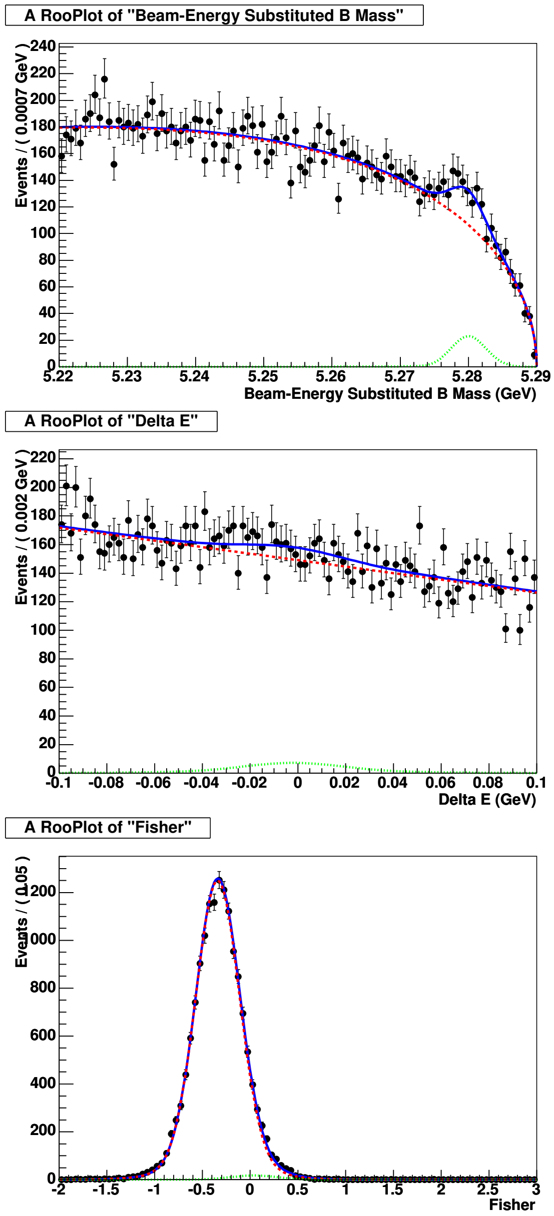

Figure 5.14: The figure shows the final fits to data for the $B^0 \rightarrow K^{**\pm}\pi^{\mp}$ decay channel. The total fit is shown as the solid blue line, the continuum fit is shown as the red dashed line and the green dotted line is the signal PDF. The top plot is m_{ES}, the middle plot is ΔE and the bottom plot is for the Fisher variable.

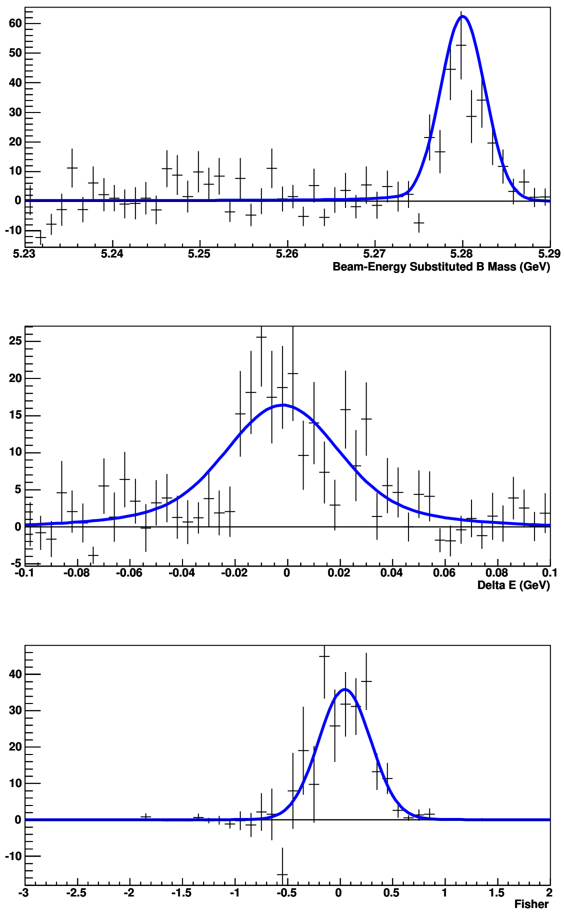

Figure 5.15: The signal-only plots for $B^0 \to K^{**\pm}\pi^{\mp}$. *The data points show the signal-only distribution and are overlaid with the solid blue line which shows the PDF which was fitted in the initial fit to data. Each variable is removed from the fit in order to show the distribution of events for that variable e.g. for the* m_{ES} *plot, the fit to data is reperformed without the* m_{ES} *PDFs being included in the ML fit. The top plot shows the* m_{ES} *distribution, the middle show the* ΔE *distribution and the bottom plot shows the distribution of the Fisher.*

which gives a total branching fraction:

$$\mathcal{B}(B^0 \to K^{**\pm}\pi^{\mp}, K^{**\pm} \to K^0\pi^{\pm}) = (24.4 \pm 2.6) \times 10^{-6} \tag{5.14}$$

where the error is statistical only.

5.3.2 The Lineshape of $K^{**\pm}$

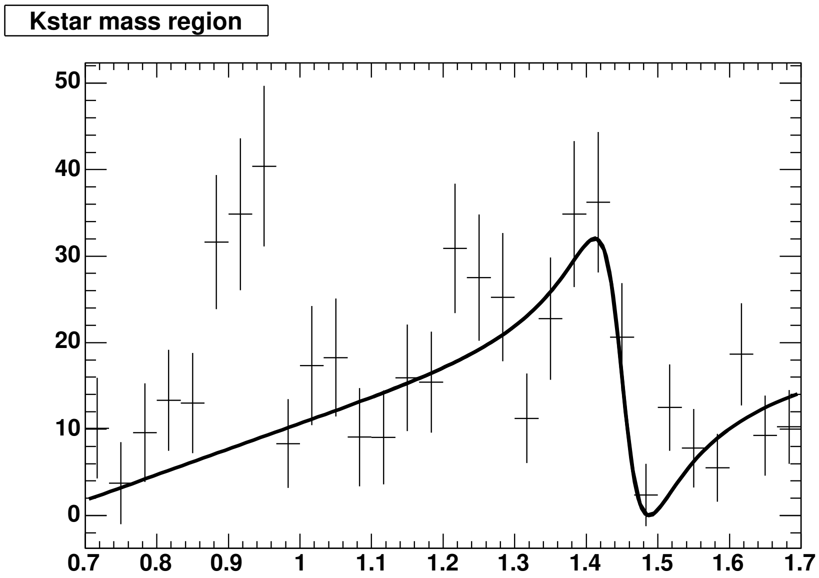

Figure 5.16: The LASS parameterisation of the scalar contribution to the $K^0_S\pi$ spectrum. The fit was performed in the range 1.1 $< m_{K^0_S\pi} <$ 1.6 GeV/c^2, with the mass of the $K_0^{*\pm}(1430)$ fixed and the other parameters floated in the fit. The fit was then extrapolated into the $K^{*\pm}(892)$ region, which estimates 40.7 events would contaminate the $B^0 \to K^{*+}\pi^-$ signal. Interference between these modes is discussed in Section 5.6.2.

In most cases, resonances can be described by a relativistic Breit-Wigner lineshape [55], but the scalar component of the $K^0_S\pi^{\pm}$ spectrum is poorly understood. The $K_0^{*\pm}(1430)$ is a known scalar resonant contribution but there may also be an "effective range" nonresonant component [56, 57], where the strength of the attractive potential between the two mesons is not strong enough to cause a resonance to form [58]. $K\pi$ scattering at the LASS experiment produced a description of this combination of contributions. Their parameterisation for a production environment is

$$\mathcal{M} = \frac{m_{K\pi}}{q\cot\delta_B - iq} + e^{2i\delta_B}\frac{m_0\Gamma_0\frac{m_0}{q_0}}{(m_0^2 - m_{K\pi}^2) - im_0\Gamma_0\frac{q}{m_{K\pi}}\frac{m_0}{q_0}} \tag{5.15}$$

where m_0 and Γ_0 are the mass and width of the $K^{*\pm}(1430)$ resonance respectively, q is the momentum of either of the resonance daughters in the rest frame of the resonance, q_0 is the value of q when $\sqrt{s} = m_0$, and $\cot\delta_B$ is defined by

$$\cot\delta_B = \frac{1}{aq} + \frac{1}{2}rq. \tag{5.16}$$

Here, a is the scattering length and r is the effective range.

The LASS parameterisation has been used to describe the scalar component in [21, 59]. Figure 5.16 shows the fit to the combined $K_S^0\pi^+$ and $K_S^0\pi^-$ spectra in the region $1.1 < m_{K_S^0\pi} < 1.7$, and extended into the $K^{*\pm}(892)$ region with only the $K_0^{*\pm}(1430)$ resonance mass fixed. The parameterisation seems to be a reasonable model for the distribution of data in the fit region for the current statistics. However, this parameterisation of the data changes the amount of $K^{**\pm}$ expected in the $K^{*\pm}(892)$ region. Integrating under the fit in the $K^{*\pm}(892)$ selection region showed 40.7 scalar events should be considered as background to the $B^0 \to K^{*+}\pi^-$ branching fraction measurement. Using the branching fraction measured above for $B^0 \to K^{**\pm}\pi^\mp$, which assumed a relativistic Breit-Wigner lineshape, 22.9 events were considered to be B background to the $B^0 \to K^{*+}\pi^-$ measurement. The change in the BF measurement due to the difference in these two estimates was taken as a systematic on the measurement. Interference between the $K^{*\pm}(892)\pi^\mp$ and the higher $K^{*\pm}\pi^\mp$ resonances is discussed in Section 5.6.2.

5.4 $B^0 \to \rho^0 K^0_S$

Until recently, no evidence had been found for $B^0 \to \rho^0 K^0_S$ and the upper limits were placed on the measurement. *BABAR* has recently presented evidence for $B^0 \to \rho^0 K^0_S$ at the 3.5σ level with a measurement of $(5.1 \pm 1.0 \pm 1.2) \times 10^{-6}$ using $227{\times}10^6$ million $\Upsilon(4S) \to B\overline{B}$ decays [20]. A time-dependent measurement of this mode is also expected to provide a measurement of $\sin 2\beta$ when statistics allow. In this thesis, the analysis of $B^0 \to \rho^0 K^0_S$ is independent of the published result.

This analysis was adapted from the inclusive analysis by selecting the region of the Dalitz plane which was consistent with the ρ^0 in $m_{\pi^+\pi^-}$. For all the following modes, a Gaussian was fitted to the mass of the resonance in the signal MC, which yielded a mean mass and the σ associated with the width of the resonance. The selection band was taken to be 3σ either side of the mean of that distribution. However, in this case an asymmetric band of $0.341 < m_{\pi^+\pi^-}(\mathrm{GeV}/c^2) < 0.816$ was selected because of the need to veto any contributions from the $B^0 \to f_0 K^0_S$. The $K^0_S\pi$ resonances ($K^{*\pm}(892)$, $K^{**\pm}$ and $D^{\mp}\pi^{\pm}$) were also vetoed in the fit. In addition, a helicity cut was implemented to try to remove some background events from the region which the vector ρ does not populate. This improved the signal-to-background ratio which is particularly low for this mode. The cut implemented was $|\cos\theta_{hel}| > 0.25$. Table 5.4 shows the final selection criteria and the efficiencies for the data and MC samples.

The methods used for the fit tests were as previously described and the model used was:

- Signal - 85 events
- Background - 15,000 events
- B background:

Cut	On-res	Off-res	MC (True-B)	MC (CF)
Reconstruction and Preselection			0.69	
Tracks 1 and 2 fail `notApion SMSKaonSelector`	0.40	0.40	0.77	0.73
Tracks 1 and 2 fail electron selector (LHESelector)	0.95	0.95	1.00	1.00
π's have opposite charge	1.00	1.00	1.00	1.00
5.22 $< m_{ES} <$ 5.29 GeV/c^2	0.71	0.71	0.99	0.91
-0.3 $< \Delta E <$ 0.3	0.87	0.87	0.99	0.94
0.879 $< m_{\pi^+\pi^-} <$ 1.069 GeV/c^2	0.23	0.23	0.70	0.30
abs($\cos\theta_{hel}$) $>$ 0.25	0.76	0.76	0.98	0.98
0.483 $< m_{K^0_S} <$ 0.513 GeV/c^2	0.70	0.70	0.98	0.94
$\lvert\cos\theta_{thr}\rvert <$ 0.9	0.34	0.34	0.87	0.82
K^0_S Lifetime significance $>$ 5.0	0.48	0.48	0.97	0.95
$\cos\theta_{K^0_S} >$ 0.999	0.86	0.86	1.00	0.97
Charm veto	0.95	0.96	0.87	0.71
$\lvert\Delta E\rvert <$ 0.1 GeV	0.33	0.32	0.98	0.50

Table 5.4: Efficiency of cuts for $B^0 \to \rho^0 K^0_S$. True-B refers to a set of particles that make up a candidate and have the same B meson parent particle. Cross-feed (CF) represents 10.4% of the final MC sample.

– $B^0 \to \eta' K^0_S, \eta' \to \rho^0\gamma$ - 16 events

– $B^0 \to D^{\mp}\pi^{\pm}, D^{\mp} \to K^0_S\pi^{\mp}$ - 21 events

– $B^0 \to K^{*\pm}\pi^{\mp}, K^{*\pm} \to K^0_S\pi^{\pm}$ - 5 events

– $B^0 \to K^0_S\pi^+\pi^-$ nonresonant - 5 events

– $B^0 \to f_0 K^0_S, f_0 \to \pi^+\pi^-$ - 10 events

– $B^0 \to K^{**\pm}\pi^\mp, K^{**\pm} \to K^0_S\pi^\pm$ - 35 events

The results of the tests can be seen in Figure 5.17, and the pull that is seen on the result of the embedded fit is taken as a systematic (Section 6.1.4).

The final model floated the number of signal and background events, as well as the Argus parameter, c, and the slope of the polynomial which is used to describe the ΔE continuum background. The shifts seen between data and MC in the $B^0 \to D^\mp\pi^\pm$ calibration channel was used to shift the signal PDF parameters in the fit. The amounts of B background that were included in the fit were:

- $B^0 \to \eta' K^0_S, \eta' \to \rho^0\gamma$ - 16.2 events
- $B^0 \to D^\mp\pi^\pm, D^\mp \to K^0_S\pi^\mp$ - 21.0 events
- $B^0 \to K^{*\pm}\pi^\mp, K^{*\pm} \to K^0_S\pi^\pm$ - 5.4 events
- $B^0 \to K^0_S\pi^+\pi^-$ nonresonant - 6.0 events
- $B^0 \to f_0 K^0_S, f_0 \to \pi^+\pi^-$ - 10.2 events
- $B^0 \to K^{**\pm}\pi^\mp, K^{**\pm} \to K^0_S\pi^\pm$ - 35.2 events

5.4.1 Results

The final fit gave:

$$\text{Signal Events} \quad 66.6 \pm 17.2 \tag{5.17}$$

$$\text{Background Events} \quad 16482 \pm 129 \tag{5.18}$$

and the plots can be seen in Figure 5.18. The ${}_sPlots$ are shown in Figure 5.19 but the repeated fits to data, which remove m_{ES}, ΔE and Fisher in turn (see Appendix A), produced wildly different results when one of the PDFs was removed from the model.

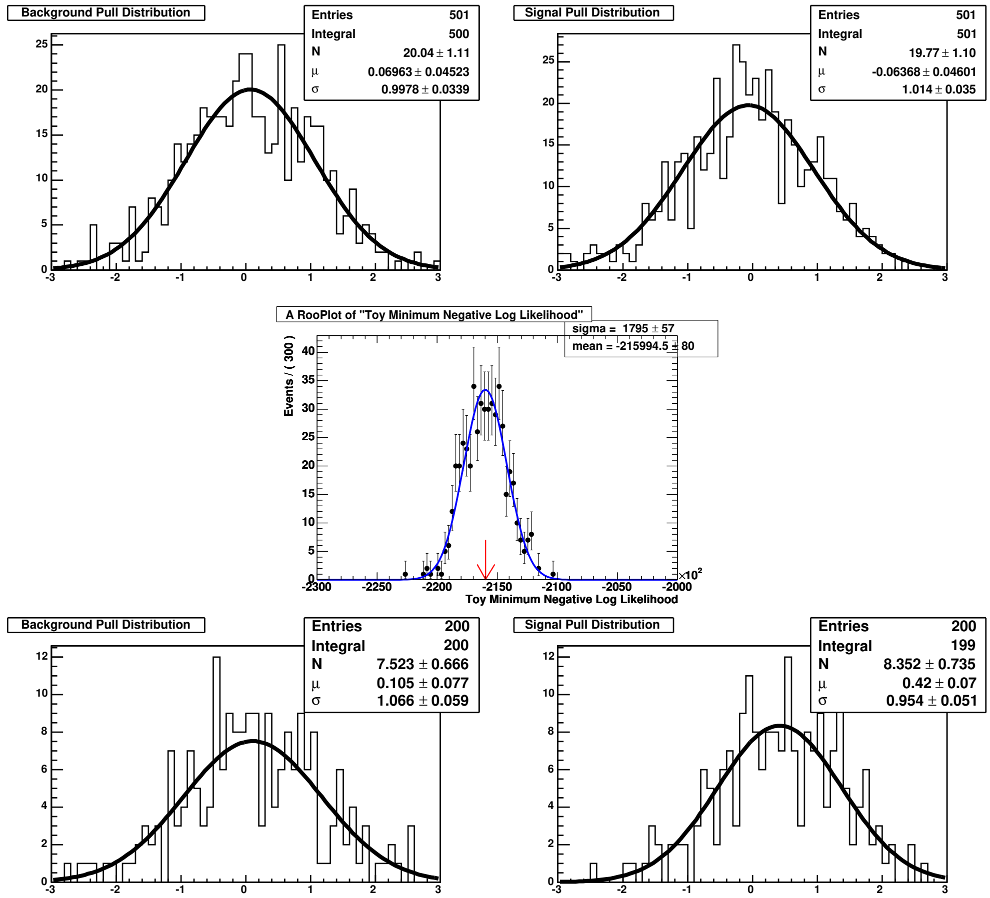

Figure 5.17: The fit tests for $B^0 \to \rho^0 K^0_S$. Top is the toy test which used the full model to run 500 experiments. The number of toy events generated was Poissonally distributed about the input for each type of event. The Argus parameter and the slope of the continuum background ΔE PDF were floated. No significant pulls are seen. The middle plot shows the outcome of the NLL test were the value of the NLL for the fit to data is in very good agreement with the distribution of the 500 toy experiments. Bottom is the result of the embedded fit tests which used the full model and again floated the Argus parameter and the slope of the ΔE continuum background PDF. The pull on the number of signal events of 0.42σ was evaluated and included as a systematic in the final result.

The most severe case was when the $m_{\rm ES}$ PDFs were left out of the fit, and -22.1 signal events were found, hence why the signal ${}_sPlot$ looks so poor. The fit to produce the Fisher ${}_sPlot$ doubles the amount of signal found (in comparison to the original fit), thereby also having a poor ${}_sPlot$. The reason for these difficulties in this case was the extremely small signal-to-background ratio, which increases the difficulty of finding a consistent result with fewer PDFs in the ML fit. Figure 5.20 shows the ratio of signal likelihood to total likelihood for both the data fit and a toy fit which uses the data results values as its input.

The efficiency for this mode was estimated to be 20.5% (Table 5.4), and using Equation 4.9, the result is:

$$\mathcal{B}(B^0 \to \rho^0 K^0) = (4.0 \pm 1.0) \times 10^{-6} \tag{5.19}$$

which is consistent, within errors, with the previous result of $(5.1 \pm 1.0 \pm 1.2) \times 10^{-6}$.

5.5 $B^0 \to f_0 K^0_S$

The mode $B^0 \to f_0 K^0_S$ is interesting since a time-dependent measurement can yield $\sin(2\beta)$. This analysis has recently been conducted at *BABAR* [60] [26] and the first iteration included a branching fraction measurement. The measured value from 123×10^6 $\Upsilon(4S) \to B\overline{B}$ decays was $\mathcal{B}(B^0 \to f_0(980)K^0, f_0(980) \to \pi^+\pi^-) = (6.0 \pm 0.9 \pm 0.6) \times 10^{-6}$. This is the only published branching fraction measurement for this mode [61].

The analysis here builds on the inclusive analysis by adding criteria to select the $f_0(980)$ resonance from the Dalitz plane. A cut 3σ about the central mass value was applied, which equated to $0.879 < m_{\pi^+\pi^-}(\,\mathrm{GeV}/c^2) < 1.069$. The efficiencies of each cut can be seen in Table 5.5, where each percentage efficiency is relative to the one above it.

For this mode, the model used for fit testing was:

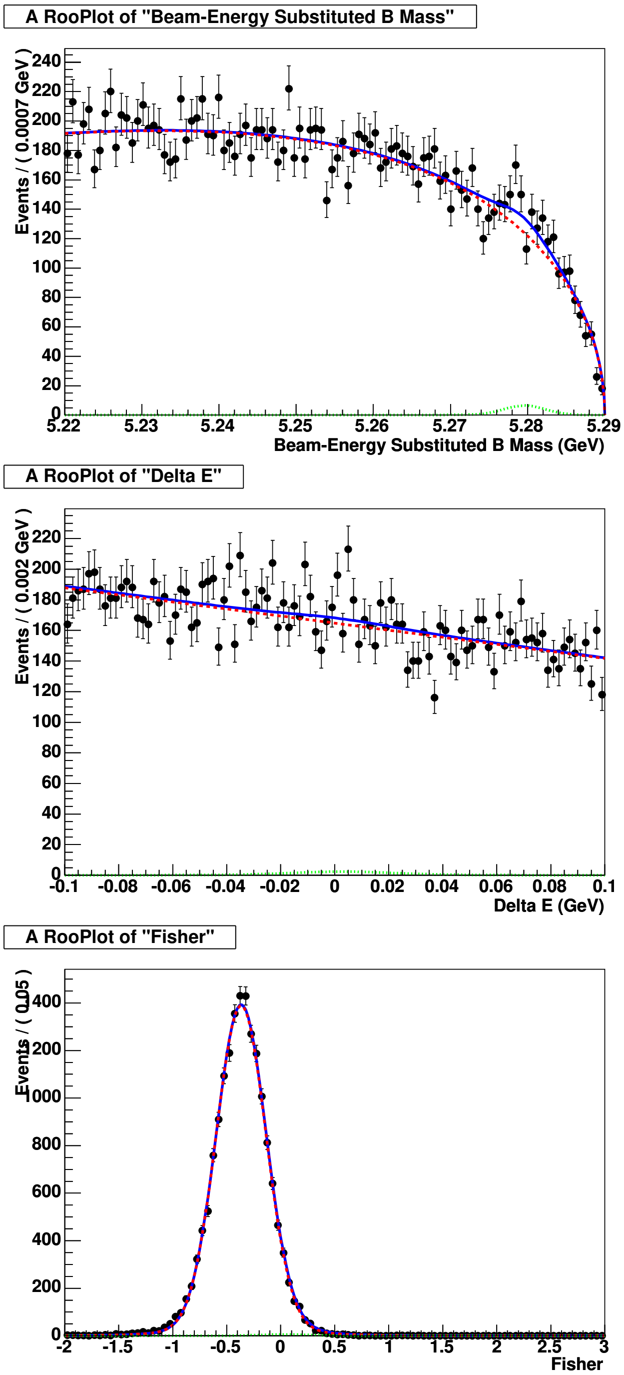

Figure 5.18: The fit to data for $B^0 \to \rho^0 K_S^0$ using the complete model. The blue solid lines represent the total PDFs, the red dashed lines represent the continuum background PDFs and the green dotted lines represent the signal PDFs. The m_{ES} fit is shown at the top, the ΔE fit is shown in the middle, and the Fisher fit is shown at the bottom.

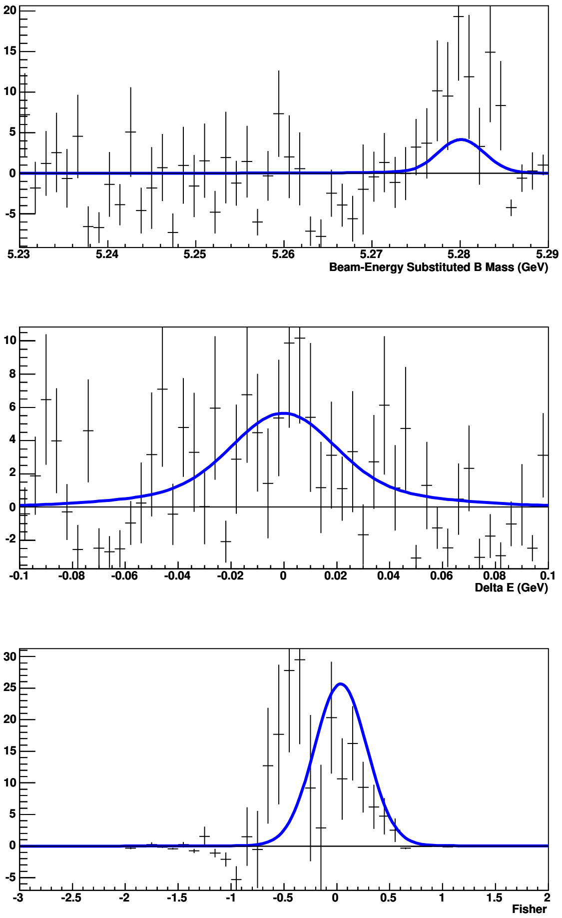

Figure 5.19: The ${}_s$Plots of the fit variables for the fit to $B^0 \to \rho^0 K^0_S$. The points show the signal distribution in each case, and the blue solid line shows the PDF which was fitted to that variable in the initial fit to data. When each plot was made, the variable shown in that plot was removed from the fit. These comparisons are fairly poor because of the extremely low signal-to-background ratio for this mode. This caused the fit results to vary widely when one variable is removed from the fit.

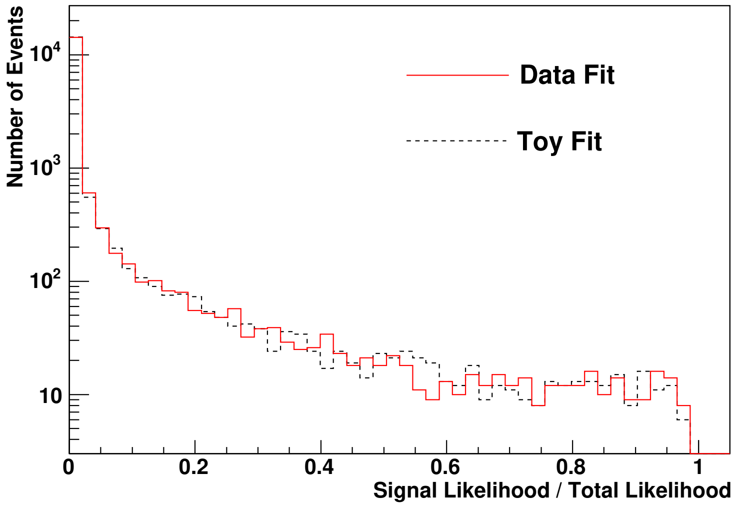

Figure 5.20: The ratio of signal likelihood to total likelihood for the fit to $B^0 \to \rho^0 K^0_S$ data is shown as the solid red line. Using the results of the fit to data, a toy MC experiment is generated and the ratio of signal likelihood to total likelihood for this fit is shown as a dashed black line. The histograms of the two fits compare well.

- Signal - 139 events
- Background - 7000 events
- B background:
  - $\eta' K^0_S, \eta' \to \rho^0 \gamma$ - 19 events
  - $D^{\mp}\pi^{\pm}, D^{\mp} \to K^0_S \pi^{\mp}$ - 13 events
  - $K^{*\pm}\pi^{\mp}, K^{*\pm} \to K^0_S \pi^{\pm}$ - 5 events
  - $K^0_S \pi^+ \pi^-$ nonresonant - 4 events
  - $\rho^0 K^0_S$ - 14 events
  - $K^{**\pm}\pi^{\mp}, K^{**\pm} \to K^0_S \pi^{\pm}$ - 31 events

The results are shown in Figure 5.21. The pull from the embedded fit is included as a systematic on this measurement.

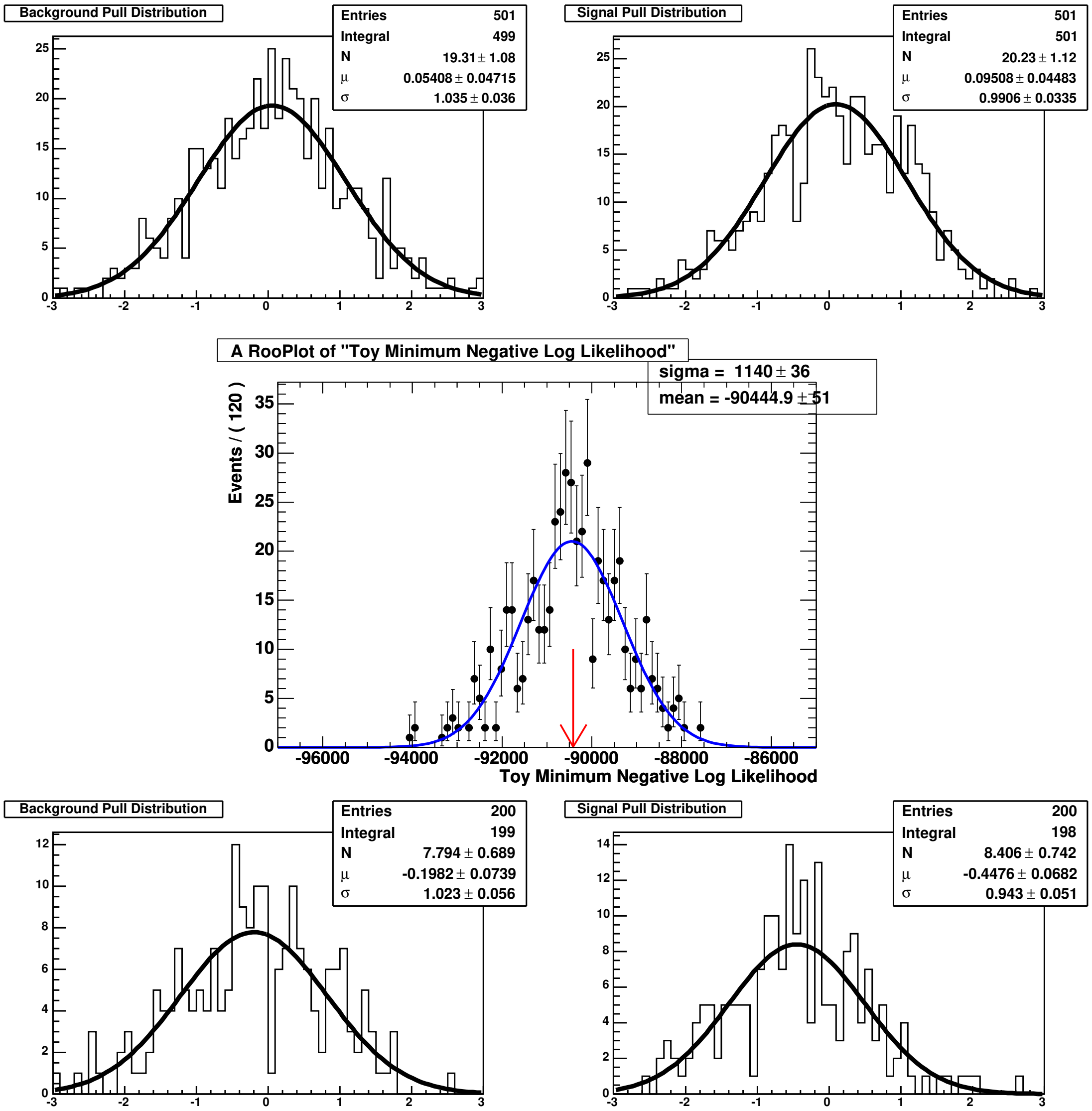

Figure 5.21: The results of the fit tests for $B^0 \to f_0 K^0_S$. The top plots show the pulls on the number of signal and background events using the full model, which also floats the Argus parameter and the slope of the continuum background. The middle plot shows good agreement between the data NLL and the toy NLL distribution. The bottom plot shows a -0.44σ pull on the signal fit and this was included as a systematic. Each tests consisted of 500 experiments.

Cut	On-res	Off-res	MC (True-B)	MC (CF)
Reconstruction and Preselection			0.70	
Tracks 1 and 2 fail `notApion SMSKaonSelector`	0.40	0.40	0.73	0.70
Tracks 1 and 2 fail electron selector (LHESelector)	0.95	0.95	1.00	1.00
π's have opposite charge	1.00	1.00	1.00	1.00
$5.22 < m_{ES} < 5.29$ GeV/c^2	0.71	0.71	1.00	0.86
$-0.3 < \Delta E < 0.3$	0.87	0.87	1.00	0.92
$0.879 < m_{\pi^+\pi^-} < 1.069$ GeV/c^2	0.08	0.08	0.85	0.23
$0.483 < m_{K^0_S} < 0.513$ GeV/c^2	0.69	0.69	0.98	0.92
$\lvert\cos\theta_{thr}\rvert < 0.9$	0.34	0.33	0.88	0.85
K^0_S Lifetime significance > 5.0	0.46	0.45	0.97	0.92
$\cos\theta_{K^0_S} > 0.999$	0.90	0.90	1.00	0.97
Charm veto	0.95	0.96	0.95	0.71
$\lvert\Delta E\rvert < 0.1$ GeV	0.33	0.33	0.98	0.54

Table 5.5: Efficiency of cuts for $B^0 \rightarrow f_0 K^0_S$. True-B refers to a set of particles that make up a candidate and have the same B meson parent particle. Cross-feed (CF) represents 4.2% of the final MC sample.

In the final fit to data, the signal and continuum background yields were once again floated, along with the Argus parameter, c, and the slope of the continuum background PDF. The final B-background model used was:

- $\eta' K^0_S, \eta' \rightarrow \rho^0\gamma$ - 18.5 events
- $D^{\mp}\pi^{\pm}, D^{\mp} \rightarrow K^0_S\pi^{\mp}$ - 13.4 events

- $K^{*\pm}\pi^{\mp}, K^{*\pm} \rightarrow K^0_S\pi^{\pm}$ - 4.7 events
- $K^0_S\pi^+\pi^-$ nonresonant - 4.2 events
- $\rho^0 K^0_S$ - 13.8 events
- $K^{**\pm}\pi^{\mp}, K^{**\pm} \rightarrow K^0_S\pi^{\pm}$ - 31.4 events

5.5.1 Results

The yields for $B^0 \rightarrow f_0 K^0_S$ were:

$$\text{Signal Events} = 119.6 \pm 16.3 \tag{5.20}$$

$$\text{Background Events} = 7274.3 \pm 86.2 \tag{5.21}$$

and the fit to data can be seen in Figure 5.22. The ${}_sPlots$ are shown in Figure 5.23.

Figure 5.24 shows the ratio of the signal likelihood to the total likelihood for data and for a toy MC experiment generated from the output of the fit to data. The two histograms compare well, which provides further confidence in the accuracy of the fitting procedure.

The MC for $B^0 \rightarrow f_0 K^0_S$ showed that the final efficiency after all selection criteria (see Table 5.5) are imposed was 27.1%. Using Equation 4.9 and knowing the data sample contains 232 million $\Upsilon(4S) \rightarrow B\overline{B}$ decays leads to a branching fraction of:

$$\mathcal{B}(B^0 \rightarrow f_0(980)K^0, f_0(980) \rightarrow \pi^+\pi^-) = (5.5 \pm 0.7) \times 10^{-6} \tag{5.22}$$

where the error is statistical only.

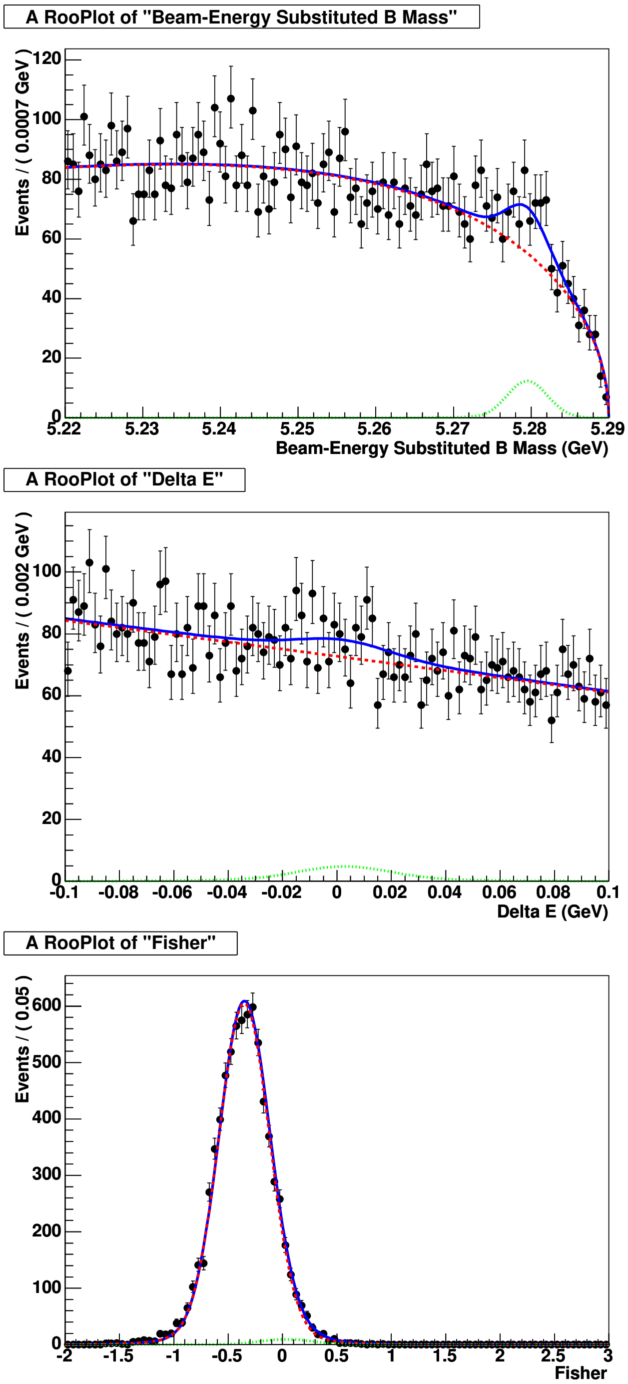

Figure 5.22: The fits to data for the $B^0 \to f_0 K_S^0$ branching fraction result. In all cases, the total PDF is shown solid blue, the continuum PDF in dashed red and the signal PDF in dotted green. The top figure shows the $m_{\rm ES}$ distribution and fit, the middle shows the fit to ΔE and the bottom shows the fit to the Fisher.

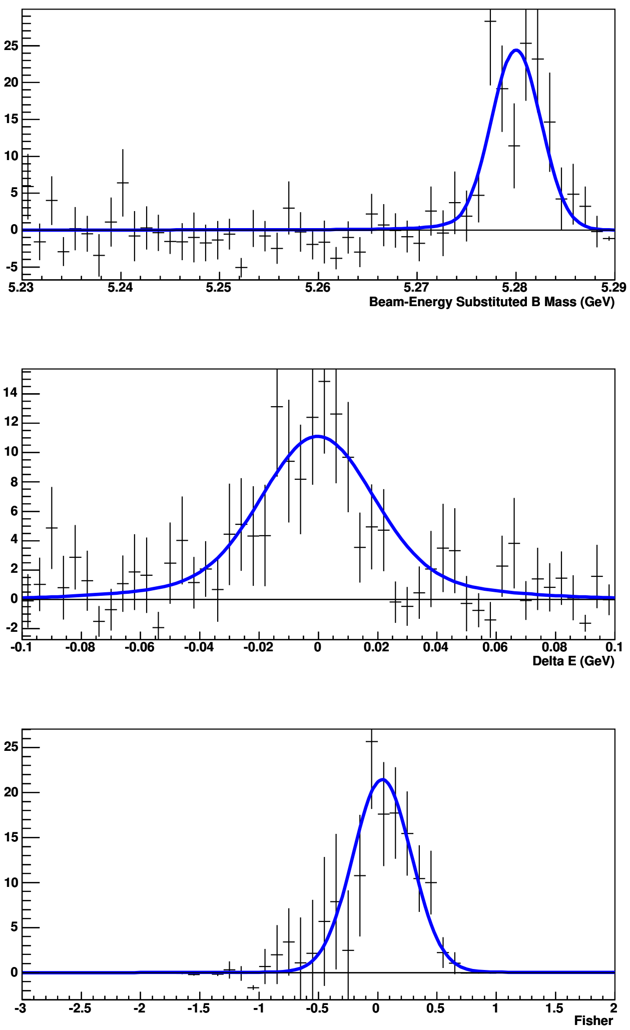

Figure 5.23: The ${}_s$Plots for the $B^0 \to f_0 K_S^0$ branching fraction measurement. These plots show the signal distribution in the three variables in the ML fit. The blue line shows the signal PDF that was fitted to the on-resonance data. The top plot is the m_{ES} distribution, the middle is ΔE and the lowest is Fisher. The ${}_s$Plot method is described fully in Appendix A.

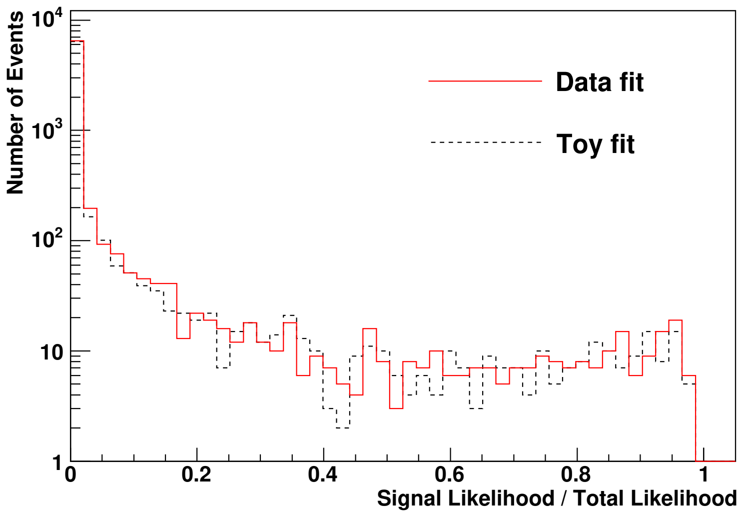

Figure 5.24: The red solid line describes the ratio of signal likelihood to total likelihood for the fit to data for $B^0 \to f_0 K^0_S$. Using the results of the fit to data, a toy MC experiment was generated and the signal likelihood to total likelihood for that is shown as the dashed black line. The two histograms compare well.

5.6 $B^0 \to K^{*+}\pi^-$ Branching Fraction and Asymmetry

As discussed in Section 1.6.1, a charge asymmetry is expected in $B^0 \to K^{*+}\pi^-$. A recent measurement of $B^0 \to K^{*\pm}\pi^\mp$ with the final state $K^\pm\pi^\mp\pi^0$ using 213 $\times 10^6$ $\Upsilon(4S) \to B\overline{B}$ decays found the charge asymmetry to be $-0.25 \pm 0.17 \pm 0.02 \pm 0.02$ [21], where the first uncertainty is statistical, the second is systematic and the third is theoretical. The previous analysis for the $K^0_S\pi^+\pi^-$ final state using 89 $\times 10^6$ $\Upsilon(4S) \to B\overline{B}$ decays found the asymmetry to be $0.23 \pm 0.18^{+0.09}_{-0.06}$ [19]. In both cases, the definition of the charge asymmetry is that which is described in Equation 1.37 and neither show a significant deviation from 0.

Table 5.6 shows the selection criteria and efficiencies for the data and MC samples

Cut	On-res	Off-res	MC (True-B)	MC (CF)
Reconstruction and Preselection			0.71	
Tracks 1 and 2 fail `notApion SMSKaonSelector`	0.40	0.40	0.71	0.71
Tracks 1 and 2 fail electron selector (LHESelector)	0.95	0.95	1.00	1.00
π's have opposite charge	1.00	1.00	1.00	1.00
$5.22 < m_{ES} < 5.29$ GeV/c^2	0.71	0.71	1.00	0.91
-0.3 $< \Delta E <$ 0.3	0.87	0.87	1.00	0.94
$0.776 < m_{K^{*\pm}\pi^{\mp}} < 1.010$ GeV/c^2	0.19	0.19	0.91	0.37
$0.483 < m_{K^0_S} < 0.513$ GeV/c^2	0.69	0.69	0.97	0.78
$\lvert\cos\theta_{thr}\rvert < 0.9$	0.34	0.34	0.87	0.84
K^0_S Lifetime significance > 5.0	0.43	0.42	0.96	0.77
$\cos\theta_{K^0_S} > 0.999$	0.78	0.78	0.98	0.79
Charm veto	0.84	0.85	0.81	0.70
$\lvert\Delta E\rvert < 0.1$ GeV	0.33	0.32	0.97	0.56

Table 5.6: Efficiency of cuts for $B^0 \to K^{*+}\pi^-$. True-B refers to a set of particles that make up a candidate and have the same B meson parent particle. Cross-feed (CF) represents 6.6% of the final MC sample.

used for $B^0 \to K^{*+}\pi^-$. The following model is used for the fit testing stage:

- Signal - 179 events, Asymmetry - -0.25
- Background - 9000 events, Asymmetry - 0
- B background:
  - $D^{\mp}\pi^{\pm}$ - 16 events, Asymmetry - 0

– $K_S^0\pi^+\pi^-$ nonresonant - 6 events, Asymmetry - 0

– $J/\psi K_S^0$ - 6 events, Asymmetry - 0

– $f_0 K_S^0$ - 4 events, Asymmetry - 0

– $\rho^0 K_S^0$ - 5 events, Asymmetry - 0

– $K^{**\pm}\pi^{\mp}$ - 23 events, Asymmetry - 0

The number of signal and background events, the signal and background asymmetries, the Argus parameter, c, and the slope of the continuum background ΔE PDF are all allowed to float in the ML fit. The results of the fit tests, each using 500 experiments, can be seen in Figures 5.25, 5.26 and 5.27.

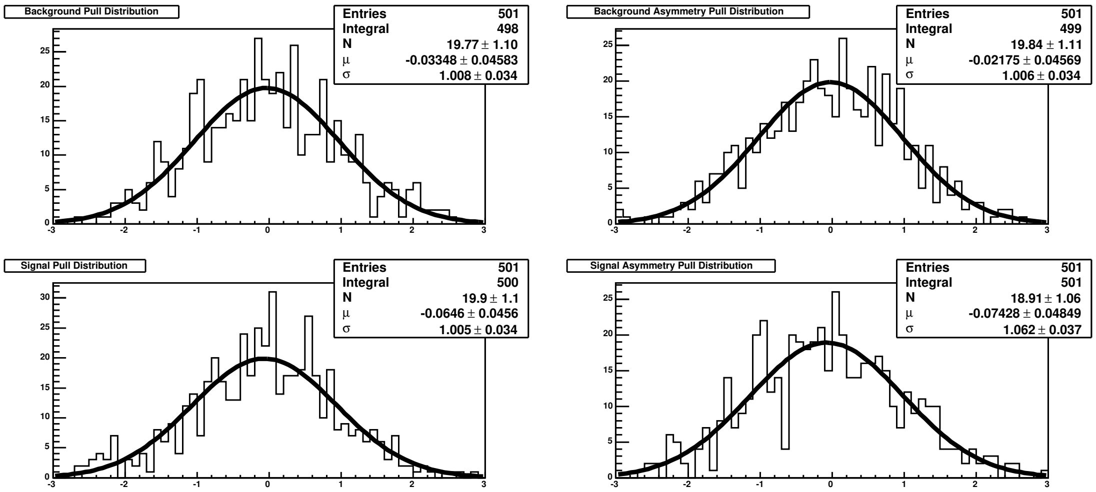

Figure 5.25: Signal and continuum events pull distributions and signal and continuum asymmetry pull distributions for the toy test of $B^0 \to K^{*+}\pi^-$. The pulls are based on 500 toy MC experiments, generated with 179 signal events and 9000 continuum background events in each experiment. The signal is generated with an asymmetry of -0.25, whilst all other backgrounds are generated with no asymmetry.

The final model for the fit to data floated the same parameters as the fit tests. The B-background model used was:

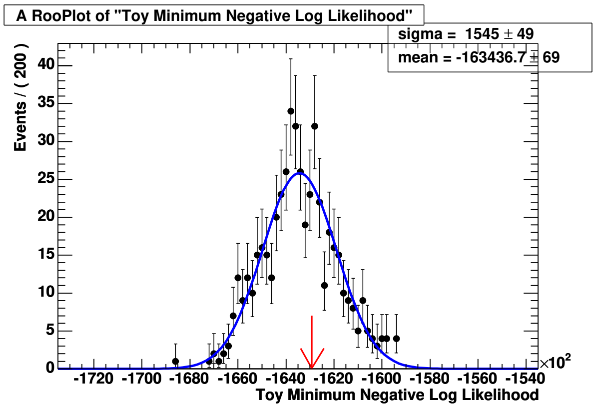

Figure 5.26: After a blind fit to data for $B^0 \to K^{*+}\pi^-$, the number of signal and background events, and the charge asymmetries, are taken as inputs to a toy test of 500 experiments. The NLL value for data is shown as the red arrow and is surrounded by the distribution of the toy experiments (which is fitted with a Gaussian). The two distributions show good agreement.

- $B^0 \to D^{\mp}\pi^{\pm}$ - 16.1 events,
- $B^0 \to K^0_S\pi^+\pi^-$ nonresonant - 6.5 events,
- $B^0 \to J/\psi K^0_S$ - 6.3 events,
- $B^0 \to f_0 K^0_S$ - 4.3 events,
- $B^0 \to \rho^0 K^0_S$ - 5.2 events,
- $B^0 \to K^{**\pm}\pi^{\mp}$ - 22.9 events.

All the B backgrounds are assumed to have a charge asymmetry of zero, but the effect that a non-zero charge asymmetry may have is investigated in the Section 6. A fit to the upper sideband finds -9.78 ± 1.56 signal events with an asymmetry of -1.00 ± 1.38, and 221.8 ± 1.5 background events with an asymmetry of 0.026 ± 0.069. Both asymmetries are consistent with zero, as is expected.

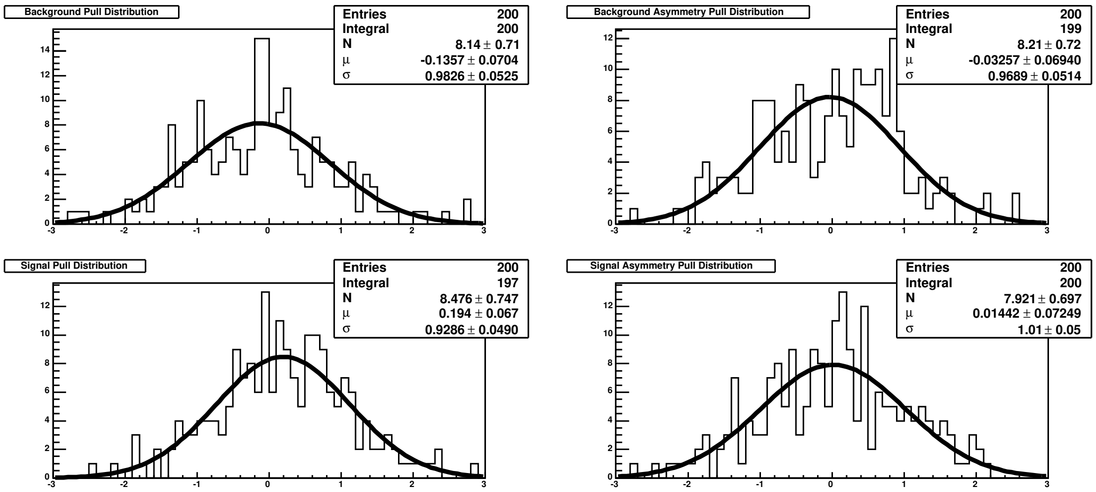

Figure 5.27: The pull distributions of the embedded fit test for the $B^0 \to K^{*+}\pi^-$ ML fit. The top plots show the pull on the number of background events (left) and the pull on the charge asymmetry of the background (right). The bottom plots show the pull on the number of signal events (left) and the pull on the signal charge asymmetry (right). The test uses 200 experiments.

5.6.1 Results

The result of the ML fit to data was:

$$\text{Signal Events} = 139.6 \pm 19.0 \tag{5.23}$$

$$\text{Signal Asymmetry} = -10.7 \pm 13.6 \tag{5.24}$$

$$\text{Background Events} = 12636 \pm 114 \tag{5.25}$$

$$\text{Background Asymmetry} = -0.018 \pm 0.009 \tag{5.26}$$

The signal asymmetry is still consistent with zero, but has changed signs when compared to the last measurement with this final state [19]. The background asymmetry is close to zero, as expected. The fit results can be seen if Figure 5.28, and Figure 5.29 shows the ${}_sPlots$.

The efficiency for $B^0 \to K^{*+}\pi^-$from signal MC is 23.7%, which gives a branching

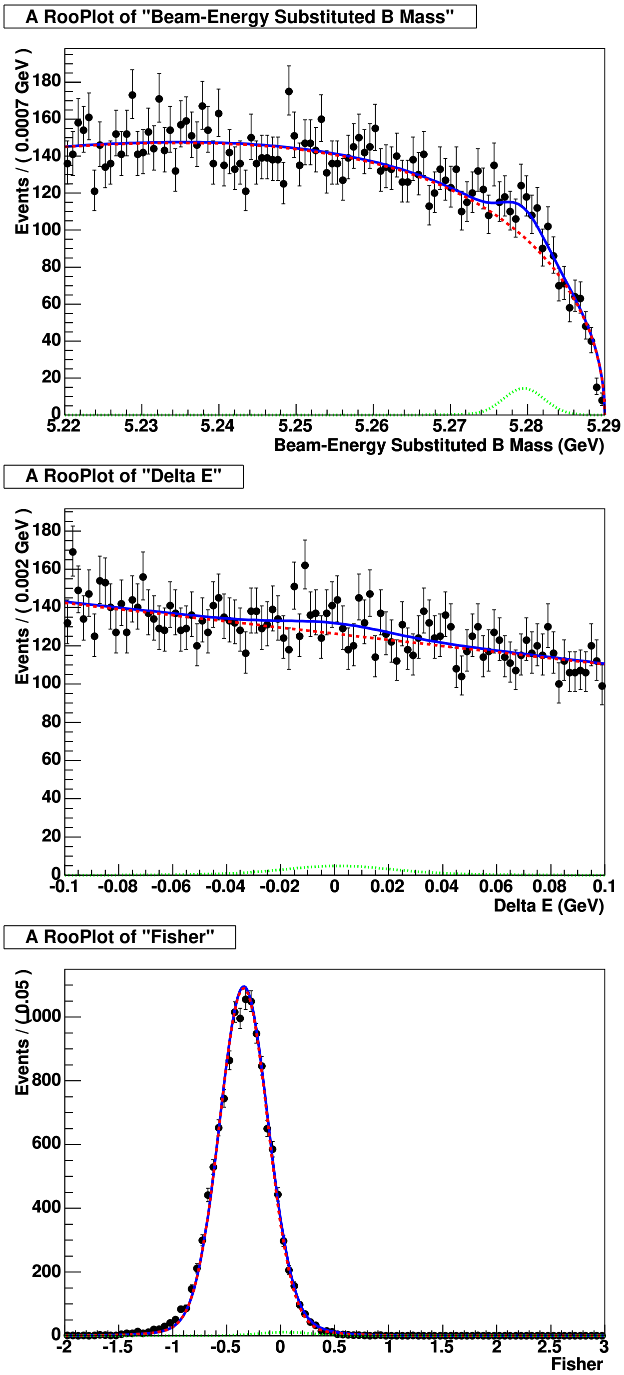

Figure 5.28: The figure shows the fits to data for the $B^0 \to K^{*+}\pi^-$ analysis. The top plot shows $m_{\rm ES}$, the middle shows ΔE and the bottom shows the Fisher distributions. The solid blue line is the total PDF for each of the variables. The dashed red line shows the continuum background PDF for each variable and the dotted green line shows in the signal PDF.

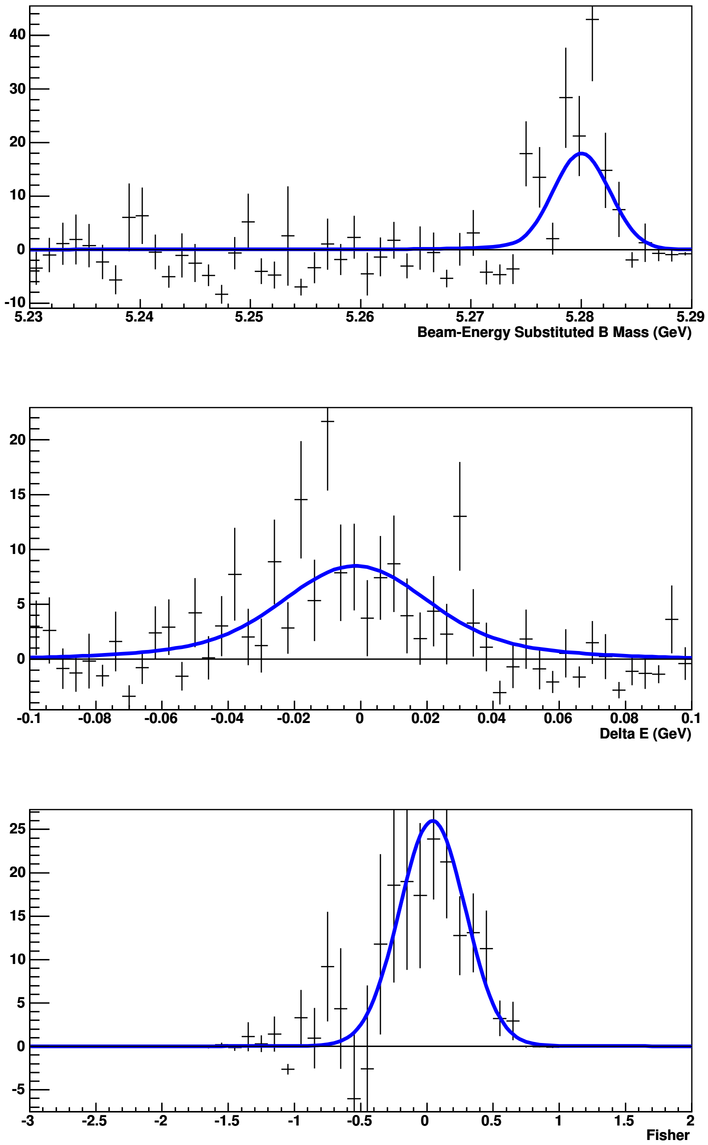

Figure 5.29: The ${}_s$Plots for the $B^0 \to K^{*+}\pi^-$ result. The top plot is for m_{ES}, the middle is for ΔE and the bottom shows the Fisher. The solid blue line represents the PDF from the initial fit to data.

fraction of

$$\mathcal{B}(B^0 \to K^{*\pm}\pi^{\mp}) = (11.0 \pm 1.5) \times 10^{-6} \tag{5.27}$$

which is consistent with previous measurements [19, 21].

$_s\mathcal{P}lots$ of the helicity distribution are shown in Figure 5.30. The left plot shows the distribution with the effects of detector acceptance. The right plot scales the distribution by efficiency to remove the detector effects. Both plots exhibit the $\cos^2\theta$ distribution which is expected from a vector particle. Figure 5.31 shows a comparison of the ratio of the signal likelihood to the total likelihood for data and toy MC, with the fit to data used as the input to the toy MC. The distributions agree very well.

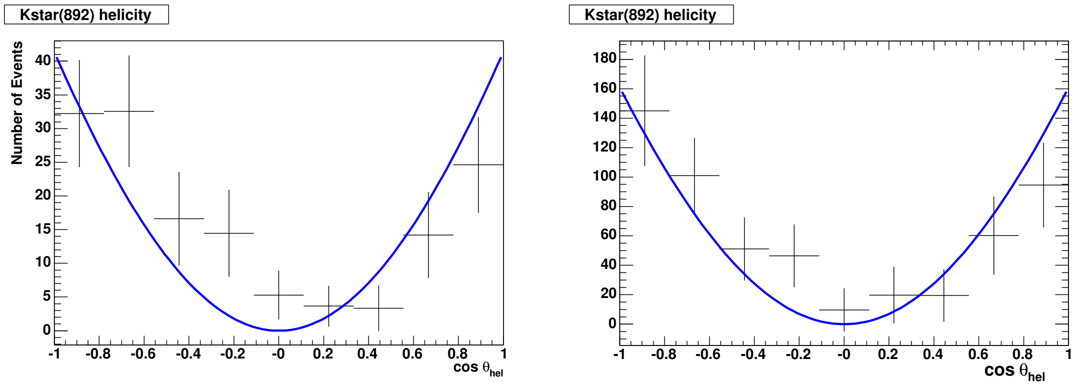

Figure 5.30: The left hand plot shows the helicity distribution for signal events without correcting for detector acceptance. The right hand plot corrects for this by weighing each event by its efficiency. For the purposes of this plot, events were removed which lay in bins which overlapped the veto regions, and which consequently caused an artificially high population in some bins. Each plot is overlaid with the expected $\cos\theta$ *distribution.*

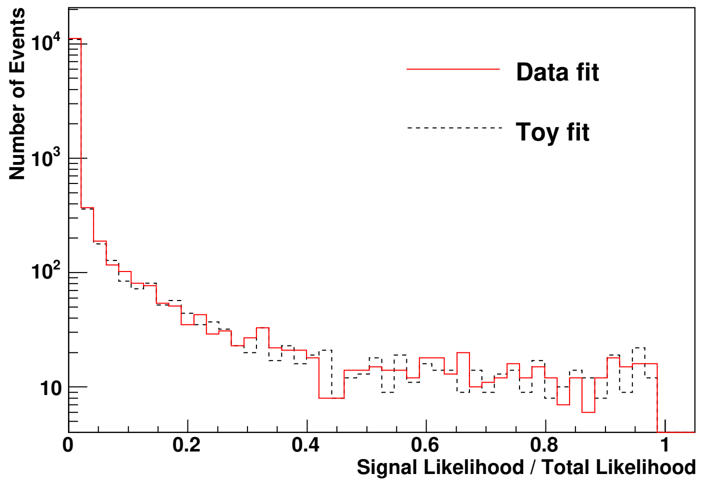

Figure 5.31: A comparison of the ratio of signal likelihood to total likelihood for $B^0 \to K^{*+}\pi^-$. The red solid line shows the result of the fit to data, and the black line shows the result of a fit to toy MC. The toy MC uses the number of events fitted in the data fit as the input to the experiment.

5.6.2 Interference

It is possible for the decay amplitudes of neighbouring resonances to interfere with each other. When measuring the branching fractions for the intermediate resonance decays, narrow bands around the resonance masses were selected for study. Figure 5.32 shows a toy MC Dalitz plot distribution, with equal branching fractions assumed for each resonance, and illustrates the helicity structure which is visible in the resonance bands. Areas in which resonances overlap perpendicularly have been removed with vetoes throughout this analysis.

The amplitude contributions to the Dalitz plot for each resonance can be written as a function of its helicity, $\cos\theta_{hel}$. For a scalar (S), vector (V) or tensor (T) resonance, the amplitude of the decay is proportional to the Legendre Polynomial of the same order as the spin:

$$A_S \quad \propto \quad k, \tag{5.28}$$

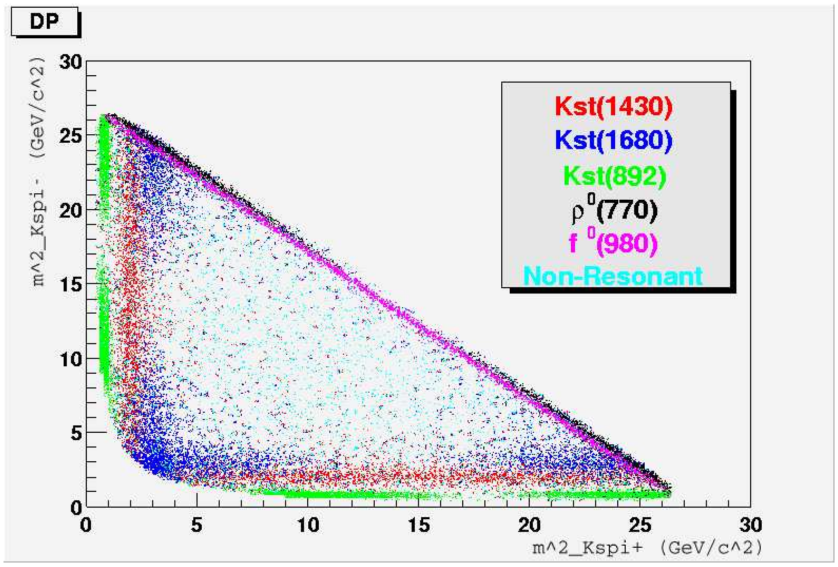

Figure 5.32: A toy Dalitz plot, with equal branching fractions assumed for all the included contributions. Neighbouring resonances, such as the K^* resonances, can quantum mechanically interfere with each other. $m^2_{K^0_S\pi^-}$ is plotted on the x-axis, and $m^2_{K^0_S\pi^+}$ on the y-axis. This figure is intended as an illustration only.

$$A_V \propto a\cos\theta_{hel}, \tag{5.29}$$

$$A_T \propto b(3\cos^2\theta_{hel} - 1) \tag{5.30}$$

where k, a and b are constants. The intensity of two neighbouring resonances can be written as:

$$| A_{S-V} |^2 \propto \int_{-1}^{1} (k + a\cos\theta_{hel})^2 \; d\cos\theta_{hel} \tag{5.31}$$

$$| A_{S-T} |^2 \propto \int_{-1}^{1} (k + b(3\cos^2\theta_{hel} - 1))^2 \; d\cos\theta_{hel} \tag{5.32}$$

$$| A_{V-V} |^2 \propto \int_{-1}^{1} (c\cos\theta_{hel})^2 \; d\cos\theta_{hel} \tag{5.33}$$

$$| A_{V-T} |^2 \propto \int_{-1}^{1} (e\cos\theta_{hel} + f(3\cos^2\theta_{hel} - 1))^2 \; d\cos\theta_{hel} \tag{5.34}$$

where c, e and f are also constants. The interference between the two resonances is described by the cross-terms in the above equations, such that the interference can be written:

$$I_{S-V} \propto \int_{-1}^{1} (\cos\theta_{hel})\ d\cos\theta_{hel} \tag{5.35}$$

$$I_{S-T} \propto \int_{-1}^{1} (3\cos^2\theta_{hel} - 1)\ d\cos\theta_{hel} \tag{5.36}$$

$$I_{V-V} \propto \int_{-1}^{1} (\cos^2\theta_{hel})\ d\cos\theta_{hel} \tag{5.37}$$

$$I_{V-T} \propto \int_{-1}^{1} (6\cos^3\theta_{hel} - 2\cos\theta_{hel})\ d\cos\theta_{hel} \tag{5.38}$$

Odd functions, such as $\cos\theta_{hel}$ and $(6\cos^3\theta_{hel} - 2\cos\theta_{hel})$, integrate to zero over helicity phase space if there are no helicity cuts, or if one is symmetric. Therefore, interference effects between $K^{*\pm}(892)$ and scalar states (nonresonant and $K_0^{*\pm}(1430)$) or tensor states ($K_2^{*\pm}(1430)$) cancel, assuming a constant efficiency. This is also true for interference between ρ^0 and $f_0(980)$, as well as any possible scalar or tensor higher ρ or f resonances.

However, the even function $\cos^2\theta_{hel}$ in the vector-vector case does not integrate to zero and this interference must be considered. There are two other vector resonances which may be present in $m_{K_S^0\pi^\pm}$, $K^{*\pm}(1410)$ and $K^{*\pm}(1680)$. Both of these have very small branching fractions, and $K^{*\pm}(1680)$ is far enough away in mass that it does not pollute the signal band of $K^* \pm (892)$. Therefore, the effect of interference between these vector resonances is considered negligible in this analysis. In the case of a scalar interfering with a tensor, however, the Legendre Polynomials are orthogonal and interference once again cancels.

The full effect of interference is best analysed using a Dalitz plot analysis, when statistics allow.

Chapter 6

Systematic Uncertainties

6.1 Systematic Uncertainties for the Branching Fraction Measurements

6.1.1 Tracking Efficiency

The MC simulation did not perfectly reproduce the detector's tracking capabilities. Therefore a correction had to be made to the efficiency of the signal MC to account for the overestimation of the track-finding efficiency. The corrections were made to each charged track in an event on the basis of their transverse momentum (p_T), their polar (θ) and azimuthal (ϕ) directions and the event multiplicity [62]. The collaboration produced a look-up table of corrections based on bins in these four variables. For each charged track (excluding the daughters of the K_S^0), the tracking efficiency for data and for MC were found from the table and the ratio was stored. For each event, the product of the ratios for each charged track formed the per event correction. The final correction was taken to be the average correction for all events, and the MC efficiency was multiplied by this amount. The tracking efficiency of the

K_S^0 daughters was treated separately and is discussed in Section 6.1.3.

The Tracking Efficiency Task Force, which produces the correction tables for each data set, recommends a systematic uncertainty on this efficiency correction of 0.8% per charged track to be applied [63]. This leads to a systematic uncertainty of 1.6% for tracking efficiency being applied to each branching fraction measurement. The net corrections to the MC efficiencies for tracking are shown in Table 6.1.

Mode	Correction	Tracking Systematic Uncertainty (%)
Inclusive	0.990	1.6
$B^0 \to K_S^0\pi^+\pi^-$ nonresonant	0.990	1.6
$B^0 \to K^{**\pm}\pi^\mp, K^{**\pm} \to K_S^0\pi^\pm$	0.985	1.6
$B^0 \to \rho^0 K_S^0$	0.981	1.6
$B^0 \to f_0 K_S^0$	0.985	1.6
$B^0 \to K^{*+}\pi^-$	0.983	1.6

Table 6.1: The Tracking corrections and systematic uncertainties for each branching fraction measurement. The variation in the corrections reflects the different angular and momentum distributions of the tracks in the different modes. The flat systematic uncertainty is as suggested by the Tracking Efficiency Task Force [63].

6.1.2 Particle Identification Efficiency

PID selectors have been found to be more efficient in MC than in data, and this difference must be corrected. Therefore, a table for the correct PID selector (in this case a pion failing `notAPion`) was applied to the MC to account for this. In this case, bins of p_T, θ and ϕ were used, and the the probability of a track being accepted or rejected was calculated using the "tweak" criteria:

- if $\epsilon_{data} < \epsilon_{MC}$, an accepted track has a probability $\epsilon_{data}/\epsilon_{MC}$ of being rejected.
- or if $\epsilon_{data} > \epsilon_{MC}$, a rejected track has a probability $(1 - \epsilon_{data})/(1 - \epsilon_{MC})$ of being accepted.

ϵ is defined as the PID efficiency for the type of data in the p_T, θ, ϕ bin of that track. In the limit of $\epsilon_{data} = \epsilon_{MC}$, the track is accepted [64].

During the previous iteration of this analysis, the systematic uncertainty was assigned to each mode based on the largest difference between its own PID efficiency and the PID efficiency of all the other signal modes (including $B^0 \to D^{\mp}\pi^{\pm}$) [19, 65]. For each mode, the PID systematic uncertainty was found to be 1.9%. This systematic uncertainty is used again for this analysis.

6.1.3 K_S^0 Efficiency

Correction factors are also needed for the tracking of K_S^0 particles to correct for the different reconstruction efficiencies in data and MC. Corrections are calculated in the following bins:

- 4 bins of transverse momentum (p_T),
- 8 bins of θ_{Lab} (the polar angle of the track in the laboratory frame) and
- 10 bins of the distance of closest approach in the xy plane.

and tables are available for a variety of K_S^0 quality cuts (e.g. the lifetime significance and $\cos\theta_{K_S^0}$) [66]. The corrections are applied in the same manner as the tracking efficiency corrections discussed in Section 6.1.1. The corrections for each branching fraction mode are shown in Table 6.2.

There are several contributions to the systematic uncertainties associated with these corrections. The systematic uncertainty due to the K_S^0 tracking correction tables is a flat uncertainty (supplied by the K_S^0 tracking group) of 0.9% for data taken in 2004 and 1.0% for data taken from 1999 to 2003. The statistical uncertainty in the correction tables is given in column 3 of Table 6.2.

The K_S^0 daughters are only required to pass the ChargedTracks criteria, which encompass all pairs of reconstructed charged tracks within 25 MeV/c^2 of the K_S^0 PDG mass, in order to make the K_S^0 default list [62]. However, the mass cut applied to the K_S^0 indirectly requires that the K_S^0 daughter tracks have hits in the DCH, increasing the chance that the daughter tracks will pass the GoodTracksLoose requirements. Therefore, an extra systematic uncertainty is required for this change in criteria and the method is prescribed by the Tracking Efficiency Task Force [63]. However, this systematic uncertainty is found to be negligible for these modes. The total efficiency due to K_S^0 reconstruction is shown in Table 6.2.

Mode	Correction	Statistical Uncertainty in Tables (%)	Total Systematic Uncertainty (%)
Inclusive	0.988	1.0	1.4
$B^0 \to K_S^0\pi^+\pi^-$ nonresonant	0.983	1.0	1.4
$B^0 \to K^{**\pm}\pi^\mp, K^{**\pm} \to K_S^0\pi^\pm$	0.987	1.3	1.6
$B^0 \to \rho^0 K_S^0$	0.991	1.5	1.7
$B^0 \to f_0 K_S^0$	0.991	1.3	1.6
$B^0 \to K^{*+}\pi^-$	0.989	1.1	1.5

Table 6.2: The K_S^0 Tracking corrections are shown in column 2. This correction is applied to the MC efficiency in order to calculate the BR measurement. Column 3 shows the systematic uncertainties on the tables used to find the efficiency corrections and includes the effect of the K_S^0 mass cut made in the selection criteria.

6.1.4 Signal Yield Fit Bias

Systematics uncertainties were assessed from the embedded fit tests (described in Section 5.1.4) for each of the modes. The uncertainty was calculated using:

$$\sigma_{sys,\mathrm{Fit\ bias}} = \frac{\mathrm{Pull} * \sigma_{N_{sig}}}{N_{sig}} \tag{6.1}$$

where $\sigma_{N_{sig}}$ is the statistical uncertainty on the signal yield, N_{sig} is the signal yield for each measurement and "Pull" is the pull (shift of the mean value of the Gaussian away from zero) on the number of signal events. The systematic uncertainties associated with each measurement are shown in Table 6.3.

Mode	Fit Bias Systematic Uncertainty (%)
Inclusive	1.7
$B^0 \to K_S^0\pi^+\pi^-$ nonresonant	0.8
$B^0 \to K^{**\pm}\pi^\mp, K^{**\pm} \to K_S^0\pi^\pm$	0.4
$B^0 \to \rho^0 K_S^0$	10.9
$B^0 \to f_0 K_S^0$	6.1
$B^0 \to K^{*+}\pi^-$	2.6

Table 6.3: The systematic uncertainties associated with fit bias on the signal yield for each BR measurement. The systematic uncertainty is calculated using Equation 6.1.

6.1.5 PDF parameterisation

In order to take into account systematic uncertainties due to PDF parameterisation, each PDF parameter used in the likelihood fit was varied by plus and minus 1σ of its uncertainty. However as shown in Appendix B, the parameters used to describe a PDF are correlated with each other. To handle the effects of this correlation, the error matrix ($cov(x, y)$) was used to determine how the other correlated variables also changed as a consequence of this shift. By changing one PDF parameter, a new set of parameters was obtained for that PDF. The likelihood fit was then re-performed using these new PDF parameters. This was repeated for each PDF parameter, where all the negative differences from the original fit value are added in quadrature, and all the positive values are treated in the same way. After all the fit parameters had been considered, the greatest of the differences (positive or negative) was taken as a symmetrical systematic uncertainty. The systematic uncertainty due to PDF parameterisation for each mode is shown in Table 6.4.

Mode	PDF Parameterisation Systematic Uncertainty (%)
Inclusive	0.1
$B^0 \to K^0_S \pi^+ \pi^-$ nonresonant	0.1
$B^0 \to K^{**\pm} \pi^\mp, K^{**\pm} \to K^0_S \pi^\pm$	0.1
$B^0 \to \rho^0 K^0_S$	0.6
$B^0 \to f_0 K^0_S$	0.1
$B^0 \to K^{*+} \pi^-$	0.3

Table 6.4: The systematic uncertainties associated with the parameterisation of the PDFs for each BR measurement.

6.1.6 B Background Contributions

Each of the B backgrounds included in the fit has an uncertainty associated with the branching fraction, and therefore an uncertainty on the number of events expected to pollute the data sample. In order to assess the systematic uncertainty associated with this uncertainty, the fit to data was repeated twice. For the first refit, the number of B-background events which were included in the fit was increased by the full uncertainty on the number anticipated for each B-background mode. For the second refit, the expected number of B-background events was reduced by the same amount. This gave the maximum effect possible on the signal yield due to uncertainties on the number of B-background events included in the ML fit. The greatest difference between one of the refits and the nominal fit was taken to be the systematic uncertainty. The uncertainties for each measurement are included in Table 6.5.

Mode	B-background Systematic Uncertainty ($\times 10^{-6}$)
Inclusive	2.0
$B^0 \rightarrow K^0_S \pi^+\pi^-$ nonresonant	0.04
$B^0 \rightarrow K^{**\pm}\pi^\mp, K^{**\pm} \rightarrow K^0_S \pi^\pm$	0.4
$B^0 \rightarrow \rho^0 K^0_S$	0.3
$B^0 \rightarrow f_0 K^0_S$	0.3
$B^0 \rightarrow K^{*+}\pi^-$	0.2

Table 6.5: The systematic uncertainty associated with the uncertainty on the signal yield for each branching fraction measurement due to the uncertainty on the B-background yield.

For the inclusive measurement, a maximum of 16.4 events was expected due to particle misidentification from $B^0 \rightarrow K^0_S K^\pm \pi^\mp$. This was estimated using the upper limit as the branching fraction. This contributed a further $\pm 0.82 \times 10^{-6}$ systematic uncertainty to the inclusive branching fraction measurement. The B background estimation to $B^0 \rightarrow K^{*+}\pi^-$ for $K^{**\pm}$ using the LASS parameterisation (Section 5.3.2) changed the branching fraction by $\pm 1.8 \times 10^{-6}$. Both of these additional systematic uncertainties are included in figures in Table 6.5.

6.1.7 Efficiency over the Dalitz Plot

The efficiency, ϵ, for each mode was calculated using signal MC for each mode which was measured. Therefore, the accuracy of the efficiency depended on the amount of MC used to find it. The uncertainty on the efficiency of a single bin is defined by Poisson statistics as:

$$\sigma_{\epsilon,bin} = \sqrt{\frac{\epsilon * (1-\epsilon)}{N_{bin}}} \tag{6.2}$$

where N_{bin} is the number of events generated in the bin. When ${}_sWeights$ were used to calculate the branching fraction, a number of bins were used in the calculation. Therefore, the uncertainties on each bin must be combined:

$$\sigma_{\epsilon}^2 = \sum \frac{{}_sWeight \ * (\sigma_{\epsilon}^2/\text{bin})}{N_{sig}}. \tag{6.3}$$

The uncertainty for each of the decays modes is given in Table 6.6.

Mode	Efficiency Systematic Uncertainty (%)
Inclusive	0.9
$B^0 \to K_S^0\pi^+\pi^-$ nonresonant	1.1
$B^0 \to K^{**\pm}\pi^{\mp}, K^{**\pm} \to K_S^0\pi^{\pm}$	0.9
$B^0 \to \rho^0 K_S^0$	0.1
$B^0 \to f_0 K_S^0$	0.1
$B^0 \to K^{*+}\pi^-$	0.1

Table 6.6: The systematic uncertainties associated with the uncertainty on the Dalitz plot efficiency for each branching fraction measurement.

6.1.8 B Counting

The number of $\Upsilon(4S) \to B\overline{B}$ events needs to be determined in order for accurate branching fractions to be determined. The procedure for determining the number of $B\overline{B}$ pairs, $N_{B\overline{B}}$, is known as B counting and is found by counting the number of muon pairs and multi-hadron events in on- and off-resonance runs. In off-resonance data, all multi-hadron events are due to continuum quark and $\tau^+\tau^-$ production, but in on-resonance data $b\overline{b}$ production also contributes. Once the rate of multi-hadron production in off-resonance data has been scaled to the on-resonance integrated luminosity, the difference between the rate of multi-hadron production when running on-resonance ($N_{MH}(\text{on})$) and when running off-resonance ($N_{MH}(\text{off})$) is due to $\Upsilon(4\text{S})$ production. The ratio of luminosities is calculated using the ratio of the number of $\mu^+\mu^-$ pairs ($N_{\mu^+\mu^-}$) and a factor which corrects for the energy spectrum of the continuum cross-section and the selection efficiency (κ). Therefore, the total number of $B\overline{B}$ pairs can be expressed as

$$N_{B\overline{B}} = \frac{1}{\epsilon_{B\overline{B}}}\left(N_{MH}(\text{on}) - N_{MH}(\text{off})\kappa\frac{N_{\mu^+\mu^-}(\text{on})}{N_{\mu^+\mu^-}(\text{off})}\right) \tag{6.4}$$

with $\epsilon_{B\overline{B}}$ representing the $B\overline{B}$ efficiency when the multi-hadronic selection criteria are applied [34]. For this analysis, the dataset was found to have $N_{B\overline{B}} = (231.8 \pm 2.6)\times10^6$. Therefore, the uncertainty on the total number of B events was 1.1%. In addition, for these analyses, equal numbers of $\Upsilon(4\text{S}) \to B^0\overline{B}^0$ and $\Upsilon(4\text{S}) \to B^+B^-$ were assumed.

6.1.9 Summary of Systematic Uncertainties

The systematic uncertainties on the branching fraction measurements are summarised in Table 6.7. For the systematic uncertainties listed, each uncertainty contribution is added in quadrature to give the total systematic uncertainty.

Type of Sys. Uncertainty \ Mode	Inclusive	$B^0 \to K_S^0\pi^+\pi^-$ nonresonant	$B^0 \to K^{**\pm}\pi^{\mp}$, $K^{**\pm} \to K_S^0\pi^{\pm}$	$B^0 \to \rho^0 K_S^0$	$B^0 \to f_0 K_S^0$	$B^0 \to K^{*+}\pi^-$
Particle Identification (%)	1.9	1.9	1.9	1.9	1.9	1.9
Tracking(%)	1.6	1.6	1.6	1.6	1.6	1.6
K_S^0 efficiency(%)	1.4	1.4	1.6	1.7	1.6	1.5
Fit Bias(%)	1.7	0.8	0.4	10.9	6.1	2.6
PDF parameterisation(%)	0.1	0.8	0.1	0.6	0.1	0.3
B background(%)	4.2	3.1	1.1	6.7	5.9	2.0
Efficiency(%)	0.9	1.1	0.9	0.1	0.1	0.1
B counting(%)	1.1	1.1	1.1	1.1	1.1	1.1
TOTAL (%)	5.4	4.6	3.6	13.2	9.1	4.5

Table 6.7: A compilation table of all the systematic uncertainties, expressed as percentages of the measured branching fraction, for all branching fraction modes.

6.2 Systematics for the Charge Asymmetry Measurement

Many of the systematic uncertainties already discussed in this chapter, such as tracking and PID efficiencies, cancel for the charge asymmetry measurement. However, the effect of any fit bias or incorrect PDF parameterisation must be included, as well as the systematic uncertainty on the branching fraction and asymmetry of all the B-background modes. A study of the charge-dependent interaction of pions within the detector found a negligible effect.

The fit bias systematic was calculated in the same way as in Section 6.1.4 but with the "Pull" in Equation 6.1 being the shift from zero of the signal asymmetry, rather than the signal yield. This provided a systematic error of 1.8%. Following the method outlined in Section 6.1.5, the uncertainty in the PDF parameterisation was found to be 3.8%.

The error due to the uncertainty in the B-background contribution was evaluated in a similar manner as in Section 6.1.6 but now the amount of charge asymmetry that may be present in each B-background mode was also accounted for. The charge asymmetry on each mode was varied to ± 0.5 and the number of expected events varied $\pm 1\sigma$ as before. Therefore, 4 refits to data were performed and the largest deviation from the value in the original fit to data was taken to be the systematic error. This value was ± 0.05. The summary of systematics is shown in Table 6.8.

Type of Sys. Error	Value of Sys. Error (%)	Value of Sys. Error (Absolute)
Fit bias	1.8	0.00
PDF parameterisation	3.8	0.00
B background		0.05

Table 6.8: A summary of the systematics errors (in percent and in absolute terms) for the $B^0 \to K^{*+}\pi^-$ charge asymmetry measurement.

Chapter 7

Discussion and Summary

In this thesis, maximum likelihood analyses of the inclusive $B^0 \to K_S^0\pi^+\pi^-$ branching fraction, the nonresonant branching fraction and the major resonance substructures yielded the results in Table 7.1. The results quotes the statistical uncertainty first and the systematic uncertainty second. The asymmetry measurement result for $B^0 \to K^{*+}\pi^-$ is shown in Table 7.2.

Mode	$\mathcal{B}$ Measurement
$B^0 \to K^0\pi^+\pi^-$ Inclusive	$(43.0 \pm 2.3 \pm 2.3) \times 10^{-6}$
$B^0 \to K_S^0\pi^+\pi^-$ nonresonant	$< 2.1 \times 10^{-6}$
$B^0 \to K^{**\pm}\pi^{\mp}, K^{**\pm} \to K^0\pi^{\pm}$	$(24.4 \pm 2.6 \pm 0.9) \times 10^{-6}$
$B^0 \to \rho^0 K^0, \rho^0 \to \pi^+\pi^-$	$(4.0 \pm 1.0 \pm 0.5) \times 10^{-6}$
$B^0 \to f_0(980)K^0, f_0(980) \to \pi^+\pi^-$	$(5.5 \pm 0.7 \pm 0.5) \times 10^{-6}$
$B^0 \to K^{*\pm}\pi^{\mp}$	$(11.0 \pm 1.5 \pm 0.5) \times 10^{-6}$

Table 7.1: A summary of Branching Fraction Results. The first uncertainty is statistical and the second is systematic. $K^{**\pm}$ is a collective term for the $K_0^{*\pm}(1430)$, $K_2^{*\pm}(1430)$, $K^{*\pm}(1410)$, and $K^{*\pm}(1680)$ resonances. The branching fractions given are for the decay as completely listed in column 1.

Mode	A_{CP} Measurement
$B^0 \to K^{*\pm}\pi^{\mp}$	$-0.11 \pm 0.14 \pm 0.05$

Table 7.2: The charge asymmetry result for $B^0 \to K^{*+}\pi^-$. The first uncertainty is statistical and the second is systematic.

The results were measured using the *BABAR* data sample of 210 million $B\overline{B}$ pairs which were recorded between 1999 and 2004. The nonresonant branching fraction was not significant (2.75σ) and so an upper limit is set. The $B^0 \to \rho^0 K^0$ measurement has a significance of 3.6σ, which is considered to be evidence of the decay but is insufficient to claim observation. The charge asymmetry measurement is consistent with zero. The $B^0 \to f_0(980)K^0$ measurement is significant at the 4.7σ level, and is therefore close to the *BABAR* criteria for discovery of 5σ. It is expected that this will change with the next addition of statistics. The other measurements are all significant at more than 5σ, although none of these are new discoveries.

The main systematic uncertainty in the branching fraction measurements comes from the uncertainty in the amount of B-background contamination which pollutes the signal region. This could be improved by improving the branching fraction measurements of the B-background modes so that the uncertainties are reduced, and by using more simulated data so that the statistical uncertainty on the efficiency is reduced. For the charge asymmetry measurement, the main systematic uncertainty is the combined effect of the uncertainties on the B-background contamination and the unknown asymmetries of each of these contributions. This uncertainty was ascertained assuming asymmetries of ± 0.5 for each mode, which is very conservative, and it could be reduced by performing charge asymmetry measurements for each mode. However, at the moment the measurement is still dominated by the statistical uncertainty.

The results compare well with previous measurements. Table 7.3 shows the previous published results for the inclusive measurement and Table 7.4 shows the previously published results for $B^0 \to K^{*+}\pi^-$. Note that [19] is the previous iteration of the analysis presented here, using a dataset of $81\,\text{fb}^{-1}$. The current analysis finds a result which is consistent with the previous Belle and *BABAR* measurements and compatible with the CLEO measurement within 2σ. Table 7.5 shows the previous results published for $B^0 \to \rho^0 K^0$ and $B^0 \to f_0(980)K^0$. The results in this thesis agree within uncertainties with these results.

Experiment	$\mathcal{B}(B \to K^0\pi^+\pi^-)$ Measurement
CLEO [17]	$50.0 \pm ^{10}_{-9} \pm 7 \times 10^{-6}$
Belle [67]	$45.4 \pm 5.2 \pm 5.9 \times 10^{-6}$
BABAR [19]	$43.8 \pm 3.8 \pm 3.4 \times 10^{-6}$

Table 7.3: The previous measurements of the inclusive $B \to K^0\pi^+\pi^-$ from CLEO, Belle and BABAR.

Experiment	$\mathcal{B}(K^{*\pm}\pi^{\mp})$ Measurement
CLEO [17]	$26.0 \pm 9.0 \times 10^{-6}$
Belle [18]	$16^{+6}_{-5} \pm 2 \times 10^{-6}$
BABAR [21]	$10.9 \pm 2.3 \pm 1.5 \times 10^{-6}$
BABAR [19]	$12.9 \pm 2.4 \pm 1.4 \times 10^{-6}$

Table 7.4: The previous measurements of the $B^0 \to K^{*+}\pi^-$ from CLEO, Belle and BABAR. The third result was measured from the Dalitz plot with the final state $B^0 \to K^{\pm}\pi^{\mp}\pi^0$.

However, these results do not consider the effects of interference on the branching fractions. The majority of the interference regions have been removed using vetoes in an attempt to minimise the effect on the results. When statistics allow, a Dalitz plot analysis will allow the interference effects to be modelled correctly, and yield measurements of the magnitudes and phases of the resonant and nonresonant amplitudes. These quantities can be used to construct several variables described

Decay Mode	Experiment	$\mathcal{B}$ Measurement
$B^0 \to \rho^0 K^0, \rho^0 \to \pi^+\pi^-$	*BABAR* [20]	$5.1 \pm 1.0 \pm 1.2 \times 10^{-6}$
$B^0 \to f_0(980)K^0, f_0 \to \pi^+\pi^-$	*BABAR* [60]	$6.0 \pm 0.9 \pm 0.6 \pm 1.2 \times 10^{-6}$

Table 7.5: The previous measurements of $B^0 \to \rho^0 K^0_S$ and $B^0 \to f_0 K^0_S$. In each case, the first uncertainty is statistical, the second is systematic and any third is theoretical.

in [8] which are sensitive to *CP* violating effects.

The branching fraction predictions using factorisation are shown in Table 1.1. The results of this analysis for $B^0 \to \rho^0 K^0$ are in broad agreement with most of the factorisation predictions. However, the predictions for $B^0 \to K^{*+}\pi^-$ are considerably lower than all the current experimental measurements. Therefore, it appears that the technique does not yet adequately describe the $B^0 \to K^{*+}\pi^-$ channel. Table 1.2 shows the predictions for the charge asymmetry in the self-tagging mode $B^0 \to K^{*+}\pi^-$. Since the experimental measurements have varied, and the zero hypothesis has not been excluded, a conclusion cannot be drawn on the accuracy of the predictions. The SU(3) and isospin technique used by Chiang *et al.* [15], however, seems to produce more reliable predictions of the branching ratios and *CP* asymmetries.

In conclusion, the following results have been measured in this thesis:

$$\begin{aligned}
\mathcal{B}(B^0 \to K^0\pi^+\pi^- \text{ Inclusive}) &= (43.0 \pm 2.3 \pm 2.3) \times 10^{-6} \\
\mathcal{B}(B^0 \to K^0_S\pi^+\pi^- \text{ nonresonant}) &< 2.1 \times 10^{-6} \\
\mathcal{B}(B^0 \to K^{**\pm}\pi^{\mp}, K^{**\pm} \to K^0\pi^{\pm}) &= (24.4 \pm 2.6 \pm 0.9) \times 10^{-6} \\
\mathcal{B}(B^0 \to \rho^0 K^0_S) &= (4.0 \pm 1.0 \pm 0.5) \times 10^{-6} \\
\mathcal{B}(B^0 \to f_0 K^0_S) &= (5.5 \pm 0.7 \pm 0.5) \times 10^{-6} \\
\mathcal{B}(B^0 \to K^{*+}\pi^-) &= (11.0 \pm 1.5 \pm 0.5) \times 10^{-6}
\end{aligned}$$

where in each case the first uncertainties is statistical and the second is systematic.

In addition, the charge asymmetry in the $B^0 \to K^{*+}\pi^-$ resonant mode was measured to be

$$\mathcal{A}_{CP}(B^0 \to K^{*+}\pi^-) = -0.11 \pm 0.14 \pm 0.05$$

where again the first uncertainty is statistical and the second is systematic. These results agree with previous measurements, but the $B^0 \to K^{*+}\pi^-$ measurement gives strong evidence that further research is needed in the area of factorisation theory when it is used for predicting branching fractions in charmless B decays. However, the results lend credibility to the predictions which rely on SU(3) and isospin relations. The $B^0 \to K^0_S\pi^+\pi^-$ Dalitz plot requires further study to investigate the interference between decay channels with the same final state once statistics allow.

Appendix A

${}_s$*Plots* and ${}_s$*Weights*

${}_s$*Plots* began as a convenient method of being able to break up a sample of events into the various species (signal, continuum background etc) for a given variable x. For an analysis with N events, and N_s species of events, the extended log-likelihood can be written as:

$$\mathcal{L} = \sum_{e=1}^{N} \ln\{\sum_{i=1}^{N_s} N_i f_i(y_e)\} - \sum_{i=1}^{N_s} N_i \tag{A.1}$$

where f_i is the PDF of the i^{th} species, and the PDF is formed using a set of discriminating variables y (m_{ES}, ΔE and Fisher for this analysis). $f_i(y_e)$ is the value of the PDF f_i for event e, for the set of discriminating variables y [49]. The method assumes that the PDFs used for the fit model the data exactly and that the fit has already been performed.

The method aims to find the true distribution, $\mathbf{M}_{\text{n}}$, of the variable x for events of the n^{th} species. This appendix gives a summary of reference [49] which shows that the $\mathbf{M}_{\text{n}}$ distributions can be reconstructed for any species when the f_i PDFs and the N_i are known.

This appendix will begin with the case of the variable y not being independent of x. If a fit has already been performed, such that the PDFs and N_i for each species are known, the weight for a given hypothesis

$$\mathcal{P}_{\mathrm{n}}(y_e) = \frac{N_{\mathrm{n}} f_{\mathrm{n}}(y_e)}{\sum_{k=1}^{N_s} N_k f_k(y_e)} \tag{A.2}$$

can be defined for all events. $\tilde{M}_{\mathrm{n}}$, defined as the reconstructed distribution of x, normalised to unity, can then be defined as

$$N_{\mathrm{n}} \tilde{M}_{\mathrm{n}}(\overline{x}) \delta x \equiv \sum_{e \subset \delta x}^{N} \mathcal{P}_{\mathrm{n}}(y_e) \tag{A.3}$$

in which the sum $\sum_{e\subset\delta x}^{N}$ is over events for which the value of x for an event e (x_e) lies in the x-bins which are centred on $\overline{x}$ and have width δx. Therefore, $N_{\mathrm{n}} \tilde{M}_{\mathrm{n}}(\overline{x}) \delta x$ describes the x-distribution of plotted events using the weight $\mathcal{P}_{\mathrm{n}}$. Using

$$\sum_{e \subset \delta x}^{N} \longrightarrow \int dy \sum_{j=1}^{N_s} f_j(y) \delta(x(y) - \overline{x}) \delta x, \tag{A.4}$$

reference [49] shows that equation A.3 reproduces the true distribution $\mathbf{M}(x)$:

$$N_{\mathrm{n}} \tilde{M}_{\mathrm{n}}(\overline{x}) \equiv N_{\mathrm{n}} \mathbf{M}_{\mathrm{n}}(\overline{x}). \tag{A.5}$$

However, since x is correlated to y, the resultant plots (${}_{in}\mathcal{P}lots$) are biased and this method is not optimal. Therefore, the method is developed for the case when x cannot be described as a function of y, with the assumption that x and y are not correlated, and the total PDF $f(x, y)$ factorises into the product $\mathbf{M}(x) f(y)$. In this case, using equations A.2 and A.3,

$$\begin{aligned}
N_{\mathrm{n}} \tilde{M}_m(\overline{x}) &= \int\int dy dx \sum_{j=1}^{N_s} N_j \mathbf{M}_j(x) f_j(y) \delta(x - \overline{x}) \mathcal{P}_{\mathrm{n}} && \text{(A.6)} \\
&= \int dy \sum_{j=1}^{N_s} N_j \mathbf{M}_j(\overline{x}) f_j(y) \frac{N_{\mathrm{n}} f_{\mathrm{n}}(y)}{\sum_{j=1}^{N_s} N_k f_k(y)} && \text{(A.7)} \\
&= N_{\mathrm{n}} \sum_{j=1}^{N_s} \mathbf{M}_j(\overline{x}) \left(N_j \int dy \frac{f_{\mathrm{n}}(y) f_j(y)}{\sum_{k=1}^{N_s} N_k f_k(y)} \right) && \text{(A.8)} \\
&\neq N_{\mathrm{n}} \mathbf{M}_{\mathrm{n}}(\overline{x}). && \text{(A.9)}
\end{aligned}$$

In this case, the true distribution of events would only be revealed if the y variables were completely discriminating. Thus, in this case,

$$N_j \int dy \frac{f_{\mathrm{n}}(y) f_j(y)}{\sum_{k=1}^{N_s} N_k f_k(y)} \tag{A.10}$$

acts as a correction term. The term is related to the inverse of the covariance matrix (given by the second derivative of the negative log likelihood, which is minimised in the analysis):

$$\mathbf{V}^{-1}_{\mathrm{n}j} = \frac{\partial^2(-\mathcal{L})}{\partial N_{\mathrm{n}} \partial N_j} = \sum_{e=1}^{N} \frac{f_{\mathrm{n}}(y_e) f_j(y_e)}{(\sum_{k=1}^{N_s} N_k f_k(y_e))^2}. \tag{A.11}$$

Reference [49] shows that the inverse of the covariance matrix can also be written:

$$\mathbf{V}^{-1}_{\mathrm{n}j} = \int dy \frac{f_{\mathrm{n}}(y) f_j(y)}{\sum_{k=1}^{N_s} N_k f_k(y)} \tag{A.12}$$

which means that Equation A.8 can be written

$$\tilde{M}_{\mathrm{n}}(\overline{x}) = \sum_{j=1}^{N_s} \mathbf{M}_j(\overline{x}) N_j \mathbf{V}^{-1}_{\mathrm{n}j}. \tag{A.13}$$

Inversion of Equation A.13 recovers

$$N_{\mathrm{n}} \mathbf{M}_{\mathrm{n}}(\overline{x}) = \sum_{j=1}^{N_s} \mathbf{V}_{\mathrm{n}j} \tilde{M}_j(\overline{x}). \tag{A.14}$$

Therefore, the true distribution is still recoverable, and when x is not a member of set y, the correct weight given to an event is

$${}_s\mathcal{P}_{\mathrm{n}}(y_e) = \frac{\sum_{j=1}^{N_s} \mathbf{V}_{\mathrm{n}j} f_j(y_e)}{\sum_{k=1}^{N_s} N_k f_k(y_e)}. \tag{A.15}$$

This is known as the ${}_s$*Weight* or the "covariance-weighted weight".

The distribution of x, the ${}_s$*Plot*, can be plotted using this ${}_s$*Weight*, since

$$N_{\mathrm{n}\,s}\tilde{M}_{\mathrm{n}}(\overline{x})\delta x \equiv \sum_{e \subset \delta x}^{N} {}_s\mathcal{P}_{\mathrm{n}}(y_e). \tag{A.16}$$

${}_s$*Plots* and ${}_s$*Weights* have several properties, described fully in reference [49], including that for any event,

$$\sum_{l=1}^{N_s} {}_s\mathcal{P}_l(y_e) = \sum_{l=1}^{N_s} \frac{\sum_{j=1}^{N_s} \mathbf{V}_{lj} f_j(y_e)}{\sum_{k=1}^{N_s} N_k f_k(y_e)} = \frac{\sum_{j=1}^{N_s} N_j f_j(y_e)}{\sum_{k=1}^{N_s} N_k f_k(y_e)} = 1 \tag{A.17}$$

which demonstrates that the contributions ${}_s\mathcal{P}_j(y_e)$ sum to the number of events actually observed in each x-bin. Each distribution is also correctly normalised:

$$\sum_{e=1}^{N} {}_s\mathcal{P}_{\mathrm{n}}(y_e) = \sum_{\delta x} N_{\mathrm{n}\,s}\tilde{M}_{\mathrm{n}}(x)\delta x = \sum_{e=1}^{N} \frac{\sum_{j=1}^{N_s} \mathbf{V}_{\mathrm{n}j} f_j(y_e)}{\sum_{k=1}^{N_s} N_k f_k(y_e)} = \sum_{j=1}^{N_s} \mathbf{V}_{\mathrm{n}j} = N_{\mathrm{n}} \tag{A.18}$$

For the purposes of this analysis, the ${}_sPlot$ method must be further extended to take the fixed B-background species into account. Since the number of these events are not floated in the fit to data, these contributions cannot be treated as a species of events in the manner above. The true distribution $\mathbf{M}_f(x)$ and number of B-background events are assumed to be known via Monte Carlo. For this extended ${}_sPlot$ method, Equation A.16 now becomes

$$N_{\mathrm{n}}\ {}_s\tilde{M}_{\mathrm{n}}(\overline{x}) = c_{\mathrm{n}}\mathbf{M}_f(x)\delta x + \sum_{e\subset\delta x}^{N} {}_s\mathcal{P}_{\mathrm{n}} \tag{A.19}$$

where $c_{\mathrm{n}} = N_{\mathrm{n}} - \sum_j \mathbf{V}_{\mathrm{n}j}$ and ${}_s\mathcal{P}_{\mathrm{n}}$ can be written as

$${}_s\mathcal{P}_{\mathrm{n}} = \frac{\sum_{j=1}^{N_s} \mathbf{V}_{\mathrm{n}j} f_j}{\sum_{k=1}^{N_s} N_k f_k + \sum_{l=1}^{N_f} N_l f_l}. \tag{A.20}$$

Here, N_s is the number of species with their coefficients floated in the fit (i.e. where the number of events of that species are floated) and N_f is the number of species in which the coefficient is fixed.

For this case, the sum over the number of events per species does not equal the total number of events in the sample:

$$\sum N_i = N - N_0\left(\sum_{e=1}^{N} \frac{\sum_{l=1}^{N_f} f_l}{\sum_{k=1}^{N_s} N_k f_k + \sum_{l=1}^{N_f} N_l f_l}\right) \neq N - N_0 \tag{A.21}$$

where N_0 is the total number of events which are fixed. However, the true distributions are produced and they are properly normalised (i.e. $\sum_{e=1}^{N}(c_n\mathbf{M}_f(x) + {}_s\mathcal{P}_n) = N_n$).

Therefore, using this method it is possible to obtain signal only plots without bias. The method also helps to calculate the branching fraction for the inclusive $B^0 \to K^0_S\pi^+\pi^-$ Dalitz plot without knowledge of the resonance, continuum and interference contributions. Since the efficiency can be calculated from MC in terms of a variable x, $\epsilon(x)$, the efficiency corrected ${}_sPlots$ can be shown:

$$\frac{1}{\epsilon(x)}N_{\mathrm{n}}\tilde{M}_{\mathrm{n}}\delta x = \frac{1}{\epsilon(x)}\sum_{e\subset\delta x}^{N} \mathcal{P}_{\mathrm{n}}(y_e). \tag{A.22}$$

Also, the branching fraction can be calculated using:

$$N_{\mathrm{n}}^{\epsilon} = \sum_{e=1}^{N} \frac{\mathcal{P}_{\mathrm{n}}(y_e)}{\epsilon(x_e)}. \tag{A.23}$$

${}_s\mathcal{P}lots$ were used extensively throughout this analysis to show that the distribution of signal events were well-matched to the fitted PDFs, and also for calculating the inclusive, nonresonant and $B^0 \to K^{**\pm}\pi^{\mp}$ branching fractions. The technique is extremely useful, especially in cases with a very low signal-to-background ratio. ${}_s\mathcal{P}lots$ show the distribution of all events in a given species, which gives them a large advantage over plots with a likelihood cut placed on them, which neither show all the signal events nor remove all the background events.

Appendix B

PDF Parameter Correlations

The fits to m_{ES}, Fisher and ΔE distributions for any of the three maximum likelihood categories of signal, continuum background and B background are performed in the one dimension so that there is no correlation between fitted parameters of different PDFs. This is shown in the correlation matrix below. This matrix was obtained by performing a fit to the m_{ES}, Fisher and ΔE distributions using the PDF shapes described in Section 4.4, using signal Monte Carlo for data. It is seen that there are only correlations between parameters describing the same PDF.

PARAMETER CORRELATION COEFFICIENTS

NO.	GLOBAL	1	2	3	4	5	6	7	8	9	10	11	12	
1	0.89675	1.000	-0.011	0.030	-0.000	0.000	0.000	0.000	-0.000	0.000	0.000	0.000	0.000	EmbcSig_mean1
2	0.06000	-0.011	1.000	-0.050	-0.000	0.000	0.000	0.000	-0.000	0.000	0.000	0.000	0.000	EmbcSig_alpha
3	0.05850	0.030	-0.050	1.000	-0.000	0.000	0.000	0.000	0.000	-0.000	-0.000	0.000	-0.000	EmbcSig_sigm1
4	0.85128	-0.000	-0.000	-0.000	1.000	-0.015	-0.767	-0.723	0.000	-0.000	-0.000	-0.000	-0.000	deltaESig_frac
5	0.09878	0.000	0.000	0.000	-0.015	1.000	0.054	-0.041	0.000	-0.000	-0.000	-0.000	-0.000	deltaESig_mean1
6	0.76847	0.000	0.000	0.000	-0.767	0.054	1.000	0.536	-0.000	0.000	0.000	0.000	0.000	deltaESig_sigm1
7	0.72518	0.000	0.000	0.000	-0.723	-0.041	0.536	1.000	-0.000	0.000	0.000	0.000	0.000	deltaESig_sigm2
8	0.67051	-0.000	-0.000	0.000	0.000	0.000	-0.000	-0.000	1.000	-0.010	0.135	0.642	0.354	fishSig_frac
9	0.06929	0.000	0.000	-0.000	-0.000	-0.000	0.000	0.000	-0.010	1.000	-0.069	-0.004	-0.008	fishSig_mean1
10	0.15957	0.000	0.000	-0.000	-0.000	-0.000	0.000	0.000	0.135	-0.069	1.000	0.123	0.069	fishSig_mean2
11	0.64536	0.000	0.000	0.000	-0.000	-0.000	0.000	0.000	0.642	-0.004	0.123	1.000	0.273	fishSig_sigm1
12	0.35909	0.000	0.000	-0.000	-0.000	-0.000	0.000	0.000	0.354	-0.008	0.069	0.273	1.000	fishSig_sigm2

B.1 Signal PDFs

The following correlations for m_{ES}, Fisher and ΔE PDF parameters were obtained from fits to signal Monte Carlo.

m_{ES}:

```
PARAMETER  CORRELATION COEFFICIENTS
      NO.  GLOBAL      1      2      3
        1  0.89675   1.000 -0.011  0.030 mESSig_alpha
        2  0.06000  -0.011  1.000 -0.050 mESSig_mean1
        3  0.05850   0.030 -0.050  1.000 mESSig_sigm1
```

Fisher

```
PARAMETER  CORRELATION COEFFICIENTS
      NO.  GLOBAL      1      2      3      4      5
        1  0.67051   1.000 -0.010  0.135  0.642  0.354 fishSig_frac
        2  0.06929  -0.010  1.000 -0.069 -0.004 -0.008 fishSig_mean1
        3  0.15957   0.135 -0.069  1.000  0.123  0.069 fishSig_mean2
        4  0.64536   0.642 -0.004  0.123  1.000  0.273 fishSig_sigm1
        5  0.35909   0.354 -0.008  0.069  0.273  1.000 fishSig_sigm2
```

ΔE

```
PARAMETER  CORRELATION COEFFICIENTS
      NO.  GLOBAL      1      2      3      4
        1  0.85128   1.000 -0.015 -0.767 -0.723 deltaESig_frac
        2  0.09878  -0.015  1.000  0.054 -0.041 deltaESig_mean1
        3  0.76847  -0.767  0.054  1.000  0.536 deltaESig_sigm1
        4  0.72518  -0.723 -0.041  0.536  1.000 deltaESig_sigm2
```

These matrices are essentially a breakdown of the first set of coefficients, where null correlations are ignored leaving correlations for each PDF.

B.2 Continuum Background PDFs

The following correlations for the Fisher PDF parameters were obtained from fits to upper sideband data.

```
PARAMETER  CORRELATION COEFFICIENTS
      NO.  GLOBAL      1      2      3      4
       1 0.90072   1.000  0.005 -0.852 -0.740  fishBg_frac
       2 0.04125   0.005  1.000  0.014 -0.020  fishBg_mean1
       3 0.85398  -0.852  0.014  1.000  0.593  fishBg_sigm1
       4 0.74413  -0.740 -0.020  0.593  1.000  fishBg_sigm2
```

Since the background PDFs for both m_{ES} and ΔE are separately described by only one parameter, they have no correlation coefficients.

B.3 B-Background PDFs

The following correlations for the Fisher PDF parameters were obtained from fits to Monte Carlo of the mode under study.

$B^0 \rightarrow \eta\prime K_S^0$

```
PARAMETER  CORRELATION COEFFICIENTS
      NO.  GLOBAL      1      2      3
       1  0.86549   1.000  0.728 -0.747 fishBBg1_mean
       2  0.74060   0.728  1.000 -0.453 fishBBg1_sigm
       3  0.75881  -0.747 -0.453  1.000 fishBBg1_sigm2
```

$B^0 \rightarrow D^- \pi^+$

```
PARAMETER  CORRELATION COEFFICIENTS
```

```
      NO.  GLOBAL      1      2      3
       1  0.88850   1.000  0.771 -0.778 fishBBg2_mean
       2  0.78116   0.771  1.000 -0.520 fishBBg2_sigm1
       3  0.78838  -0.778 -0.520  1.000 fishBBg2_sigm2
```

$B^0 \to D^- \pi^+, D^- \to K_s^0 K^-$

```
PARAMETER  CORRELATION COEFFICIENTS
      NO.  GLOBAL      1      2      3
       1  0.82809   1.000  0.679 -0.687 fishBBg3_mean
       2  0.69445   0.679  1.000 -0.359 fishBBg3_sigm2
       3  0.70177  -0.687 -0.359  1.000 fishBBg3_sigm1
```

$B^0 \to D^- \rho^+$

```
 PARAMETER  CORRELATION COEFFICIENTS
      NO.  GLOBAL      1      2      3
       1  0.84900   1.000  0.765 -0.641 fishBBg4_mean
       2  0.77449   0.765  1.000 -0.395 fishBBg4_sigm1
       3  0.65810  -0.641 -0.395  1.000 fishBBg4_sigm2
```

$B^0 \to J/\psi K_S^0$

```
PARAMETER  CORRELATION COEFFICIENTS
      NO.  GLOBAL      1      2      3
       1  0.83470   1.000  0.681 -0.702 fishBBg5_mean
       2  0.69675   0.681  1.000 -0.374 fishBBg5_sigm1
       3  0.71650  -0.702 -0.374  1.000 fishBBg5_sigm2
```

$B^0 \to \psi(2S) K_S^0$

```
 PARAMETER  CORRELATION COEFFICIENTS
      NO.  GLOBAL      1      2      3
       1  0.91069   1.000  0.852 -0.755 fishBBg6_mean
       2  0.85754   0.852  1.000 -0.577 fishBBg6_sigm1
       3  0.76511  -0.755 -0.577  1.000 fishBBg6_sigm2
```

$B^{\pm} \to D^0\pi^{\pm}, D^0 \to K_S^0\pi^0$

```
PARAMETER  CORRELATION COEFFICIENTS
      NO.  GLOBAL      1      2      3
       1  0.87561   1.000  0.771 -0.734 fishBBg7_mean
       2  0.78135   0.771  1.000 -0.480 fishBBg7_sigm1
       3  0.74649  -0.734 -0.480  1.000 fishBBg7_sigm2
```

$B^0 \to D^{\pm}\pi^{\mp}, D^{\pm} \to K_S^0\pi^{\pm}\pi^0$

```
PARAMETER  CORRELATION COEFFICIENTS
      NO.  GLOBAL      1      2      3
       1  0.87561   1.000  0.771 -0.734 fishBBg8_mean
       2  0.78135   0.771  1.000 -0.480 fishBBg8_sigm1
       3  0.74649  -0.734 -0.480  1.000 fishBBg8_sigm2
```

$B^{\pm} \to D^{*\pm}\pi^{\mp}, D^{*\pm} \to D^0\pm^{\pm}, D^0 \to K_S^0\pi^0$

```
PARAMETER  CORRELATION COEFFICIENTS
      NO.  GLOBAL      1      2      3
       1   0.88919   1.000  0.801 -0.746 fishBBg9_mean
       2   0.80941   0.801  1.000 -0.518 fishBBg9_sigm1
       3   0.75709  -0.746 -0.518  1.000 fishBBg9_sigm2
```

Therefore, no PDF variables have any correlations with variables from another PDF, and no systematics need to be added for such an effect.

Appendix C

The $B^0 \to D^{\mp}\pi^{\pm}$ Fit Tests

The fit tests that were described in Section 5.1 were also carried out for the $B^0 \to D^{\mp}\pi^{\pm}$mode. No bias was seen in the toy tests, and the data arrow in the NLL test is in the centre of the distribution. For the embedded fit, a slight pull of -0.06σ was found. Each experiment was conducted for 500 experiments and the results can be seen in Figure C.1. The ${}_sPlots$ for the ML fit are shown in Figure C.2.

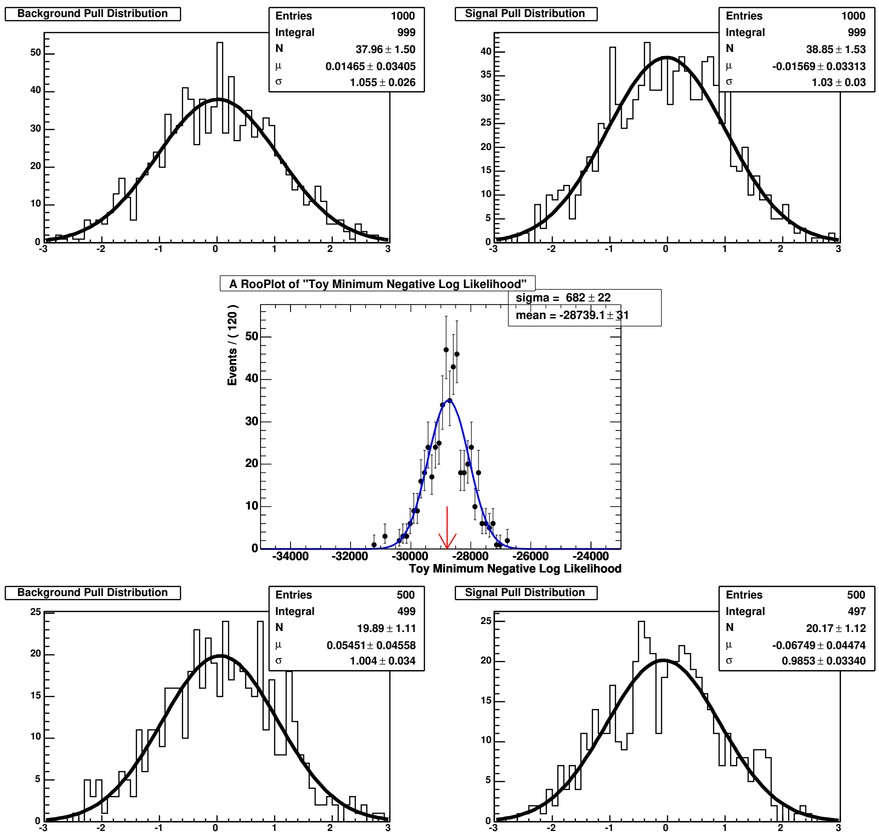

Figure C.1: The results of the fit tests for $B^0 \to D^{\mp}\pi^{\pm}$. The top plots show the pulls on the number of signal and background events using the full model, which also floats the Argus parameter, the slope of the continuum background, the background fisher parameters and all the signal parameters except for n and α in the $m_{\rm ES}$ signal PDF. The top plot shows the results of the toy tests which show no evidence of any pull in the yields. The middle plot shows excellent agreement between the data NLL and the toy NLL distribution. The embedded fit test is shown in the bottom plot with a small pull on the signal yield of -0.06σ. Each test consisted 500 experiments.

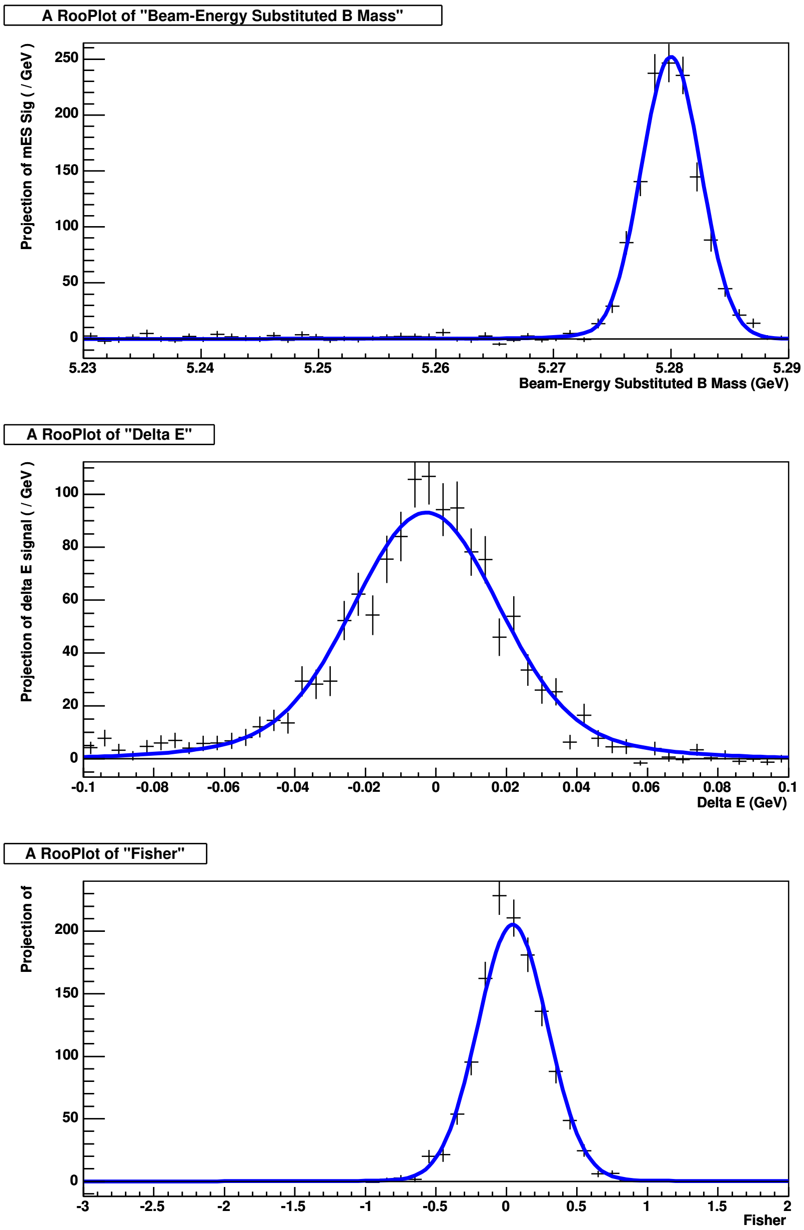

Figure C.2: The $_s$Plots for the calibration fit to $B^0 \rightarrow D^{\mp}\pi^{\pm}$. The signal distribution is overlaid with the signal fit for m_{ES} (top), ΔE (middle) and fisher (bottom).

Bibliography

[1] R. W. Hayward D. D. Hoppes C. S. Wu, E. Ambler and R. P. Hudson, Experimental test of parity conservation in beta decay, *Phys. Rev.* **105** (1957).

[2] V. L. Fitch J. H. Christenson, J. W. Cronin and R. Turlay, Evidence for the 2 pi decay of the K(2)0 meson, *Phys. Rev. Lett.* **13** (1964).

[3] M. Kobayashi and T. Maskawa, *Prog. Theor. Phys.* **49**, 652 (1973).

[4] ed. Harrison, P. F. and ed. Quinn, Helen R., The *BABAR* physics book: Physics at an asymmetric B factory, Papers from Workshop on Physics at an Asymmetric B Factory (*BABAR* Collaboration Meeting), Rome, Italy, 11-14 Nov 1996, Princeton, NJ, 17-20 Mar 1997, Orsay, France, 16-19 Jun 1997 and Pasadena, CA, 22-24 Sep 1997.

[5] H. Quinn, (1997), http://pdg.lbl.gov/1999/bbmix_s042224.pdf.

[6] K. Hagiwara *et al.* Particle Data Group, *Phys. Lett. B* **592**, 1–1109 (2004).

[7] R. H. Dalitz, *Phil. Mag.* **44** (1953).

[8] D. M. Asner *et al.*, Search for CP violation in D^0 –> $K_S^0\pi^+\pi^-$, *Phys. Rev.* **D70**, 091101 (2004).

[9] H. R. Quinn H. J. Lipkin, Y. Nir and A. Snyder, Penguin trapping with isospin analysis and CP asymmetries in B decays, *Phys. Rev. D* **44**, 1454 (1991).

[10] N. G. Deshpande, N. Sinha and R. Sinha, *Phys. Rev. Lett.* **90**, 61802 (2003).

[11] A. J. Buras G. Buchalla and M. E. Lautenbacher, Weak decays beyond leading logarithms, *Rev. Mod. Phys.* **68** (1996).

[12] M. Neubert M. Beneke, G. Buchalla and C. T. Sachrajda, QCD factorization for $B \to \pi\pi$ decays: Strong phases and CP violation in the heavy quark limit, *Phys. Rev. Lett.* **83** (1999).

[13] Jun-feng Sun, Guo-huai Zhu, and Dong-sheng Du, Phenomenological analysis of charmless decays B/s –> P P, P V with QCD factorization, *Phys. Rev.* **D68**, 054003 (2003).

[14] N. de Groot, W. N. Cottingham, and I. B. Whittingham, Factorization fits and the unitarity triangle in charmless two-body B decays, *Phys. Rev.* **D68**, 113005 (2003).

[15] Cheng-Wei Chiang, Michael Gronau, Zumin Luo, Jonathan L. Rosner, and Denis A. Suprun, Charmless B –> V P decays using flavor SU(3) symmetry, *Phys. Rev.* **D69**, 034001 (2004).

[16] Dong-sheng Du, Hai-jun Gong, Jun-feng Sun, De-shan Yang, and Guo-huai Zhu, Phenomenological analysis of charmless decays B –> P V with QCD factorization, *Phys. Rev.* **D65**, 094025 (2002).

[17] E. Eckhart *et al.*, Observation of B to $K^0_S\pi^+\pi^-$ and evidence for B to $K^{*\pm}\pi^{\mp}$, arXiv:hep-ex/0206024, (2002).

[18] A. Garmash *et al.*, Three-body charmless B –> Khh decays at Belle, arXiv:hep-ex/0207003, (2002).

[19] B. Aubert *et al.*, Measurements of neutral B decay branching fractions to $K^0_S\pi^+\pi^-$ final states, *Phys. Rev. D* **70**, 091103.

[20] B. Aubert *et al.*, Evidence for B0 –> rho0 K0(S), arXiv:hep-ex/0408079, (2004).

[21] B. Aubert *et al.*, $B^0 - > K^+\pi^-\pi^0$ Dalitz plot analysis, arXiv:hep-ex/0408073, (2004).

[22] B. I. Eisenstein *et al.*, Measurement of the charge asymmetry in $B^0 -> K^{*\pm}(892)\pi^{\mp}$, *Phys. Rev.* **D68**, 017101 (2003).

[23] B. Aubert *et al.*, Observation of direct CP violation in B0 –> K+ pi- decays, *Phys. Rev. Lett.* **93**, 131801 (2004).

[24] The Belle Collaboration, http://belle.kek.jp.

[25] B. Aubert *et al.*, Improved measurement of CP asymmetries in B^0 –> $(c\ anti-c)K^{(*)0}$ decays, arXiv:hep-ex/0408127, (2004).

[26] B. Aubert *et al.*, A measurement of CP violating asymmetries in B^0 –> $f_0(980)K_S^0$ decays, arXiv:hep-ex/0408095, (2004).

[27] Heavy Flavor Averaging Group, http://www.slac.stanford.edu/xorg/hfag/triangle/ichep2004/index.shtml.

[28] B. Aubert *et al.*, Improved measurements of CP-violating asymmetries in B^0 –> $\pi^+\pi^-$ decays, arXiv:hep-ex/0408089, (2004).

[29] B. Aubert *et al.*, Measurement of CP-violating asymmetries in B0 –> (rho pi)0 using a time-dependent Dalitz plot analysis, arXiv:hep-ex/0408099, (2004).

[30] Lydia Roos, Measurements related to CKM angle alpha in BaBar, arXiv:hep-ex/0407051, (2004).

[31] B. Aubert *et al.*, Constraints on r(B) and gamma in B+- –> $D^{(*)0}K^{\pm}$ decays by a Dalitz analysis of D^0 –> $K_S^0\pi^+\pi^-$, (2004).

[32] An asymmetric B factory based on PEP: Conceptual design report, SLAC-0372.

[33] B. Aubert *et. al*, The *BABAR* detector, *Nucl. Instrum. Meth.* **A479**, 1–116 (2002).

[34] C. Hearty, Measurement of the Number of Upsilon(4S) Mesons Produced in Run 1 (B Counting), *BABAR* Analysis Document 134, (2001).

[35] D.J. Lange and A.Ryd, EvtGen documentation, *BABAR* ANALYSIS DOCUMENT 52, (2003).

[36] Torbjörn Sjöstrand, PYTHIA 5.7 and JETSET 7.4, http://dino.ip.fmph.uniba.sk/pythia_html3/pythia57.html, (1993).

[37] S. Agostinelli *et al.*, GEANT4: A simulation toolkit, *Nucl. Instrum. Meth. A* **506** (2003).

[38] K. Hagiwara *et al.* Particle Data Group, *Phys. Rev. D* **66**, 010001 (2002).

[39] Available Lists and Maps in the Micro Database, http://hepunx.rl.ac.uk/BFROOT/www/doc/workbook/nanomicro/v8.8/Micro/CandLists.html#trackneutral.

[40] W. M. Dunwoodie, Simple observations on b bbar kinematics, http://www.slac.stanford.edu/~wmd/bbkinematics/kinematics.note.

[41] R. Brun and F. Rademakers, http://root.cern.ch.

[42] Argus Collaboration, *Z.Phys. C* **48**, 543 (1990).

[43] R. A. Fisher, *Ann. Eugenics* **7**, 179 (1936).

[44] G. Cowan, *Statistical Data Analysis*, Oxford University Press, 1998.

[45] J. Beringer, BTagger - A Multivariate Tagging Algorithm with Categories Based on the Physics of the Btag Decay, *BABAR* Analysis Document 317, (2002).

[46] D. M. Asner *et al.*, *Phys. Rev. D* **53**, 1039 (1996).

[47] S. Spanier and G. Mancinelli, Kaon selection at *BABAR*, *BABAR* ANALYSIS DOCUMENT 116, (2001).

[48] T. Brandt, Electron likelihood selector, http://www.slac.stanford.edu/~tbrandt/electronid/.

[49] F. Le Diberder and M. Pivk, ${}_s\mathcal{P}lots$, arXiv:physics/040208, (2004).

[50] T. Skwarnicki, A Study of the Radiative Cascade Transitions Between the Upsilon Prime and Upsilon Resonances, *DESY F31-86-02 (thesis, unpublished)* (1986).

[51] K.S. Cranmer, Kernel estimation in high-energy physics, *Comput. Phys. Commun.* **136**, 198–207 (2001).

[52] A. Soffer J. Smith and R. Waldi, Recommendation for exclusive B reconstruction analysis variables, *BABAR* note 497, (1999).

[53] F. James, Minuit reference manual (version 94.1), *Program Library Long Writeup D506, CERN, Geneva* .

[54] B. Bajc, S. Fajfer, R. J. Oakes, T. N. Pham, and S. Prelovsek, The CP violating asymmetry in $B^{\pm}$ –> $M\overline{M}\pi^{\pm}$ decays, *Phys. Lett.* **B447**, 313–320 (1999).

[55] S. Spanier, Paramerization of the Dynamics of Partial Wave Amplitudes, *BABAR* Analysis Document 303, (2001).

[56] D. Aston *et al.*, *Nucl. Phys. B* **296** (1988).

[57] W. M. Dunwoodie, Fits to K pi I=1/2 S-wave amplitude and phase data, http://www.slac.stanford.edu/∼wmd/kpi_swave/kpi_swave_fit.note.

[58] L. B. Madsen, Effective range theory, http://www.phys.au.dk/quantop/lars/spredningsteori/ajpeffective.pdf.

[59] B. Aubert *et al.*, Amplitude analysis of $B^{\pm} \rightarrow \pi^{\pm}\pi^{\mp}\pi^{\pm}$ and $B^{\pm} \rightarrow K^{\pm}\pi^{\mp}\pi^{\pm}$, arXiv:hep-ex/0408032, (2004).

[60] B. Aubert *et al.*, Measurements of the branching fraction and CP-violation asymmetries in B^0 –> $f_0(980)K^0_S$, arXiv:hep-ex/0406040, (2004).

[61] Heavy Flavor Averaging Group, http://www.slac.stanford.edu/xorg/hfag/rare/ichep04/charmless/OUTPUT/TABLES/charmless.pdf.

[62] The *BABAR* Tracking Efficiency Task Force, http://www.slac.stanford.edu/BFROOT www/Organization/CollabMtgs/2004/detFeb04/Fri2/cavoto.pdf.

[63] The *BABAR* Tracking Efficiency Task Force, http://www.slac.stanford.edu/BFROOT/www/Physics/TrackEfficTaskForce/TrackingTaskForce-2004.html.

[64] The *BABAR* PID Group, http://www.slac.stanford.edu/BFROOT/www/Physics/Tools/Pid/PidOnMc/pidonmc.html.

[65] P. F. Harrison K. E. Ford and E. O. Olaiya, Studies of the Decays $B^0 \to K_S^0\pi^+\pi^-$, *BABAR* Analysis Document 581, (2004).

[66] *BABAR* K_S^0 Reconstruction Efficiency Group, http://www.slac.stanford.edu/BFROOT/www/Physics/TrackEfficTaskForce/Recipe/R14/KsEff_R14.html.

[67] A. Garmash *et al.*, Study of B meson decays to three-body charmless hadronic final states, arXiv:hep-ex/0307082, (2003).